



UNIVERSITÉ DE STRASBOURG  
École Doctorale des Sciences Chimiques  
Institut de Science et d'Ingénierie Supramoléculaires

## THÈSE

présentée par

**Victoire GOUST**

Soutenue le 7 novembre 2011

pour obtenir le grade de : **Docteur de l'Université de Strasbourg**

Discipline/ Spécialité : Chimie

### FLUORESCENT SILICA NANOPARTICLES FOR MULTIDIMENSIONAL BARCODING IN DROPLETS: TOWARDS HIGH-THROUGHPUT SCREENING IN TWO-PHASE MICROFLUIDICS

THÈSE dirigée par :

**M. GRIFFITHS Andrew**

Professeur, Université de Strasbourg

RAPPORTEURS :

**Mme ANDERSSON Svahn Helene**

Professeur, KTH, Stockholm

**M. BIBETTE Jérôme**

Professeur, ESPCI, Paris

---

AUTRES MEMBRES DU JURY :

**Mme KRAFFT Marie-Pierre**

Directrice de recherche, Université de  
Strasbourg

**M. PERSELLO Jacques**

Professeur, Université de Nice



XXIII.

D'un plus savant que toi ne cesse point d'apprendre ;  
Toi-même instruis les ignorants.  
La science est un bien qu'il faut partout répandre,  
Et qu'on doit préférer aux trésors les plus grands.

XXIX.

Fais-toi gloire d'apprendre, étant dans l'ignorance ;  
Et pour croître en savoir, ne néglige aucun soin ;  
C'est vertu d'aimer la science,  
Et vice de rougir de s'instruire au besoin.

- Caton, *Distiques*, livre quatrième.





# Acknowledgments

This PhD would not have been possible without the support of many people from many different places; I am grateful to them all to have guided and helped me during these three years.

First, I want to thank Prof. Andrew Griffiths for welcoming me in his laboratory as part of the dScreen project. I am grateful to you for supporting my 6-month mission at RainDance Technologies, and for your trust and positive input all throughout. This PhD was a challenge that I am honored you offered me to take up.

I am also grateful to Ministère de l'Enseignement Supérieur et de la Recherche for providing the scholarship which has enabled me to carry out the work reported in this thesis.

It is a great honor for me that Prof. Helene Andersson-Svahn, Prof. Jérôme Bibette, Prof. Jacques Persello and Dr. Marie-Pierre Krafft have agreed to participate in the evaluation of this PhD work.

Furthermore, this PhD would not have been the same without the precious advice and support of several advisors: thanks to Abdeslam El Harrak, for all your patience, wisdom, always interesting discussions (scientific or not) and unlimited stocks of Stoptou candy. Many thanks as well to Jean Christophe Baret for recruiting me here, offering his scientific curiosity at all times and later hosting me for two weeks in his new lab in lovely Göttingen. I wish your group a lot of success and exciting results. Finally, I am deeply grateful to Brian Hutchison for his guidance, patience, and constant support since my first experience at RainDance Technologies five years ago. I hope we will keep in touch!

As a PhD is a human as well as a scientific journey, I would like to thank all the LBC members I worked with during these years. First, thanks to all the members of the dScreen team: it has been really fulfilling to work with you on such a multidisciplinary and exciting project. Thanks to Thomas Mangeat, who took a lot of his time to initiate me to the many intricacies of optics, to teach me how to ask myself the most relevant scientific questions and to taste my numerous culinary experimentations. Thanks also to Estelle Mayot, my office and home neighbor: I will miss the chemistry talk, the good time in the office and your delicious mojitos! Finally, thanks to Oliver Miller and Felix Kleinschmidt: it is rare to meet people with such outstanding scientific curiosity and skills to teach and discuss even complicated scientific issues.

I shall not forget to acknowledge the other LBCees. First, thanks to Isabelle, without whom the lab would certainly not run so smoothly! Thanks to all the former PhD candidates who paved the way for us and showed us that yes, it is possible to graduate and remain sane: Lucia, Diana,

Jeni, Lucas, Dave, Linas, good luck to all of you in your new careers and life paths. Some special thoughts to the group of soon-to-be PhDs: Ali, Thomas B, Youssr and Bachir, being in your company has been really fun, and exchanging tips about Word formatting, administrative hurdles or final experiments, very helpful. Good luck to the still-PhD candidates Deniz, Alexei and Jean François: keep going, it is totally worth it!! Special thanks to our two lovely long-term visitors Ashleigh and Gabrielle: your sense of fun, optimism and kindness were a permanent sunshine in the lab. Finally, thanks to all the other current and former lab members: Valérie, Chaouki, Btisse, Mickaël, Shigeyoshi, Faith, Annick, Yannick, Nisha, Raphaël D, Hwa Seng, Antoine, Majdi, Raphaël C, Putu, Christian, Christoph, Sophie, Philippe: it's been a pleasure to interact with you.

This PhD would not have been the same without all the collaborations and the teamwork it brought. I owe all my gratitude to RainDance Technologies for hosting me twice: not only did it give me invaluable training in droplet microfluidics, but also was a really fulfilling cultural and human experience. Special thanks to Brian Hutchison, Darren Link, to the Chemistry group, to Qun Zhong, Roland Ferenczhalmy and Martina Medkova for their valuable advice and help. Thanks to Quentin Brosseau, Benoît Semin and the DMI team of Max Planck Institute in Göttingen, for bringing enthusiasm, ideas and new tools to explore interfacial tensions dynamics. Thanks to Katarzyna Blazewska for her work on the oil exchange project. Finally, thanks to Martin Galvan and Eamonn Rooney from Sanofi-Aventis, for interesting discussions during our quarterly dScreen meetings.

I am also grateful to my former research supervisors: Krassimir Velikov, for supporting my first research experience in colloids about fascinating microemulsions, as well as Benoît Dubertret and all the Quantum dots team of ESPCI, for introducing me to the wonders and intricacies of these colorful small crystals. Finally, I am indebted to Jérôme Bibette, for supporting my first experience at RainDance, and instigating valuable discussions all throughout my research years. Your honest and acute advice gave me a lot of food for thought. I shall not forget all my past physics and chemistry teachers, who were my first inspiration to pursue the exploration of these fields.

And because this PhD would not have been so fulfilling without side activities, thanks to the Scout group of St Germain des Prés for the 3 memorable summer camps I had with you. Thumbs up to the FunDu molecular cooking gang at RDT: Steve, Mysoon, Hadeel, Elodie and Smiiti, thanks for accepting to be part of this fun project. Spread the word: egg whites rule! Finally, thanks to the board members of Addal: I was glad to belong to your team and to organize fun activities for young researchers of Alsace.

Thanks to all my family, especially my father, who stirred my curiosity about science from the earliest age (and still does, in a greater variety of subjects), and my mother, who let me follow a scientific path in spite of her stronger inclination for literature.

Finally, my last lines will be for all my friends who really helped me go through hard times and brought lots of good ones. Ségolène, my precious friend and nearly sister, what a funny coincidence that we will complete our greatest life achievement at the same time! Who knows? Maybe your child will read this thesis one day... Thanks to Kim, my dear friend from Connecticut, for your hospitality and warmth: I hope we'll keep seeing each other when one of us travels across the Pond? Thanks also to Elodie, the other *petite française* at RDT: thanks for your friendship, advice and passenger seat, you really helped me go through ups and downs during this rough Bostonian winter. Good luck for the continuation of your project, maybe our new respective paths will cross soon!



## Abstract

High-throughput screening assays require small sample volumes to reduce costs and to allow rapid sample manipulation. However, further miniaturization of conventional microtiter plate technology is problematic, due to evaporation and capillarity. Microarray technology, although more miniaturized, is not suitable for all types of assays. To overcome the limitations of these two technologies, implementation of drug screening on droplet-based microfluidic platforms could potentially bring a breakthrough in terms of throughput and reduction of costs.

However, as opposed to the two previously mentioned technologies, droplets, once out of the chip, lose positional information to identify drop contents. It is thus necessary to find a way to label the compounds encapsulated in each droplet. Since fluorescence is already widely used for assay readout, a fluorescent label seems the most straightforward strategy. The goal of this PhD was to find and characterize a fluorescent material compatible with the specificities of droplet microfluidics then to generate several optically encoded droplet libraries with it.

Based on the stringent requirements of our system, we opted for silica nanoparticles (SNPs) covalently encapsulating organic fluorophores. We developed a novel synthesis route based on acidification of silicates by an exchange resin that enabled us to reach sizes between 2.5 and 6.5 nm: our nanoparticles are the smallest fluorescent SNPs ever synthesized. Compared to the starting fluorophores in solution, they exhibit similar absorption/emission spectra, but 2.2-fold higher brightness, significantly better resistance to photobleaching and tunable fluorescence polarization, leaving potential for coding in the FP dimension as well.

Subsequently, we studied the surface properties of these particles, especially their interaction with the surfactant, with regards to adsorption kinetics and long-term stabilization. At sub-second time scales, no noticeable influence was observed; however at longer times, competition between particles and surfactant was shown. In addition, dramatic osmotic effects were highlighted in case of unequal particle concentration across droplets: for our code, we would hence equilibrate particle concentration with non-fluorescent particles.

To conclude our work and meet our initial goal, we investigated crucial parameters to design a fluorescent code, then generated two- and three-color encoded droplet libraries. From these sets of data, we discussed the quality of our code, together with several ways to offset crosstalk and to do on-the-fly identification of codes within droplets. Finally, we discuss different applications that would benefit from this encoding system. Together, this work at the frontier of materials science, emulsion science, microfluidics and optics opens many perspectives to confirm droplet-based microfluidics as a powerful high-throughput screening platform.

# Contents

<b>Acknowledgments</b> .....	<b>v</b>
<b>Abstract</b> .....	<b>ix</b>
<b>Contents</b> .....	<b>xi</b>
<b>Chapter 1. General introduction</b> .....	<b>1</b>
1.1 Droplet microfluidics, a promising technique for high-throughput screening.....	2
1.1.1 Non-fluidic HTS methods .....	2
1.1.2 Fluidic HTS systems .....	4
1.1.3 Advantages of droplet-based microfluidics for HTS .....	7
1.1.4 Microfluidic modules for manipulation of droplets .....	9
1.1.5 A broad range of applications.....	15
1.2 Fundamentals of droplet formation and stabilization.....	18
1.2.1 Hydrodynamic principles of droplet microfluidics.....	18
1.2.2 The role of surfactant, and how to choose it .....	21
1.2.3 Emulsion destabilization mechanisms.....	23
1.3 Fluorescence-based droplet labeling.....	26
1.3.1 Principles and advantages of fluorescence.....	27
1.3.2 Fluorescence-based detection systems .....	30
1.3.3 Principle of fluorescent encoding .....	31
1.3.4 Fluorescent materials for droplet encoding.....	33
1.4 Scope of the thesis .....	35
1.5 References.....	36
Chapter 2. Synthesis and characterization of novel fluorescent silica nanoparticles .....	47
2.1 Preliminary considerations .....	47
2.1.1 Generalities about silica .....	47
2.1.2 Colloidal stabilization of silica nanoparticles.....	48
2.1.3 Colloidal silica: synthesis routes .....	52
2.1.4 Fluorescently labeled silica nanoparticles.....	55
2.2 Optimization of the reaction steps.....	58

2.2.1	Silica synthesis at pH 9: optimal conditions .....	59
2.2.2	Core synthesis: finding the maximal size .....	59
2.2.3	Shell growth: exploring several strategies.....	61
2.2.4	Dye grafting in the silica cores.....	67
2.2.5	PEG grafting efficiency .....	69
2.2.6	Overall synthesis scheme: size characterization and long-term stability .....	72
2.3	Radiative properties of F-SNP.....	74
2.3.1	Absorption/emission spectra .....	74
2.3.2	Extinction coefficient/ Quantum yield.....	75
2.3.3	FP modulation vs. quenching.....	78
2.3.4	Photobleaching .....	81
2.4	Conclusion .....	82
2.5	Experimental section.....	83
2.5.1	Coupling of fluorophores with silane precursor.....	83
2.5.2	Silica nanoparticles synthesis .....	83
2.5.3	Dynamic light scattering.....	84
2.5.4	TEM observation .....	84
2.5.5	Steady absorbance/fluorescence/FP measurements .....	85
2.5.6	Photobleaching .....	85
	References .....	85
	Acknowledgment of collaboration .....	89
	<b>Chapter 3. Silica nanoparticles at fluorinated oil-water interfaces .....</b>	<b>91</b>
3.1	Introduction.....	91
3.1.1	Surfactant adsorption at the interface.....	91
3.1.2	Colloidal particles at interfaces .....	93
3.1.3	Nanoparticles and surfactant: what interaction?.....	95
3.1.4	Goal of this chapter .....	96
3.2	Droplet size at generation: influence of aqueous phase.....	96
3.3	Interaction between nanoparticles and surfactant at the interface: a kinetic study.....	98
3.3.1	Preliminary experiment: determination of the CMC and micelle size of EA in HFE	
7500	.....	99

3.3.2	Preliminary calculations: diffusion times of SNP and surfactant .....	99
3.3.3	Short timescale (0.05 – 1 s): on-chip droplet deformation kinetics .....	101
3.3.4	Medium time range (1 – 300 s): dynamic interfacial tension measurements with pendant drop tensiometer.....	107
3.4	Long-term stability of emulsions containing SNP .....	115
3.5	Conclusion and perspectives .....	119
3.6	Materials and methods .....	120
3.6.1	Chemicals.....	120
3.6.2	CMC measurement by DLS.....	121
3.6.3	CMC measurement by pendant drop tensiometry .....	121
3.6.4	Generation of microfluidic droplets for size at generation and long-term stability measurements .....	121
3.6.5	Measurements of droplet size at generation.....	122
3.6.6	Fabrication of droplet deformation chip .....	122
3.6.7	On-chip measurement of surfactant adsorption kinetics .....	123
3.6.8	Interfacial tension measurements by pendant drop technique.....	124
3.6.9	Fabrication of droplet generation (LRS 6.6) and ‘droplet’ chips.....	124
3.6.10	Microfluidic emulsion characterization by image analysis.....	125
	References .....	125
	Acknowledgment of collaboration .....	128
	<b>Chapter 4. Fluorescently encoded droplet libraries .....</b>	<b>129</b>
4.1	Introduction.....	129
4.1.1	Current multiplexing platforms.....	129
4.1.2	Droplet microfluidic assays using fluorescent barcodes.....	131
4.1.3	Spectral crosstalk and compensation.....	135
4.1.4	Goal of this chapter .....	155
4.2	Preliminary considerations .....	137
4.2.1	Choice of optical setup.....	138
4.2.2	Determination of optimal SNP concentration range.....	138
4.2.3	Code spacing and standard deviation vs tolerance for overlap .....	138
4.2.4	Minimization of standard deviation of distributions.....	141



4.2.5	Calibration of PMTs gain vs SNP concentration .....	143
4.3	Two- and three-dimensional fluorescent codes .....	146
4.3.1	Two colors (F-SNP and RhB-SNP) .....	146
4.3.2	Three colors (F-SNP, RhB-SNP and Dylight 680-SNP).....	147
4.4	Spectral crosstalk reduction and compensation .....	150
4.4.1	Influence of optical setup.....	150
4.4.2	“Quick and dirty” post-processing: visual adjustment.....	151
4.4.3	Mathematical post-processing .....	153
4.5	Barcode identification: towards automation .....	155
4.5.1	First “easy” strategy: binning of 2- or 3-D space.....	155
4.5.2	Second “refined” strategy: cluster analysis.....	156
4.6	Barcode strategy vs. application.....	157
4.6.1	General considerations .....	157
4.6.2	First case: detection of a rare mutation .....	157
4.6.3	Second case: digital PCR with 25-plex assay .....	158
4.6.4	Third case: HTS of inhibitor libraries.....	158
4.7	Conclusion and outlook.....	159
4.8	Materials and methods .....	161
4.8.1	Chemicals.....	161
4.8.2	Chip fabrication .....	162
4.8.3	Preparation of barcode libraries .....	162
4.8.4	Library encapsulation in droplets.....	165
4.8.5	On-chip droplet fluorescence measurements.....	166
4.8.6	Data acquisition and plotting.....	167
4.8.7	Compensation matrix calculation.....	168
4.8.8	Cluster recognition .....	169
	References .....	169
	Acknowledgment of collaboration .....	171
	<b>Chapter 5. Summary and perspectives .....</b>	<b>173</b>
5.1	Context.....	173
5.2	Synthesis and characterization of novel fluorescent silica nanoparticles.....	173

5.3	Silica nanoparticles at fluorinated oil/water interfaces.....	175
5.4	Fluorescently encoded droplet libraries.....	176
5.5	Perspectives .....	177
<b>Chapter 6. Résumé de thèse .....</b>		<b>179</b>
6.1	Contexte du projet.....	179
6.2	Synthèse et caractérisation de nanoparticules de silice fluorescentes.....	180
6.3	Nanoparticules de silice aux interfaces eau/huile fluorée.....	182
6.4	Banques de gouttes codées en fluorescence .....	183
6.5	Conclusion et perspectives .....	184
<b>Appendix A. Fluorinated compounds .....</b>		<b>187</b>
A.1	Fluorinated oil HFE 7500 .....	187
A.2	Fluorinated surfactant EA.....	187
<b>Appendix B. Microfluidic designs.....</b>		<b>189</b>
B.1	Library generation chip ‘LRS 6.6’ .....	189
B.2	‘Dropslot’ emulsion analysis chip.....	189
B.3	Library reinjection chip ‘test 32.2’ .....	190
<b>Appendix C. Optical stations .....</b>		<b>191</b>
C.1	‘PLS 3’ station.....	191
C.2	‘dScreen’ station .....	192

# Chapter 1. General introduction

In the 1950s, the invention of integrated circuits led to a revolution in electronics, allowing a dramatic decrease in cost of electronic components, as well as a level of automation and miniaturization never reached before. The rush for miniaturization soon spread to other fields such as sensor technology and medical devices with the rise of MEMS (Microelectromechanical systems).

However, some fields like drug discovery still have not managed to implement such level of miniaturization in their processes. High-throughput screening platforms still widely consist of microplate-based assays. Unfortunately, this technology has reached its maximal miniaturization level: to keep increasing the throughput, new screening platforms are necessary. Two miniaturized platforms have recently emerged as the most promising successors of microplates: microarrays and microfluidics. The former has shown some potential but has serious limitations; while the latter, based on microfabrication techniques from the microelectronics industry, still holds great promise. In particular, two-phase microfluidics consists of encapsulating reagents in picoliter emulsion droplets at a rate of several kHz, then manipulating them on a chip the size of a credit card. Such unprecedented small volumes and high throughput could enable considerable parallelization and multiplexing of bioassays. Nevertheless, to track millions of droplets hosting thousands of distinct reactions, it is necessary to label each of them: a specific encoding system has to be integrated to the platform.

This chapter will first present the origins, advantages and technical features of droplet microfluidics, then describe some recent high-throughput assays developed with this platform. In order to better assess the parameters to take into account when developing labeling materials and applications for such two-phase microsystems, fundamentals of microfluidics and emulsions physics and chemistry will be discussed in a second part. Next, fluorescence-based detection methods will be presented. Finally, strategies to implement fluorescent barcodes, in particular fluorescence multiplexing and novel fluorescent materials, will be discussed.

## 1.1 Droplet microfluidics, a promising technique for high-throughput screening

### 1.1.1 Non-fluidic HTS methods

#### Microplates

In the last 20 years, the pharmaceutical industry has constantly been pushing boundaries to develop faster and more cost-effective drug screening assays. The outcome of this quest has been termed “high-throughput screening”. The most well-known HTS tool, the microtiter plate, was introduced in the 1950s [1]. Thanks to its standardized format, automation was progressively implemented in all assay steps, from plate handling to fluid dispensing, mixing, plate incubation and finally assay readout [2]. Miniaturization of wells has also played a crucial role in the reduction of assays times and volumes: from 96- and 384-well format [3] with volumes of 100 and 20  $\mu\text{L}$  respectively, plates have been optimized up to 3,456 and 9,600 wells [4] for 1 and 0.2  $\mu\text{L}$  assays respectively.



**Figure 1.1** Example of an automated HTS platform using microplates. Operations performed include plate storage, incubation, reading on a fluorimeter and washing. Picture taken from ref [2].

Consequently, from 100 compounds tested per week in 1990, drug-screening platforms handling several plates in parallel reached throughputs of 100,000 assays per hour [5], [6]. However, this drastic reduction in volumes brought new issues: loss of pipetting accuracy, capillarity and evaporation problems as well as difficult reproducibility. Moreover, the lowest reachable volumes still did not allow cost-efficient single-cell analysis. Finally, the maximal speed of fluid-handling robots became the bottleneck, preventing further increase in speed: early screening of million-compound libraries had to be limited to one or two concentration points

each, severely impeding the quality of dose-response data. For all those reasons, further miniaturization appeared as a necessary effort, as highlighted by the scaling laws on **Table 1.1**.

Parameter	Macroscopic example	Factor change	Microscopic example
Length of edge	1 mm	d	1 $\mu\text{m}$
Surface	1 $\text{mm}^2$	$d^2$	1 $\mu\text{m}^2$
Volume	1 $\mu\text{l}$	$d^3$	1 fl
Number of molecules	$10^9$	$d^3$	1
Diffusion time over d ( $D = 10^{-6} \text{ cm}^2\text{s}^{-1}$ )	15 min	$d^2$	1 ms
<i>Example: in flowing systems</i>			
Linear flow rate	1 $\mu\text{m/s}$	d	1 mm/s
Separation time	$10^5 \text{ s}$ (>1 day)*	$d^2$	100 ms
<i>Example: in planar array</i>			
Number of volumes per microwell plate	96	$d^2$	$10^8$

\*Typically, for example, high-performance liquid chromatography in packed column.

**Table 1.1** Influence of system miniaturization from 1 mm to 1  $\mu\text{m}$  characteristic length. Scaling laws give the influence of the system size on reaction parameters like reaction volume, diffusion time and number of assays in parallel. Table taken from ref [7].

## Microarrays

Pushing miniaturization further, microarray technology emerged in the 1980s, evolved from Southern blotting [8]. It consists of arranging multiple assays as a 2D array on a solid substrate (usually a glass slide, plastic chip or silicon film). This platform allows a high number of simultaneous assays using high-throughput screening methods. Several kinds of microarrays exist, depending on the type of assay: DNA microarrays, protein microarrays [9], antibody microarrays [10], cell microarrays [11], tissue microarrays [12] or chemical compound microarrays.

All microarrays rely on the same principle: microscopic spots of biological material (DNA, RNA, proteins, antibodies, drug molecules, etc.) are printed as a 2D array on a solid surface. These spots are attached to the surface, covalently or not, to be used as probes against a target (DNA, RNA, cells, proteins, etc.). Probe-target hybridization is then detected and quantified, usually by detection of fluorescence or chemiluminescence.

The flexibility of microarrays has led to an explosion in commercial platforms like the ones launched by Affymetrix [13], Illumina [14] or Applied Microarrays [15]. However, this technology suffers from several drawbacks [16]: first, the hybridization between target and probe can take a long time because of slow diffusion-limited kinetics. Second, even if chips are miniaturized, reagent consumption is still high to cover the whole array surface (1  $\text{cm}^2$  for high density chips). Third, the covalent bond between the probe and the chip can undergo solution-dependent cleavage at long incubation times. For all those reasons, a novel technology offering faster

reaction times and lower reagent consumption has emerged as an appealing alternative: microfluidics.

## 1.1.2 Fluidic HTS systems

### Continuous flow microfluidics

Based on technology derived from microelectronics, microfluidics initially aimed to increase efficiency of separation techniques, using hydrodynamic or electrokinetic forces to move fluids. In the 1990s, it brought significant miniaturization of electrophoresis platforms [17], [18], eventually leading to commercial platforms like Agilent's Bioanalyzer [19] and Caliper's LabChip [20] for electrophoresis of DNA, RNA and proteins [21]. This new technique provided many advantages: consumption of minute quantities of samples and reagents, low cost, high resolution and sensitivity of separation and detection, short analysis times as well as compact and reusable devices.

Progressively, these appealing characteristics raised interest in many other fields: logical operations [22], protein crystallization [23], single-cell [24] and single molecule analysis [25], optics [26] and our topic of interest, HTS [17], [27]. In particular, clever chip engineering optimized the synergy between miniaturization and parallelization to achieve rapid combinatorial synthesis outcomes without requiring large volumes of expensive reagents. From conventional methods using 4 chips (**Figure 1.2 a**)), 3D lithography made parallel synthesis of 4 components possible on a single one (**Figure 1.2 b**)). Another development provided rapid dose-response analysis, based on devices allowing gradients of drug concentration (**Figure 1.2 c**)) as well as opening/closing of valves (**Figure 1.2 d**)).

In spite of all their advantages, these continuous-flow devices have two major impediments [30]: dispersion of the solutes along the channel and slow mixing. The first problem, also called Taylor-Aris dispersion [31], [32] is caused by the parabolic flow profile in the channel described by the Poiseuille law: the reagents are not transported at a single velocity  $U$ , but a whole range of them  $U(y)$  depending on the distance  $y$  from the channel axis: the further from the axis, the slower the speed. Therefore, a given channel length  $l$  corresponds to a range of reaction times

$t(y) = \frac{l}{U(y)}$ , which renders precise kinetic measurements difficult and can cause cross-

contamination problems between successive plugs. The second drawback is that in microfluidic channels, flow is laminar, which means that two streams injected side-by-side into a channel mix only by diffusion. Mixing can only be accelerated by introducing complex modules: either passive mixers such as grooves, intersecting, zig-zag or 3D channels, or active mixers actuated externally

by pressure perturbation or by acoustic, ultrasonic, dielectrophoretic, electrokinetic, electrohydrodynamic, magnetic or thermal techniques [33].

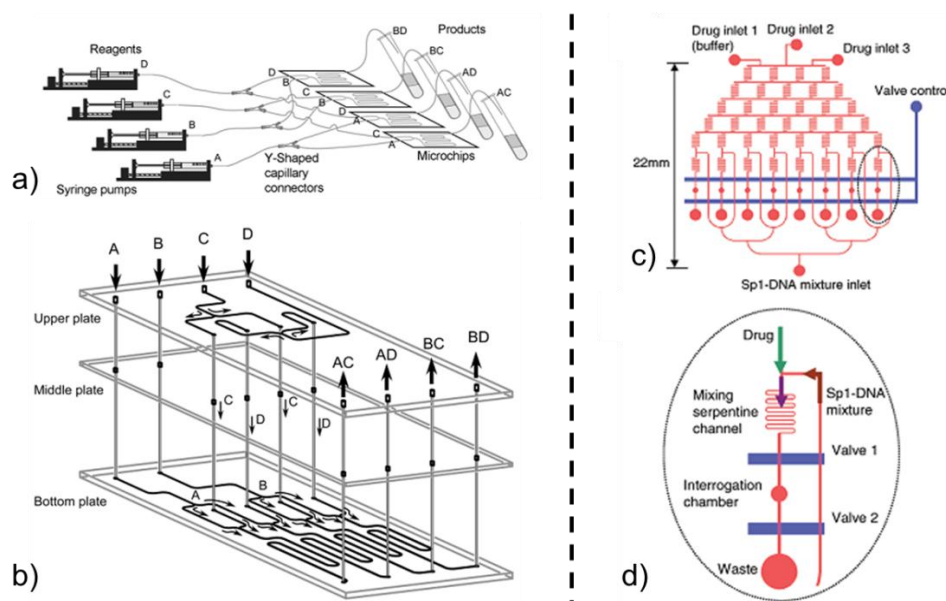


**Figure 1.2** Continuous-flow microfluidics for HTS: combinatorial chemistry and dose-response assays. a) A conventional parallel microreactor system comprising four parallel microfluidic devices, and b) a 3D microreactor chip to carry out a 2 x 2 combinatorial amide synthesis. Reproduced from ref [28]). c) and d) A PDMS-based microfluidic chip used for investigation on the dissociation of Sp1–DNA complex by a drug, doxorubicin. Reproduced from ref [29]).

An alternative strategy emerged in 2003, solving both problems at once [30]: instead of being mixed in a single laminar flow, the two co-flowing miscible liquids were fragmented in small droplets separated by an immiscible fluid. If each droplet occupies the whole channel width, it travels at a single speed, solving the dispersion problem. They also undergo convection, yet its axisymmetric nature does not accelerate mixing of co-flowing liquids. To circumvent this limitation, the straight channel was replaced by a winding channel, to break the symmetry of internal recirculation and generate chaotic mixing, as highlighted on **Figure 1.3**. The breakthrough of droplet-based microfluidics had just started.

### Compartmentalization of biological material: towards droplet-based microfluidics

Based on the previous findings, droplet-based microfluidic hence seemed very suitable to perform chemical reactions. Yet, work from decades earlier had already proved that encapsulation in droplets also offered many advantages for biology. Indeed, in 1954 Joshua Lederberg published a ‘simple method for isolating individual microbes’ [34] that consisted in compartmentalizing single cells into droplets sprayed from a capillary and dispersed in mineral

oil. These droplets adhered on a glass slide, allowing easy observation of the dispersed cells under a microscope. Subsequently, he exploited this method to demonstrate the ‘one cell = one antibody’ rule [35] and Rotman used it later to perform activity measurements of single  $\beta$ -galactosidase molecules [36].

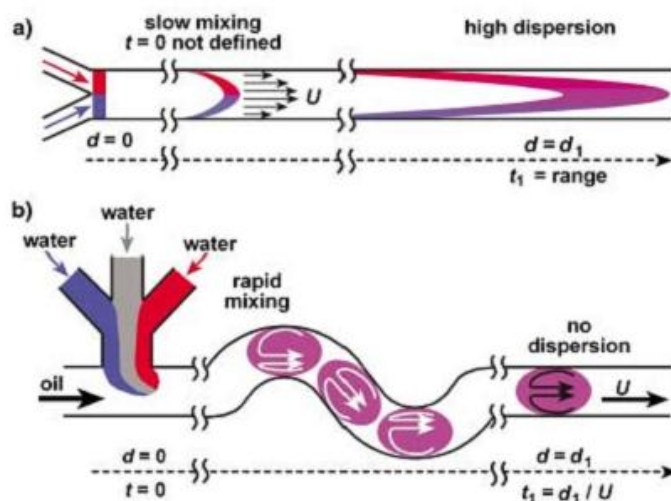


**Figure 1.3** Mixing behaviour of two coflowing liquids as a continuous flow in a straight channel (a) and oil-separated droplets in a winding channel (b). Reproduced from ref [30].

Four decades later, the principle of encapsulation was pushed further with *in vitro* compartmentalization (IVC) of phenotype and genotype together, mimicking what takes place in the cell [37] in order to perform directed evolution [38], whose principle is explained on **Figure 1.4**. Since phenotype (enzymatic activity) and genotype (encoded mutant) were coupled *in vitro*, it was possible to select large libraries of protein variants for catalytic activity.

In spite of all its potential applications, encapsulation by conventional stirring produced very polydisperse bulk emulsions, on which quantitative measurements and further manipulations were problematic. The droplet microfluidic platform presented on **Figure 1.3** appeared as a promising alternative encapsulation technique in order to solve these issues and expand assay capabilities. Progressively, droplet-based microfluidics emerged as a platform with many advantages for development of high-throughput bioassays.



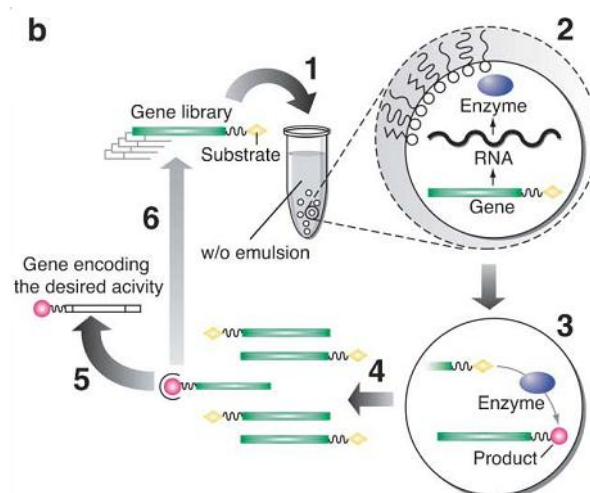


**Figure 1.4** Selection for catalysis using IVC. (1) A library of genes, with substrate molecule(s) attached, is emulsified, isolating single genes in the aqueous compartments, which contain all the ingredients necessary for In-Vitro Transcription. The genes are expressed (2), producing enzymes which may be capable of converting substrate into product (3). Expressed protein or RNA molecules are trapped in the compartment, thus creating a linkage between genotype and phenotype. Consequently, only genes encoding active enzymes have their attached substrate molecules turned over into product molecules. The genes are recovered from the emulsion (4) and those encoding active enzymes are isolated (5) by, for example, specific binding of product molecules. Further rounds of mutagenesis and selection may also be performed (6). Reprinted from ref [39].

### 1.1.3 Advantages of droplet-based microfluidics for HTS

#### Controlled and long-lasting encapsulation

As discussed above, the first advantage of performing biological assays and chemical reactions in fL-nL droplets rather than at the microliter scale, is that it enables individual compartmentalization of single molecules or cells [40]. Once the objects are encapsulated in droplets, the oil provides them long-lasting insulation from the outside and sealing between droplets. This provides good conditions for long-lasting cell-based assays over hours [41–44], days [45–47] or even weeks [48].

As far as drug screening goes, droplet encapsulation of libraries with thousands of compounds could save considerable sample preparation time before assays: instead of transferring each compound from one microplate to another before each assay, the library could be transferred to droplet format. All compounds would be emulsified one after the other: at 10 kHz, droplet generation during 1 min would lead to 600,000 identical droplets of each kind. Then, this library could be split in hundreds of small volume aliquots that could each be used for a separate assay. The long emulsion generation time (16 hours for 1000 compounds) would thus

be compensated by the time saved over each assay. Moreover, if encapsulation is robust, it would allow running experiments with slow kinetics, or running cell-based assays over days or weeks.

### **Monodispersity for quantitative measurements on droplet populations**

As introduced earlier, early encapsulation methods led to very polydisperse emulsions. Therefore, the wide range of volumes implied a broad distribution in concentrations of reagents and products. These diverging reaction conditions make quantitative and reproducible measurements difficult. Conversely, the possibility to generate many droplets with less than 3 % polydispersity [49] opens the way to highly controlled and precise quantitative measurements. In the case of a compounds library, this monodispersity is also a great advantage for the fusion step on-chip: since the both types of droplets being fused have very controlled sizes, the concentration of reagents within the resulting droplet will be very precise as well. This is of great importance for the assay and code readout downstream.

Moreover, as all microfluidic droplets have the same size, concentration of species and follow the same exact path in the channel, it is possible to compare them. This is very valuable in the case of single cell or single molecule studies of random variations that require statistics and analysis on large numbers of experiments and populations.

### **Smaller volumes, more efficient assays**

In section 1.1.1, we already highlighted the drive towards reduction of assay volumes in order to cut development costs. Compared to microliter assays in microplates, picoliter drop volumes obtained in microfluidic channels represent a 6-order of magnitude cut in reagent consumption. Or, alternatively,  $10^6$  times more assays can be performed with the same volume of reagents, allowing screening of a much wider range of conditions or against a broader range of targets. Apart from the cost factor, smaller volumes also mean much shorter mass and heat diffusion times as well as higher surface-to-volume ratios, as emphasized on **Table 1.1.**: such conditions are optimal for studying chemical reactions in the droplet phase or at the interface [50], [51]. Finally, if cells are encapsulated in such small volumes, the substances they release quickly reach detectable concentrations, reducing assay times.

### **High throughput: rapid operations on large droplet numbers**

In most publications, reported droplet generation rates range from 0.1 to 10 kHz. This means that millions of individual reactions are performed in just a single hour. Such a high throughput, only rivaled by modern flow cytometers, enables rapid analysis and statistics, provided sufficiently fast detection techniques are available (some of which are presented later in section 1.3.2). Apart

from detection, fast manipulation techniques have also been developed: controlled coalescence in less than 100  $\mu\text{s}$  by active [52] or passive [53] methods, along with droplet sorting by dielectrophoresis in the kHz range [54].

## **Droplet manipulation, towards a “lab on a chip”**

In order to achieve full “lab-on-chip” integration, the modules corresponding to each individual lab operation need to be miniaturized, connected in line or in parallel and synchronized. This goal has motivated numerous efforts in the last 10 years: their outcome is summarized in the next section.

### **1.1.4 Microfluidic modules for manipulation of droplets**

#### **Why PDMS?**

The first step in designing microfluidic modules is to determine the best material with which to fabricate the channels. Several different materials are reported in the literature: glass, silicon, thermoplastics and elastomers. The requirements for biology applications are quite stringent: the material must be (i) optically transparent to allow microscope observation and detection, (ii) chemically inert and biocompatible, (iii) permeable to gases required to maintain cells alive ( $\text{O}_2$ ,  $\text{N}_2$  and  $\text{CO}_2$ ), (iv) it must support patterning at the micron level and (v) its surface must be functionalizable to tune hydrophilicity or graft molecules of interest.

One material fulfills all these requirements and more: polydimethylsiloxane (PDMS), also called ‘silicone rubber’. Commercially available formulations for producing PDMS consists of an initially liquid base (a vinyl-terminated PDMS) that becomes crosslinked through hydrosilylation by a curing agent, turning into a transparent flexible solid. Thanks to its initial fluid state, PDMS creates a conformal contact with surfaces, even at the micrometer scale. Once crosslinked, it is easily released from a rigid mold, even if it contains complex, quasi-three-dimensional structures. This molding process is called ‘soft lithography’ [55–57]. After release from the mold, holes are punched in the PDMS slab for fluid inlets/outlets and the channels are closed by activating the channel side of PDMS and covalently bonding it to a glass slide (see **Figure 1.5** ⑤ to ⑨).

#### **Mold fabrication: photolithography**

After determining the chip material and fabrication route, comes the fabrication of the mold containing the channel patterns. One of the most used microfabrication techniques is projection photolithography. The entire pattern negatively printed on a photomask is projected onto a thin film of photoresist all at once: the exposed resist gets crosslinked and hardens, whereas the

screened part remains fluid and is washed away (as sketched on **Figure 1.5** ① to ④). SU-8 is a popular photoresist for MEMS applications, as it allows features with high aspect ratios (above 1:18) and vertical sidewalls up to the millimeter range [58]. Furthermore, SU-8 has advantageous chemical and mechanical properties, which make each SU-8-based master reusable many times to mold PDMS.

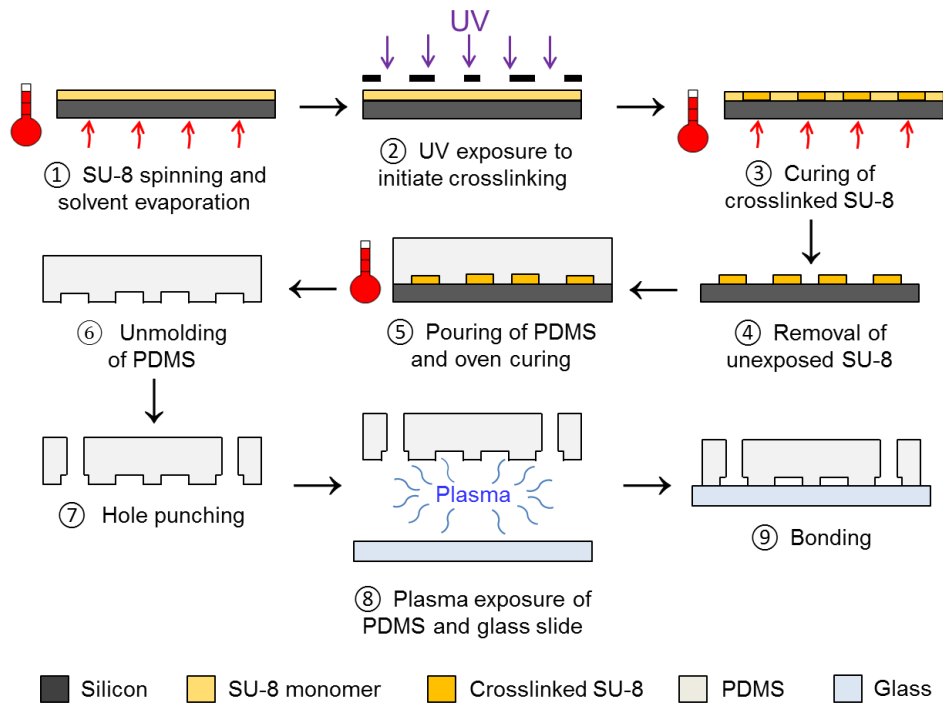


**Figure 1.5** Overview of the microfabrication process. 1 to 4: SU-8 mold photolithography; 5 to 9: PDMS chip soft lithography.

## Droplet creation

Once the chip is operational, droplets of aqueous phase must be generated before being manipulated. The two most used modules for this purpose are T junctions and flow-focusing (FF) nozzles, as pictured in **Figure 1.6** [59], [60]. In T junctions, droplet breakup is driven by the competition between shear forces, which tend to elongate the drop and increase the interfacial area, and interfacial forces which oppose the elongation of the liquid neck connecting the emerging droplet with the inlet [61], [62]. For a given channel geometry, droplet size decreases when the ratio between flow rates of continuous and dispersed phase increases: the more shear, the smaller the droplet.

In the flow-focusing configuration, the continuous phase and the dispersed phases are forced through a nozzle, in which the continuous phase symmetrically shears the dispersed phase into droplets [63]. Droplet breakup is driven by the Plateau-Rayleigh instability: small variations in the

local curvature cause pressure fluctuations inside the liquid; as a result, such variations grow until the liquid film eventually breaks into drops.

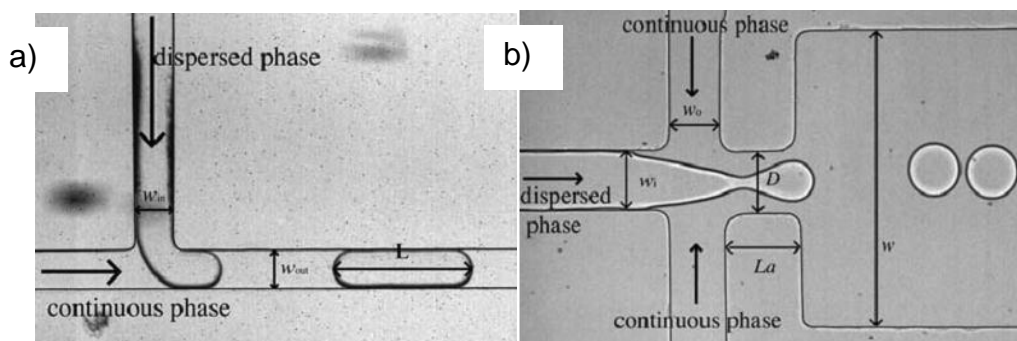


**Figure 1.6** Typical geometries and important length parameters for droplet generation in microfluidic channels. a) T junction; b) Flow-focusing nozzle. Reprinted from ref [60].

For given oil and water phases, channel sections and flow conditions, the choice between a FF nozzle or T junction to get a certain droplet size will depend on the velocity of the continuous phase and on the flow rate ratio between oil and water phases [59]. Also, if proteins are present in the aqueous phase, they might favor sticking of the droplet as it is pressed against the channel before breakup. Hence, for biology applications, flow focusing geometry is more preferable because it limits this issue.

## Droplet mixing

In section 1.1.2, we already highlighted how the possibility of mixing inside droplets pushed the shift from reaction in continuous flow microfluidics to reactions in droplets. To fully take advantage of chaotic advection into droplets, some adaptation of the flow sequence of reagents to be mixed is necessary (see **Figure 1.8**). First, the droplets can go through serpentine channels to rotate the separation line between the two reagents at each turn and make advection asymmetric (**Figure 1.8 b**) and [64]). Another strategy is to rotate the separation line by  $90^\circ$ , by fusing alternating droplets of each kind for example (**Figure 1.8 c**) and [65]). Finally, it is possible to split the flow of one of the reagents in two lateral flows around the other one (Figure 1.7 d)).

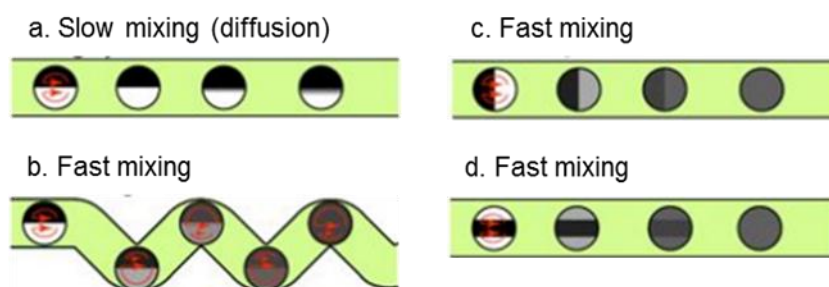


**Figure 1.8** Various mixing strategies within microfluidic droplets. Two solutions, black and white, are emulsified using co-flow through two inlets. Droplets flow from left to right. Red arrows indicate the recirculating flow inside the droplets. (a) Separation between the two solutions is along the straight channel axis. Advantage can be taken of convection to accelerate the mixing, by 3 strategies: (b) former droplets go through winding channels. (c) The two solutions are localized in the front and back halves of the droplet. (d) The first solution (black) is localized in the middle, while the second solution (white) is localized in the upper and lower halves. Adapted from [66].

## Droplet fusion

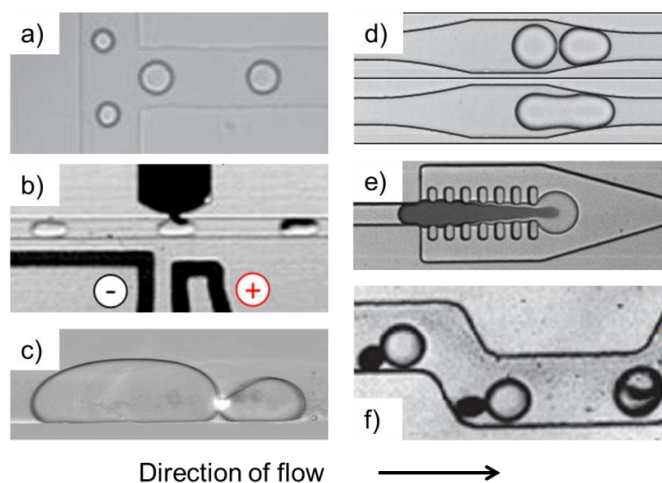


**Figure 1.9** Several droplet fusion techniques. a) to c): active fusion, d) to f): passive fusion. a) Electro-coalescence [67]; b) Picoinjection [68], c) Laser-induced coalescence [69], d) Coalescence by controlled decompression [70], e) Pillar-induced droplet merging [71], f) Passive fusion in winding channels [53].

We have already presented how two reagents can be combined by co-flowing them before encapsulation in droplets. However, once droplets are formed, several strategies have been found to add more reagents to them in a controlled fashion. Active fusion methods relying on external triggering of electric fields have been designed, to enable fast on- and off switching [67], [68] (**Figure 1.9** a) and b)). Coalescence actuation was also successfully achieved by local heating from a focused laser [69] (**Figure 1.9** c)). However, these active fusion techniques have several

shortcomings: (i) electrocoalescence requires sophisticated equipment and microfluidics chips with integrated electrodes and good electrical shielding to prevent unwanted coalescence (ii) laser fusion has low throughput and the induced heating is not suitable for many bioapplications. Consequently, passive fusion methods (**Figure 1.9** d) to f)) were introduced by Bremond et al [70], Niu et al [71] and Mazutis et al [53], all relying on the destabilization of the film between two droplets by decompression.

### **Droplet incubation**

Once all the reagents have been introduced in the droplet, sufficient time must be given for the reaction to reach completion. The most straightforward approach is to collect the emulsion, incubate it out of the chip and reinject it later for additional reaction steps or analysis. This method relies on the use of surfactants to stabilize the droplets, preventing coalescence. Additionally, great care has to be taken to minimize unwanted droplet coalescence by static electricity or shear in tubing or connectors. The emulsion can be collected in a syringe, in PTFE tubing [72], in a glass capillary [73], in PCR tubes closed by a PDMS plug [74] or in custom emulsion collection/reinjection glass vials, such as those sold by RainDance Technologies [75].

However, off-chip incubation does not provide the level of control that is possible if the droplets remain on-chip. Hence, several strategies of on-chip incubation have been elaborated.

The most straightforward one is to design long delay lines with sufficient channel widths and height to retain the droplets on chip the desired time. However, in such conditions, several droplets flow side-by-side and their residence time on-chip undergoes dispersion due to inhomogeneous velocities. This problem has been studied by Frenz et al, who found two strategies to solve it [76] (**Figure 1.10**): (i) if most of the spacing oil is withdrawn, droplets pack hexagonally and do not undergo dispersion anymore; (ii) if narrow constrictions are positioned at regular intervals within the delay line, it causes shuffling of droplets that offsets dispersion. This delay line design supported residence times up to one hour.

For longer incubation times on chip, it is necessary to immobilize the droplets. Several devices for trapping droplets were described in the literature over the last years (see **Figure 1.10** e) to g)) [77]: dropspot array [43], bypass storage [78], reservoirs [79], [44] and single droplet traps array [80]. With such devices, on-chip storage times extended to 15 hours.

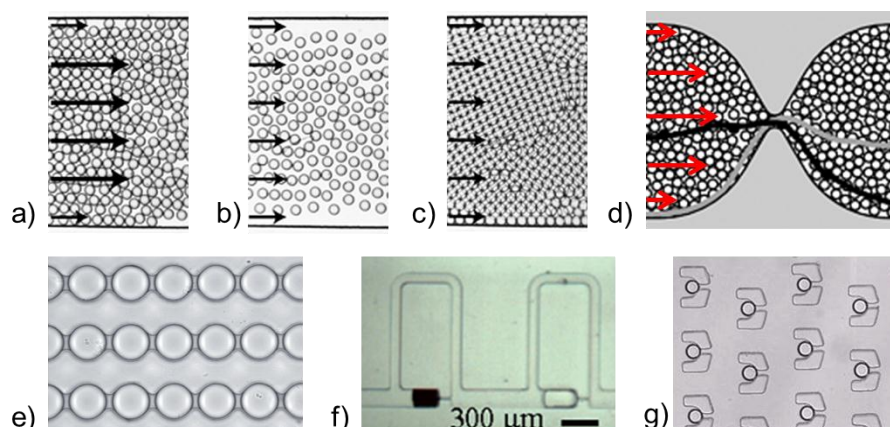


**Figure 1.10** Increasing storage time on-chip. a) to d): droplets in motion. Arrows indicate flow velocities. a) For water/oil ratio around 1, droplet velocity is inhomogeneous across the channel and leads to high dispersions in residence time. At very low (b) or very high (c) water/oil ratio, droplet velocity is nearly uniform across the channel. d) Droplet shuffling in constrictions. Adapted from ref [76]. e) to g): immobilized droplets. e) Dropslot array [43]; f) Bypass storage [78]; g) single droplet traps array [80].

## Droplet sorting

After the reaction is completed, an important part of screening is to be able to keep the reaction products of interest among the pool of synthesized compounds, DNA variants or expressed proteins. Sorting can be done depending on several criteria, for example droplet size or fluorescence activity. In the former case, passive sorting is possible, based on size-dependent hydrodynamics [81], [82]. In the latter case, if the fluorescent can be used to trigger droplet deviation. Some very interesting proofs of principle have been published, using electric fields to initiate droplet motion [83], [73], [84] (see **Figure 1.11**).

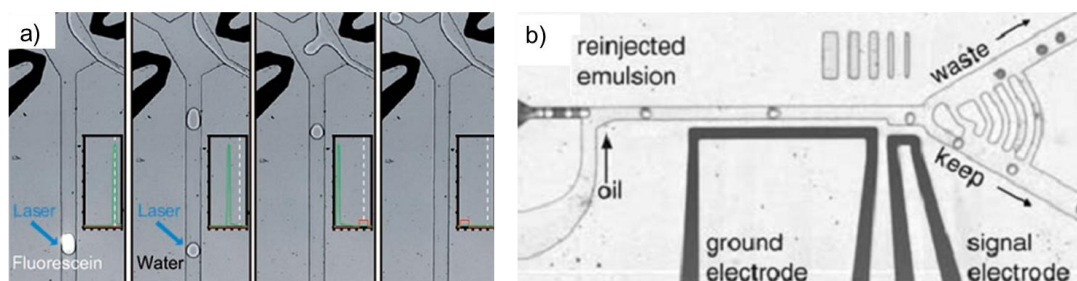


**Figure 1.11** Fluorescence-activated droplet sorting by an electric field. a) Fluorescent droplets are merged in a continuous aqueous stream Reprinted from ref [83]. b) Fluorescent droplets are deviated from the upper arm to the lower arm. Reprinted from ref [84].

With all available modules in mind, let us now investigate how they have been recently combined and engineered for complex, multi-step assays in microfluidic droplets.



### 1.1.5 A broad range of applications

As discussed in section 1.1.3, the advantages offered by compartmentalization of biological and chemical reactions in picoliter droplets have been already been exploited in the past. The high level of control given by a microfluidic approach offers new possibilities for ultra-high-throughput screening and analysis.

As a result, in the last five years, this technology has driven the emergence of countless applications: synthesis of small molecules or particles, single-molecule PCR, directed evolution, encapsulation of cells or organisms, enzymatic assays etc. A number of recent reviews give an excellent overview of them [17], [50], [51], [85–87]. We will focus on two applications that have a very high potential to bring dramatic advances in high-throughput screening and would benefit from a system of tracking droplet identity, such as the method proposed in this thesis.

#### Combinatorial chemistry

In the drug discovery process, an early step consists in generating sufficiently large libraries of compounds with structural diversity. This library creation is commonly performed by combinatorial chemistry: it consists in creating all the different combinations between two families of reagents ( $A_1, A_2, \dots, A_m$ ), and ( $B_1, B_2, \dots, B_n$ ), resulting in  $m \times n$  distinct compounds. The bottleneck in that process is that generating libraries of millions of compounds is extremely time-consuming using conventional robotics to load the compounds. Diverse parallel synthesis methods have been engineered by combining miniaturization and automation [88]. Continuous-flow microfluidic systems have also been introduced in the last 10 years [89], [90]: one of them is sketched on **Figure 1.2 a)**.

The first proof-of principle of efficient combinatorial synthesis in microfluidic droplets was established by Theberge et al. in 2011 [91] on a  $7 \times 3$  library of thrombin inhibitors obtained by a 3-component Ugi reaction. The principle of the on-chip combinatorial synthesis is explained on **Figure 1.12**. Full parallelization was reached by first encapsulating amines  $B_1$  to  $B_3$  in droplets one after the other, then mixing the three emulsions together. Droplets containing aldehyde/isocyanide mixtures  $A_1$  to  $A_7$  were formed on chip at 2 kHz, fused by electrocoalescence with the reinjected amine droplets library and incubated to complete the reaction.

In parallel, the thrombin inhibition assay was also transferred in droplet microfluidics format. Performing the assay in series after combinatorial library synthesis would constitute a complete thrombin inhibitor screening in droplets. Nevertheless, to make it truly efficient, it would be

optimal to find a way to identify during the assay readout which  $A_m$  and  $B_n$  species are present in each droplet. This would save the step of identifying each active compound separately afterwards.

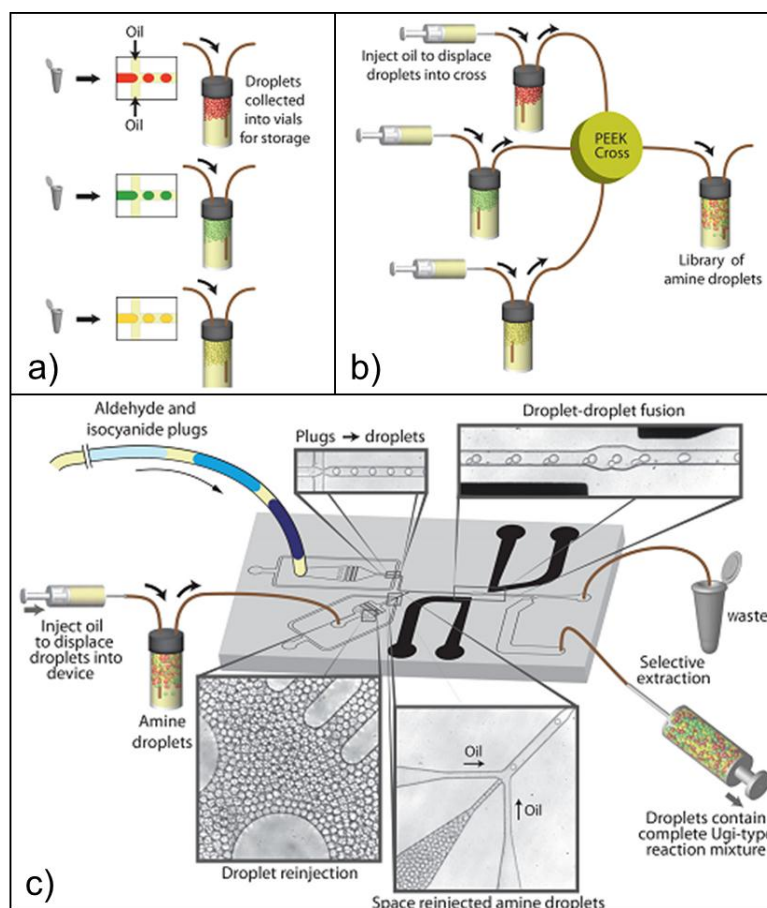


**Figure 1.12** Ugi-type combinatorial enzyme inhibitor synthesis in droplets. a) Encapsulation of 3 amines in droplets. b) Constitution of the mixed library of amine droplets. c) On-chip generation of 7 types of aldehyde and isocyanide droplets, fusion with the amine droplet library and collection off-chip. Reprinted from [91].

## Dose-response screening of compounds

As highlighted in section 1.1.1, one of the major drawbacks of classic HTS platforms is that their throughput is limited by fluid-handling robotics to 1 million assays per day. Since libraries nowadays can contain hundreds of thousands compounds, each compound is often only assayed at a single concentration in early screening stage. This lack of dose-response information early on potentially causes potential candidates to be ruled out, or on the contrary, false positives to be selected. The throughput offered by droplet microfluidics, up to one million assays per hour, could enable full dose-response assays even at early screening stages.

In our laboratory, two dose-response screening assays of enzyme inhibitors have been recently implemented on a two-phase microfluidic platform. First, Clausell-Tormos et al. recently built an automated microfluidic system for the screening of compound libraries [72] (see principle on **Figure 1.13**). Compounds at several dilution levels in microtiter plates were injected with an autosampler in tubing as an array of distinct plugs separated by inert oil. Each array was then split into multiple 150 nL copies, thus allowing several parallel screens of the same library. Finally, enzyme and fluorogenic substrate were added on-chip to react with each compound, then fluorescence was detected. Dose-response curves were generated: they overlapped very well those obtained in bulk on a 96-well plate, yet required 1000-fold less reagents.

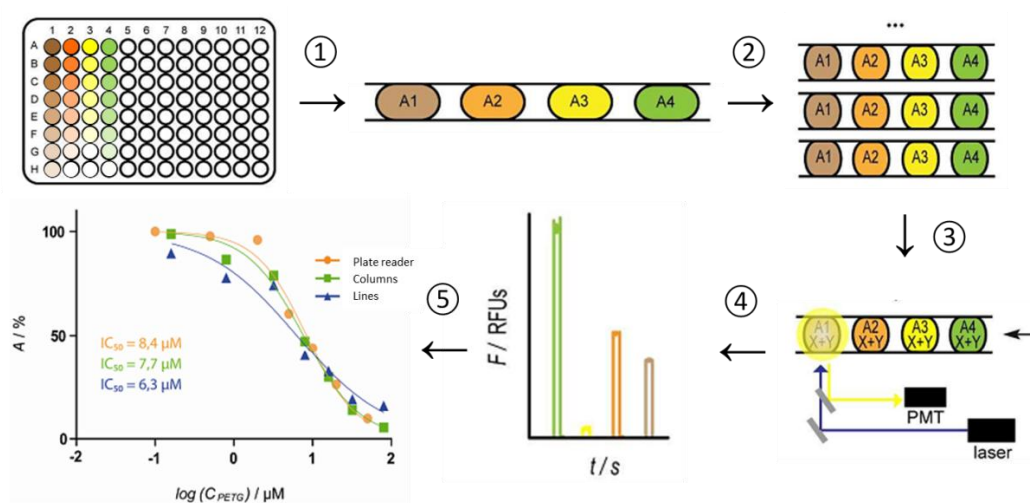


**Figure 1.13** Overview of the automated screening platform. Adapted from [72]. 1) Compounds are pipetted one by one with an autosampler into tubing, separated by oil. 2) Each plug is split into 8 identical smaller plugs of 150 nL each. 3) Substrate and enzyme are fused on-chip to each small plug, incubated and read out by fluorescence. 4) Fluorescence signals of each compound are compared. 5) Dose-response curves are generated.  $IC_{50}$  values are in very good agreement with those obtained in bulk on a plate reader.

Although this setup offers very good integration between the macro world (microplates) and processes on-chip, its main drawback is that to retain identification information about each assay, the samples are sequentially loaded in a tubing as big plugs, considerably slowing down the final throughput. It would be very beneficial to remove this constraint altogether by tagging the compound encapsulated in each plug.

In parallel, Granieri et al designed a complementary on-chip enzymatic assay to screen for the activity of tissue plasminogen activator (tPA) displayed at the surface of retroviruses [92]. Conventional phase display strategies do not allow convenient selection of efficient catalysts; encapsulation of the assay in droplets solved this issue. From a model library with a 1000-fold excess of retroviruses displaying a non-active control enzyme, the active wild-type enzyme was

sorted, reaching more than 1300-fold enrichment. Once again, compared to conventional screening techniques, this droplet-based system allowed more than 100-fold increased throughput and almost one million-fold reduced consumables costs. However, to implement this screening on a real library, it would also be advantageous to add a tag to each enzyme variant, in order to directly link variant species and enzymatic activity.

As outlined, in all these applications, the main missing element to use them as routine HTS assays is the possibility to retain information on which active species assayed is present in each droplet. Indeed, the main drawback of transferring assays from microplates or microarrays to droplets is that when the droplet library is collected, all spatial or temporal identification of each individual assay is lost. In the library, all different kinds of droplets are mixed together and are processed in random order without keeping track of the species until during the final detection. This is why adding a tag of some sort to each library member before encapsulation in droplets would be extremely useful. But before choosing a material for this tag, it is essential to ensure that it is compatible with droplet formation, stabilization on-chip and incubation or storage. Below we review the specific notions to keep in mind.

## 1.2 Fundamentals of droplet formation and stabilization

Before transferring high-throughput assays and encoding materials from microplates to droplets in chips, some attention must be given to the specifics of two-phase microfluidics systems. In particular, the physics of flows at such small scale and the conditions to create stable droplets have to be considered. Furthermore, once the reagents are encapsulated, great care has to be taken to keep the emulsion stable for the time of the experiment. This section gives an overview of the important fluidic parameters driving droplet formation on chip and presents the main mechanisms of emulsion destabilization.

### 1.2.1 Hydrodynamic principles of droplet microfluidics

#### Laminar flow

The first characteristic of fluids in micron-sized channels is that their flow is laminar, compared to macroscopic environments where it is turbulent [62], [93]. The transition between these two regimes can be predicted using a dimensionless number called the Reynolds number ( $Re$ ), defined by:

$$Re = \frac{\rho \cdot U \cdot L}{\eta} \quad (1.1)$$

where  $\rho$  is the fluid density,  $U$  the fluid velocity,  $L$  the characteristic length, and  $\eta$  the fluid dynamic viscosity.  $Re$  reflects the ratio of inertia to viscous stresses or, in other words, the tendency of a flowing liquid phase to develop turbulence. The lower the velocity of the liquid flow, the diameter of the channel or the density of the liquid are, the lower  $Re$  is. Laminar flow occurs for  $Re < 2000$  and turbulent flow when  $Re > 2000$ . In microfluidic systems having channel cross-sections  $\sim 1000 \mu\text{m}^2$ , Reynolds numbers are almost always lower than 1: viscous stresses and pressure gradients dominate, while inertial effects become negligible.

In laminar flows, diffusive mixing is slow compared to convection. The dimensionless number describing the relative rate of convection to diffusion in a flow is the Péclet number [93]:

$$Pe = \frac{U.L}{D} \quad (1.2)$$

where  $D$  is diffusivity. Common values of these parameters are  $U = 10^{-3}$ - $10^{-2}$  m/s,  $L = 10^{-5}$ - $10^{-4}$  m and  $D = 10^{-11}$ - $10^{-9}$  m<sup>2</sup>/s, where the smaller value correspond to macromolecules, proteins and nanoparticles. Hence, in microfluidic systems,  $10 < Pe < 10^5$ : two streams of miscible fluids injected into a microchannel flow side-by-side and mix only by diffusion [93], as already mentioned in section 1.1.2. Slow diffusive mixing can be advantageous for some microfluidic applications, such as controlled gradient generation and laminar flow patterning, but impedes conduction of fast reactions.

In droplets, an additional phenomenon contributes to mixing. When droplets flowing through microfluidic channels are large enough to ‘touch’ the channel walls, leaving only a thin film of continuous phase, shear interactions with the walls create internal flow circulations in the droplet. These flow circulations mix the contents within the halves of the droplet, but not across the entire droplet (see **Figure 1.14**). This phenomenon was exploited in the mixing strategies described in section 1.1.4.

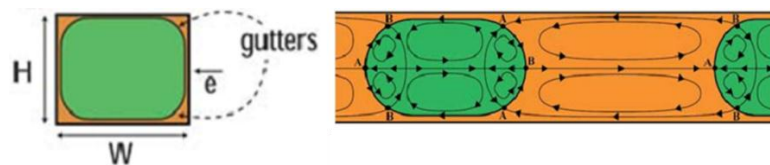


**Figure 1.14** Cross-section and lateral view of a channel of height  $H$  and width  $W$  occupied by a large droplet moving left to right. The flow lines are indicated by arrows. Reprinted from ref [60].

## Droplet formation and capillary number

The formation of droplets is a complex and dynamic process, which is affected by several parameters: fluid velocity, flow rate ratio between dispersed and continuous phases, viscosity ratio of the liquids, presence of surfactant and geometry of the device. Up-to-date, there is no single unifying model describing droplet formation in microfluidic systems: in most cases, explanations are specific for particular geometries or cases considered.

In section 1.1.4, we presented the two main types of drop generation modules: flow-focusing nozzles and T junctions. In both configurations, an important parameter determining drop size is the capillary number  $Ca$  which is the balance between viscous and capillary stresses [59], defined by:

$$Ca = \frac{U_{out}\eta_{out}}{\gamma} \quad (1.3)$$

Where  $U_{out}$  is the velocity of the outer phase,  $\eta_{out}$  its viscosity and  $\gamma$  the interfacial tension between both phases.

### Choosing a suitable carrier oil

In order to form our droplets and put them in motion in the channels, we must find a suitable carrier oil. It must be (i) transparent, (ii) immiscible with water and organic compounds to avoid solubilization of compounds dissolved in the droplets, (iii) chemically inert, (iv) compatible with PDMS, (v) biocompatible, (vi) permeable to gases and (vii) possibly have moderate viscosity, to limit pressure buildup from flow. Most organic or mineral oils are unsuitable because they swell PDMS, dissolve organic compounds and are sometimes toxic to cells. On the other hand, fluorocarbon liquids are very good candidates and satisfy all these criteria [94].

### Wetting and contact angle

The control of drop breakup in microdevices is influenced significantly by wetting characteristics. To obtain consistent droplet production and clean transport of the reagents inside the droplets, the continuous phase should be the phase that most strongly wets the boundaries [95]. If this condition is satisfied, then the aqueous phase does not come in contact with the walls and remains isolated by a thin film of the carrier fluid as sketched on **Figure 1.14**. Wetting of the channels walls can be described by two parameters: the interfacial tension  $\gamma$  and the contact angle  $\theta$ .

When two immiscible liquids are in contact with each other, the molecules at the interface experience an imbalance of forces that leads to an accumulation of free energy at the interface. Interfacial (surface) tension is a measurement per unit area of this cohesive excess energy.

Contact angle is the angle at which the droplet interface meets a solid surface (in our case, PDMS or glass). If  $\theta < 90^\circ$  (low contact angle), wetting of the surface occurs and the fluids spreads. On the other hand, if  $\theta > 90^\circ$ , fluid will minimize contact with the surface. To satisfy the aforementioned condition for droplet production, we must maximize contact angle between our channels and water. Unfortunately for us, water has a very low contact angle with glass ( $8^\circ$ ), and fluorinated oil does not completely wet PDMS. To solve these problems, it is possible to change wetting properties by covalently grafting a monolayer of fluorophilic (hence very hydrophobic) molecules on these surfaces. Popular molecules for that purpose are perfluorotrichlorosilanes. The covalent bonding is done by hydrolysis of the very reactive trichlorosilane moiety followed by condensation on the activated surface silanol groups [96]. As a result, the surface becomes fluorophilic, dramatically decreasing setting by water droplets, while promoting wetting of the surface by the perfluorinated oil.

### 1.2.2 The role of surfactant, and how to choose it

#### Reducing channel wetting by droplets

In addition to surface functionalization by perfluorinated molecules, wetting by droplets on the channels by can be diminished further by adding perfluorinated surfactant to the fluorocarbon oil [62], [97]. In these conditions the contact angle between water droplets and glass (or any other surface) reaches  $\sim 180^\circ$ , completely ruling out wetting [98].

#### Interface stabilization

Even if wetting by water is suppressed, droplet formation is still not easy if only water and fluorinated oil are used. Even at high shear rates, droplets do not break up readily from the nozzle and form long jets. To facilitate droplet breakup, fluorinated surfactant is added to the oil [60], [62].

Surfactants are long molecules composed of a hydrophilic head and a hydrophobic tail: they are called “amphiphilic” molecules. When an interface is created with a surfactant solution, surfactant dissolved in oil diffuses onto the interface and orients itself with the polar head group facing the aqueous (dispersed) phase and the hydrophobic tail facing the continuous phase. This adsorption occurs spontaneously because it lowers the free energy of the interface, thus the

interfacial tension value  $\gamma$ . Consequently, the value of the capillary number  $Ca$  increases, leading to decrease in droplet size [59].

Moreover, if no surfactant is added, the droplets will always spontaneously coalesce in order to decrease the interfacial area, thereby decreasing the energy state of the system. Hence, surfactants are also used to increase the long-term stability of the drops; their fluorophilic tails form a steric barrier that prevents coalescence when droplets come into contact.

### Choosing the optimal surfactant

For mineral oils, there is a wide choice of commercially available surfactants whose properties have been studied in great detail. However, for fluorinated oils, the choice is much more restricted. Over the last years, some efforts have been invested in designing fluorinated surfactant allowing robust encapsulation of bioassays in droplets.

The first criterion of evaluation is of course droplet stability: unwanted coalescence of droplets jeopardizes compartmentalization, which is a key feature of droplet microfluidics. But other criteria come into play: the hydrophilic head of the surfactant must not promote undesired adsorption of proteins or compounds contained in the droplet. Some positive results were obtained with small polyethylene glycol molecules, compared to surfactants terminated by a carboxylic acid.

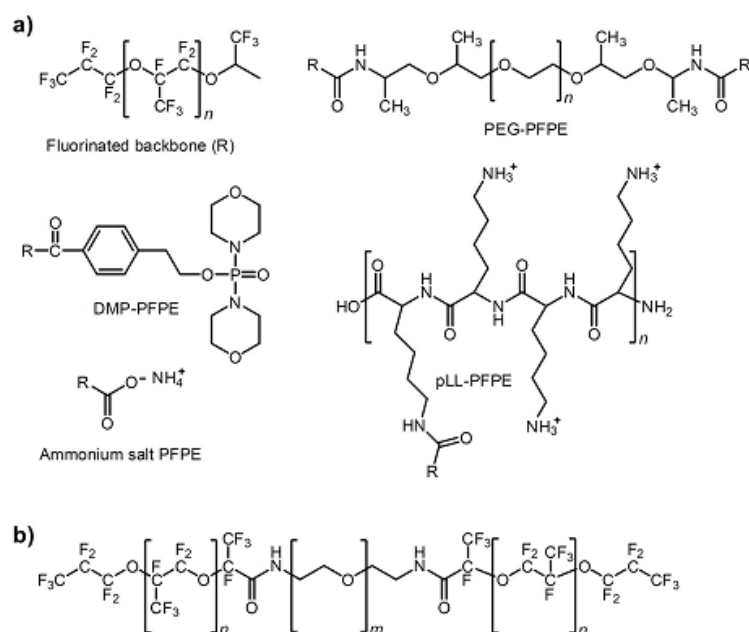


**Figure 1.15** PFPE-based surfactants with different hydrophilic moieties. a) Adapted from ref [48]. b) Adapted from [99].



If cells or organisms are encapsulated in the droplet, the surfactant must not be cytotoxic. A whole survey of the biocompatibility of perfluoropolyether (PFPE) surfactants with different hydrophilic headgroups was performed by Clausell-Tormos et al. on the structures presented on **Figure 1.15 a)** [48]. The ammonium salt of carboxy-PFPE and poly-L-lysine-PFPE (PLL-PFPE) mediated cell lysis. However, polyethyleneglycol-PFPE (PEG-PFPE) and dimorpholinophosphate-PFPE (DMP-PFPE) showed good biocompatibility, did not affect the integrity of the cellular membrane and even allowed for cell proliferation. The last molecule provided excellent droplet stability even after 14 days.

### 1.2.3 Emulsion destabilization mechanisms

Because of the high surface area per drop, emulsions have important excess free energy which is not compensated by entropy contributions. As a consequence, emulsions are thermodynamically unstable systems [100]. However, in favorable conditions, they may remain intact and maintain kinetic stability for months or even years. Since we want to encapsulate compounds and tagging materials for long-term storage, it is important to understand the mechanisms leading to emulsion destabilization, in order to take all possible precautions in to prevent it in our system.

#### Creaming

Creaming is the migration of the dispersed phase under the influence of buoyancy. Emulsion droplets of radius  $R$  and density  $\rho_{aq}$  dispersed in oil of viscosity  $\eta_{oil}$  and density  $\rho_{oil}$  cream at a velocity  $v_c = \frac{2}{9} \frac{|\rho_{oil} - \rho_{aq}|}{\eta_{oil}} gR^2$ . In our case, droplets are lighter than the fluorinated oil.  $\rho_{oil} - \rho_{aq} \sim 600$ ,  $R \sim 10^{-5}$  m and  $\eta_{oil} = 1.25 \times 10^{-3}$  cP, which leads to  $v_c \sim 10^{-4}$  m/s: in a matter of minutes, droplets collected in a tube or a syringe cream to the top. This property enables close packing of droplets that is useful to accelerate reinjection or separate droplets from oil. However, this also has drawbacks: droplets in close contact are more prone to undergo irreversible coarsening through coalescence or Ostwald ripening [101].

#### Coalescence

As discussed previously, coalescence is the most easily observed degradation phenomenon. It consists of the rupture of the thin oil film between two droplets, leading them to fuse into a single one [101]. This phenomenon is absolutely harmful for droplet-based encoded assays, because if droplet contents mix, the code is damaged and the separation between distinct library members is lost. Coverage of the interface by surfactant contributes to limit this process by steric

repulsion between hydrophobic tails. Nevertheless, if the oil film between droplets is drained down to a few atomic layers, an instability can cause nucleation of a thermally activated hole that reaches a critical size above which it becomes unstable and grows (see **Figure 1.16**) [102].

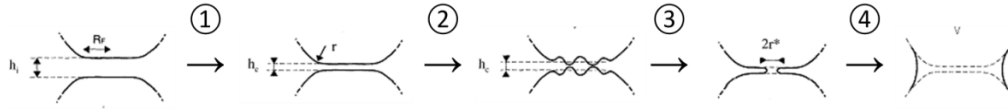


**Figure 1.16** Mechanism of coalescence. 1) Oil between the droplets is drained, 2) instability occurs, 3) a hole is nucleated by thermal activation and grows until a radius  $r^*$  above which 4) irreversible coalescence occurs. Adapted from [102].

The high level of control offered by droplet microfluidics has recently allowed better identification of mechanisms that cause coalescence [70]. As already introduced in section 1.1.4 and shown on **Figure 1.9 d**), when two droplets in close contact are sheared (like for example when drops travel from chip to tubing), oil draining is accelerated and some small areas of the interface can be depleted of surfactant, leading to coalescence. That is why dead volume and sudden diameter changes have to be avoided as much as possible.

### Ostwald ripening

Another coarsening mechanism, known as Ostwald ripening, is driven by the difference in Laplace pressure  $P_L = \frac{2\gamma}{R}$  between droplets having different radii: water transfers from the smaller droplets of high  $P_L$  to the larger ones of smaller  $P_L$  by diffusion through the oil phase [102]. In our system,  $\gamma = 1-10$  mN/m and  $R \sim 10^{-5}$  m, so  $P_L \sim 1000$  Pa, which is very low. Moreover, the polydispersity of our droplets is extremely low (CV < 3 %) so the difference in Laplace pressure is even smaller: we can neglect this effect in our system.

### Compositional ripening

Compositional ripening takes place if the emulsion contains droplets with different compositions of dissolved molecules and if these molecules are slightly soluble in the oil. Molecular exchange will take place until an equilibrium composition is reached across droplets. In our case, the fluorinated oil has very low solubility for water-soluble components, so this effect should be negligible. Still, when the excess surfactant in the oil forms micelles, some transport of small molecules has been observed between droplets in a dual microfluidic emulsion containing droplets with either high or low dye concentration (see example on **Figure 1.17 a**) [103], [104]. Transport of molecules at such a fast rate is absolutely detrimental for screening assays of small

molecule libraries in droplets: they would become totally meaningless if the molecules exchange across droplets.

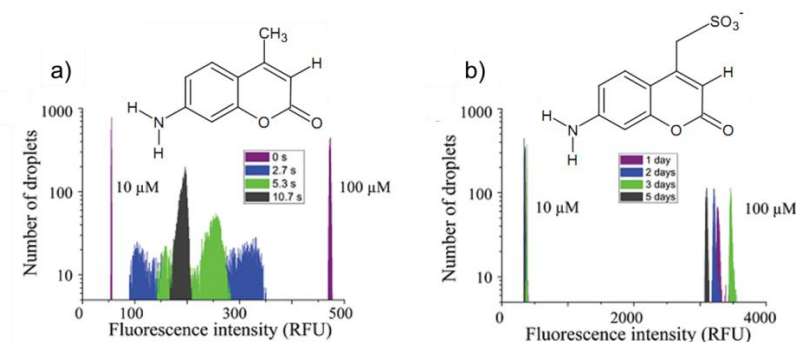


**Figure 1.17** Transport of various coumarins between droplets. a) 7-Amino-4-methylcoumarin (7-AMC): at  $t=0$ , 50% droplets contain 10  $\mu\text{M}$  coumarin and the others contain 100  $\mu\text{M}$  coumarin. The dye rapidly transfers from concentrated to diluted droplets. After only 10 s, equilibrium is reached: coumarin concentration is identical in all droplets. b) Sulfonated 7-AMC: no transfer of dye is detected over 5 days. Adapted from ref [104].

This diffusion of small molecules across the oil phase has been extensively studied in double emulsions, where transport occurs from the internal aqueous phase to the external one and vice-versa [105], [106]. For ions, counterintuitive observations were made of increased transport rate with increasing thickness of the oil+surfactant layer [106]. The researchers concluded that the transport of ions mainly relies on reverse micelles rather than direct diffusion, because it is impeded when oil layer thickness was too low to allow room for a micelle.

To solve this major issue on the way of screening libraries in emulsions on-chip, three main approaches were taken to control the retention of molecules inside droplets. First, various biopolymers were included in the droplets [79]: the addition of bovine serum albumin (BSA) led to significantly higher levels of retention, presumably due to the excellent ability of BSA to adsorb on oil water interface.

The importance of partition coefficient of the molecules in the aqueous phase was also demonstrated: addition of carbonate or sulfonate groups to fluorescein increased their retention, while substitution of hydrogens by methyl groups accelerated transport [79]. Complete blockage of coumarin transfer across the oil phase was achieved by sulfonating the molecule (see **Figure 1.17 b**) [104].

Finally, reducing surfactant concentration also proved to significantly decrease transfer rates [79], which is in agreement with the micelle-driven transport mechanism. However, since droplet stabilization kinetics on-chip depends on surfactant concentration [107], it is not possible to

simply cut the concentration of surfactant used to generate the droplets. Instead, Kleinschmidt et al in our group have investigated ways to withdraw excess surfactant once the droplet is well stabilized on chip (**Figure 1.18**) [108]. To do so, they designed an extraction module where most of the surfactant-rich oil is extracted and replaced by surfactant-free oil. This drastically reduced the overall surfactant concentration without impeding droplet stability. As a result, leakage of the dye was not observed over 15 min.

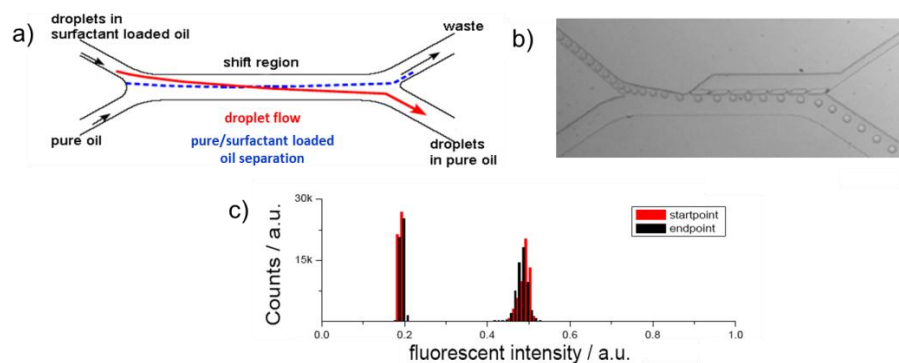


**Figure 1.18** Microfluidic module for removal of excess surfactant. a) Principle of the module. b) Module in operation. c) Fluorescence of a dual emulsion before the module right after droplet generation (red histogram) and after going through the module and 15 minute incubation on chip. Courtesy of F. Kleinschmidt.

## Osmotic pressure imbalance

If within an emulsion there is a wide range of solute concentrations inside the droplets, some water transport takes place through the oil in order to balance the chemical potential of dissolved species in each droplet. As a result, diluted droplets shrink while concentrated ones expand [109]. This size variation is not acceptable for assays where detection is based on fluorescence for example, since it changes the concentration of the fluorescent probe in time. This phenomenon will be described and discussed in greater detail in chapter 3.

Now that we have in mind all the possible droplet destabilization mechanisms, we can take them into account to choose the best material to tag compound libraries in droplets.

## 1.3 Fluorescence-based droplet labeling

In order to design a droplet encoding strategy, one important question is: “how will the code be detected?”. Since the detection of many bioassays is based on fluorescence, using fluorescent labels seems the most straightforward strategy. This section will introduce the principles and

advantages of fluorescence as a detection technique, followed by an overview of the available fluorescence-based detection methods for microfluidic platforms. Then, we will explain the overall principle of fluorescent encoding. Finally, we will present recent advances in fluorescent materials to guide the choice of a good candidate for our purpose.

### 1.3.1 Principles and advantages of fluorescence

When a light beam is sent a sample, two main interactions can take place: scattering or absorbance [110]. In the second case, absorption of a photon brings the absorbing species into an electronic excited state, at a higher energy level. In the case of a fluorescent species, the main two mechanisms it uses to return to its ground energy level are vibrational relaxation and fluorescence emission. Fluorescence is the emission of photons that occurs within nanoseconds after the molecule excitation by light. The remaining excited electrons can operate what is called intersystem crossing to their triplet state [111] (see **Figure 1.19**). Finally, the relaxation can be completed at much longer timescales (microseconds to seconds) by photon emission known as phosphorescence. In all cases, emitted photons are typically of longer wavelength than the excitation light: this difference is called the Stokes shift.

Fluorescence is a very popular detection technique because of its intrinsic selectivity and sensitivity. Compared to absorbance detection for example, the contrast and dynamic range of fluorescence are far superior: even single fluorescent molecules are visible if the background has no autofluorescence [111].

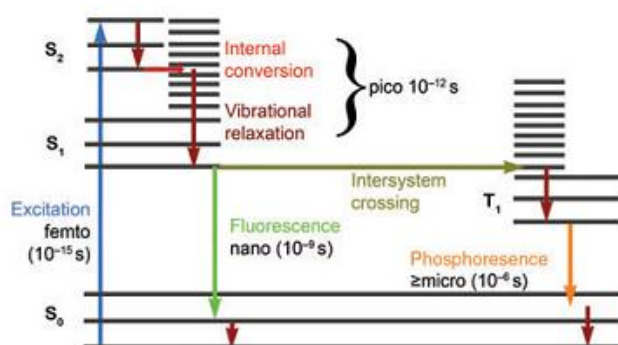


**Figure 1.19** Energy levels of a molecule and the associated possible excitation and emission phenomena, characterized by their corresponding timescales. So is the ground level,  $S_1$  and  $S_2$  are the excited levels. Reprinted from [111].

Emission of light from a fluorophore is characterized by several parameters: first, its maximal absorption and emission wavelengths, that in some cases highly depend on the local environment

of the molecule [110]: polarity, pH, temperature, viscosity, pressure, proximity of another fluorophore, etc.

Two other important parameters characterize fluorophores: fluorescence lifetime  $\tau_F$  and fluorescence quantum yield  $\phi_F$ . Fluorescence lifetime is the time the molecule remains excited before yielding a photon. It is an indication of the duration the molecule spends in the lowest level of S1 (see **Figure 1.19**). Quantum yield is a measure of the total light emission over the entire fluorescence spectral range. It is measured as the ratio of emitted photons over absorbed photons, which translates the proportion of fluorescence emission against non-radiative energy losses (intersystem crossing, for example).

Another criterion of choice for fluorophores is their resistance to bleaching. Bleaching is a generic term for all of the processes that cause permanent fading of the fluorescent signal. Photobleaching, among others, is often caused by the presence of oxygen in the close environment of the molecule. If energy is transferred from the excited fluorophore to an oxygen molecule, the latter may become reactive with the former and covalently alter its ability to fluoresce [111]. Due to this phenomenon, illumination of a fluorophore during long times is often challenging.

### **Förster resonance energy transfer (FRET)**

If two fluorophores are in close proximity (typically less than 10 nm), and if one is in its electronic excited state, it may transfer energy to its neighbor through non-radiative dipole-dipole coupling (see **Figure 1.20 a**). It can occur if the emission spectrum of the donor overlaps the absorption spectrum of the acceptor. The acceptor can be identical (homo-FRET) or different (hetero-FRET) from the donor species. This phenomenon can be detrimental to quantitative fluorescence measurements if several fluorophores are used at high concentration. However, this phenomenon can be utilized to finely measure intra- or intermolecular distances much smaller than accessible by light microscopy [112].

However, if distance is decreased further and the two fluorophores are overlapping, quenching of fluorescence might take place. So when several fluorophores are combined at high concentration in a droplet or a solid material, some attention has to be given to both phenomena.

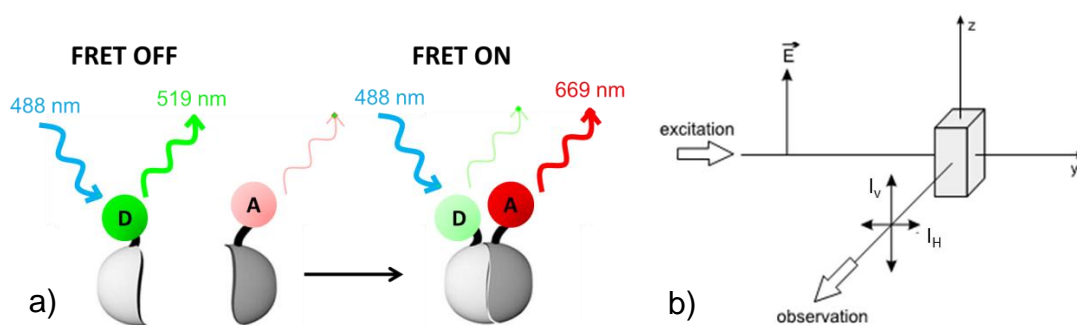


**Figure 1.20** Fluorescence-based phenomena: FP and FRET. a) Explanation of the FRET phenomenon through a protein binding assay. When the proteins are separated, the donor and acceptor are too far away: only the donor fluoresces. When the two proteins bind, distance is sufficiently low between the two fluorophores: energy is transferred from the donor to the acceptor and only the latter fluoresces. Adapted from [113]. b) Principle of an FP detection setup. The box represents the fluorescent sample. Adapted from [110].

### Fluorescence polarization (FP)

Most fluorophores absorb light in a preferred direction. If the incident light is linearly polarized, the probability of excitation is dependent on the relative orientation between the electric field wave and the molecule: the smaller the angle, the higher the probability. Because the distribution of excited fluorophores is anisotropic, the emitted fluorescence is also anisotropic. If the orientation of the molecule changes during its excited state lifetime, it will partially or totally depolarize. Among others, there are two main sources of depolarization. The first is rotational Brownian motion of the molecule [110]: the smaller the molecule, the faster it rotates, hence the more depolarized it gets. Consequently, FP is a valuable tool to measure sizes of fluorescent objects, and has many applications in biology. A typical FP assay is explained on **Figure 1.21**. Depolarization can also take place if the fluorophore of interest is in close proximity to another fluorophore oriented differently [110]. Hence, if conditions are gathered for FRET to occur, depolarization might take place as well.

To measure FP, a polarized light beam is sent on the sample. Its polarization is determined from measurements of fluorescence intensities vertical and horizontal with respect to the polarization plane of the excitation light (see **Figure 1.20 b**), using the equation:

$$FP = \frac{I_H - I_V}{I_H + I_V} \quad (1.4)$$

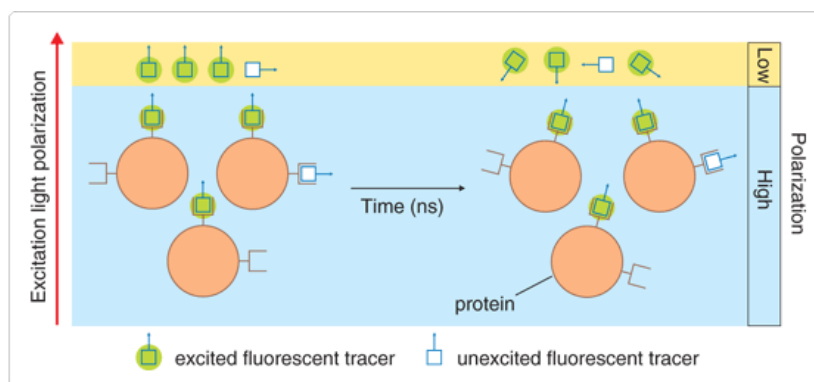


**Figure 1.21** Principle of a FP-based binding assay. A small fluorophore is functionalized so that it binds to elements at the surface of the protein. Before it is bound, it rotates fast and depolarizes quickly. Once it is attached to the protein, the rotation speed is much lower and FP value is higher. Reprinted from [114].

### 1.3.2 Fluorescence-based detection systems

The basic components of droplet-based microfluidic detection systems are the same as in many other spectroscopy methods and are comprised of light source(s), lenses, sample holder and optical detector(s). Usually in microfluidics, the chip is mounted on a microscope to enable direct visual observation. This platform, combined to the transparency and planar shape of PDMS-glass microfluidic devices makes them suitable for use with different light sources and detection systems [26]. However, droplets in channels bring additional complexity: due to the high droplet generation frequencies and femto- to nanolitre sample size, online droplet detection is challenging in terms of extracting the huge amount of information produced. So far, two kinds of setups have been used primarily.

The first one is the most common way of observing fluorescence: widefield fluorescence microscopy. It requires only a fluorescence microscope equipped with a sensitive camera to image areas of interest. It has been first used by Song et al to measure millisecond enzyme kinetics in flowing droplets [115]. Using a similar setup, simultaneous detection of several droplets moving at the same speed in parallel channels was later achieved, speeding up measurements [116]. Nevertheless, in most cases, the droplet frequency is much higher than the frame rate of the CCD camera recording. This lack of throughput prevents the detection of individual droplets and only gives averaged signals.

To allow optimal use of a classic fluorescent microscope setup for imaging, the droplet flow has to be slowed down or stopped. This can be achieved with one of the droplet array designs pictured on **Figure 1.10**. This strategy has been successfully applied to follow enzyme kinetics in hundreds [80] or thousands [43] of droplets simultaneously over hours, or to study transport phenomena between droplets [79].



To enable fluorescence readout of droplets in motion, detection frequencies in the 10-100 kHz range are needed. That was achieved by a technique inspired from flow cytometry detection systems [117], called “laser-induced fluorescence spectroscopy”: lasers excite one or several fluorophores, whose emitted signals are collected with highly sensitive optical detectors [41] and separated with appropriate filters. An example is given on **Figure 1.22**.

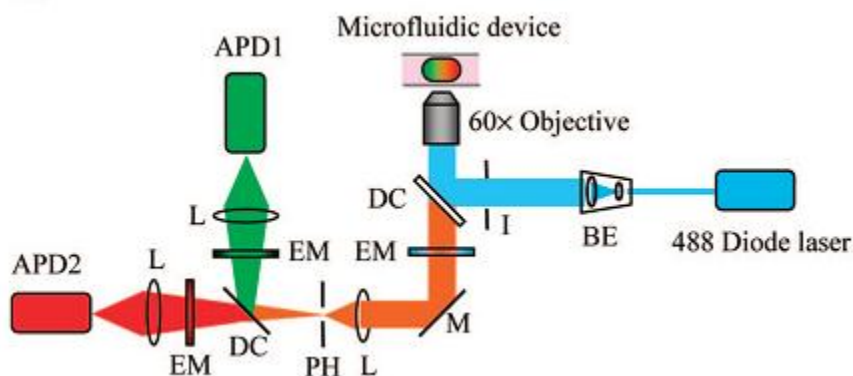


**Figure 1.22** Schematic of a laser-induced fluorescence detection system. Here the blue laser excites two fluorophores simultaneously; their respective signals are separated from the excitation signal and from each other by a combination of appropriate filters and dichroic mirrors. APD: avalanche photodiode detector; BE: beam expander; DC: dichroic mirror; EM: emission filter; I: iris; L: lens; M: mirror; and PH: pinhole. Reprinted from [118].

Lasers are used owing to their intense, collimated and coherent excitation light. The most common optical detectors for fluorescence microscopy are photomultiplier tubes (PMTs) and avalanche photodiode detectors (APDs). Both types show outstanding sensitivity to detect even single photons and are especially well-suited for applications requiring low noise. Signal output from the detectors is usually analyzed using a data acquisition (DAQ) card executing a program written in a computer software (for example LabView), which allows the identification of droplets by their width and fluorescence signal in each channel. Additional FP information on each channel can be obtained by replacing each detector by a polarization beam splitter and two detectors at  $90^\circ$  from each other.

### 1.3.3 Principle of fluorescent encoding

According to the Oxford dictionary, a code is “a series of letters, numbers, or symbols assigned to something for the purposes of classification or identification” [119]. Currently, the most widely used type of code is the barcode. Fast, simple, and accurate, barcoding has become since its patenting in 1952 [120] the most popular data-entry method to track the ever-expanding amount of information in the macroscopic world. In the meantime, an increasing demand for tracking smaller items has pushed the exploration of novel barcoding methods at much smaller

scales [121], [122]. A variety of methods has been used for generating codes allowing on-the-fly detection [121], [123], [124]: graphical encoding (1- or 2-dimensional barcodes), physical encoding (by size, shape or density), electronic encoding, magnetic encoding and spectrometric encoding (NMR, X-ray, infrared, UV-visible).

This very last subtype has been substantially developed over the past few years, because of its multiplexing capacity (which is explained on **Figure 1.23** in the case of fluorescent droplets flowing in a microfluidic channel). The use of a single color at 10 intensity levels from 1 to 10 gives only 10 unique codes, but if a second color is added, the number of codes rises to  $10 \times 10 = 100$ . The number of codes increases exponentially when multiple wavelengths and multiple intensities are used at the same time [125]. Combination of  $m$  chromophores, each at  $n$  levels of intensity, gives a total number of codes  $N$  equal to:

$$N = n^m \quad (1.5)$$

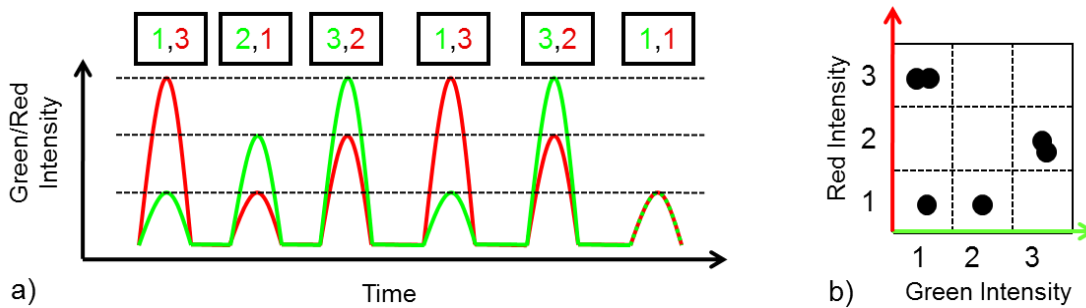


**Figure 1.23** Principle of fluorescence multiplexing in droplets. a) Each droplet contains various concentrations of two fluorophores (green and red), each at a concentration among 1, 2 or 3. Each droplet passes in front the detectors and the intensity timeline in each channel is detected. b) The combinations of green and red intensities are plotted on a 2D scatterplot. Here the 6 droplets shown in a) appear on plot b) as well. Courtesy of Brian Hutchison, RainDance Technologies.

Moreover, the multiplexing capacity can be boosted further if for each color and intensity level, it is possible to get several ( $= p$ ) FP levels. Then, the total number of codes is equal to:

$$N = (p.n)^m \quad (1.6)$$

To implement this encoding strategy, one must keep two requirements in mind [122]: in each color, the codes must be (i) mixable at different ratios with negligible signal crossover and (ii) readily distinguishable by a simple readout method. The laser induced-fluorescence detection setup fulfills condition (ii) because of its readout speed and automation. Condition (i) is dependent on both the optical setup and the materials chosen. The next section reviews latest

advances in fluorescent materials and outlines the criteria to choose the most suitable type for encapsulation in droplets.

### 1.3.4 Fluorescent materials for droplet encoding

Of all available fluorophores, the most common are certainly organic fluorophores. Over the past several decades, organic chemists have devised thousands of fluorescent molecules to cover the whole light spectrum from ultraviolet to near infrared [110]. For example, the Molecular Probes Handbook 11<sup>th</sup> online edition [126] describes 3,000 or so fluorescent probes for virtually any biological application. Organic fluorophores generally consist of  $\pi$ -conjugated ring structures such as xanthenes, pyrenes or cyanines and their quantum yield can reach up to 97%. In spite of their wide availability, they have several drawbacks [127]: first, they have relatively large emission spectra (Full width at half maximum –FWHM–  $\sim$ 50–200 nm). Moreover, they are known for their tendency to photobleach or quench and their fluorescence is highly dependent on pH or solvent [110].

A class of novel materials emerged in 1993 as a promising alternative: quantum dots or QDs [128]. These nanocrystals are traditionally made of II–VI or III–V semiconductors (PbS, CdSe, CdS etc.) and may be synthesized in many different colors by tuning the particle size. They exhibit fundamentally different absorption and emission behavior from dyes and fluorescent proteins, characterized by wide absorption bands, large Stokes shifts and narrow emission bands (FWHM  $\sim$ 20–40 nm). All these properties, especially the latter, are very appealing to achieve high multiplexing; however these materials suffer from several drawbacks: first, they are difficult to fabricate. Also, they are made from heavy metal ions such as  $\text{Pb}^{2+}$  and  $\text{Cd}^{2+}$  which are very toxic. In addition, they are hydrophobic, thus need to be thoroughly functionalized to become water-soluble [129]. Finally, they present the notorious disadvantage of stochastically blinking, which impairs their use for quantitative measurements.

To circumvent some of these issues, many groups have encapsulated these dyes in a variety of host nanometer- to micron-sized matrixes. The two favorite matrix materials are (i) polymers such as polystyrene [125], [130–132] and (ii) silica [121], [127], [133–137]. Both have been successfully used as fluorescent multiplexed labels; two examples are showed on **Figure 1.24**. Organic dyes in polystyrene beads have even been used in the first commercialized bead-based fluorescence multiplexing system, launched by Luminex in 1997 [138]. Fluorescent silica exists in a wide range of sizes from 10 nm to a few microns.

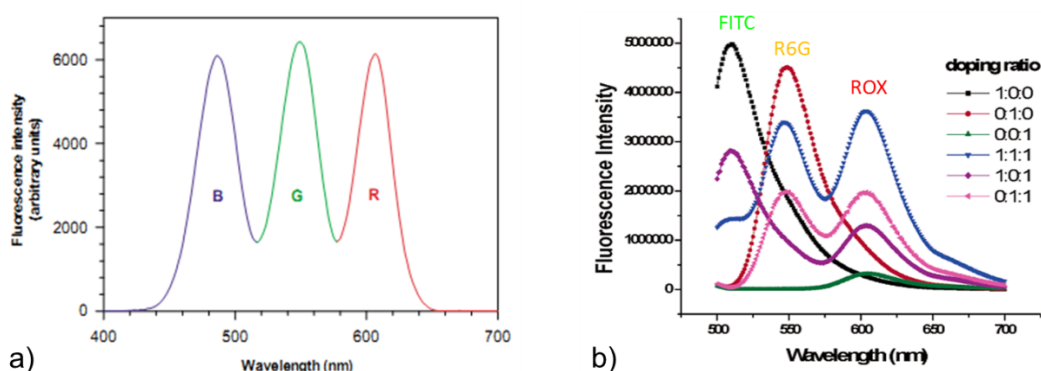


**Figure 1.24** Two examples of bead-based fluorescence multiplexing systems. a) Three types of CdSe/ZnS QDs (blue, green, red) encapsulated in equal quantities in 5  $\mu\text{m}$  polystyrene beads. Reprinted from [125]. b) Three organic dyes (FITC, Rhodamine 6G and ROX) covalently bound at various ratios in 70 nm silica nanoparticles. Adapted from [139].

To choose the best system in this wide range of possibilities, we considered the requirements for a droplet-based microfluidic HTS system: the material should be (i) stable in water/DMSO, (ii) chip & droplet compatible (meaning it should not stick to PDMS or glass, or leak out of the droplets, obstruct the channels or sediment), (iii) biocompatible, (iv) optically and chemically stable during assay incubation and readout, (v) it should neither interfere with the assay mechanism, nor obstruct or modify its fluorescent readout and (vi) possibly be easy and cheap to buy or to make. Conditions (i), (iii), (iv) and (vi) ruled out quantum dots and condition (ii) eliminated micron-sized beads. Free organic dyes were ruled out by (ii) because of transport and (iv) due to photobleaching. Consequently we chose a strategy based on silica nanoparticles.

Various fluorescent composite materials based on silica have been synthesized in the last years. By combining metals, organic fluorophores, QD or magnetic particles, multifunctional materials were obtained. Some examples are displayed on **Figure 1.25**. Although very appealing, these materials are quite big (100 nm to 1 micron), which reduces their scope of applicability and makes them prone to sediment. Moreover, they involve multi-step syntheses of various materials. That is why, as a starting point, we chose to simply encapsulate classic organic fluorophores, and to do so in the smallest possible silica particles.

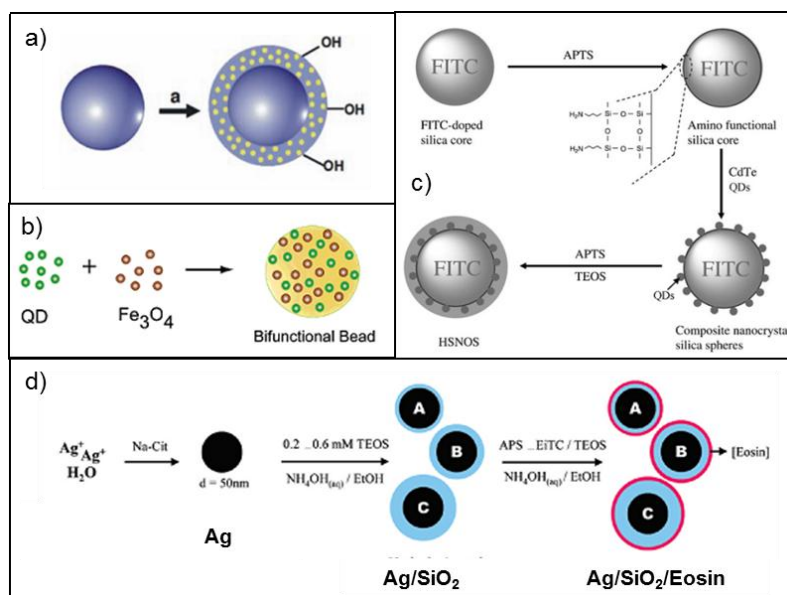


**Figure 1.25** Various silica-based fluorescent nanomaterials. a) Core-shell silica particles with QDs in the shell. Reprinted from [140]. b) Silica beads encapsulating both QDs and magnetic nanoparticles. Reprinted from [141]. c) Core-shell silica particles with FITC in the core and QDs. Reprinted from [137]. d) Core-shell-shell particles with a silver core, a silica intermediate layer and a silica/eosin outer shell. Reprinted from [142].

## 1.4 Scope of the thesis

As presented in this general introduction, recent innovations in microfluidic modules as well as detection techniques have laid a solid ground for implementation of high-throughput, miniaturized assays. The proof of principle of a dose-response screening assay by Clausell et al shows that HTS on chip is within reach. However, the throughput of this approach is severely limited by the necessity to load the plugs one after the other to keep track of their identity. Hence, it would be very beneficial to implement a strategy to optically encode compounds with fluorescent labels: libraries of hundreds of thousands compounds could then be encapsulated in droplets at once, mixed, aliquotted and reinjected when necessary for the assay, following the scheme outlined on **Figure 1.26**.

As discussed in section 1.2.3, the fluorescent material has to be chosen carefully in order to avoid exchange phenomena and other emulsion degradation processes. Moreover, it has to fulfill many other requirements highlighted in section 1.3.4. For this reason, we chose to encapsulate organic fluorophores in silica. To do so, we conceived a range of novel silica-based composite fluorophores. The next chapter describes this synthesis strategy and optimization as well as the fluorescent properties of the resulting materials. The third chapter investigates the consequences

of encapsulating these nanoparticles on the stability and interfacial properties of the droplets. Finally, Chapter 4 describes how these fluorescent particles were utilized to create the first multi-color barcode in droplets. Together, the work presented in this thesis is a significant step towards multiplexed, parallelized high-throughput screening in droplets.

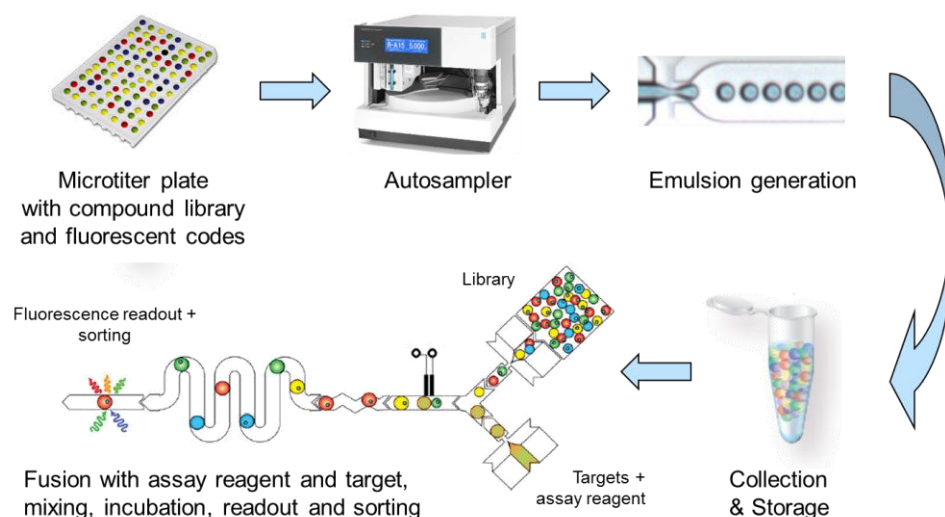


**Figure 1.26** Possible sequence of steps for an on-chip HTS assay in droplets. First, a droplet library is created as explained above. An aliquot of this emulsion is reinjected and fused with droplets containing the assay reagents. After mixing the resulting droplet to initiate the reaction, it is incubated on- or off-chip to terminate the reaction. Then, assay readout is performed and the output signal is compared to a preset threshold: positive droplets containing the targeted compounds are finally sorted from the others for further analysis.

## 1.5 References

- [1] G. Takátsy, "The use of spiral loops in serological and virological micro-methods.," *Acta Microbiologica Et Immunologica Hungarica*, vol. 3, pp. 191-202, 1955.
- [2] C. Smith, "Tools for drug discovery: Tools of the trade," *Nature*, vol. 446, no. 7132, pp. 219-222, Mar. 2007.
- [3] A. Dove, "High-throughput screening goes to school," *Nat Meth*, vol. 4, no. 6, pp. 523-532, Jun. 2007.
- [4] K. R. Oldenburg et al., "Assay Miniaturization for Ultra-High Throughput Screening of Combinatorial and Discrete Compound Libraries: A 9600-Well (0.2 Microliter) Assay System," *Journal of Biomolecular Screening*, vol. 3, no. 1, pp. 55 -62, Spring 1998.
- [5] A. Dove, "Drug screening - beyond the bottleneck," *Nat Biotech*, vol. 17, no. 9, pp. 859-863, 1999.

- [6] M. Weber et al., "Ultra-high-throughput screening for antagonists of a Gi-coupled receptor in a 2.2-microl 3,456-well plate format cyclicAMP assay," *Assay and Drug Development Technologies*, vol. 5, no. 1, pp. 117-125, Feb. 2007.
- [7] P. S. Dittrich and A. Manz, "Lab-on-a-chip: microfluidics in drug discovery," *Nature Reviews Drug Discovery*, vol. 5, no. 3, pp. 210-218, Mar. 2006.
- [8] U. Maskos and E. M. Southern, "A novel method for the analysis of multiple sequence variants by hybridisation to oligonucleotides.," *Nucleic Acids Research*, vol. 21, no. 9, pp. 2267-2268, May 1993.
- [9] U. Korf and S. Wiemann, "Protein microarrays as a discovery tool for studying protein-protein interactions," *Expert Review of Proteomics*, vol. 2, no. 1, pp. 13-26, Jan. 2005.
- [10] J. Glökler and P. Angenendt, "Protein and antibody microarray technology," *Journal of Chromatography. B, Analytical Technologies in the Biomedical and Life Sciences*, vol. 797, no. 1-2, pp. 229-240, Nov. 2003.
- [11] D. S. Chen and M. M. Davis, "Molecular and functional analysis using live cell microarrays," *Current Opinion in Chemical Biology*, vol. 10, no. 1, pp. 28-34, Feb. 2006.
- [12] J. Kononen et al., "Tissue microarrays for high-throughput molecular profiling of tumor specimens," *Nat Med*, vol. 4, no. 7, pp. 844-847, Jul. 1998.
- [13] "Affymetrix - Home." [Online]. Available: <http://www.affymetrix.com/estore/>.
- [14] "Illumina, Inc." [Online]. Available: <http://www.illumina.com/>.
- [15] "Applied Microarrays." [Online]. Available: <http://www.appliedmicroarrays.com/>.
- [16] C. Situma, M. Hashimoto, and S. A. Soper, "Merging microfluidics with microarray-based bioassays," *Biomolecular Engineering*, vol. 23, no. 5, pp. 213-231, Oct. 2006.
- [17] P. S. Dittrich and A. Manz, "Lab-on-a-chip: microfluidics in drug discovery," *Nature Reviews Drug Discovery*, vol. 5, no. 3, pp. 210-218, Mar. 2006.
- [18] G. M. Whitesides, "The origins and the future of microfluidics," *Nature*, vol. 442, no. 7101, pp. 368-373, Jul. 2006.
- [19] "Agilent 2100 Bioanalyzer." [Online]. Available: <http://www.genomics.agilent.com/CollectionOverview.aspx?PageType=Application&SubPageType=ApplicationOverview&PageID=275>.
- [20] "Caliper - Microfluidics LabChip® Technology." [Online]. Available: <http://www.caliperls.com/tech/microfluidics.htm>.
- [21] J. Clayton, "Go with the microflow," *Nature Methods*, vol. 2, no. 8, pp. 621-627, Aug. 2005.
- [22] T. Thorsen, "Microfluidic Large-Scale Integration," *Science*, vol. 298, no. 5593, pp. 580-584, Sep. 2002.

- [23] C. L. Hansen, "A robust and scalable microfluidic metering method that allows protein crystal growth by free interface diffusion," *Proceedings of the National Academy of Sciences*, vol. 99, no. 26, pp. 16531-16536, Dec. 2002.
- [24] A. R. Wheeler et al., "Microfluidic Device for Single-Cell Analysis," *Analytical Chemistry*, vol. 75, no. 14, pp. 3581-3586, Jul. 2003.
- [25] P. S. Dittrich and A. Manz, "Single-molecule fluorescence detection in microfluidic channels—the Holy Grail in  $\mu$ TAS?," *Analytical and Bioanalytical Chemistry*, vol. 382, no. 8, pp. 1771-1782, Jun. 2005.
- [26] D. Psaltis, S. R. Quake, and C. Yang, "Developing optofluidic technology through the fusion of microfluidics and optics," *Nature*, vol. 442, no. 7101, pp. 381-386, Jul. 2006.
- [27] D. L. Chen and R. F. Ismagilov, "Microfluidic cartridges preloaded with nanoliter plugs of reagents: an alternative to 96-well plates for screening," *Current Opinion in Chemical Biology*, vol. 10, no. 3, pp. 226-231, Jun. 2006.
- [28] Y. Kikutani, T. Horiuchi, K. Uchiyama, H. Hisamoto, M. Tokeshi, and T. Kitamori, "Glass microchip with three-dimensional microchannel network for 2  $\times$  2 parallel synthesis," *Lab on a Chip*, vol. 2, no. 4, p. 188, 2002.
- [29] H.-C. Yeh et al., "A microfluidic-FCS platform for investigation on the dissociation of Sp1-DNA complex by doxorubicin," *Nucleic Acids Research*, vol. 34, no. 21, p. e144, Dec. 2006.
- [30] H. Song, J. D. Tice, and R. F. Ismagilov, "A Microfluidic System for Controlling Reaction Networks in Time," *Angewandte Chemie International Edition*, vol. 42, no. 7, pp. 768-772, Feb. 2003.
- [31] G. Taylor, "Dispersion of Soluble Matter in Solvent Flowing Slowly through a Tube," *Proceedings of the Royal Society of London. Series A, Mathematical and Physical Sciences*, vol. 219, no. 1137, pp. 186-203, 1953.
- [32] R. Aris, "On the Dispersion of a Solute in a Fluid Flowing through a Tube," *Proceedings of the Royal Society of London. Series A, Mathematical and Physical Sciences*, vol. 235, no. 1200, pp. 67-77, Apr. 1956.
- [33] C.-Y. Lee, C.-L. Chang, Y.-N. Wang, and L.-M. Fu, "Microfluidic Mixing: A Review," *International Journal of Molecular Sciences*, vol. 12, no. 5, pp. 3263-3287, May 2011.
- [34] J. Lederberg, "A simple method for isolating individual microbes," *Journal of Bacteriology*, vol. 68, no. 2, pp. 258-259, Aug. 1954.
- [35] G. J. V. Nossal and J. Lederberg, "Antibody Production by Single Cells," *Nature*, vol. 181, no. 4620, pp. 1419-1420, May 1958.
- [36] B. Rotman, "Measurement of activity of single molecules of beta-D-galactosidase," *Proceedings of the National Academy of Sciences of the United States of America*, vol. 47, pp. 1981-1991, Dec. 1961.



- [37] D. S. Tawfik and A. D. Griffiths, "Man-made cell-like compartments for molecular evolution," *Nature Biotechnology*, vol. 16, no. 7, pp. 652-656, Jul. 1998.
- [38] H. M. Cohen, D. S. Tawfik, and A. D. Griffiths, "Altering the sequence specificity of HaeIII methyltransferase by directed evolution using in vitro compartmentalization," *Protein Engineering Design and Selection*, vol. 17, no. 1, pp. 3-11, Jan. 2004.
- [39] B. T. Kelly, J.-C. Baret, V. Taly, and A. D. Griffiths, "Miniaturizing chemistry and biology in microdroplets," *Chemical Communications*, no. 18, pp. 1773-1788, 2007.
- [40] J. F. Edd et al., "Controlled encapsulation of single-cells into monodisperse picolitre drops," *Lab on a Chip*, vol. 8, no. 8, p. 1262, 2008.
- [41] A. Huebner et al., "Quantitative detection of protein expression in single cells using droplet microfluidics," *Chemical Communications*, no. 12, p. 1218, 2007.
- [42] H. N. Joensson et al., "Detection and Analysis of Low-Abundance Cell-Surface Biomarkers Using Enzymatic Amplification in Microfluidic Droplets," *Angewandte Chemie International Edition*, vol. 48, no. 14, pp. 2518-2521, Mar. 2009.
- [43] C. H. J. Schmitz, A. C. Rowat, S. Koster, and D. A. Weitz, "Dropspots: a picoliter array in a microfluidic device," *Lab on a Chip*, vol. 9, no. 1, pp. 44-49, 2009.
- [44] L. Boitard, "Mesure du métabolisme de la levure par flux osmotiques entre gouttes d'émulsion," Université Paris VII- Denis Diderot, 2010.
- [45] E. Brouzes et al., "Droplet microfluidic technology for single-cell high-throughput screening," *Proceedings of the National Academy of Sciences*, vol. 106, no. 34, pp. 14195-14200, 2009.
- [46] J.-C. Baret, Y. Beck, I. Billas-Massobrio, D. Moras, and A. D. Griffiths, "Quantitative Cell-Based Reporter Gene Assays Using Droplet-Based Microfluidics," *Chemistry & Biology*, vol. 17, no. 5, pp. 528-536, May 2010.
- [47] L. Yu, M. C. W. Chen, and K. C. Cheung, "Droplet-based microfluidic system for multicellular tumor spheroid formation and anticancer drug testing," *Lab on a Chip*, vol. 10, no. 18, p. 2424, 2010.
- [48] J. Clausell-Tormos et al., "Droplet-Based Microfluidic Platforms for the Encapsulation and Screening of Mammalian Cells and Multicellular Organisms," *Chemistry & Biology*, vol. 15, no. 5, pp. 427-437, May 2008.
- [49] P. B. Umbanhowar, V. Prasad, and D. A. Weitz, "Monodisperse Emulsion Generation via Drop Break Off in a Coflowing Stream," *Langmuir*, vol. 16, no. 2, pp. 347-351, Jan. 2000.
- [50] H. Song, D. L. Chen, and R. F. Ismagilov, "Reactions in Droplets in Microfluidic Channels," *Angewandte Chemie International Edition*, vol. 45, no. 44, pp. 7336-7356, 2006.

- [51] A. B. Theberge et al., "Microdroplets in Microfluidics: An Evolving Platform for Discoveries in Chemistry and Biology," *Angewandte Chemie International Edition*, vol. 49, no. 34, pp. 5846-5868, 2010.
- [52] K. Ahn, J. Agresti, H. Chong, M. Marquez, and D. A. Weitz, "Electrocoalescence of drops synchronized by size-dependent flow in microfluidic channels," *Applied Physics Letters*, vol. 88, no. 26, p. 264105, 2006.
- [53] L. Mazutis, J.-C. Baret, and A. D. Griffiths, "A fast and efficient microfluidic system for highly selective one-to-one droplet fusion," *Lab on a Chip*, vol. 9, no. 18, p. 2665, 2009.
- [54] K. Ahn, C. Kerbage, T. P. Hunt, R. M. Westervelt, D. R. Link, and D. A. Weitz, "Dielectrophoretic manipulation of drops for high-speed microfluidic sorting devices," *Applied Physics Letters*, vol. 88, no. 2, p. 024104, 2006.
- [55] Y. Xia and G. M. Whitesides, "Soft lithography," *Annual Review of Materials Science*, vol. 28, no. 1, pp. 153-184, Aug. 1998.
- [56] S. R. Quake and A. Scherer, "From Micro- to Nanofabrication with Soft Materials," *Science*, vol. 290, no. 5496, pp. 1536-1540, Nov. 2000.
- [57] J. C. McDonald et al., "Fabrication of microfluidic systems in poly(dimethylsiloxane)," *Electrophoresis*, vol. 21, no. 1, pp. 27-40, Jan. 2000.
- [58] H. Lorenz, M. Despont, N. Fahrni, J. Brugger, P. Vettiger, and P. Renaud, "High-aspect-ratio, ultrathick, negative-tone near-UV photoresist and its applications for MEMS," *Sensors and Actuators A: Physical*, vol. 64, no. 1, pp. 33-39, Jan. 1998.
- [59] A. R. Abate, A. Poitzsch, Y. Hwang, J. Lee, J. Czerwinska, and D. A. Weitz, "Impact of inlet channel geometry on microfluidic drop formation," *Physical Review E*, vol. 80, no. 2, p. 026310, 2009.
- [60] C. N. Baroud, F. Gallaire, and R. Danga, "Dynamics of microfluidic droplets," *Lab on a Chip*, vol. 10, no. 16, p. 2032, 2010.
- [61] T. Thorsen, R. W. Roberts, F. H. Arnold, and S. R. Quake, "Dynamic Pattern Formation in a Vesicle-Generating Microfluidic Device," *Physical Review Letters*, vol. 86, no. 18, p. 4163, Apr. 2001.
- [62] C. Baroud and H. Willaime, "Multiphase flows in microfluidics," *Comptes Rendus Physique*, vol. 5, no. 5, pp. 547-555, Jun. 2004.
- [63] S. L. Anna, N. Bontoux, and H. A. Stone, "Formation of dispersions using 'flow focusing' in microchannels," *Applied Physics Letters*, vol. 82, no. 3, p. 364, 2003.
- [64] H. Song, M. R. Bringer, J. D. Tice, C. J. Gerdt, and R. F. Ismagilov, "Experimental test of scaling of mixing by chaotic advection in droplets moving through microfluidic channels," *Applied Physics Letters*, vol. 83, no. 22, p. 4664, 2003.

- [65] F. Sarrazin, L. Prat, N. Dimiceli, G. Cristobal, D. Link, and D. Weitz, "Mixing characterization inside microdroplets engineered on a microcoalescer," *Chemical Engineering Science*, vol. 62, no. 4, pp. 1042-1048, Feb. 2007.
- [66] L. Mazutis, "Droplet-based microfluidics for protein evolution," PhD Thesis, Université de Strasbourg, ISIS, 2009.
- [67] D. R. Link et al., "Electric Control of Droplets in Microfluidic Devices," *Angewandte Chemie International Edition*, vol. 45, no. 16, pp. 2556-2560, 2006.
- [68] A. R. Abate, T. Hung, P. Mary, J. J. Agresti, and D. A. Weitz, "High-throughput injection with microfluidics using picoinjectors," *Proceedings of the National Academy of Sciences*, vol. 107, no. 45, pp. 19163-19166, Oct. 2010.
- [69] C. N. Baroud, M. R. de S. Vincent, and J.-P. Delville, "An optical toolbox for total control of droplet microfluidics," *Lab on a Chip*, vol. 7, no. 8, pp. 1029-1033, 2007.
- [70] N. Bremond, A. R. Thiam, and J. Bibette, "Decompressing Emulsion Droplets Favors Coalescence," *Physical Review Letters*, vol. 100, no. 2, p. 024501, Jan. 2008.
- [71] X. Niu, S. Gulati, J. B. Edel, and A. J. deMello, "Pillar-induced droplet merging in microfluidic circuits," *Lab on a Chip*, vol. 8, no. 11, p. 1837, 2008.
- [72] J. Clausell-Tormos, A. D. Griffiths, and C. A. Merten, "An automated two-phase microfluidic system for kinetic analyses and the screening of compound libraries," *Lab on a Chip*, vol. 10, no. 10, pp. 1302-1307, 2010.
- [73] J.-C. Baret et al., "Fluorescence-activated droplet sorting (FADS): efficient microfluidic cell sorting based on enzymatic activity," *Lab on a Chip*, vol. 9, no. 13, p. 1850, 2009.
- [74] D. Pekin et al., "Quantitative and sensitive detection of rare mutations using droplet-based microfluidics," *Lab on a Chip*, vol. 11, no. 13, p. 2156, 2011.
- [75] "RainDance Technologies." [Online]. Available: <http://www.raindancetechnologies.com/>.
- [76] L. Frenz, K. Blank, E. Brouzes, and A. D. Griffiths, "Reliable microfluidic on-chip incubation of droplets in delay-lines," *Lab on a Chip*, vol. 9, no. 10, pp. 1344-1348, May 2009.
- [77] R. R. Pompano, W. Liu, W. Du, and R. F. Ismagilov, "Microfluidics Using Spatially Defined Arrays of Droplets in One, Two, and Three Dimensions," *Annual Review of Analytical Chemistry*, vol. 4, no. 1, pp. 59-81, Jul. 2011.
- [78] H. Boukellal, S. Selimovic, Y. Jia, G. Cristobal, and S. Fraden, "Simple, robust storage of drops and fluids in a microfluidic device," *Lab on a Chip*, vol. 9, no. 2, pp. 331-338, 2009.
- [79] F. Courtois et al., "Controlling the Retention of Small Molecules in Emulsion Microdroplets for Use in Cell-Based Assays," *Analytical Chemistry*, vol. 81, no. 8, pp. 3008-3016, Apr. 2009.

- [80] A. Huebner et al., “Static microdroplet arrays: a microfluidic device for droplet trapping, incubation and release for enzymatic and cell-based assays,” *Lab on a Chip*, vol. 9, no. 5, pp. 692-698, 2009.
- [81] L. Mazutis and A. D. Griffiths, “Preparation of monodisperse emulsions by hydrodynamic size fractionation,” *Applied Physics Letters*, vol. 95, no. 20, p. 204103, 2009.
- [82] H. N. Joensson, M. Uhlén, and H. A. Svahn, “Droplet size based separation by deterministic lateral displacement—separating droplets by cell-induced shrinking,” *Lab on a Chip*, vol. 11, no. 7, p. 1305, 2011.
- [83] L. M. Fidalgo, G. Whyte, D. Bratton, C. F. Kaminski, C. Abell, and W. T. S. Huck, “From Microdroplets to Microfluidics: Selective Emulsion Separation in Microfluidic Devices13,” *Angewandte Chemie International Edition*, vol. 47, no. 11, pp. 2042-2045, 2008.
- [84] J. J. Agresti et al., “Ultrahigh-throughput screening in drop-based microfluidics for directed evolution,” *Proceedings of the National Academy of Sciences*, vol. 107, no. 9, pp. 4004-4009, Feb. 2010.
- [85] S. Vyawahare, A. D. Griffiths, and C. A. Merten, “Miniaturization and Parallelization of Biological and Chemical Assays in Microfluidic Devices,” *Chemistry & Biology*, vol. 17, no. 10, pp. 1052-1065, Oct. 2010.
- [86] M. M. Crane, K. Chung, J. Stirman, and H. Lu, “Microfluidics-enabled phenotyping, imaging, and screening of multicellular organisms,” *Lab on a Chip*, vol. 10, no. 12, p. 1509, 2010.
- [87] D. Lombardi and P. S. Dittrich, “Advances in microfluidics for drug discovery,” *Expert Opinion on Drug Discovery*, vol. 5, no. 11, pp. 1081-1094, Nov. 2010.
- [88] J. Cargill, “New methods in combinatorial chemistry — robotics and parallel synthesis,” *Current Opinion in Chemical Biology*, vol. 1, no. 1, pp. 67-71, Jun. 1997.
- [89] E. Garcia-Egido, V. Spikmans, S. Y. F. Wong, and B. H. Warrington, “Synthesis and analysis of combinatorial libraries performed in an automated micro reactor system,” *Lab on a Chip*, vol. 3, no. 2, pp. 73-76, 2003.
- [90] M. C. Mitchell, V. Spikmans, and A. J. de Mello, “Microchip-based synthesis and analysis: Control of multicomponent reaction products and intermediates,” *The Analyst*, vol. 126, no. 1, pp. 24-27, 2001.
- [91] A. B. Theberge, “Droplet-based microfluidics for chemical synthesis and integrated analysis,” PhD Thesis, University of Cambridge, Cambridge, UK, 2011.
- [92] L. Granieri, J.-C. Baret, A. D. Griffiths, and C. A. Merten, “High-throughput screening of enzymes by retroviral display using droplet-based microfluidics,” *Chemistry & Biology*, vol. 17, no. 3, pp. 229-235, Mar. 2010.
- [93] T. Squires and S. Quake, “Microfluidics: Fluid physics at the nanoliter scale,” *Reviews of Modern Physics*, vol. 77, no. 3, pp. 977-1026, Oct. 2005.

- [94] K. C. Lowe, M. R. Davey, and J. B. Power, "Perfluorochemicals: their applications and benefits to cell culture," *Trends in Biotechnology*, vol. 16, no. 6, pp. 272-277, Jun. 1998.
- [95] H. A. Stone, A. D. Stroock, and A. Ajdari, "Engineering flows in small devices," *Annual Review of Fluid Mechanics*, vol. 36, no. 1, pp. 381-411, Jan. 2004.
- [96] J. Sagiv, "Organized monolayers by adsorption. 1. Formation and structure of oleophobic mixed monolayers on solid surfaces," *Journal of the American Chemical Society*, vol. 102, no. 1, pp. 92-98, Jan. 1980.
- [97] J. D. Tice, H. Song, A. D. Lyon, and R. F. Ismagilov, "Formation of Droplets and Mixing in Multiphase Microfluidics at Low Values of the Reynolds and the Capillary Numbers," *Langmuir*, vol. 19, no. 22, pp. 9127-9133, Oct. 2003.
- [98] R. Dreyfus, P. Tabeling, and H. Willaime, "Ordered and Disordered Patterns in Two-Phase Flows in Microchannels," *Physical Review Letters*, vol. 90, no. 14, p. 144505, Avril 2003.
- [99] C. Holtze et al., "Biocompatible surfactants for water-in-fluorocarbon emulsions," *Lab on a Chip*, vol. 8, no. 10, pp. 1632-1639, 2008.
- [100] J. Sjöblom, *Emulsions and emulsion stability*. Taylor & Francis, 2006.
- [101] F. Leal-Calderon, V. Schmitt, and J. Bibette, *Emulsion science: basic principles*. 2007.
- [102] J. Bibette, F. L. Calderon, and P. Poulin, "Emulsions: basic principles," *Reports on Progress in Physics*, vol. 62, no. 6, pp. 969-1033, Jun. 1999.
- [103] Y. Bai et al., "A double droplet trap system for studying mass transport across a droplet-droplet interface," *Lab on a Chip*, vol. 10, no. 10, p. 1281, 2010.
- [104] G. Woronoff et al., "New Generation of Amino Coumarin Methyl Sulfonate-Based Fluorogenic Substrates for Amidase Assays in Droplet-Based Microfluidic Applications," *Analytical Chemistry*, vol. 83, no. 8, pp. 2852-2857, Apr. 2011.
- [105] K. Pays, J. Giermanska-Kahn, B. Pouligny, J. Bibette, and F. Leal-Calderon, "Double emulsions: how does release occur?," *Journal of Controlled Release*, vol. 79, no. 1-3, pp. 193-205, Feb. 2002.
- [106] J. Cheng, J.-F. Chen, M. Zhao, Q. Luo, L.-X. Wen, and K. D. Papadopoulos, "Transport of ions through the oil phase of W1/O/W2 double emulsions," *Journal of Colloid and Interface Science*, vol. 305, no. 1, pp. 175-182, Jan. 2007.
- [107] J.-C. Baret, F. Kleinschmidt, A. El Harrak, and A. D. Griffiths, "Kinetic Aspects of Emulsion Stabilization by Surfactants: A Microfluidic Analysis," *Langmuir*, vol. 25, no. 11, pp. 6088-6093, Jun. 2009.
- [108] F. Kleinschmidt, A. D. Griffiths, F. Caron, A. El Harrak, E. Brouzes, and D. R. Link, "Microfluidic Systems And Methods For Reducing The Exchange Of Molecules Between Droplets," U.S. Patent WO/2011/07917630-Jun-2011.

- [109] L. Wen and K. D. Papadopoulos, "Visualization of water transport in W1/O/W2 emulsions," *Colloids and Surfaces A: Physicochemical and Engineering Aspects*, vol. 174, no. 1-2, pp. 159-167, Nov. 2000.
- [110] B. Valeur, *Molecular fluorescence: principles and applications*. Weinheim ;;New York: Wiley-VCH, 2002.
- [111] J. W. Lichtman and J.-A. Conchello, "Fluorescence microscopy," *Nat Meth*, vol. 2, no. 12, pp. 910-919, Dec. 2005.
- [112] N. G. Walter, C.-Y. Huang, A. J. Manzo, and M. A. Sobhy, "Do-it-yourself guide: how to use the modern single-molecule toolkit," *Nature Methods*, vol. 5, no. 6, pp. 475-489, Jun. 2008.
- [113] M. Srisa-Art et al., "Analysis of protein-protein interactions by using droplet-based microfluidics," *Chembiochem: A European Journal of Chemical Biology*, vol. 10, no. 10, pp. 1605-1611, Jul. 2009.
- [114] "Invitrogen - Fluorescence Polarization (FP)." [Online]. Available: <http://www.invitrogen.com/site/us/en/home/References/Molecular-Probes-The-Handbook/Technical-Notes-and-Product-Highlights/Fluorescence-Polarization-FP.html>. [Accessed: 14-Sep-2011].
- [115] H. Song and R. F. Ismagilov, "Millisecond Kinetics on a Microfluidic Chip Using Nanoliters of Reagents," *Journal of the American Chemical Society*, vol. 125, no. 47, pp. 14613-14619, Nov. 2003.
- [116] N. Damean, L. F. Olguin, F. Hollfelder, C. Abell, and W. T. S. Huck, "Simultaneous measurement of reactions in microdroplets filled by concentration gradients," *Lab on a Chip*, vol. 9, p. 1707, 2009.
- [117] H. M. Shapiro, *Practical flow cytometry*. John Wiley and Sons, 2003.
- [118] M. Srisa-Art, E. C. Dyson, A. J. deMello, and J. B. Edel, "Monitoring of Real-Time Streptavidin-Biotin Binding Kinetics Using Droplet Microfluidics," *Analytical Chemistry*, vol. 80, no. 18, pp. 7063-7067, 2008.
- [119] "Definition of code from Oxford Dictionaries Online." [Online]. Available: <http://oxforddictionaries.com/definition/code>.
- [120] N. Woodland and B. Silver, "Classifying apparatus and method," U.S. Patent 2612994Oct-1952.
- [121] K. Braeckmans, S. C. De Smedt, M. Leblans, R. Pauwels, and J. Demeester, "Encoding microcarriers: present and future technologies," *Nat Rev Drug Discov*, vol. 1, no. 6, pp. 447-456, Jun. 2002.
- [122] N. H. Finkel, X. Lou, C. Wang, and L. He, "Barcoding the Microworld," *Analytical Chemistry*, vol. 76, no. 19, p. 352 A-359 A, Oct. 2004.

- [123] A. W. Czarnik, "Encoding methods for combinatorial chemistry," *Current Opinion in Chemical Biology*, vol. 1, no. 1, pp. 60-66, Jun. 1997.
- [124] K. Cederquist, S. Dean, and C. Keating, "Encoded anisotropic particles for multiplexed bioanalysis," *WILEY INTERDISCIPLINARY REVIEWS-NANOMEDICINE AND NANOBIO TECHNOLOGY*, vol. 2, no. 6, pp. 578-600, Dec. 2010.
- [125] M. Han, X. Gao, J. Z. Su, and S. Nie, "Quantum-dot-tagged microbeads for multiplexed optical coding of biomolecules," *Nat Biotech*, vol. 19, no. 7, pp. 631-635, Jul. 2001.
- [126] "Molecular Probes: The Handbook." [Online]. Available: <http://www.invitrogen.com/site/us/en/home/References/Molecular-Probes-The-Handbook.html>.
- [127] A. Burns, H. Ow, and U. Wiesner, "Fluorescent core-shell silica nanoparticles: towards 'Lab on a Particle' architectures for nanobiotechnology," *Chemical Society Reviews*, vol. 35, no. 11, pp. 1028-1042, 2006.
- [128] C. Murray, D. Norris, and M. Bawendi, "Synthesis and characterization of nearly monodisperse CdE (E = sulfur, selenium, tellurium) semiconductor nanocrystallites," *Journal of the American Chemical Society*, vol. 115, no. 19, pp. 8706-8715, 1993.
- [129] J. M. Klostranec and W. C. W. Chan, "Quantum Dots in Biological and Biomedical Research: Recent Progress and Present Challenges," *Advanced Materials*, vol. 18, no. 15, pp. 1953-1964, Aug. 2006.
- [130] R. J. Fulton, R. L. McDade, P. L. Smith, L. J. Kienker, and J. R. Kettman, "Advanced multiplexed analysis with the FlowMetrix™ system," *Clin Chem*, vol. 43, no. 9, pp. 1749-1756, Sep. 1997.
- [131] C. Xu and E. Bakker, "Multicolor Quantum Dot Encoding for Polymeric Particle-Based Optical Ion Sensors," *Analytical Chemistry*, vol. 79, no. 10, pp. 3716-3723, May 2007.
- [132] S. Fournier-Bidoz et al., "Facile and Rapid One-Step Mass Preparation of Quantum-Dot Barcodes<sup>13</sup>," *Angewandte Chemie International Edition*, vol. 47, no. 30, pp. 5577-5581, 2008.
- [133] J. Xu, J. Liang, J. Li, and W. Yang, "Multicolor Dye-Doped Silica Nanoparticles Independent of FRET," *Langmuir*, vol. 26, no. 20, pp. 15722-15725, Oct. 2010.
- [134] X. Zhao, R. P. Bagwe, and W. Tan, "Development of Organic-Dye-Doped Silica Nanoparticles in a Reverse Microemulsion," *Advanced Materials*, vol. 16, no. 2, pp. 173-176, 2004.
- [135] A. Burns, H. Ow, and U. Wiesner, "Fluorescent core-shell silica nanoparticles: towards 'Lab on a Particle' architectures for nanobiotechnology," *Chemical Society Reviews*, vol. 35, no. 11, pp. 1028-1042, 2006.
- [136] A. L. Rogach, D. Nagesha, J. W. Ostrander, M. Giersig, and N. A. Kotov, "'Raisin Bun'-Type Composite Spheres of Silica and Semiconductor Nanocrystals," *Chemistry of Materials*, vol. 12, no. 9, pp. 2676-2685, 2000.

- [137] C. Wu et al., “Hybrid Silica–Nanocrystal–Organic Dye Superstructures as Post-Encoding Fluorescent Probes,” *Angewandte Chemie International Edition*, vol. 46, no. 28, pp. 5393-5396, Jul. 2007.
- [138] “Luminex Technology Overview.” [Online]. Available: [http://www.panomics.com/index.php?id=product\\_96](http://www.panomics.com/index.php?id=product_96).
- [139] L. Wang and W. Tan, “Multicolor FRET Silica Nanoparticles by Single Wavelength Excitation,” *Nano Letters*, vol. 6, no. 1, pp. 84-88, Jan. 2006.
- [140] P. P. Pillai, S. Reisewitz, H. Schroeder, and C. M. Niemeyer, “Quantum-dot-encoded silica nanospheres for nucleic acid hybridization,” *Small (Weinheim an Der Bergstrasse, Germany)*, vol. 6, no. 19, pp. 2130-2134, Oct. 2010.
- [141] T. R. Sathé, A. Agrawal, and S. Nie, “Mesoporous Silica Beads Embedded with Semiconductor Quantum Dots and Iron Oxide Nanocrystals: Dual-Function Microcarriers for Optical Encoding and Magnetic Separation,” *Analytical Chemistry*, vol. 78, no. 16, pp. 5627-5632, 2006.
- [142] M. Lessard-Viger, M. Rioux, L. Rainville, and D. Boudreau, “FRET Enhancement in Multilayer Core–Shell Nanoparticles,” *Nano Letters*, vol. 9, no. 8, pp. 3066-3071, 2009.



# Chapter 2. Synthesis and characterization of novel fluorescent silica nanoparticles

## 2.1 Preliminary considerations

As seen in the previous chapter, in spite of their numerous advantages, organic fluorophores present serious shortcomings to be reliably utilized as optical labels in microfluidic droplets. Hence, to circumvent this problem while keeping and even improving their optical properties, we decided to incorporate them in a colloidal host matrix. A list of requirements guided our choice of matrix material: first, the fluorophore had to easily and durably bind to it and possibly have its fluorescence properties improved. It also had to be water and DMSO-soluble, inert to pH and salinity changes, non-toxic and compatible with the microfluidic platform. In addition, it had to allow tuning of fluorophore FP. After some investigation of the available materials presented in the General Introduction, we opted for silica as our material of choice.

### 2.1.1 Generalities about silica

#### Why silica?

Silica is the most abundant chemical species present in the Earth's crust and mantle. It is also widely found in nature, in quartz crystals, sand or diatoms shells, to name only a few. Its hardness and transparency properties have been known since Antiquity, for use in everyday objects such as windows, drinking glasses, bottles or eyeglasses. Recently, silica has been adopted in more high-tech products such as abrasives, optical fibers for telecommunications, solid phases for chromatography or insulating modules for microelectronics [1].

The appeal for this material comes from its many advantages: (i) except when in very fine crystalline powder (which can cause silicosis), it is non-toxic and biofriendly; (ii) it is optically transparent in the visible and near-infrared range; (iii) it is chemically inert and can stay intact in a wide range of pH conditions and temperatures; (iv) nevertheless, its surface bears reactive silanol groups, prone to many chemical modifications, as detailed further in this section; (v) due to its wide availability, it is an inexpensive raw material [1].

## The chemistry of silica

The basic chemical formula of silica is  $\text{SiO}_2$  (silicon dioxide). It can have many crystalline structures as well as amorphous forms. All silica is made of the same tetrahedral building block, formed of a central Si atom bound to 4 oxygen atoms. The Si-O bond, which is the most stable of all Si-X bonds has a length of 0.162 nm, which is shorter than the sum of the radius of the Si and O atoms. This short bond is thus a quite stable one [2].

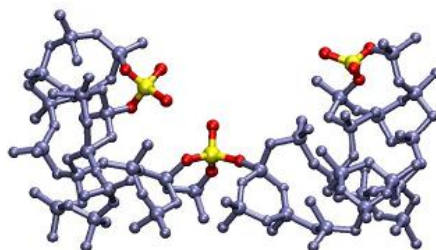


**Figure 2.1** 3D ball-and-stick structure of amorphous silica. Yellow balls are silicon atoms, red ones are oxygen atoms. Reprinted from [3].

The polymorphism of silica is due to the several possible arrangements of the tetrahedral  $\text{SiO}_4$  units. In amorphous silica, as opposed to crystalline silica, they are randomly packed, which results in a non-periodic structure (see **Figure 2.1**). Amorphous silica can be found under several forms including fused quartz, fumed silica, silica gel, aerogel and colloidal silica [1]. The latter consists in a dispersion (also called “sol”) of sub-micron silica particles in a solvent. To produce silica sols, several synthesis routes exist, depending on the targeted particle size, monodispersity and density desired. However, in all cases, colloidal stability of the particles must be preserved to keep them a long time.

### 2.1.2 Colloidal stabilization of silica nanoparticles

#### Colloidal stability: the DLVO theory

The DLVO theory (named after its contributors, Derjaguin [4], Landau [4], Verwey [5] and Overbeek [5]) suggests that the stability of a particle in solution depends on its total potential energy function  $V_T$ .  $V_T$  is expressed as the balance of several competing contributions:

$$V_T = V_A + V_R + V_S \quad (2.1)$$

where  $V_S$  is the potential energy due to the solvent, which usually only makes a marginal contribution to the total potential energy over the last few nanometers of separation. Much more

important is the balance between  $V_A$  and  $V_R$ , the attractive and repulsive contributions, which are much larger and operate over a greater distance. The attractive potential between two identical spherical particles can be expressed as in equation (2.2) [6]:

$$V_A = \frac{-A.R}{12D_{p-p}} \quad (2.2)$$

where  $A$  is the material-dependent Hamaker constant,  $R$  the particles radius and  $D_{p-p}$  the distance between the two particles. For silica,  $A = 6.5 \times 10^{-21}$  J, which is one to two orders of magnitude smaller than other colloidal oxides.

The repulsive potential  $V_R$  between two identical spherical particles is a far more complex function [7]:

$$V_R = 2\pi\varepsilon\varepsilon_0\xi^2 e^{-\kappa D_{p-p}} \quad (2.3)$$

$\varepsilon$  and  $\varepsilon_0$  are respectively the dielectric constant of the bulk solution and vacuum,  $\kappa$  is a function of the ionic composition and  $\xi$  is the zeta potential, defined as the electrostatic potential measured at the shear plane of the particle. The potential  $V_R$  rises from the overlap of the electrical double layers of particles similarly charged.

As two particles approach each other due to Brownian motion, an energy barrier resulting from the repulsive force prevents them from adhering together (**Figure 2.2 a**)). But if the particles collide with sufficient energy to overcome that barrier, the attractive force will bring them into contact and lead them to adhere strongly and irreversibly together. As a result, if the particles have a sufficiently high repulsion potential, the dispersion will resist flocculation and the colloidal system will be stable. On the other hand, if a repulsion mechanism does not exist or is too weak, flocculation or coagulation will eventually take place (**Figure 2.2 b**)).

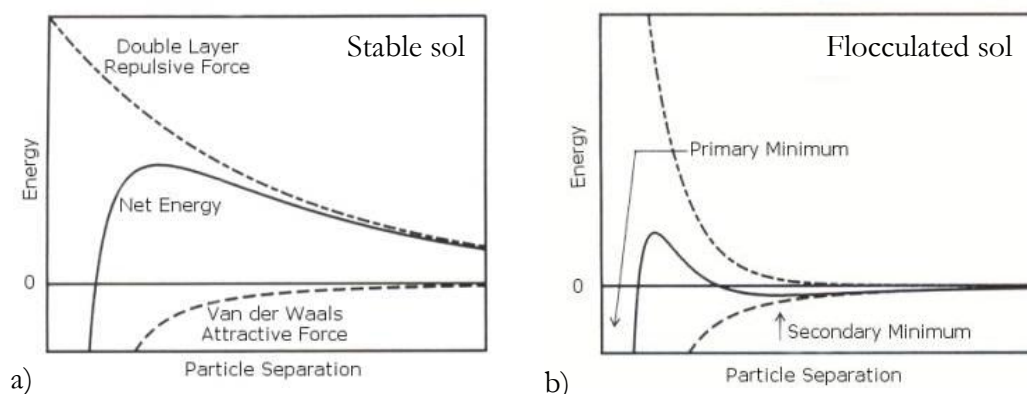


**Figure 2.2** Schematic diagram of the variation of free energy with particle separation. According to the DLVO theory, the net energy is given by the sum of the double layer repulsion and the van der Waals attractive forces that the particles experience as they approach one another. a) Stable colloidal dispersion. b) Flocculated colloidal dispersion. Reprinted from [8].

Depending on the aqueous pH, the surface silanol groups will be more or less charged, impacting the zeta potential, hence the stability. **Figure 2.3** below displays the effect of pH on the stability (gelling time) of the colloidal silica-water system. It is relatively in line with predictions from the DLVO theory. For  $\text{pH} > 2$ , the surface is negatively charged with  $\text{SiO}^-$  groups. Silica coagulates if surface charge is too low (near the isoelectric point at  $\text{pH} 2\text{-}3$ ) or if it is screened by monovalent or divalent salts [1]. Coagulation is also observed at extreme pH values, due to the screening of charges by  $\text{H}^+$  or  $\text{OH}^-$  ions [6].

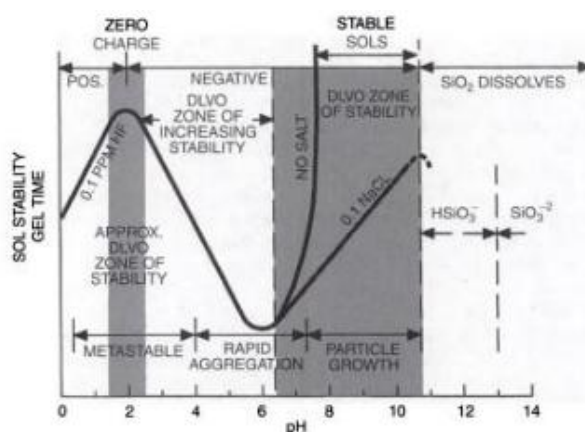


**Figure 2.3** Effect of pH on the stability of the colloidal silica-water system. Thick solid lines represent experimental results. Shaded and white areas are approximate zones corresponding to behavior predicted by the DLVO theory. Reprinted from [2].

To put all odds on our side and overcome pH and salinity issues, we investigated strategies to enable maximal stability of our silica colloids.

## Steric stabilization of silica suspensions

As described by the DLVO theory, stabilization of a colloid can be reached by opposing long-range Van der Waals attractive forces by repulsive forces of equivalent or superior strength. This can be achieved by surrounding particles either with a thick electrical double layer (electrostatic stabilization), or with adsorbed or covalently attached polymeric molecules (steric stabilization).

In order to get stable suspensions for all pH values as well as buffer compositions and concentrations, we opted for the second approach, which coincides very well with the reactive nature of surface silanol groups [2]: they can undergo several types of modifications, such as electrophilic addition, nucleophilic substitution or condensation. Chloro- and alcoxysilanes are commonly used as grafting reagents, because resulting Si-O-Si bonds are very stable.

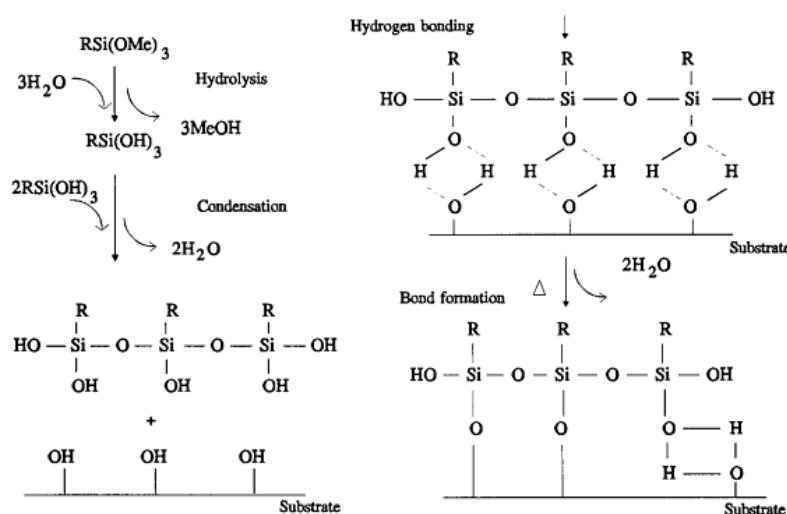


**Figure 2.4** Mechanism of silane deposition in aqueous solvent. Reprinted from [9].

In contact with water, halogen or alkoxy groups of silanes are hydrolyzed, as depicted on **Figure 2.4** [9]. The newly formed silanol groups go into hydrogen-bonding interaction with silanol groups on the silica surface as well as neighboring hydrolyzed silanes, eventually forming siloxane bonds. This double reactivity leads to simultaneous horizontal and vertical polymerization of the coating silanes: a three dimensional polymeric silane network is formed on the surface. These reactions in water are delicate to control, so the thickness of the grafted layer can be variable. To favor vertical polymerization over self-condensation in our aqueous reaction medium, we ruled out trichlorosilanes: they are so sensitive to moisture that they would immediately self-condense; therefore, we instead opted for triethoxysilanes that hydrolyze more slowly. To fully covalently attach the adsorbed hydrolyzed molecules, we found that curing between 80 and 200°C was necessary [10].

For the R group pictured on **Figure 2.4**, a broad range of hydrophilic polymers was available: polyethers, polyelectrolytes, polyacrylates, sugars... We opted for polyethylene glycol (PEG), a biocompatible synthetic polyether which is extensively used in pharmaceutical formulations, foods, and cosmetics [11]. It is non-charged, thus avoids interaction with the charged contents of the droplets. It is also very soluble in water as well as in many organic solvents and its behavior shows little dependence on pH. To avoid parasite reaction of PEG OH endgroups, we chose methoxy-encapped PEG-triethoxysilane as a reagent.

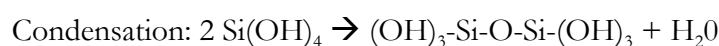
### 2.1.3 Colloidal silica: synthesis routes

After choosing the type of colloid in which to encapsulate our fluorophore, as well as the way to stabilize it, we then researched the literature to determine which synthesis route was the best to match our requirements, which are: (i) the fluorophore must be reliably encapsulated and stay inside the particle over periods of months; (ii) the particles must retain colloidal stability over a long time as well; (iii) if possible, the synthesis should involve a minimal number of steps and be performed in aqueous solution.

#### Aqueous Stöber synthesis

The most quoted synthesis route in literature is the aqueous synthesis method developed by Stöber in 1968 [12]. It consists in the hydrolysis and condensation of alcoxysilanes in a mixture of ammonia, water and alcohols.

The reactions involved are the following:



The formation of particles is based on the nucleation-growth process [13]. First, silica nuclei are formed by homogeneous nucleation, then aggregate in a controlled fashion to form small silica particles. These particles keep growing by monomer addition until hydrolysis and condensation have consumed all the alcoxysilanes. Combining tetraethoxysilane (TEOS), ethanol, water and ammonia and finely adjusting the relative proportions of these reagents, particles diameter can be tuned from 20 nm to 2  $\mu\text{m}$ , with a relatively low polydispersity (8-20 %).

#### Microemulsion route

A variation of the base-catalyzed, controlled hydrolysis of TEOS was developed in 1986 by Yanagi et al and later improved [2], [14]. A water-in-oil microemulsion of aqueous ammonia, surfactant and oil is prepared and TEOS is subsequently added. It migrates to the nanometer-

range aqueous pools, where its hydrolysis takes place. The growth mechanism observed is driven by aggregation of nuclei during micellar collisions, which leads to high porosity of the final particles. They are also extremely monodisperse (less than 4 % polydispersity) due to the regular pattern provided by the microemulsion micelles.

These two routes, although appealing, display three major practical drawbacks for our application: (i) to reliably encapsulate the fluorophore, it is safer to overcoat the dye-labeled silica core with a bare silica shell, which increases the particle size, favoring long-term sedimentation; (ii) the porosity of these particles could impede long-term trapping of the dye; (iii) both schemes involve non aqueous solvents: an additional washing step is required to redisperse them in aqueous environment, making the whole process more labor-intensive and possibly threatening the colloidal stability. That is why we sought alternative aqueous synthesis schemes.

### Synthesis from silicates

Interestingly, we found that the oldest developed route (1861) for the synthesis of colloidal silica was matching both requirements. Currently the most used industrially, this scheme is based on the acidification of a dilute sodium silicate solution (also called “water glass”) from pH 11-12 to pH 2-4 [2], [15]. The silicate ions are consequently converted into active silicic acid, which is an unstable colloidal solution of 1-2 nm that can easily gel due to the high degree of polymerization. Hence, pH is increased to 8-10.5 for the growth step of nuclei into 4-100 nm particles, leading to a stable silica sol (see **Figure 2.5**).

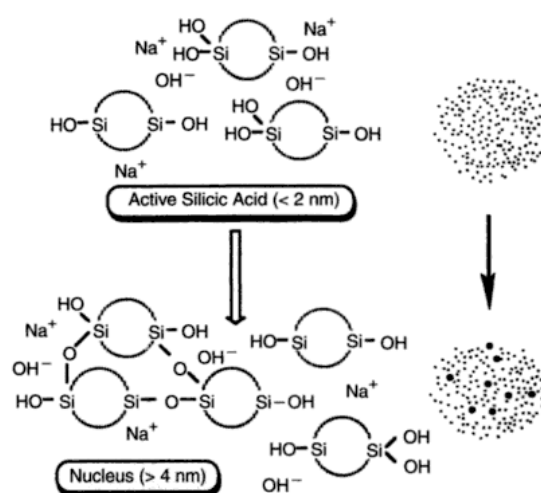


**Figure 2.5** Polymerization of active silicic acid to form nuclei. Reprinted from [2].

Historically, the acidification step was first performed by simple addition of hydrochloric acid. This had a major drawback: the sodium and chloride ions still present in solution led to

accelerated destabilization of the silica sol. To solve this problem, several methods were developed to remove this excess of ions: peptization (washing the sol with water), dialysis, and electro dialysis. A breakthrough came with the introduction of a new method for acidification of the silicates, based on an ion-exchange process [16], [17] that consists in exchanging the sodium ions with  $H^+$  ions, thus keeping the solution ionic strength low. This is now the most widely used in large-scale manufacturing. The sequence of steps is presented on **Figure 2.6**.

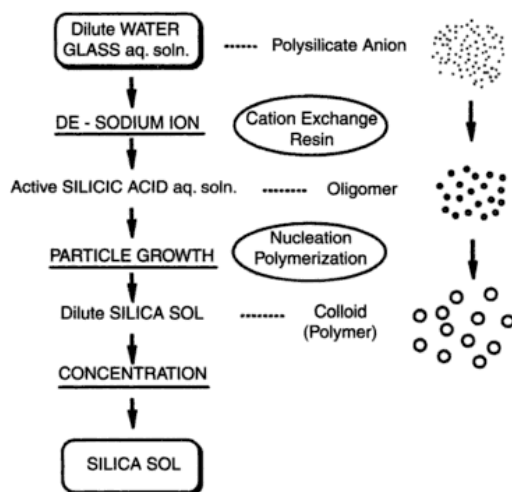


**Figure 2.6** Flow chart of ion exchange method form manufacturing silica sols from polysilicates. Reprinted from [2].

This method, significantly cheaper than the previous two, looked very promising. Given the particle stability conditions reported on **Figure 2.3**, we looked further if protocols existed to nucleate and grow the particles in only a single step at basic pH.

### Persello synthesis

A variation of the acidification process was developed by Persello et al in 1991 [18], [19]: they performed acidification of silicates down to pH 8-10 only, instead of 2-4. In this pH range, silica sols are stable as well (as **Figure 2.3** shows) and their growth takes place much more slowly, allowing more control. However, in this protocol, acidification is still carried out by a strong acid; exchange resins are introduced only in the final washing step to remove excess salts. Based on a later patent [20] and on the work by Vinas [21], we finally found a way to solve the salinity issue: to perform the acidification step with an acidic cation exchange resin as well. With no more extra ions added, salinity would then be as low as possible all along the synthesis, maintaining colloidal stability and low particle size around 2-4 nm.

With this process, the nuclei formation mechanism is the following:



- 1) Ion exchange and acidification:  $\text{Na}_2\text{Si}_3\text{O}_7 + 2 \text{H}^+ \rightarrow 2 \text{Na}^+ + \text{H}_2\text{Si}_3\text{O}_7$
- 2) Dehydrating condensation polymerization :  $2 \text{H}_2\text{Si}_3\text{O}_7 \rightarrow \text{HSi}_3\text{O}_6\text{-O-Si}_3\text{O}_6\text{H} + \text{H}_2\text{O}$

### 2.1.4 Fluorescently labeled silica nanoparticles

The last step before starting our syntheses was to determine the best strategy to incorporate the fluorophore in the silica matrix. We had two requirements: (i) lose as little fluorophore as possible during the reaction (it is the most expensive reagent in the process) and (ii) keep it durably bound.

#### Several fluorophore encapsulation strategies

Dyes can be encapsulated inside a silica matrix via several mechanisms such as electrostatic attraction, spatial constraint or covalent bonding [22]. The first one can be quite challenging, even though positively charged dye molecules are expected to have a high affinity to negatively charged silica surfaces. However, such an electrostatic interaction is not very strong and the fluorophores often aggregate [23]. Moreover, this strategy excludes negatively charged dyes.

The second approach, steric attachment, is hardly applicable to graft hydrophobic organic dyes into hydrophilic silica because of their limited solubility. The limitation can be overcome, by attaching water-soluble groups to the dye molecules before the next step, e.g. Dextran [24], sulfonate [25] or carbonate groups. However, if the added hydrophilic moiety is negatively charged, it brings back the previously mentioned charge problem; if it is a polymer, steric repulsion severely limits the maximum number of grafted molecules in 2 nm silica particles.

That is why we chose the third approach: covalent binding to a silane coupling agent. Among the variety of couplings available, we opted for the most frequently used: reaction of a primary amine on either a N-hydroxysuccinimide ester (NHS) or an isothiocyanate (ITC) (**Figure 2.7**): these two varieties of functionalized dyes are the most available and the resulting thiourea and amide bonds are strong. For the three other groups constituting the silane, we chose three ethoxy moieties, which enable robust grafting into the silica matrix while limiting self-condensation [13], [26]. Aminopropyltriethoxysilane (APTES) was our starting silane binder.

To cover the whole visible-NIR range, we chose to encapsulate four different fluorophores with absorption/emission maxima sufficiently spaced from each other, to limit problems of spectral crosstalk further discussed in Chapter 4. Their molecular structures and absorption/emission maxima are gathered on **Figure 2.8**.

## 2. Novel fluorescent core-shell silica nanoparticles

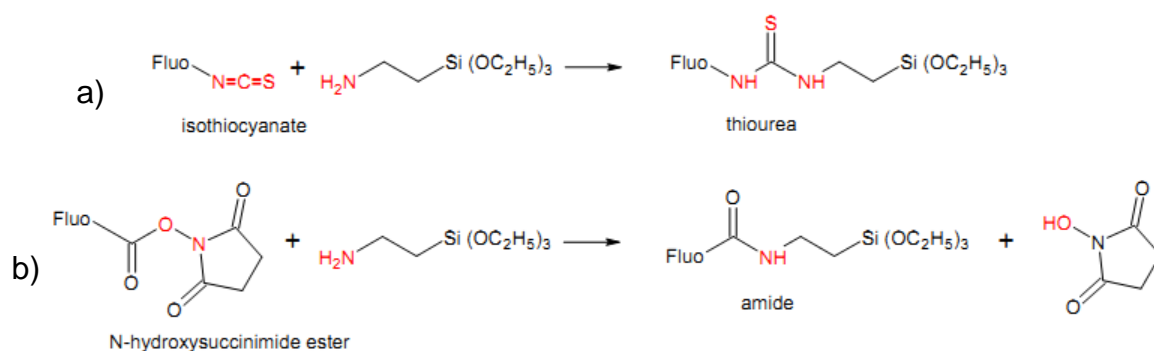


**Figure 2.7** Coupling mechanisms of APTES to amine-reactive fluorophores: a) isothiocyanate or b) N-hydroxysuccinimide ester.

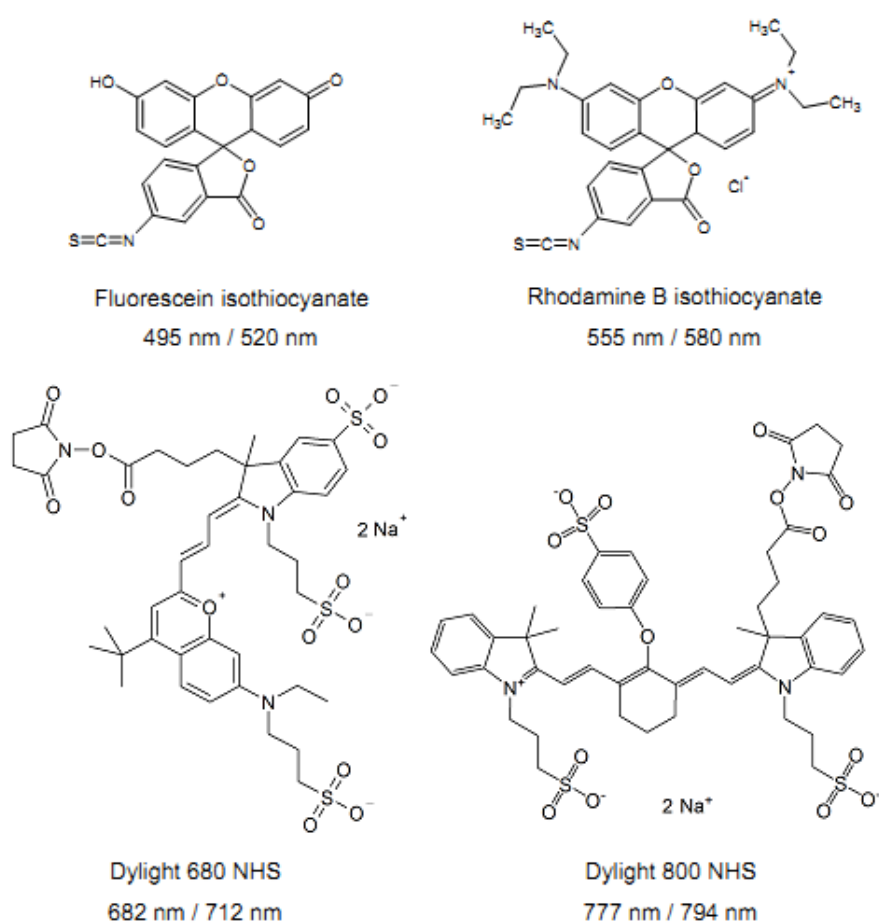


**Figure 2.8** Chemical structures and absorption/emission maxima of the four amine-reactive fluorophores used in our F-SNP.

## Fluorescence properties of fluorophores in silica particles: a review

Since the first synthesis of covalently-labeled fluorescent silica nanoparticles [13], their versatility has been exploited for many applications: bio-imaging, drug delivery, sensing and therapeutics [27–29]. Among all properties, enhancement of their fluorescence intensity raised particular attention. The group of Ulrich Wiesner in Cornell showed the interest of a fine-tuned core-shell architecture (fluorescent silica core/bare silica shell) towards optimal reduction of non-radiative emission [30], [31]. An example is given on **Figure 2.9**:

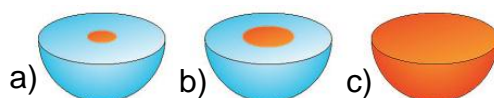


**Figure 2.9** Three examples of dye spatial repartition in the silica matrix: a) compact core-shell, b) expanded core-shell, c) homogeneous particle. Reprinted from [31].

Other groups combined several colors per nanoparticle to get multi-fluorescent emission and generate integrated barcodes [29], [32], [33]. This proved to be quite delicate due to aggregation-caused quenching [34], [35] and FRET effects [36].

Since we were aiming for a small particle size, we chose the safe option of encapsulating our different fluorophores separately. Given our end goal of multiplexing in droplets, it drastically simplified the protocol: with only one synthesis per type of dye, we could still reach large number of barcodes by mixing various amounts of each SNP color.

Nevertheless, as pointed out in Chapter 1, adding the FP dimension to our code would drastically increase the multiplexing capacity, as highlighted by equation (1.6) of Chapter 1. Due to the larger size of silica particles compared to bare fluorophore, the rotation of the fluorescence emitter is slower, thus its steady-state FP value is expected to be higher (see **Figure 1.20** in Chapter 1). Consequently, the most straightforward way to tune FP is to vary the size of the silica particle encapsulating the fluorophores.

However, this requires different synthesis conditions for each size and is limited by our requirement of long-term colloidal stability. Thus, we investigated an alternative effect: the depolarization of fluorescent signal by resonance energy transfer between two neighboring dye molecules in the same particle [34], [37], [38]. We sought to establish if we could possibly tune FP values by varying the concentration of grafted dye, thus the distance between embedded fluorophores. Given that the Förster distance for FITC is 5.5 nm, a good inter-fluorophore distance range to get maximal depolarization without quenching is 3-5 nm. We hence calculated

the optimal particle size and number of fluorophores to satisfy this condition (highlighted in yellow on **Figure 2.10**): a particle diameter of 8-10 nm would be our end goal.

Particle radius (nm)	1	2	3	4	5
Particle volume (nm <sup>3</sup> )	4	34	113	268	524
Number of dyes in particle	Average distance between particles $\bar{d} = \sqrt[3]{\frac{V_{part}}{N_{dyes}}}$				
2	1.28	2.56	3.84	5.12	6.40
3	1.12	2.24	3.35	4.47	5.59
4	1.02	2.03	3.05	4.06	5.08
5	0.94	1.89	2.83	3.77	4.71
6	0.89	1.77	2.66	3.55	4.44
7	0.84	1.69	2.53	3.37	4.21
8	0.81	1.61	2.42	3.22	4.03
9	0.77	1.55	2.32	3.10	3.87
10	0.75	1.50	2.24	2.99	3.74

**Figure 2.10** Calculation of average distance between fluorophores embedded in a silica particle. The combinations giving a distance between 3.0 and 5.0 nm are highlighted in yellow.

As a result of all these considerations, we decided to realize the following 5-step reaction scheme (**Figure 2.11**). The following section discusses the characterization and optimization of each reaction step, followed by optical properties of our nanomaterials.

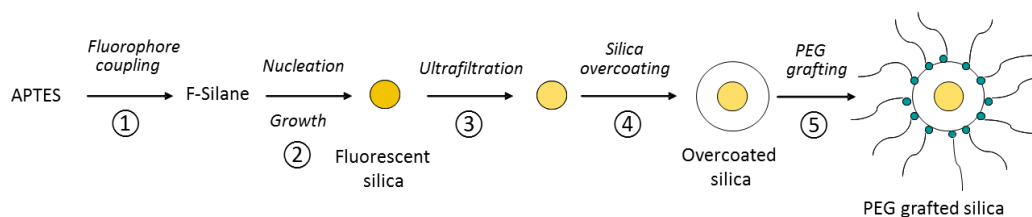


**Figure 2.11** Five-step overall F-SNP synthesis scheme.

## 2.2 Optimization of the reaction steps

Before starting to encapsulate fluorophores in the silica particles, we needed to get a grasp on the optimal reaction conditions. Especially, we sought to tune them in order to explore particle size ranges between 2 and 10 nm. Indeed, the particle size mentioned by Vinas [21] using this method was around 2.5 nm using 5 wt% sodium silicate. Since our dye molecules have hydrodynamic radii of 1 to 2 nm, we aimed for a particle size of at least 3-fold this value, to fully

encapsulate several molecules and take advantage of the homo-FRET-induced depolarization effect.

### 2.2.1 Silica synthesis at pH 9: optimal conditions

Our first task in this synthesis scheme was to find the appropriate  $m(\text{silicate})/m(\text{Amberlite IR 120})$  ratio to reach an equilibrium pH of 9.0 for silica nucleation and growth. Since the  $\text{H}^+$  ions are embedded in the resin, reaction is not immediate like an acid-base reaction with a strong acid. Thus, before trying the silicate/Amberlite reaction, we first separately quantified  $\text{H}^+$  ions in the resin with NaOH, as well as how much HCl is necessary to bring a silicate solution to pH 9.0. We got the following results:

- Amberlite IR 120: 1.9 mmol  $\text{H}^+$  were measured per gram resin;
- On 100 g sodium silicate solution (2.65 wt% equivalents  $\text{SiO}_2$ ), 28.5 mmol  $\text{H}^+$  were added until pH 9.0 was reached. If we added more acid, we noticed a quick gelation right below pH 8.5, due to the decrease in negative surface charges, combined to their screening by increased  $\text{Na}^+$  concentration. This observation confirmed our choice to use acidic exchange resin rather than a classical strong acid.

From these two measurements, we deduced that  $28.5/1.9 = 15$  g resin would be necessary to bring that same silicate solution to pH 9.0. The experimental result gave us  $m_{\text{resin}} = 12.5$  g, probably because NaOH reacted too fast to release all  $\text{H}^+$  in the resin, as opposed to the slow acidification of silicate. This time, we did not notice immediate gelling, even at pH = 8.0. However, we decided to follow Vinas's advice [21], supported by the pH-stability chart presented before on **Figure 2.3**. We performed all our syntheses at pH 9.0, and kept our solutions at this same pH.

### 2.2.2 Core synthesis: finding the maximal size

We first tried to increase the core size somewhat by using initial sodium silicate solution concentrations from 10 wt% to 20 wt% (not more to avoid gelation). By quadrupling the quantity of silica compared to Vinas, we were expecting to multiply the initial diameter by a factor of  $\sqrt[3]{4} = 1.59$ , provided the number of nuclei remained constant. The sizes obtained did slightly increase as **Figure 2.12** shows, but not as much as expected. This indicates that the supersaturation level is between 5 and 10 wt%. Above this level, the size does not increase anymore, meaning that the number of nuclei increases instead, proportionately to the concentration.

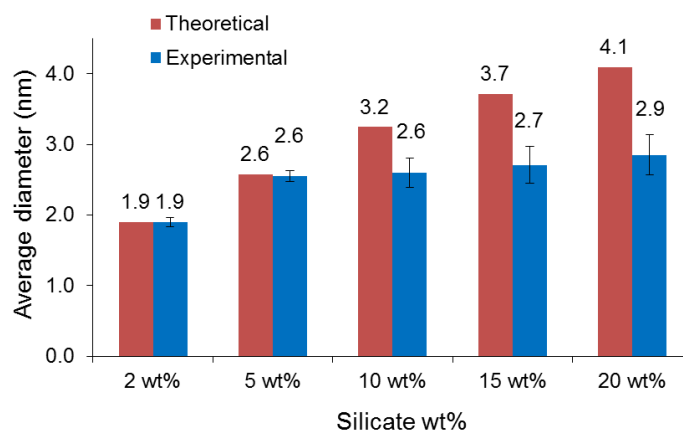


**Figure 2.12** Influence of initial silicate weight percentage on average diameter of SNP cores. Size stops increasing beyond 5 wt% silicate.

Another approach we tested to increase size further was to perform controlled aggregation after completion of the silica synthesis at pH 9. After the reaction was completed overnight, we added several quantities of Amberlite to the batch with the biggest size (20 wt% silicate), in order to bring down the pH to various levels. The resulting size and pH measurements made after 2 hours are displayed on **Figure 2.13**. With a 2-fold increase of the diameter, this method looked promising; however after a few days, the two dispersions with low pH values had gelled irreversibly, very likely because of a decrease in double layer repulsion due to very low surface potential. We therefore had to rule out this method.

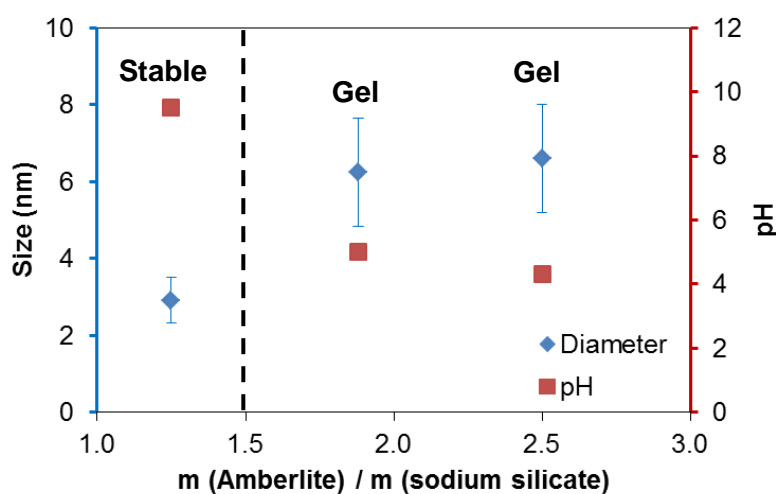


**Figure 2.13** Influence of Amberlite/silicate weight ratio on pH and average diameter of SNP cores. Gelling takes place above an Amberlite/silicate weight ratio of 1.5.

Next, we investigated if it was possible to grow bigger particles by adding silicates on the seed cores. From the observations on **Figure 2.12**, we chose to grow our seeds with 10 wt% silicate, slightly above the supersaturation threshold to control the number of nuclei.

### 2.2.3 Shell growth: exploring several strategies

The first strategy we tried was very progressive, to avoid going over the supersaturation level and causing secondary nucleation: it consisted in doing layer-by-layer shell growth by adding one equivalent silicate at each step. The principle and result of these experiments are described below (**Figure 2.14**). To calculate the theoretical diameter, we took the core size as a starting point: if there is no secondary nucleation, addition of  $n$  silicate equivalents to a core of diameter  $d_0$  gives a particle diameter  $d_n$  expressed as:

$$d_n = \sqrt[3]{(1+n)}.d_0 \quad (2.4)$$

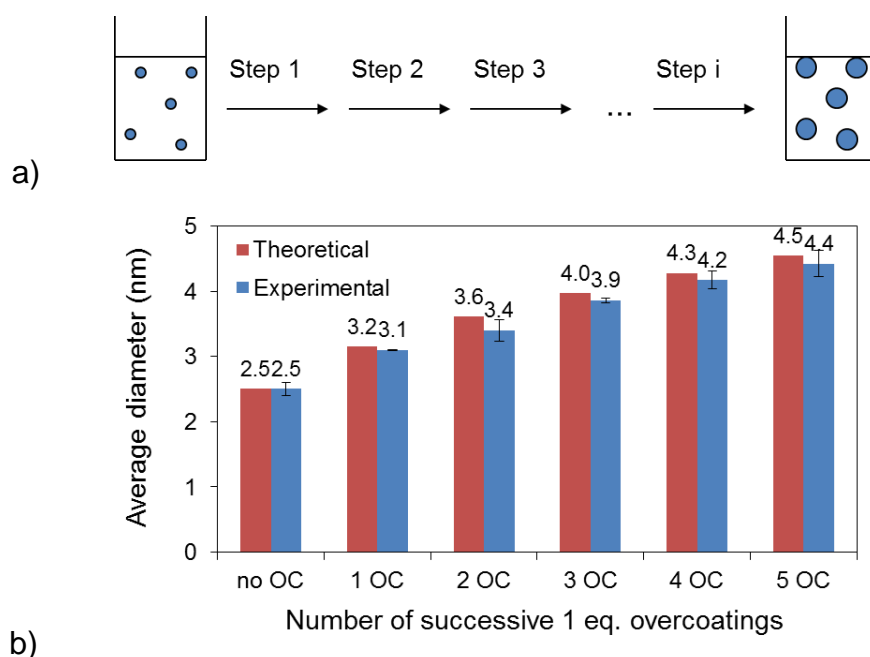


**Figure 2.14** 1-equivalent layer-by-layer shell growth: a) principle of the successive overcoatings strategy, b) Average theoretical and experimental SNP diameters after each step.

The size we obtain experimentally is quite close to the theoretical level: this validates our approach. However, if we want to reach a diameter of 10 nm to encapsulate enough dye molecules in the particle to get fluorescence depolarization, we need to perform  $n$  successive steps, with  $n$  calculated as:

$$n = \left( \frac{10}{d_0} \right)^3 = 64 \quad (2.5)$$

This number is far too high to be practically implemented. In order to reach this number of equivalents faster, we then sought to see if it was possible to add more than one equivalent per overcoating, while avoiding secondary nucleation. So we performed six sets of experiments, adding  $n = 1$  to 50 equivalents. To avoid using considerable volumes of silicate, we took a fraction  $1/n$  of the total cores solution, diluted it back to the initial volume ( $n$ -fold dilution) and added the same volume of silicate as for the core synthesis, which equals  $n$  equivalents of the amount of silicate in the cores fraction.

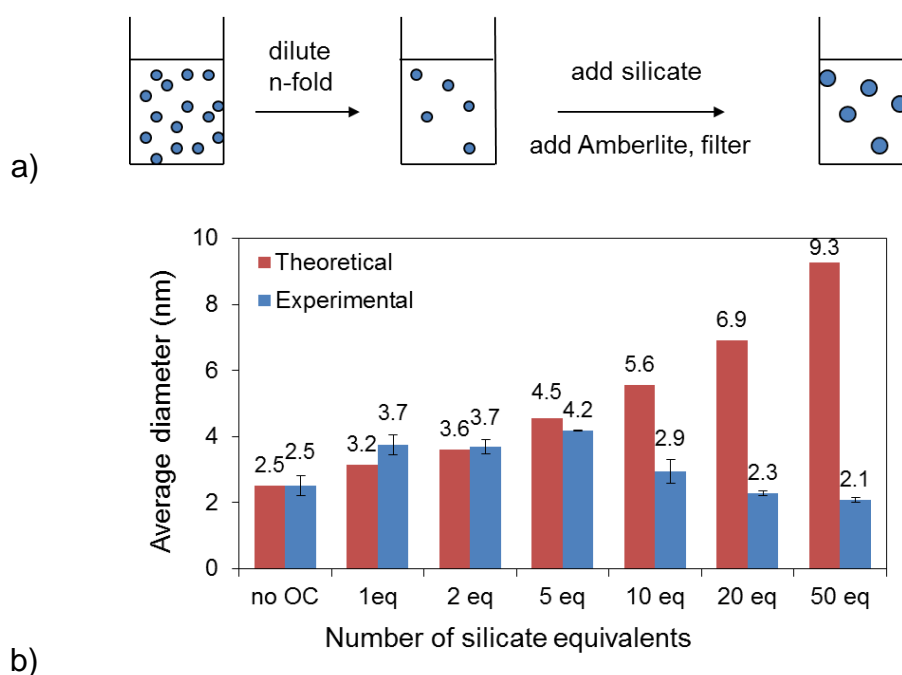


**Figure 2.15** Shell growth by addition of  $n$  equivalents: a) principle of the successive overcoatings strategy, b) Average theoretical and experimental SNP diameters after one addition of  $n$  equivalents.

The resulting trend in nanoparticles sizes (**Figure 2.15**) follows the theoretical calculation from equation

$$d_n = \sqrt[3]{(1+n) \cdot d_0} \quad (2.4)$$

up to 5 equivalents then decreases significantly for higher  $n$  values. As before, this is very likely due to secondary nucleation occurring for  $n > 5$  equivalents.



To reach diameters above the one at 5 equivalents, we decided to combine the previous two approaches: we performed successive 5-fold dilutions and overcoatings, using 5 equivalents silicate at each step. The principle is sketched on **Figure 2.16**.

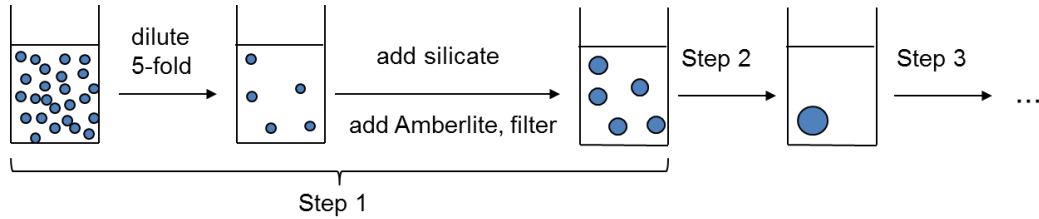


**Figure 2.16** Shell growth by  $i$  additions of 5 equivalents: principle of the successive overcoatings strategy.

By this method, the number of silica particles  $N$  is divided by 5 at every  $i$ -th step (if there is no secondary nucleation):

$$N_{i+1} = \frac{N_i}{5} = N_0 \left( \frac{1}{5} \right)^i \quad (2.6)$$

while the total volume of silica in the container at step  $i$  follows a series law:

$$V_{i+1}^{silica} = V_0^{silica} + \frac{V_i^{silica}}{5} \quad (2.7)$$

As a result, the volume of each particle dramatically increases at every step:

$$\frac{v_{i+1}^{particle}}{v_0^{particle}} = \frac{V_{i+1}^{silica}}{N_{i+1}} \cdot \frac{N_0}{V_0^{silica}} = \frac{v_i^{particle}}{v_0^{particle}} + 5^{i+1} \quad (2.8)$$

For  $i = 0$  to  $i = 3$ , these parameters values are reported on table **Table 2.1**. The theoretical and experimental particle diameters are plotted on **Figure 2.17**.

As the histogram shows, the more overcoatings are done, the further away the average size is from the theoretical size: for  $i = 1$  and 2, there is some secondary nucleation taking place in parallel of the silica growth on the original cores. But for  $i = 3$ , only secondary nucleation seems to take place: the particle diameter is similar to the initial core size. This can have two meanings: (i) either the bigger particles are redissolved in the short time between silicate addition (pH = 11.8) and Amberlite addition to bring back pH down to 9.0, or (ii) at every additional step, there is more small particle nucleation than large particle growth; small particles accumulate at the expense of large ones and finally dominate at the last step. Our DLS measurements do not allow

us to precisely conclude. Overall, the maximal particle size reached was around 6 nm in 2 steps, a larger size than what was previously achieved in 5 steps.

$i$	$V_i^{silica} / V_0^{silica}$	$N_i / N_0$	$v_i^{particle} / v_0^{particle}$	$d_i^{particle} / d_0^{particle}$
0	1	1	1	1
1	1.2	0.2	6	1.82
2	1.24	0.04	31	3.14
3	1.248	0.008	156	5.38

**Table 2.1:** Theoretical silica volume, particles number, volume and diameter relative to the values of the core SNP sol, using the method described on **Figure 2.16**.

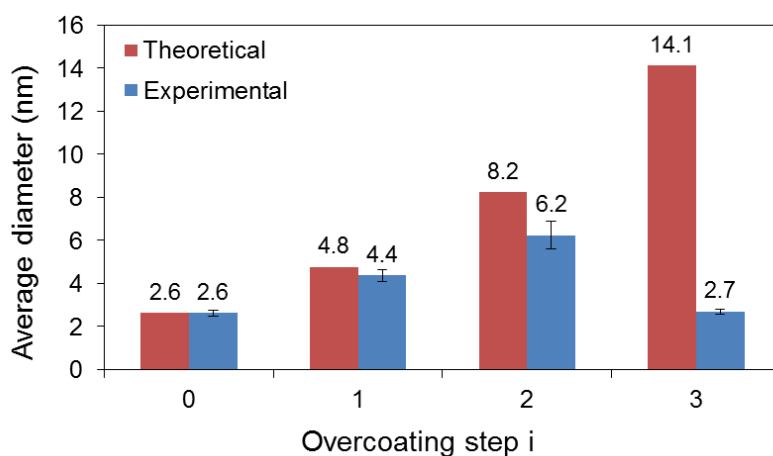


**Figure 2.17** Average theoretical and experimental SNP diameters after  $i$  additions of 5 silicate equivalents.

After this relative success towards our 10 nm goal, we tried to implement these successive additions of 5 equivalents silicate in a more “real-life” situation: this time we added APTES together with silicate, in the same concentration that would be used to graft fluorophores in the matrix. All other reaction parameters were kept constant. We obtained the diameters plotted on **Figure 2.18**:

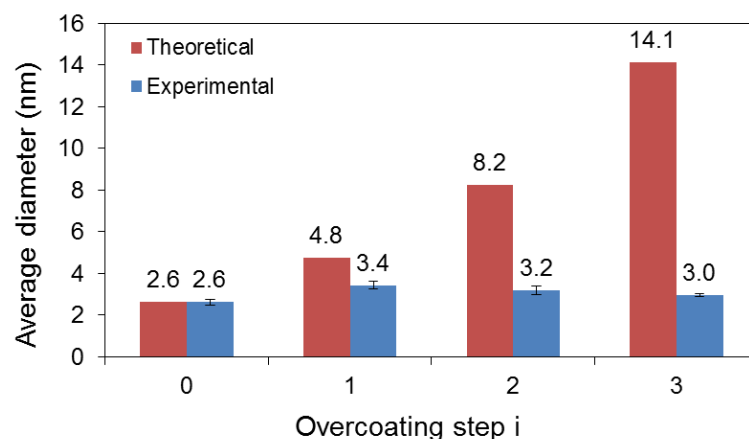


**Figure 2.18** Average theoretical and experimental SNP diameters after  $i$  additions of 5 (silicate + APTES) equivalents.

At all steps, size remained about equal to the initial one. With regard to previous results, APTES seems to promote secondary nucleation, which unfortunately rules out this strategy to encapsulate several fluorophores in bigger particles.

As a last attempt to increase particle size, we tested a new approach: to circumvent potential core redissolution at basic pH during additional silicate addition steps, we designed an overcoating experiment where pH was kept around 9.0 at all times. The setup is sketched on **Figure 2.19**.

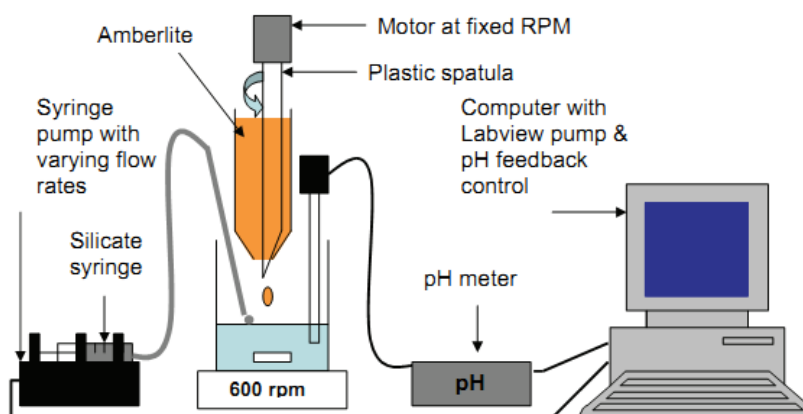


**Figure 2.19** Experimental setup for shell growth by continuous silicate and Amberlite addition.

In a 100-fold diluted suspension of silica cores, Amberlite acid resin and 10-fold diluted sodium silicate solution were simultaneously added. These dilute concentrations were chosen to avoid going over the supersaturation level. Dispensing of the Amberlite resin was done continuously by a DC motor. Addition of silicate solution was done dropwise with a syringe

pump. An in-house Labview feedback control program adjusted the flow rate of the syringe pump in order to keep pH around 9.0 at all times. This precaution was taken to avoid both gelling at  $\text{pH} < 8.5$  as well as redissolution of the growing particles.

We checked the regularity and effectiveness of our Labview feedback control program by recording pH and number of added equivalents (**Figure 2.20**).

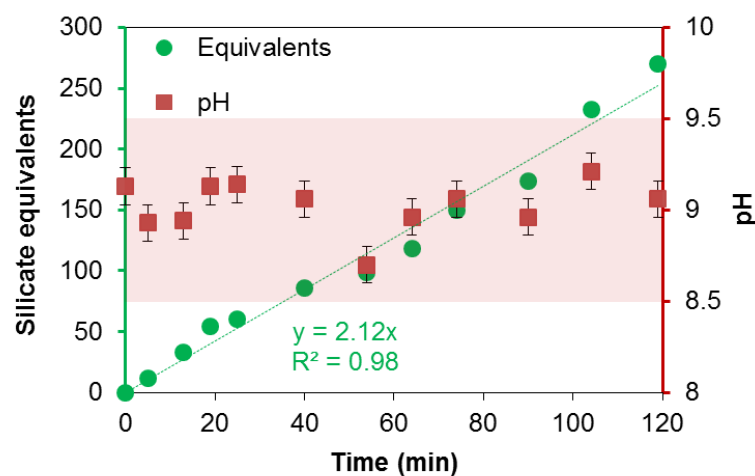


**Figure 2.20** Kinetics of added silicate equivalents and pH during shell growth by continuous silicate and Amberlite addition.

The steadiness of silicate addition is good ( $R^2 = 0.98$ ) at about 2.12 equivalents per minute. pH remains quite constant, with slight variations between 8.7 and 9.2, all of them within the 1 pH unit zone. The theoretical and experimental particles diameters obtained are plotted on **Figure 2.21**.

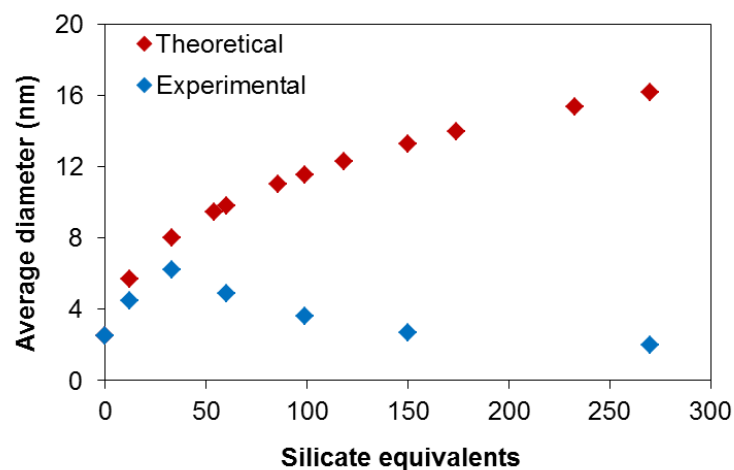


**Figure 2.21** Average theoretical and experimental SNP diameters during continuous shell growth.

In all cases, the sizes reached are always below the theoretical values. As observed in another case previously described, maximal diameter climaxed at 6.5 nm for 30 equivalents, before gradually decreasing back to its initial value.

All these tests led us to conclude that the most reliable way to increase size in a controlled fashion without secondary nucleation is the first method tested: to perform successive additions of one equivalent silicate. Since this does not allow reaching diameters above 7 nm in a rapid fashion, we set aside the idea of grafting many fluorophores per particle and extensively use the FRET depolarizing effect. Consequently, we followed the most simple 2-step strategy: first, incorporate silanized dye into a silica core, then overcoat it with one equivalent bare silica shell.

### 2.2.4 Dye grafting in the silica cores

As introduced earlier, fluorophore grafting is performed in two phases: 1) reaction of an amine-reactive dye derivative on APTES, then 2) covalent bonding of this dye-silane compound into the silica matrix.

For the first step, we chose to use a molar ratio  $\frac{n_{APTES}}{n_{dye}} = 20$  to ensure no dye remains unsilanized. As far as solvent is concerned, we could choose between ethanol and DMSO [39]. In spite of being widely used in the literature, we soon ruled out the first one. Indeed, one of the dyes we initially intended to use, Dylight 800 NHS, displayed some anomalous solvent-induced behaviour summarized in **Table 2.2**: when the silanization reaction took part in anhydrous ethanol, the solution underwent significant color change from dark green to blue as well as a blue shift and quenching of its absorption and emission. On the other hand, its spectrum remained unmodified in anhydrous DMSO. The same blue shift occurred when the dye-silane synthesized in DMSO was transferred into ethanol or water: its color went from green to blue. However, the color change did not occur in any of the solvents when the fluorophore was alone.

The necessary presence of silane for this shift to happen, combined to the presence of OH groups in the solvent, led us to investigate hydrolysis of the dye-silane as a potential culprit. As a matter of fact, blue shift can be caused by a phenomenon called exciton splitting of dimers [40], schemed on **Figure 2.22 a**): when two fluorophores get ordered in parallel sandwich-type dimers, a blue shift of the absorption/emission maximum can occur. In our case, these dimers could be formed in presence of minute traces of water that would lead to hydrolysis and self-condensation if the dye-triethoxysilanes. Literature reports that solvent -OH groups can catalyze aminosilanes self-condensation [41], [42], which would explain why this phenomenon did not occur in DMSO, even if it also contains traces of water.

Solvent	APTES present?	Color	Max abs (nm)	Max em (nm)
Ethanol	No		780	820
	Yes		635	740
DMSO	No		780	810
	Yes		780	810
Water	No		770	800
	Yes		635	740

**Table 2.2** Influence of APTES and solvent on color and absorption/emission maxima of Dylight 680 NHS.

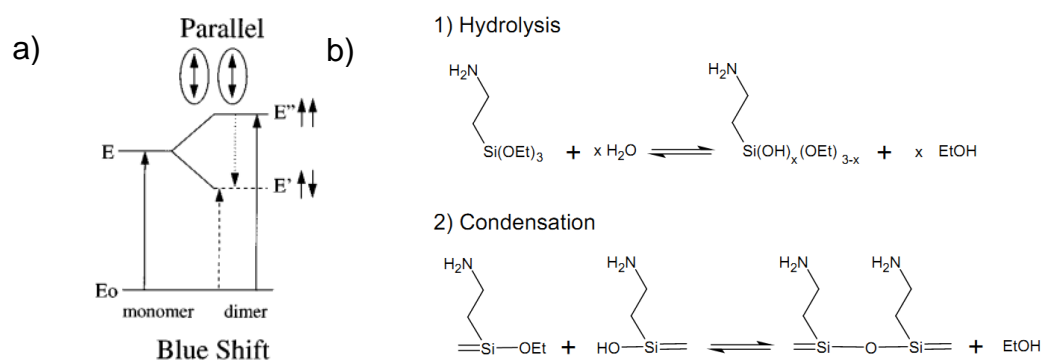


**Figure 2.22** Mechanisms causing Dylight 800 spectral shift. a) Exciton splitting occurring when two dyes come into close proximity and form dimers. Reproduced from [40] b) Hydrolysis-condensation mechanism bringing the two fluorophores together. Reproduced from [41].

As a result, we ruled out Dylight 800 NHS as a possible dye for our system, because its spectra after reaction in DMSO would logically also be degraded upon aqueous encapsulation into the growing silica particle. Although our other dyes (FITC, RhBITC and Dylight 680 NHS) were not affected by spectral changes, we chose to perform their silanization in DMSO, to avoid formation of a dye-silane polymer before the encapsulation in the silica matrix.

Since the fluorophore is the most precious material in the synthesis, we checked if most of it was trapped in the silica matrix after the core synthesis, and how much had been left out. To do so, we performed ultrafiltration (UF) of the cores and compared the maximal absorbance of the filtrate with the maximal absorbance of a dilution series of dye-silane in buffer pH 9.0. We got the following results:

Fluorophore	FITC	RhBITC	Dylight 680 NHS
Measured [dye-silane] in retentate ( $\mu\text{M}$ )	$15 \pm 2$	$2.0 \pm 0.4$	$2.4 \pm 0.4$
% grafted in NP	$70 \pm 4$	$96.0 \pm 0.8$	$95.2 \pm 0.8$

**Table 2.3** Efficiency of FITC, RhBITC and Dylight 680 NHS grafting in the silica cores.

The grafting of FITC appears far less efficient than for the other two dyes. If we compare RhBITC and FITC molecules (see **Figure 2.8**), the main difference between them lies in the positive charge, which is not present in FITC: the overall negative charge of FITC may impede its grafting into the negatively charged silica matrix. However, this does not explain why Dylight 680, which has three negative sulfonate groups, does graft well. We can just hypothesize that these groups are spaced enough from the silane reactive moieties to not impede grafting. Better grafting of Dylight 680 is perhaps also explained by better reactivity of NHS compared to isothiocyanate. Grafting fluorescein-NHS instead of FITC would enable to conclude about this hypothesis.

### 2.2.5 PEG grafting efficiency

The last step of our synthesis scheme left to optimize was the PEG-silane grafting step. Based on previous works on polymer grafting on silica surfaces [9], [10], we opted for a grafting density of 0.5 PEG/nm<sup>2</sup> and a temperature of 110°C. To prevent aggregation of the particles upon heating, we diluted the core-shell suspension down to 0.5 wt% with borate buffer pH 9.0 at 10 mM ionic strength. At this pH the surface of the particles was negatively charged, favoring the grafting of the hydrolyzed PEG-silanes on the silica surface rather than polycondensation on each other.

Next we had to determine which PEG molecular weight to use. In order to get satisfactory steric repulsion while enabling sufficient coverage of the surface, we chose methoxy-PEG-propyl-triethoxysilane with 21 PEG repeat units: its molecular weight is  $M_w = 1264$  g/mol and its hydrodynamic radius  $R_h$  about 1.4 nm [43]. To limit self-condensation of PEG-silane, we first heated the core-shell particles suspension up to 110°C then introduced the silane just dissolved in a few mL of water.

To characterize the proportion of polycondensation with regards to grafting, we performed two PEG silanizations in parallel: one on core-shell particles in buffer and a control experiment on buffer alone, all other parameters kept equal. On the first batch, separation between grafted and ungrafted PEG was carried out by ultrafiltration of the reaction product through a

membrane of MWCO = 3000 Da, which corresponds to an average pore size of 1.9 nm [44]. Based on the manufacturer datasheet, at this MWCO, 90 % of ungrafted PEG silane molecules pass through the membrane if they are not polycondensed. As far as grafted core-shell silica particles are concerned, if they are about 4 nm in diameter, 95 % of them remain in the retentate.

We then performed DLS measurements on all samples. We got the following correlation data and size measurements (**Table 2.4**).

Sample	Counts (kcps)	Attenuator	Correlation function $g_2(t)-1$ (t=0)	Measured diameter	Number of populations
CSP 0.5% before UF 3000MWCO	477	11	0.8	6.2	1
CSP filtrate after UF3000 MWCO	28	11	0.035	<1	0
PEG alone, 0.5% eq, refluxed like CSP	172	11	0.77	50	1

**Table 2.4** DLS measurements on various PEGylated samples.

From these measurements, we could draw several conclusions: first, when PEG-silane was reacted alone, it self-condensed into aggregates of 60 nm in size. However, no presence of such big PEG-polysiloxanes was detectable on the core-shell-PEG sample: the correlation curve detected only a single population with an average diameter of 6.2 nm, corresponding to the grafted particles. In addition, the correlation values on the filtrate sample are extremely low: if there was a significant amount of PEG-silane, even in the form of individual hydrolyzed molecules, correlation values would be higher. Grafting of PEG-silane appears probably much more favorable with the silica surface than with itself.

However, this still did not give any estimation the yield of reaction. To do so, we performed two NMR experiments: first, we sampled a known volume of the ultrafiltration filtrate, lyophilized it then dissolved it in D<sub>2</sub>O with a known small quantity of pyridine as an internal reference. As a comparison, we also ran <sup>1</sup>H NMR of a known quantity of the PEG-triethoxysilane in D<sub>2</sub>O and pyridine as well. Both spectra are presented on **Figure 2.23**.



## 2. Novel fluorescent core-shell silica nanoparticles

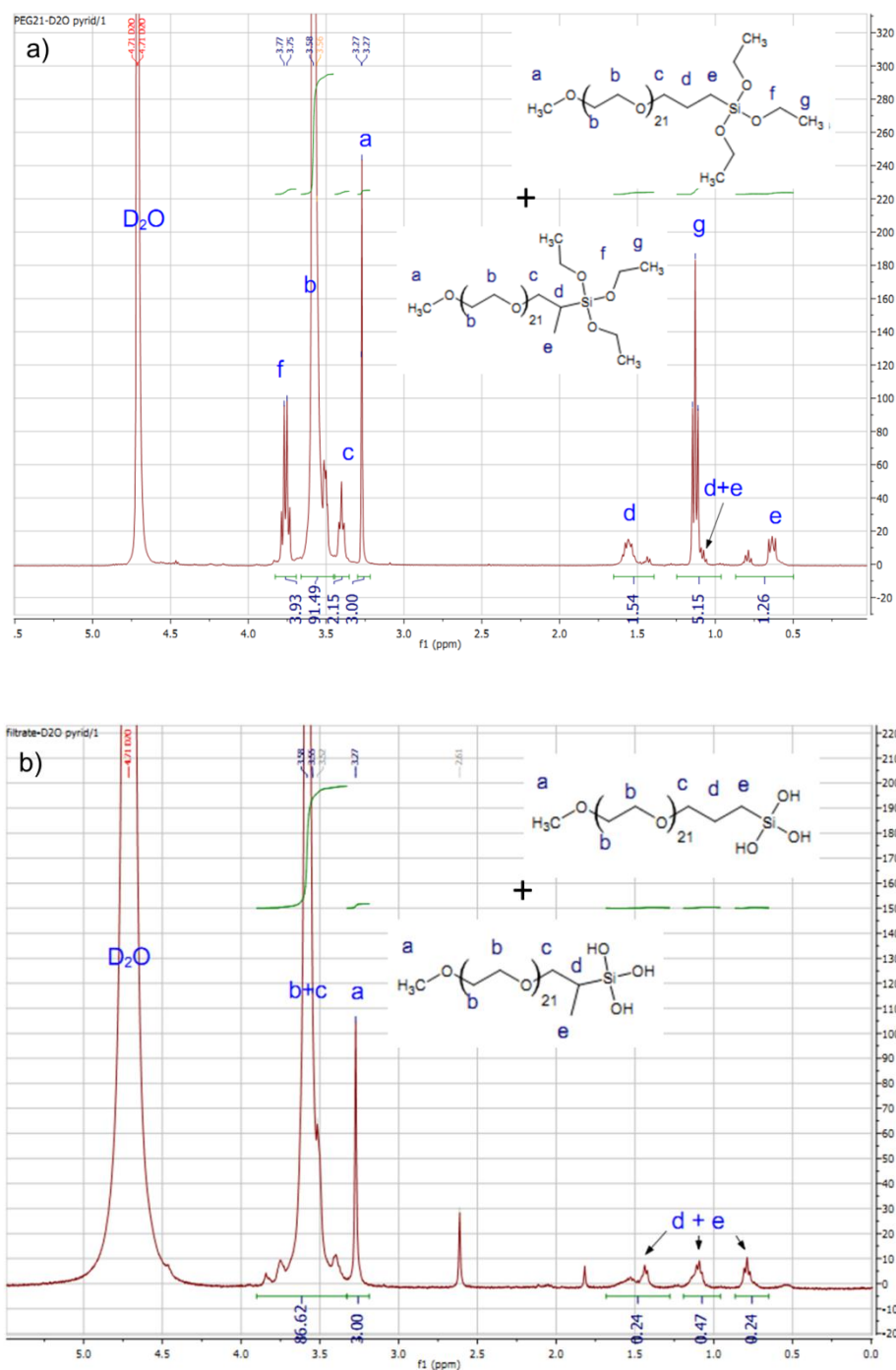


**Figure 2.23** NMR analysis of the PEG grafting reaction on the silica surface. a) Starting m-PEG triethoxysilanes; b) filtrate of the reaction product containing m-PEG silanols.

We can already notice on **Figure 2.23** a) that there are more peaks than expected for the alkyl hydrogens. According to the manufacturer, this is because the starting reagent to make the commercial m-PEG-propyl-ethoxysilane is m-PEG-allyl. During the hydrosilylation, the triethoxysilane attacks the alkene on both carbons, leading to the two m-PEG-triethoxysilanes

drawn on the first spectrum. The integration ratios between propyl protons a and e protons roughly match the expected value, meaning that the product of hydrosilylation of this allyl leading to our PEGylation reagent was pure. However, the integration ratios between protons f and c is not equal to 3 as expected, but rather 2: since we opened and closed the vial several times, maybe partial hydrolysis has taken place: our starting reagent thus contains about 30% m-PEG-silanols and 70% m-PEG-triethoxysilanes.

On the second spectrum (**Figure 2.23 b**)), as expected, the f and g hydrogens belonging to the ethoxy group have disappeared: the silane has been hydrolyzed. Given the integration values of d and e peaks compared to those in the first spectrum, the PEG species in the filtrate is 88 % m-PEG and 12 % m-PEG-propyltrihydroxysilane. To get the proportion of PEG product in the filtrate compared to the quantity of reagent used, we integrated the PEG peaks b on both spectra and compared them to the pyridine reference integration. The calculations let us conclude that ~30 % of the PEG introduced is present in the filtrate (most of it being m-PEG without silane moiety): the grafting yield is thus ~70 % of the introduced reagent, which corresponds closely to the measured initial proportion of m-PEG-triethoxysilane.

### 2.2.6 Overall synthesis scheme: size characterization and long-term stability

To review our whole synthesis scheme, we performed DLS measurements on ultrafiltration retentates of core, core-shell and core-shell-PEG SNP. In addition, in order to determine the shape of our particles and get a complementary size measurement, we took some TEM micrographs of our core, core-shell and core-shell-PEG colloids. They are reproduced on **Figure 2.24 a) to c)**, together with DLS and TEM size histograms gathered on **Figure 2.24 d)**.

On all TEM pictures, aggregation of the particles is very noticeable: drying of the TEM grid leads particles to cluster: the smaller the individual particles, the more difficult it is to distinguish them from each other. Because of this cluster formation, the average size calculated from TEM measurements is larger than the estimation by DLS. However, in the case of core-shell-PEG samples, PEG lessens the aggregation and the size observed is closer to the corresponding DLS measurement. In all cases, particles are amorphous as expected: no crystalline ordering of the atoms is visible. Their shape is not perfectly spherical, but they are not markedly anisotropic.

To check long-term stability and efficiency of the PEG grafting, we also measured these values again after one month at room temperature. It is noticeable that in this time lapse, average size of core- and core-shell samples has significantly increased, whereas size of core-shell-PEG did not: covalently grafted PEG is indeed an efficient barrier against aggregation.

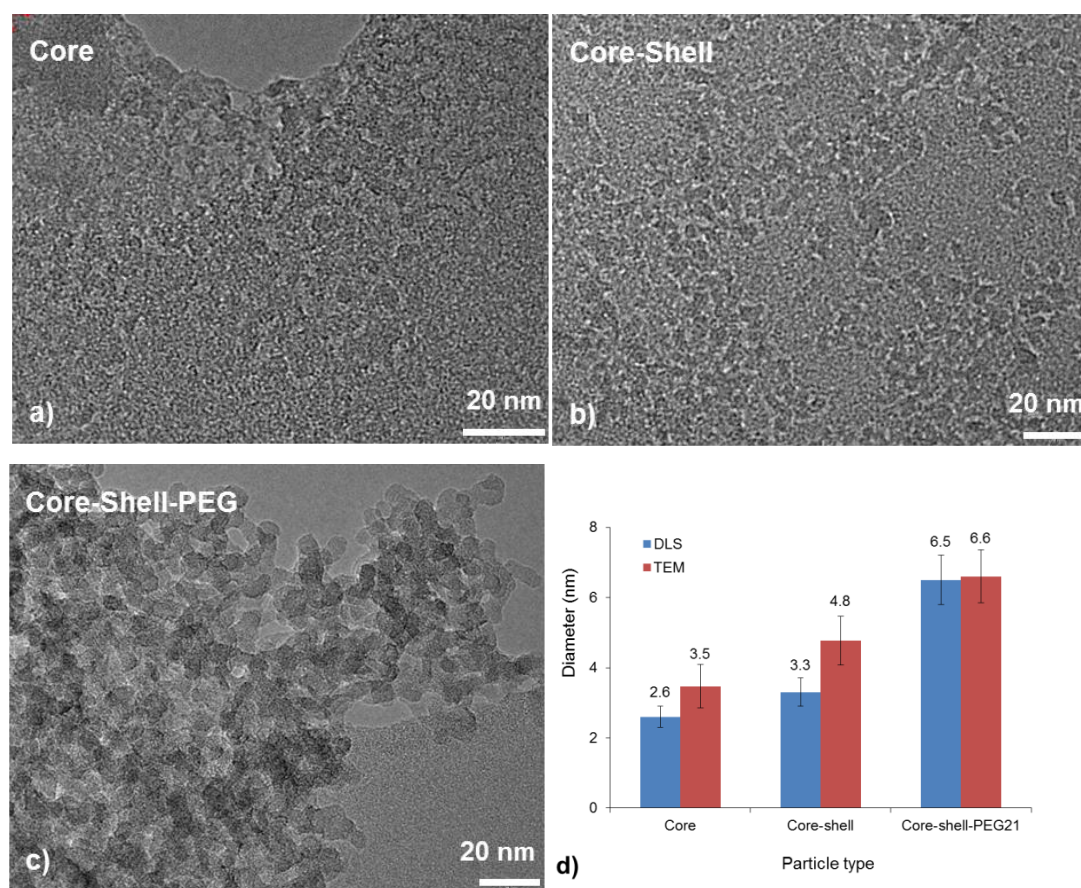


**Figure 2.24** Particles observation and size measurements by TEM. a) Core particles, b) core-shell particles, c) core-shell-PEG21, d) Comparison of size measurements by TEM and DLS.

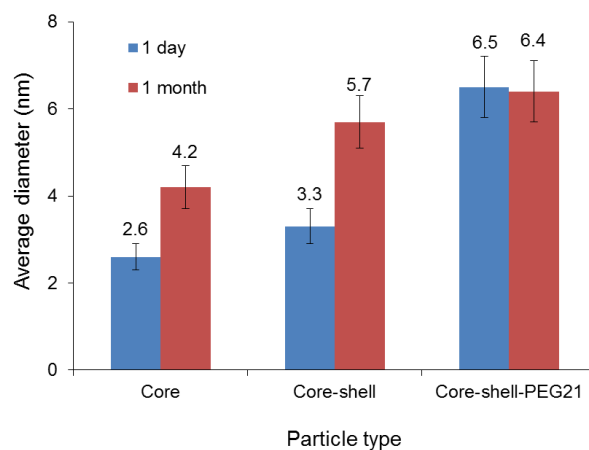


**Figure 2.25** Long-term stability of silica nanoparticles measured by DLS. Core and core-shell particles undergo aggregation whereas PEGylated particles stay intact over a month.

## 2.3 Radiative properties of F-SNP

The second and essential part of our characterization aimed to determine how much encapsulation in the Persello silica matrix enhanced the fluorescence properties of the dye. We focused our study on four parameters: absorption and emission spectra, quantum efficiency, FP modulation and photobleaching.

### 2.3.1 Absorption/emission spectra

The first thing we checked was if the absorbance and fluorescence spectra of our dyes were modified upon encapsulation in the silica matrix. We measured them at the same concentration in borate buffer pH 9.0. To enable easier comparison, the normalized absorbance and emission spectra are plotted together below (**Figure 2.26**), as well as a table of absorption and emission maxima for all samples (**Table 2.5**).

Reaction step/Fluorophore	Absorbance maxima (nm)			Fluorescence maxima (nm)		
	FITC	RhBITC	Dylight 680 NHS	FITC	RhBITC	Dylight 680 NHS
Free dye	494	554	677	514	580	699
Cores	490	556	680	514	575	702
Cores UF	490	558	680	513	576	697
<i>Filtrate</i>	<i>492</i>	<i>553</i>	<i>680</i>	<i>512</i>	<i>578</i>	<i>693</i>
Core-Shell	490	558	680	511	579	700
Core-Shell-PEG21	492	556	683	515	579	699

**Table 2.5** Comparison of absorption and emission spectra of all silica nanoparticles.

Absorbance spectra of our FITC samples do not show noticeable shifts or peak shape modification. As already reported in the literature, there is a small contribution of silica to absorbance below 450 nm, partly because of minor scattering. This is of little importance in our case, since we do not excite our fluorophore at such low wavelengths. For RhBITC and Dylight 680 samples, the absorption spectrum of the free dye appears slightly broader than when the dye is embedded in silica. As this broadening does not take place in other buffers (PBS for example) either, we conclude that this must be an effect of the borate buffer on the fluorophore alone. A small contribution of PEG to the absorbance around 550 nm is also noticeable on the Dylight 680 C-S-P spectrum. For all three fluorophores, emission spectra remain largely unchanged at all

synthesis stages and all overlap very well. Emission maxima are all in the same 5 nm wavelength window.

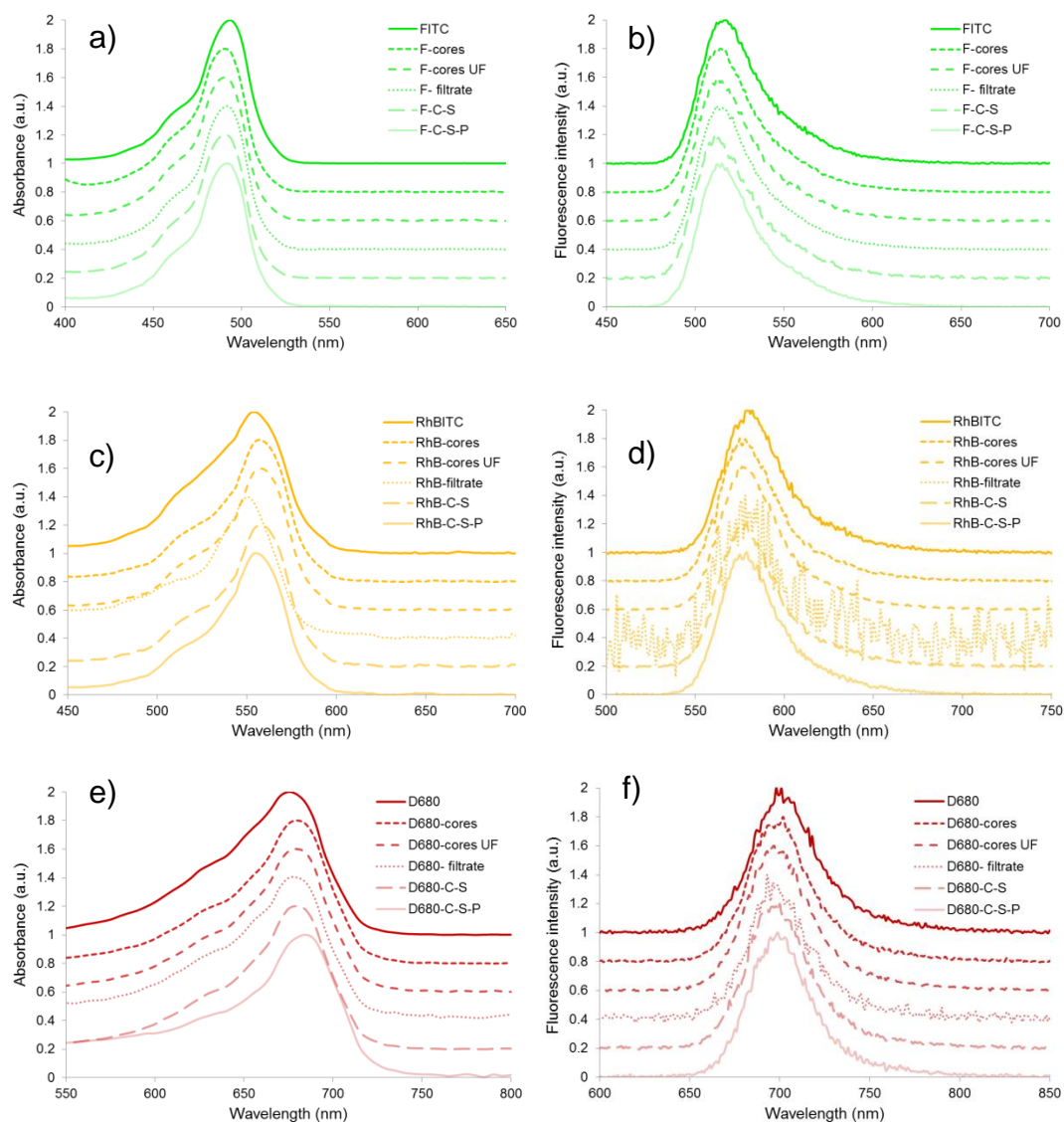


**Figure 2.26** Comparison of absorption and emission spectra of all silica nanoparticles. a), b) FITC-based samples; c), d) RhBITC-based samples; e), f) Dylight 680-NHS-based samples.

### 2.3.2 Extinction coefficient/ Quantum yield

Given the numerous reports in literature about enhanced quantum efficiency of fluorophores when trapped in silica, we investigated if our novel silica matrix also provoked such effects and at which magnitude. If we excite the sample at a wavelength  $\lambda_{exc}$  and collect its emission spectrum, its quantum yield is by definition proportional to the integrated fluorescence spectrum divided by its absorbance at  $\lambda_{exc}$ , given that the measurements are done in the fluorescence and absorbance

linearity range and on diluted samples ( $A(\lambda_{exc}) < 0.2$ ) to avoid inner filter effect [45]. Based on this, we calculated these values for the three fluorophores in borate buffer at all reaction steps, and normalized them by the value of the free dye in borate buffer, following the classic equation by Williams [46]:

$$\frac{\varphi_{dye-SNP}}{\varphi_{dye}} = \frac{I_{dye-SNP}}{OD_{dye-SNP}} \frac{OD_{dye-SNP}}{I_{dye}} \quad (2.9)$$

This gave us the relative quantum efficiency compared to the free dye in solution. The values obtained are gathered on **Figure 2.27**.

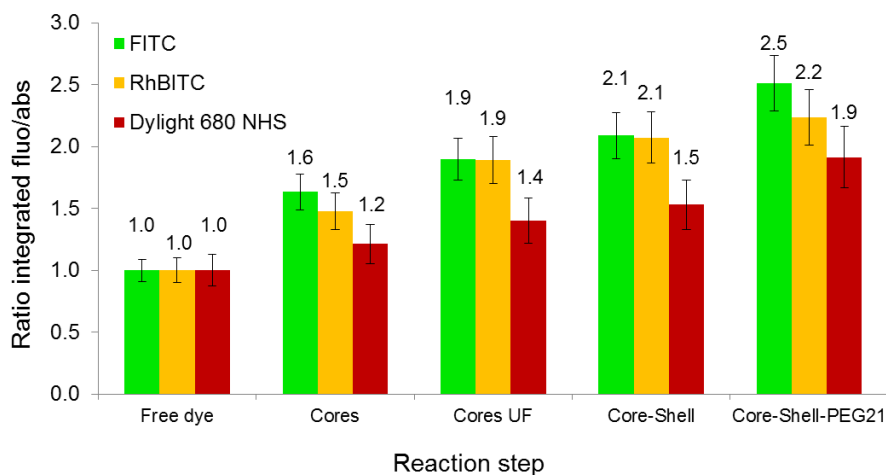


**Figure 2.27** Quantum yield of the three dyes grafted in silica compared to the ungrafted dye in buffer. The further along in the reaction step, the higher the quantum yield.

For all three dyes, the trend is the same: the ratio is continuously increasing from one reaction step to the next, up to values between 1.9 and 2.5. In particular, for core-shell architecture, FITC and RhBITC give ratios of 2.1: this is in good agreement with the 2.2 quantum efficiency enhancement reported in the literature [31] for TRITC in Stöber silica particles with a compact core-shell structure. Like FITC and RhBITC, TRITC belongs to the family of xanthene dyes and has a very similar structure; moreover, the “compact” core-shell particles mentioned in this article is very close to our system, although the core diameter is 1.7-fold larger than ours.

The ratio increase at each step can be explained the same way as Larson et al [31]: the quantum efficiency increases because radiative rate increases as well. This can be explained partly because once the dye is encapsulated in the silica particle, the refractive index surrounding the

fluorophore is altered. Toptygin et al. [47] published an expression for the radiative rate of a fluorophore embedded in a small dielectric ellipsoid of refractive index  $n_1$  surrounded by a dielectric material of refractive index  $n_0$ . This equation predicts that if  $n_0$  is increased relative to  $n_1$  (which is our case), the radiative rate can increase as well. For free dye in buffer, the fluorophore is considered to be in an empty ellipsoidal cavity ( $n_1 = 1.00$ ) surrounded by a homogeneous dielectric fluid ( $n_0 = 1.33$ ; see equation 34 from the article). If this principle is applied to the dye in the nanoparticle, the fluorophore would be in an empty ellipsoidal cavity surrounded by the silica matrix ( $n_0 = 1.46$ ), which in turn is surrounded by water. Assuming a slightly prolate ellipsoidal cavity ( $L_m = 0.75$  in Toptygin's original notation), it results in  $\frac{k_r^{SNP}}{k_r^{free}} =$

2.2. If we assume  $k_{nr} \gg k_r$  as is the case in Larson's article, we get  $\frac{\phi_F^{SNP}}{\phi_F^{free}} \simeq \frac{k_r^{SNP}}{k_r^{free}} = 2.2$ , which is close to the ratios observed for all our core-shell samples.

Another noticeable observation is that for all silica synthesis steps, the ratio values follow the trend FITC>RhBITC>Dylight 680 NHS. This can be correlated to the dye hydrodynamic radius and molecular weight that both follow the trend FITC<RhBITC<Dylight 680 NHS: the smaller the dye, the better it is trapped in the silica matrix, isolated from the outer solvent: the more radiative rate is increased. As will be discussed in the next subsection, this influence of the dye size also plays a role in its FP value.

From these ratio values relative to the free dye in buffer, we initially intended to measure absolute quantum yields of our samples, by applying equation 2.9 with reference dyes of known absolute quantum yield values (for example, FITC and RhBITC in ethanol). However, in the FITC case, this method led us to quantum yield in borate buffer equal to 0.93: it would mean that all quantum yield values of FITC in silica are superior to 1, which does not make sense physically: there should not be more photons emitted than absorbed, except if there is some laser effect. After some literature search, we found that Russin et al [48] recently discussed the shortcomings of the classical Williams quantum efficiency measurement technique [45] for fluorophores embedded in nanoparticles: it provides only the  $\phi_F$  of the smallest fluorescing unit, (in our case, the nanoparticle itself). Hence it does not directly offer an accurate description of the  $\phi_F$  of the embedded fluorophores. To do so, a more accurate equation would then be equation 9 of the article [48], where  $n_{dye-SNP}$  and  $n_{ref}$  are the refractive indices of the two solutions and  $\epsilon$  an



enhancement factor proportional to the field intensity experienced by the fluorophore in the particle compared to the case in solution:

$$\frac{\varphi_{dye-SNP}}{\varphi_{ref}} = \frac{1}{\varepsilon} \frac{I_{dye-SNP}}{OD_{dye-SNP}} \frac{OD_{ref}}{I_{ref}} \frac{n_{dye-SNP}^2}{n_{ref}^2} \quad (2.10)$$

Moreover, as discussed right before, if the nanoparticle is treated as a spherical cavity, this might lead to some interesting resonance effects that deserve further investigation.

For now, we can safely say that the ratio between integrated fluorescence and absorbance at excitation wavelength is increased in our nanoparticles, without giving any conclusion on the absolute quantum yield value. Encapsulation of the dye in the silica matrix definitely increases its brightness. The additional influence of PEG is less clear; it may decrease the scattering of emitted light by the refractive index gradient its coverage provides. Practically speaking, this increased brightness means that our silica-trapped fluorophores are a very suitable alternative to free dyes as multiplex fluorescence barcodes.

### 2.3.3 FP modulation vs. quenching

As introduced in the first part of this chapter, we also tried to monitor variations of fluorescence polarization of our dye in silica along the synthesis steps. Since the size of our objects is increasing at every step, we expect the FP value to rise as well. We performed FP measurements on samples of similar absorbance values and got the following data (**Figure 2.28**):

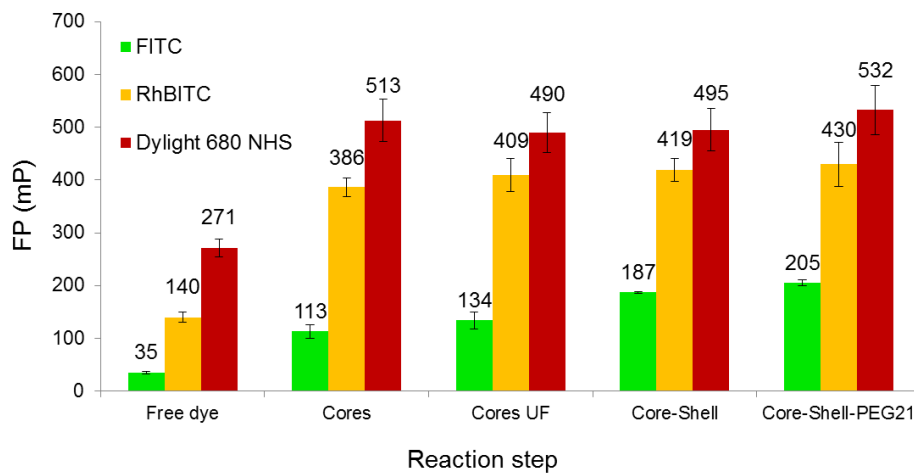


**Figure 2.28** FP of the three dyes in free state and grafted in silica at all synthesis steps. For FITC, he further along in the reaction step, the higher the quantum yield. For the two others, FP leaps upon grafting in cores then stays about constant.



As expected from their molecular size, free fluorophores molecules have FP values following the trend FITC < RhBITC < Dylight 680 NHS. In the FITC case, FP keeps increasing at all synthesis steps, whereas for both other dyes, it abruptly rises after initial grafting then remains relatively constant. As FP/anisotropy depend on both the volume of the rotating unit and the fluorescence lifetime, according to the Perrin equation:

$$r = \frac{r_0}{1 + \tau_F \frac{kT}{\eta V}} \quad (2.11)$$

it seems to indicate that fluorescence lifetime does not decrease in the same magnitude for all three dyes. Some complementary lifetime measurements would be helpful to confirm these observations. In both latter cases, FP values are also very close to the theoretical upper limit value of 500 mP for spherical rotating objects in an isotropic fluid, which may explain why the value does not increase further. In the case of Dylight 680, the last read slightly above 500 mP might be due to slight measurement inaccuracy from the instrument.

Knowing these high FP values for intermediate dye concentrations in SNP, we checked if increasing or decreasing the average number of dye molecules per particle would provoke some variation of FP and brightness. We consequently synthesized SNP cores suspensions containing various concentrations of FITC or RhBITC (we did not do this with Dylight 680, due to the prohibitive cost of the dye for such an experiment). We then measured the FP values at emission maximum, as well as the (integrated emission/absorbance) ratio. The results are plotted on **Figure 2.29**.

The first observation was that at high dye concentration (250  $\mu$ M), FP is lower than at lower concentrations, possibly due to homo-FRET. However, at 250  $\mu$ M, the integrated fluorescence/absorbance ratio of both dyes also sharply drops. The first hypothesis that can explain this is the presence of several dyes in or on such a small core (2.6 nm) might bring them too close together below the Förster distance and cause some fluorescence quenching. The calculated effective concentration of fluorophore in silica (which makes 1.1 % of the volume) equals 22.1 mM for the most concentrated case: it corresponds to an average distance of 13 nm between fluorophores, which is way above the critical Förster distance, about 5 nm for FITC and RhBITC [26], [46].

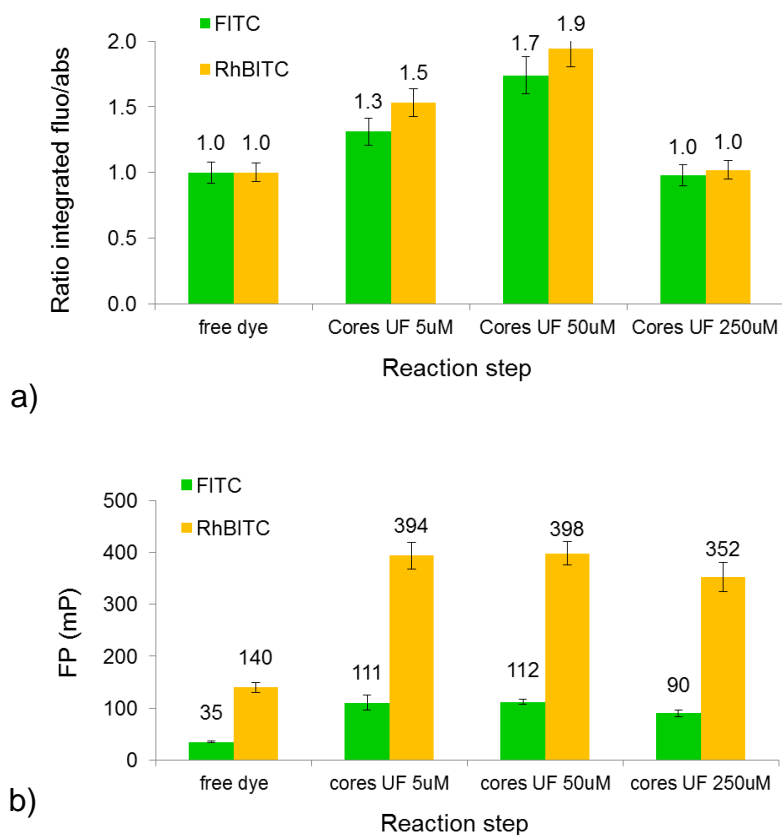


**Figure 2.29** Influence of grafted dye concentration on a) quantum yield and b) FP.

To refine this analysis more on a single-particle level, we calculated the average number of dye molecules per particle, based on the fluorophore concentration in each suspension and on the diameter of the cores (2.6 nm). We found values far below 1 (see **Table 2.6**). Based on a Poisson distribution, we calculated the percentage of particles containing  $k = 0, 1, 2$  or 3 fluorophores for all three solutions. It follows equation:

$$P(\lambda; k) = \frac{\lambda^k e^{-\lambda}}{k!}$$

where  $\lambda$  is the average number of dye molecules per particle. We reported the calculated percentages in **Table 2.6**. Unfortunately, this analysis does not support our observation: going from 50  $\mu\text{M}$  up to 250  $\mu\text{M}$ , it is impossible that  $0.70 - 0.03 = 0.67\%$  more quenched particles containing two fluorophores would account for a 80 to 90% decrease in fluorophore brightness.

[dye] ( $\mu\text{M}$ )	$\lambda$ (average number of fluorophores per 2.6 nm core)	k			
		0	1	2	3
5	0.00252	99.75%	0.25%	0.00%	0.00%
50	0.0252	97.51%	2.46%	0.03%	0.00%
250	0.126	88.16%	11.11%	0.70%	0.03%

**Table 2.6** Poisson analysis of dye loading of SNPs. The average fluorophore loading is calculated from the each dye concentration, and the percentage of particles containing k fluorophores is calculated in each case using a Poisson distribution.

Another more probable explanation is that since the core size is not much greater than the size of the fluorophores themselves, a significant fraction of them might show partly or completely on the surface, all the more when the dye concentration increases. If the particles with surface dyes become prominent, then the effective brightness will be similar to brightness of free dyes, based on results from **Figure 2.29**. Hence, we chose 50  $\mu\text{M}$  as optimal concentration.

### 2.3.4 Photobleaching

Among the properties that are enhanced by trapping fluorophores in silica, resistance to photobleaching is probably the most drastically affected. Literature reports dramatic enhancements of photostability, from 75 % fluorescence loss in 10 minutes for the free dye to less than 10% when it is in silica [26], [27], [49].

The photostabilities of free and silica-bound FITC and RhBITC immobilized on polyacrylamide gel were monitored by fluorescence microscopy under continuous illumination for 60 s by a 130 W mercury lamp. The following decay curves were obtained (**Figure 2.30**):

As expected, decay is slower for silica-trapped dyes than when they are free. However this effect is more drastic for RhBITC than for FITC: after 10 s, silica-trapped RhBITC is 2-fold brighter than when unbound, whereas the ratio is only 1.35 for FITC. One explanation could be our previous observation of different binding efficiency between FITC and RhBITC, leading to a different local environment of the dye molecule.

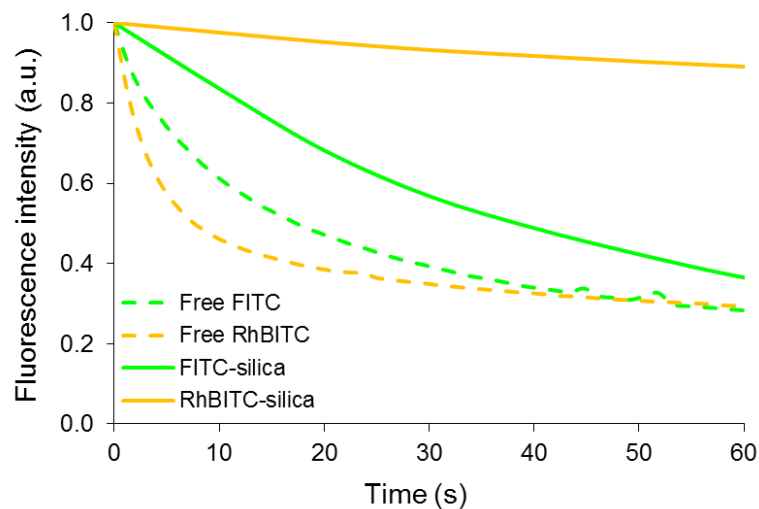


**Figure 2.30** Photobleaching of silica-bound FITC and RhBITC compared to free dyes. Grafting slightly improves FITC resistance to bleaching and dramatically enhances RhBITC photostability.

## 2.4 Conclusion

In this chapter, we have developed a novel route to encapsulate fluorophores in a silica matrix, leading to the smallest fluorescent silica nanoparticles ever synthesized (down to 2.5 nanometers). To optimize our overall process, we have explored several possibilities for tuning core diameter and shell thickness, with an overall upper limit of 6 nm. In terms of performances, our silica-bound fluorophores have properties comparable to those encapsulated by alternative routes: an enhanced quantum yield, together with a significantly improved resistance to photobleaching. Moreover, they exhibit good colloidal stability in time: their average size remains stable over a month at room temperature. Finally, the reaction conditions we used make our synthesis strategy the cheapest, least work-intensive and most environmentally-friendly way to covalently incorporate fluorophores in silica nanoparticles.

However, photophysical measurements such as fluorescence lifetime or fluorescence correlation spectroscopy still remain to be studied, to better assess the influence of the silica matrix on the dye behaviour.

To expand these materials potential as fluorescent barcodes, an interesting path would be to explore in greater detail the possibility to significantly reduce the FP value of the fluorophore in the silica matrix. Combining various ratios of high- and low-FP nanoparticles would enable to use the FP dimension in addition to fluorescence intensity. This could dramatically increase the

number of barcodes reached, or allow to get the same number of labels with less colors and a more simple optical setup.

Due to their exceptionally small size and excellent brightness, these particles are very appealing for other applications, such as high resolution imaging or diagnostics; yet some thorough biocompatibility assays remain to be carried out. Functionalization with alternative polymers or bioreagents (antibodies, enzymes, streptavidin, other proteins...) would dramatically open up possibilities and allow these particles to rival the smallest quantum dots or Stöber-type silica nanoparticles, such as those currently developed by Hybrid Silica Technologies [50].

## 2.5 Experimental section

### 2.5.1 Coupling of fluorophores with silane precursor

Separate stock solutions of Fluorescein isothiocyanate 98%, (Sigma), Rhodamine B isothiocyanate (Aldrich), Dylight 680 NHS (Pierce), Dylight 800 NHS (Pierce) were prepared at 5 mM in anhydrous DMSO (Sigma). For synthesis of cores with 50  $\mu\text{M}$  dye, 970  $\mu\text{L}$  of each stock solution ( $4.85 \times 10^{-6}$  mol) were mixed with 22.7  $\mu\text{L}$  ( $9.7 \times 10^{-5}$  mol) APTES (Sigma) in a microcentrifuge tube (Axygen) and incubated in the dark at 50°C for 1h to complete the coupling.

### 2.5.2 Silica nanoparticles synthesis

Cores: 4  $\times$  12.5 g Amberlite IR 120 strong acid exchange resin (Fluka) were weighed and rinsed twice with 100 mL milliQ water (Millipore) to remove their brown color, then filtered under vacuum on a Büchner with a paper filter (Whatman) and kept aside. In four large-neck 250 mL PTFE bottles (Roth), 10 g (2.65 g equivalents  $\text{SiO}_2$ ) sodium silicate solution reagent grade (Sigma) were added under stirring to 90 g milliQ water (Millipore). pH was measured with a Eutech Cyberscan PCD 6500 pH meter and a Eutech 6737X pH electrode: the value was 11.75. The four dye-silane mixtures were individually added to each bottle: pH remain unchanged. The 12.5 g Amberlite IR 120 were quickly added to each bottle; the solution was stirred until pH reached 9.00. It was immediately filtered under vacuum on a Büchner, poured back into the rinsed bottle, covered with aluminium foil to protect it from light and stirred at 400 rpm overnight. The next day, pH of the silica sols was about 10.0. 1.2 g rinsed Amberlite was added to each bottle until pH was back down to 9.0. It was immediately filtered under vacuum on a Büchner and poured back into the rinsed bottle.

Ultrafiltration: The cores solutions were ultrafiltrated using a 50 mL Amicon stirred cell (Millipore) and a 3000 Da MWCO cellulose membrane (Ultracel PL, Millipore) under 2 bar pressure and 400 rpm stirring. The filtration was stopped when 20% of the initial volume remained in the cell. MilliQ water (Millipore) was added to the retentate up to the initial suspension volume and transferred back to a clean plastic bottle. The filtrate was kept aside for further analysis.

Shell growth: 4×12.5 g Amberlite IR 120 strong acid exchange resin (Fluka) were weighed and rinsed twice with 100 mL milli Q water (Millipore) to remove their brown color, then filtered under vacuum on a Büchner with a paper filter (Whatman) and kept aside. In each bottle, 10 g sodium silicate (1 eq, 2.65 g equivalent silica) were added to the retentate: pH was around 11.6. The 12.5 g Amberlite IR 120 were quickly added to each bottle; the solution was stirred until pH reached 9.00. It was immediately filtered under vacuum on a Büchner, poured back into the rinsed bottle covered with aluminum foil to protect it from light and stirred at 400 rpm for one hour to complete the shell growth.

PEG grafting: in a 2-necked 100 mL round bottom flask, 4 mL of core-shell sol were mixed to 34 mL borate buffer 10 mM, pH 9.0. The flask was equipped with a Dimroth condenser and the solution was heated to 110°C under reflux and stirring at 400 rpm. In a separate vial, 75.4 mg m-PEG21-triethoxysilane (Specific Polymers) was dissolved in 2 mL borate buffer 10 mM, pH 9.0 and immediately added. The mixture was left to reflux at 110°C and 400 rpm stirring for 2 h, then left to cool down to room temperature. The solution was then filtered under vacuum on a Stericup filtration system (Millipore) with a 0.22 µm PVDF membrane.

Ultrafiltration: A fraction of the core-shell-PEG21 dispersions was ultrafiltrated using the same protocol as above. The filtrate was kept aside for further analysis.

### 2.5.3 Dynamic light scattering

Particle dispersions were filtered with a syringe filter (Acrodisc, Pall) with a 0.22 µm Supor membrane to remove dust then transferred to plastic semi-micro cuvettes (Brand). DLS measurements were performed on a Zetasizer Nano S (Malvern). Scattering distance was set to 0.45 mm and each sample was read 3 times. The correlation curves were fit with a double exponential in ALV correlator software (ALV GmbH). From the lowest calculated coefficient, the diffusion coefficient and the average diameter were calculated.

### 2.5.4 TEM observation

Samples were deposited on a 4 mm carbon-coated copper grid (200 mesh) by depositing a drop of diluted solution on it and letting it dry under a lamp. TEM images were then acquired on a Topcon field electron gun microscope.

### 2.5.5 Steady absorbance/fluorescence/FP measurements

Absorption spectra were measured with a Spectronic 200 UV/vis double-beam spectrophotometer (Shimadzu), using borate buffer as a reference. Fluorescence spectra were measured with a Fluorolog 3 spectrofluorimeter (Jobin-Yvon Horiba). The samples were contained in plastic semi-micro cuvettes (Brand). Fluorescence was detected at 90°. For both measurements the excitation slit width was set at 1 nm. The samples were first absorbance-matched to a free dye solution on the UV/vis spectrophotometer and then their fluorescence intensities immediately recorded on the spectrofluorimeter in the same cuvette.

FP measurements were performed on a SpectraMax M5 plate reader (Molecular Devices) from 100  $\mu$ L samples in a black 96-well plate (Corning).

### 2.5.6 Photobleaching

For each dye sample, 500  $\mu$ L of sample were mixed with 500  $\mu$ L Rotiphorese acrylamide gel 40 wt% (Roth), 1  $\mu$ L tetramethylethylenediamine (TEMED, Roth) and 10  $\mu$ L ammonium persulfate (APS, Roth). The solution was vigorously shaken then 10  $\mu$ L of it were immediately taken and spotted on a microscope slide (Roth). The drop was covered with a coverslip (Roth) and left to wait until solidification.

The slide was then installed on an inverted fluorescence microscope (Nikon Eclipse Ti) with a 40X objective illuminated by a 130 W mercury lamp (Nikon Intensilight C-HGFI). The appropriate filter cubes were selected according to the sample (GFP for FITC samples, TRITC for RhBITC samples). At regular intervals, pictures were acquired during 200 ms each by a color CCD camera (Nikon DS-Fi 1); the stack of images was recorded on Nikon Elements BR 3.0 software. The average intensity of each picture was calculated with ImageJ software and the decay curves subsequently plotted.

## References

- [1] R. K. Iler, *The chemistry of silica: solubility, polymerization, colloid and surface properties, and biochemistry*. Wiley, 1979.

- [2] H. E. Bergna and W. O. Roberts, *Colloidal Silica: Fundamentals and Applications*. CRC Press, 2005.
- [3] P. M. Dove, N. Han, A. F. Wallace, and J. J. De Yoreo, "Kinetics of amorphous silica dissolution and the paradox of the silica polymorphs," vol. 105, no. 29, pp. 9903-9908, Jul. 2008.
- [4] B. Derjaguin and L. Landau, "Theory of the Stability of Strongly Charged Lyophobic Sols and of the Adhesion of Strongly Charged Particles in Solutions of Electrolytes," *Acta Phys. Chim. URSS*, vol. 14, pp. 633-662, 1941.
- [5] E. J. W. Verwey and J. T. G. Overbeek, *Theory of the Stability of Lyophobic Colloids*. Amsterdam: Elsevier, 1948.
- [6] J. N. Israelachvili, *Intermolecular and Surface Forces, Second Edition: With Applications to Colloidal and Biological Systems*, 2nd ed. Academic Press, 1992.
- [7] R. J. Hunter, *Introduction to modern colloid science*. Oxford University Press, 1993.
- [8] "DLVO theory - Malvern.com." [Online]. Available: [http://www.malvern.com/LabEng/industry/colloids/dlvo\\_theory.htm](http://www.malvern.com/LabEng/industry/colloids/dlvo_theory.htm).
- [9] E. F. Vansant, P. Voort, and K. C. Vrancken, *Characterization and chemical modification of the silica surface*. Elsevier, 1995.
- [10] A. El Harrak, "Nanoparticules Hybrides Silice/Polymère: Synthèses, Analyses DNPA. Applications au Renforcement Mécanique des Polymères.," PhD Thesis, Université Paris 11-Orsay, 2005.
- [11] F. Fuertges and A. Abuchowski, "The clinical efficacy of poly(ethylene glycol)-modified proteins," *Journal of Controlled Release*, vol. 11, no. 1-3, pp. 139-148, Jan. 1990.
- [12] W. Stöber, A. Fink, and E. Bohn, "Controlled growth of monodisperse silica spheres in the micron size range," *Journal of Colloid and Interface Science*, vol. 26, no. 1, pp. 62-69, Jan. 1968.
- [13] A. van Blaaderen and A. Vrij, "Synthesis and characterization of colloidal dispersions of fluorescent, monodisperse silica spheres," *Langmuir*, vol. 8, no. 12, pp. 2921-2931, 1992.
- [14] H. Yamauchi, T. Ishikawa, and S. Kondo, "Surface characterization of ultramicro spherical particles of silica prepared by w/o microemulsion method," *Colloids and Surfaces*, vol. 37, pp. 71-80, 1989.
- [15] H. Elimelech and D. Avnir, "Sodium-Silicate Route to Submicrometer Hybrid PEG@Silica Particles," *Chemistry of Materials*, vol. 20, no. 6, pp. 2224-2227, Mar. 2008.
- [16] P. G. Bird, "Colloidal solutions of inorganic oxides," U.S. Patent 224432503-Jun-1941.
- [17] M. F. Bechtold and O. E. Snyder, "Chemical processes and composition," U.S. Patent 257490213-Nov-1951.



- [18] J. Persello, "Silica Of Controlled Porosity And Process For Obtaining It," U.S. Patent EP0407262 (A1)09-Jan-1991.
- [19] J. Persello, A. Magnin, J. Chang, J. M. Piau, and B. Cabane, "Flow of colloidal aqueous silica dispersions," *Journal of Rheology*, vol. 38, no. 6, pp. 1845-1870, Nov. 1994.
- [20] J. Persello, "Silica sol, composition containing the same, method for treating said silica sol and uses thereof," U.S. Patent WO/2000/06997623-Nov-2000.
- [21] J. Vinas, "Matériaux hybrides polymères-particules de silice : synthèse et caractérisation.," PhD Thesis, Université de Provence - Aix-Marseille I, 2008.
- [22] D. Ma, A. J. Kell, S. Tan, Z. J. Jakubek, and B. Simard, "Photophysical Properties of Dye-Doped Silica Nanoparticles Bearing Different Types of Dye-Silica Interactions," *The Journal of Physical Chemistry C*, vol. 113, no. 36, pp. 15974-15981, 2009.
- [23] M. Ogawa, T. Nakamura, J.-ichi Mori, and K. Kuroda, "Luminescence of Tris(2,2'-bipyridine)ruthenium(II) Cations ( $[\text{Ru}(\text{bpy})_3]^{2+}$ ) Adsorbed in Mesoporous Silica," *The Journal of Physical Chemistry B*, vol. 104, no. 35, pp. 8554-8556, 2000.
- [24] X. Zhao, R. P. Bagwe, and W. Tan, "Development of Organic-Dye-Doped Silica Nanoparticles in a Reverse Microemulsion," *Advanced Materials*, vol. 16, no. 2, pp. 173-176, 2004.
- [25] G. Woronoff et al., "New Generation of Amino Coumarin Methyl Sulfonate-Based Fluorogenic Substrates for Amidase Assays in Droplet-Based Microfluidic Applications," *Analytical Chemistry*, vol. 83, no. 8, pp. 2852-2857, Apr. 2011.
- [26] A. Imhof, M. Megens, J. J. Engelberts, D. T. N. de Lang, R. Sprik, and W. L. Vos, "Spectroscopy of Fluorescein (FITC) Dyed Colloidal Silica Spheres," *The Journal of Physical Chemistry B*, vol. 103, no. 9, pp. 1408-1415, Mar. 1999.
- [27] G. Yao et al., "FloDots: luminescent nanoparticles," *Analytical and Bioanalytical Chemistry*, vol. 385, no. 3, pp. 518-524, May 2006.
- [28] A. Burns, H. Ow, and U. Wiesner, "Fluorescent core-shell silica nanoparticles: towards 'Lab on a Particle' architectures for nanobiotechnology," *Chemical Society Reviews*, vol. 35, no. 11, pp. 1028-1042, 2006.
- [29] L. Wang et al., "Watching Silica Nanoparticles Glow in the Biological World," *Analytical Chemistry*, vol. 78, no. 3, pp. 646-654, Feb. 2006.
- [30] H. Ow, D. R. Larson, M. Srivastava, B. A. Baird, W. W. Webb, and U. Wiesner, "Bright and Stable Core-Shell Fluorescent Silica Nanoparticles," *Nano Letters*, vol. 5, no. 1, pp. 113-117, Jan. 2005.
- [31] D. R. Larson, H. Ow, H. D. Vishwasrao, A. A. Heikal, U. Wiesner, and W. W. Webb, "Silica Nanoparticle Architecture Determines Radiative Properties of Encapsulated Fluorophores," *Chemistry of Materials*, vol. 20, no. 8, pp. 2677-2684, Apr. 2008.

- [32] E. Herz et al., "Fluorescent core-shell silica nanoparticles: an alternative radiative materials platform," in *Colloidal Quantum Dots for Biomedical Applications*, San Jose, CA, USA, 2006, vol. 6096, pp. 609605-12.
- [33] M. Nakamura, M. Shono, and K. Ishimura, "Synthesis, Characterization, and Biological Applications of Multifluorescent Silica Nanoparticles," *Analytical Chemistry*, vol. 79, no. 17, pp. 6507-6514, 2007.
- [34] B. Valeur, *Molecular fluorescence: principles and applications*. Weinheim ;;New York: Wiley-VCH, 2002.
- [35] F. Mahtab et al., "Covalent Immobilization of Aggregation-Induced Emission Luminogens in Silica Nanoparticles Through Click Reaction," *Small*, vol. 7, no. 10, pp. 1448-1455, May 2011.
- [36] J. Xu, J. Liang, J. Li, and W. Yang, "Multicolor Dye-Doped Silica Nanoparticles Independent of FRET," *Langmuir*, vol. 26, no. 20, pp. 15722-15725, Oct. 2010.
- [37] I. Gryczynski, Z. Gryczynski, and J. R. Lakowicz, "Fluorescence Anisotropy Controlled by Light Quenching," *Photochemistry and Photobiology*, vol. 67, no. 6, pp. 641-646, Jun. 1998.
- [38] E. Vignati, R. Piazza, and T. P. Lockhart, "Pickering Emulsions: Interfacial Tension, Colloidal Layer Morphology, and Trapped-Particle Motion," *Langmuir*, vol. 19, no. 17, pp. 6650-6656, 2003.
- [39] J. Desclés et al., "New tools for labeling silica in living diatoms," *New Phytologist*, vol. 177, no. 3, pp. 822-829, Feb. 2008.
- [40] T. Kikteva, D. Star, Z. Zhao, T. L. Baisley, and G. W. Leach, "Molecular Orientation, Aggregation, and Order in Rhodamine Films at the Fused Silica/Air Interface," *The Journal of Physical Chemistry B*, vol. 103, no. 7, pp. 1124-1133, février 1999.
- [41] R. Peña-Alonso, F. Rubio, J. Rubio, and J. Oteo, "Study of the hydrolysis and condensation of  $\gamma$ -Aminopropyltriethoxysilane by FT-IR spectroscopy," *Journal of Materials Science*, vol. 42, no. 2, pp. 595-603, Jan. 2007.
- [42] V. Bennevault-Celton, O. Maciejak, B. Desmazières, and H. Cheradame, "Condensation of alkoxysilanes in alcoholic media: II. Oligomerization of aminopropylmethyldiethoxysilane and co-oligomerization with dimethyldiethoxysilane," *Polymer International*, vol. 59, no. 9, pp. 1273-1281, Sep. 2010.
- [43] K. Devanand and J. C. Selser, "Asymptotic behavior and long-range interactions in aqueous solutions of poly(ethylene oxide)," *Macromolecules*, vol. 24, no. 22, pp. 5943-5947, Oct. 1991.
- [44] K. J. Wilkinson and J. R. Lead, *Environmental colloids and particles: behaviour, separation and characterisation*. John Wiley and Sons, 2007.

- [45] A. T. R. Williams, S. A. Winfield, and J. N. Miller, "Relative fluorescence quantum yields using a computer-controlled luminescence spectrometer," *The Analyst*, vol. 108, no. 1290, p. 1067, 1983.
- [46] J. R. Lakowicz, *Principles of Fluorescence Spectroscopy*, 3rd ed. Springer, 2006.
- [47] D. Toptygin, R. S. Savtchenko, N. D. Meadow, S. Roseman, and L. Brand, "Effect of the Solvent Refractive Index on the Excited-State Lifetime of a Single Tryptophan Residue in a Protein," *The Journal of Physical Chemistry B*, vol. 106, no. 14, pp. 3724-3734, Apr. 2002.
- [48] T. J. Russin, E. I. Altinoğlu, J. H. Adair, and P. C. Eklund, "Measuring the fluorescent quantum efficiency of indocyanine green encapsulated in nanocomposite particulates," *Journal of Physics: Condensed Matter*, vol. 22, no. 33, p. 334217, Aug. 2010.
- [49] S. Santra et al., "Fluorescence lifetime measurements to determine the core-shell nanostructure of FITC-doped silica nanoparticles: An optical approach to evaluate nanoparticle photostability," *Journal of Luminescence*, vol. 117, no. 1, pp. 75-82, Mar. 2006.
- [50] "Hybrid Silica Technologies - Technology." [Online]. Available: <http://www.hybridsilica.com/technology.html>.

## Acknowledgment of collaboration

I designed and conducted this research with specific contributions from others as follows: Dr. Abdeslam El Harrak suggested the Persello synthesis route as an alternative to the Stöber method. He also helped me for the silica syntheses, fluorescence measurements and DLS data analysis. Dr Antoine Drevelle helped me run the photobleaching measurements. Dris Ihiawakrim performed the TEM experiments at IPCMS (Strasbourg). Dr Oliver Miller wrote the Labview software that I used to regulate silicate and resin addition according to measured pH. Dr Thomas Mangeat suggested the possibility to tune FP of fluorophores in silica by homo-FRET.



# Chapter 3. Silica nanoparticles at fluorinated oil-water interfaces

## 3.1 Introduction

Before using our silica nanoparticles as fluorescent labels in microfluidic droplets, we undertook to determine whether their presence had an impact on droplet formation, kinetics of surfactant adsorption and long-term droplet stability. Indeed, if they prevent droplet stabilization or induce loss of emulsion monodispersity by coalescence or ripening, it would prohibit their use for long-term storage of encoded droplet libraries. We hence researched literature about mechanisms of surfactant adsorption at interfaces along with effects of nanoparticles on emulsion stability.

### 3.1.1 Surfactant adsorption at the interface

As mentioned in the first chapter, above a certain threshold bulk concentration called “critical micelle concentration” or CMC, surfactant molecules in solution begin to assemble into aggregate structures called “micelles” to minimize interfacial free energy [1]. In oil, surfactant hydrophilic groups cluster together, away from the oil in the micelle core, whereas the hydrophobic groups extend away from the center into the oil. Above the CMC, the surfactant is present in two forms: surfactant monomers at  $C_{mono} = CMC$  and micelles for the remaining part.

When an oil/surfactant solution comes in contact with an interface, for example water, surfactant molecules spontaneously migrate to the interface, consequently lowering its interfacial tension. This dynamic accumulation at the interface is called adsorption. Mechanisms of adsorption differ, depending on the bulk surfactant concentration relative to the CMC [2], [3], as explained on **Figure 3.1**.

For  $C < CMC$  (**Figure 3.1 a**)), two time scales govern the dynamic adsorption behavior and define the time required for surfactant to form an equilibrium monolayer on a surface initially void of surfactant [4]. The first is kinetic adsorption process characterized by  $\tau_K$ , the time necessary for monomers in the sublayer to come to equilibrium in the absence of diffusion. The second is the diffusion (and sometimes convection) of monomers from the bulk to the

subsurface, defined by a characteristic time  $\tau_D^{monomer}$ . For dilute concentrations, modeling indicates that usually  $\tau_K < \tau_D^{monomer}$  [2].

As the surfactant concentration increases above the CMC (**Figure 3.1 b**)), the transport of surfactant to the interface accelerates. Although micelles diffuse more slowly than individual molecules due to their larger size, each micelle contains hundreds of molecules; overall micelles increase transport speed. However, a mechanism widely accepted until recently stated that micelles do not directly adsorb but have to first break into monomers that adsorb [3]. Recently, some experimental evidence showed that if  $C \gg CMC$  (**Figure 3.1 c**)), micelles themselves could directly diffuse and adsorb to the interface [2].

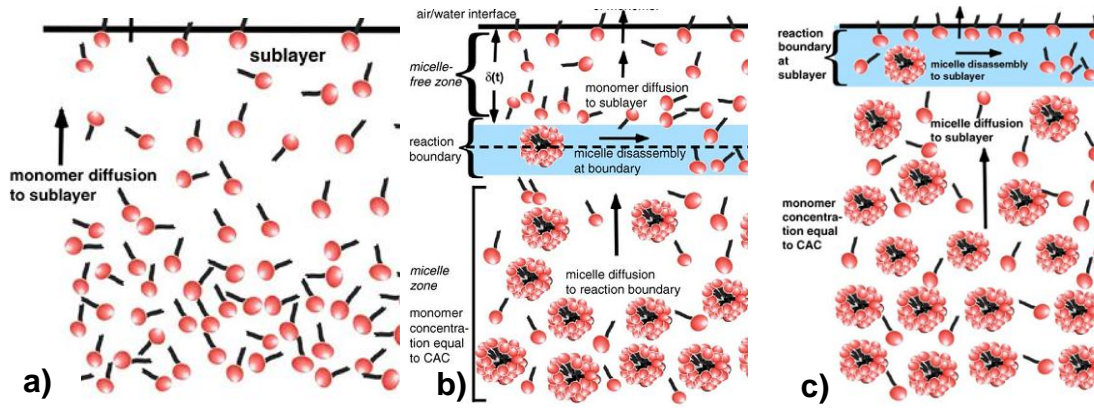


**Figure 3.1** Three observed mechanisms for surfactant repartition in bulk after adsorption at the interface: a)  $C < CMC$ ; b)  $CMC < C < n^*.CMC$ ; c)  $C > n^*.CMC$ . Factor  $n^*$  depends on monomer and micelle diffusion coefficients, kinetic rate of monomer adsorption,  $\tau_K$  and  $\tau_D^{monomer}$ . Reproduced from [2].

To characterize surfactant adsorption, variation of equilibrium interfacial tension with logarithm of surfactant bulk concentration is usually measured, based on the Gibbs adsorption equation [1]:

$$-d\gamma = RT \sum \Gamma_i d(\ln a_i) \quad (3.1)$$

where  $\gamma$  is the interfacial tension at equilibrium,  $R$  the molar gas constant,  $T$  the temperature,  $\Gamma_i$  and  $a_i$  respectively the surface concentration and activity of each component. In the case of a single and dilute surface-active species,

$$\Gamma = - \frac{1}{RT} \left. \frac{\partial \gamma}{\partial (\ln C)} \right|_T \quad (3.2)$$

That is why a very common way to characterize a surfactant is to plot its  $\gamma_{eq}(\log C)$  curve. In most cases, interfacial tension reaches its minimum equilibrium value after a few minutes; however, sometimes tension keeps decreasing even after several hours [1]. This slow aging can be due to trace impurities which also adsorb at the interface, but at very different timescales.

However, these equilibrium values do not provide understanding of the dynamic adsorption process; henceforth, it is useful to plot  $\gamma(t)$  as well. If adsorption is uniform over the whole interface, the link between  $\Gamma(t)$  and  $\gamma(t)$  is the same as at equilibrium and the Gibbs equation applies [4]. Depending on the system parameters, several models describe the relationship between  $\Gamma(t)$ , monomer diffusion coefficients and adsorption/desorption rates [2], [4].

### 3.1.2 Colloidal particles at interfaces

As an alternative to surfactants, solid colloidal particles are also powerful emulsifying agents. Their role in stabilizing emulsions was recognized by Pickering a century ago [5]: giving colloid-stabilized emulsions the widely used name of ‘Pickering emulsions’. As the affinity of a surfactant for one phase or the other is defined by its hydrophilic-lipophilic balance (HLB), in the case of solid particles, the main parameter is the contact angle  $\theta$  between the particle and the interface, as sketched on **Figure 3.2 a)** [6].

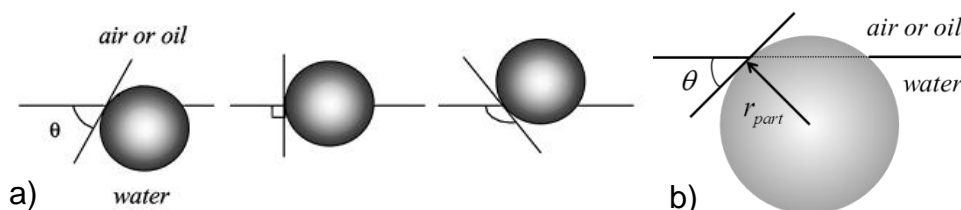


**Figure 3.2** a) Position of a small spherical particle at a planar fluid-water interface for a contact angle measured through the aqueous phase less than  $90^\circ$  (left), equal to  $90^\circ$  (centre) and greater than  $90^\circ$  (right). Reproduced from [6]. b) Detail of the ‘hydrophilic particle’ case: the horizontal dotted line is a profile view of the interfacial area that has been replaced by the particle.

When particles dispersed in one phase meet the interface with the other, they tend to spontaneously adsorb there and remain strongly anchored. The reason for this spontaneous strong attachment is that it lowers the interfacial free energy. The explanation is the following: when a particle moves from a phase A to the interface A/B, an area of the A/B interface (with

high interfacial tension  $\gamma_{AB}$ ) is lost due to the presence of the particle. Based on **Figure 3.2 b)**, the corresponding decrease in interfacial free energy, which is the opposite of the energy required to remove the particle from the interface, is [6]:

$$\Delta E = -\gamma_{AB}\pi r_{part}^2 (1 \pm \cos \theta)^2 \quad (3.3)$$

The sign inside the bracket is negative for particles coming from water, and positive if they come from oil or air. Since this value is proportional to the square of the particle radius, detachment energies very quickly reach values of several tens of thousands  $kT$  for particles not even a micron in size. However, when particle size drops to a few nanometers, anchorage is not so robust anymore. Experiments performed on quantum dots of different sizes showed that particles of radius  $r_{part} = 2.3$  nm stabilized emulsions for days, whereas droplets with  $r_{part} = 1.35$  nm particles coalesced within hours, owing to a reduced surface coverage by desorption [7]. In the case of our silica particles of radius  $r_{part} = 1.75$  nm and interfacial tension value between borate buffer and HFE 7500  $\gamma_{AB} = 38$  mN/m, considering that our particles are hydrophilic ( $\theta \sim 20^\circ$ ), the absolute value drops to  $0.32 kT$ : thermal energy could indeed partially desorb them.

In addition to the decrease of interfacial area by the particles, a decrease in surface tension, similar to the action of surfactant, could also be expected as an alternative free energy-lowering mechanism. Divergent observations have been made on this question: Levine et al observed a drastic decrease of carbon tetrachloride/water interfacial tension by adsorbed silica nanoparticles (570 nm diameter), from 44 to 33 mN/m in one hour [8]. This confirmed his theoretical calculations that predicted decrease of effective  $\gamma_{AB}$  with increasing  $\theta$ , down to 50 % its normal value if  $\theta = 90^\circ$ . However, in more recent experiments by Vignati et al on silica particles of similar size, adsorption of particles of diverse roughnesses caused no variation of isooctane/water interfacial tension, even at concentrations as high as 8 g/L [9]. More generally accepted claims are that particles stabilize emulsions by providing steric hindrance to coalescence, by slowing down water drainage and by modifying the rheological properties of the interface [9–11].

When it comes to dynamics, a simple diffusion-limited model was recently proposed to describe particle adsorption [12]. Once the particles are anchored to the interface, their lateral movement follows two-dimensional Brownian motion [9]. Their diffusion coefficient on the surface is about 4 times lower than in bulk [7].



### 3.1.3 Nanoparticles and surfactant: what interaction?

Since both surfactants and particles stabilize interfaces, some groups have investigated what happens when both are combined. An early study by Midmore [13] on 12 nm diameter hydrophilic silica proposed a nanoparticle adsorption mechanism in the case of low HLB surfactants that are insoluble in water (as ours): since silica and surfactant are in different phases, the surfactant cannot flocculate the particles before they reach the interface. Hence, monomeric silica adsorbs at the interface, forming a monolayer of 300-nm close-packed flocs. PEG can adsorb at the silica surface [14]. Binks et al, as the previous reports, also related synergistic enhancement of emulsion stabilization by combining silica particles and PEG-alkyl surfactants in the aqueous phase: at intermediate surfactant concentration, surfactant promotes silica flocculation, which leads to optimal emulsion stability [15]. However, in our case, non-PEGylated particles are negatively charged at pH 9, which may prevent this process.

A very recent molecular dynamics study by Ranatunga et al [16] gave some insight on the synergy between uncharged nanoparticles and non-ionic surfactants at oil/water interfaces, depending on the relative interfacial concentrations of each. Sketches of various conditions tested are shown on **Figure 3.3**.

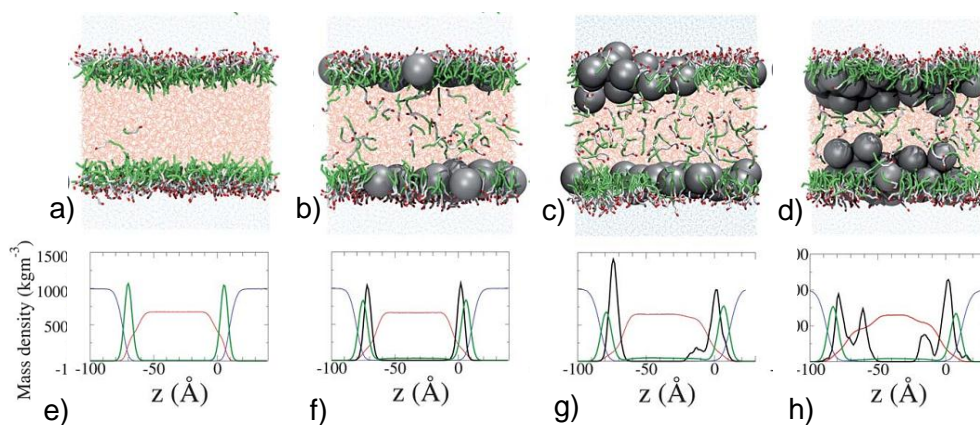


**Figure 3.3** Influence of nanoparticles concentration on oil/water interface coverage by particles and surfactant. a) to d): Side views of representative configuration. The oil layer is in red and the two aqueous layers in blue. Surfactant molecules have a green hydrophobic chain (dodecyl ether) and a green-red hydrophilic chain (triethyleneglycol). The particles are the dark grey spheres, 1.2 nm in diameter. e) to h): Mass density profiles of the system components. For all 4 examples, surfactant surface coverage equals 65 Å per molecule and number of NPs ranges from 0 (left) to 24 (right) in the total  $125 \times 125$  Å<sup>2</sup> area. Each profile matches the component of the same color on the sketch. Reproduced from [16].

Interfacial tension simulations for this set of conditions show that for increasing NP concentration, the interfacial tension is lowered initially (supporting Levine's observations [17]

and then plateaus: after an initial diminution of  $\gamma_{ow}$ , the free energy of the system is no longer dominated by the oil–water interface. Particle-particle interactions come into play: as displayed on **Figure 3.3**, particles desorb and pack in layers, highlighting some competition between the surfactant and NPs to populate the interface.

As far as dynamics are concerned, Vashisth et al have shown that addition of anionic surfactant on a dodecane-in-water emulsion stabilized by 12 nm silica particles can lead to particle displacement from the interface, if final surfactant concentration is above the CMC [18]. They proposed that the resulting decrease in interfacial tension makes particle desorption less energy-consuming, hence favoring competitive adsorption of the surfactant; however, this displacement was only achieved by applying high shear. In our case, strong interfacial shear takes place in the nozzle on the advancing aqueous finger during less than a millisecond. Once the droplet is formed, minor shear still takes place, because surfactant induces a slight acceleration of droplets compared to the surrounding flow (Baret et al, personal communication): consequently, shear-induced displacement could take place. In addition, recirculation flows in the droplet [19] could also play a role in particle adsorption and desorption dynamics.

#### 3.1.4 Goal of this chapter

Based on this literature search review, there are several questions we wanted to answer. The first one was very practical: “do silica nanoparticles in the aqueous phase of a water-in-fluorinated oil emulsion have an impact on droplet formation and stability?”. From a more fundamental standpoint, we also wanted to better understand the adsorption dynamics of our system, to know whether our silica particles and triblock non-ionic surfactant were competing or cooperating, and over which time range. Our study followed several steps: first, we determined on-chip if droplet size at generation varied with silica content. We then used a prototype of microfluidic dynamic tensiometer to compare sub-second surfactant adsorption kinetics with or without nanoparticles. To get longer timescale kinetics, we performed some dynamic interfacial tension measurements on a pendant drop tensiometer. Finally, we monitored variations in monodispersity of microfluidic droplets over several days for several silica concentrations in the aqueous phase.

## 3.2 Droplet size at generation: influence of aqueous phase

Given that our project endgoal was to generate droplet libraries on chip, we first needed to determine which oil and aqueous flow rates needed to be applied to get a certain droplet volume. Moreover, since our final libraries would consist of droplets containing several concentration levels of fluorescent nanoparticles, we also checked if the percentage of nanoparticles in the

aqueous phase had an impact on the droplet size. If so, we would then have to tune our flow rates during library generation, in order to get the same exact droplet size for all library members.

On LRS 6.6 chip (the same device on which we would generate our libraries later), we generated droplets with constant aqueous flow rate of 150  $\mu\text{L}/\text{h}$ . We tuned oil flow rates between 75 and 1050  $\mu\text{L}/\text{h}$  and monitored droplet volume all throughout. An example of is pictured on **Figure 3.4**. We repeated this experiment for several concentrations of core-shell-PEG21 SNPs in borate buffer and plotted all series together (**Figure 3.5**).

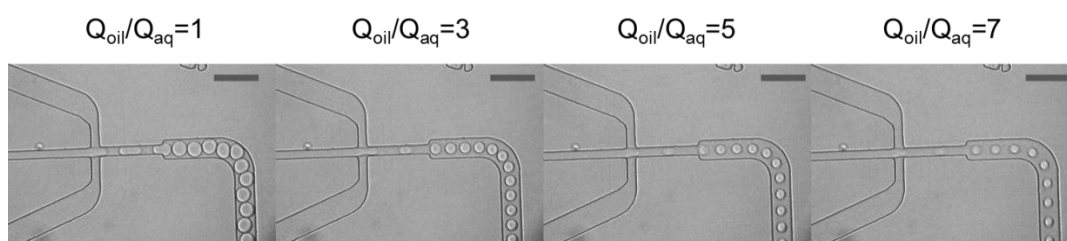


**Figure 3.4** Snapshots of droplet generation on LRS 6.6 chip using various  $Q_{\text{oil}}/Q_{\text{aq}}$  ratios. Here the aqueous phase is 0.025 wt% core-shell-PEG21 in borate buffer 10 mM and  $Q_{\text{aq}} = 150 \mu\text{L}/\text{h}$ . Nozzle dimensions are  $15 \times 15 \times 20 \mu\text{m}$  (length  $\times$  width  $\times$  depth). Scale bars are 100  $\mu\text{m}$ .

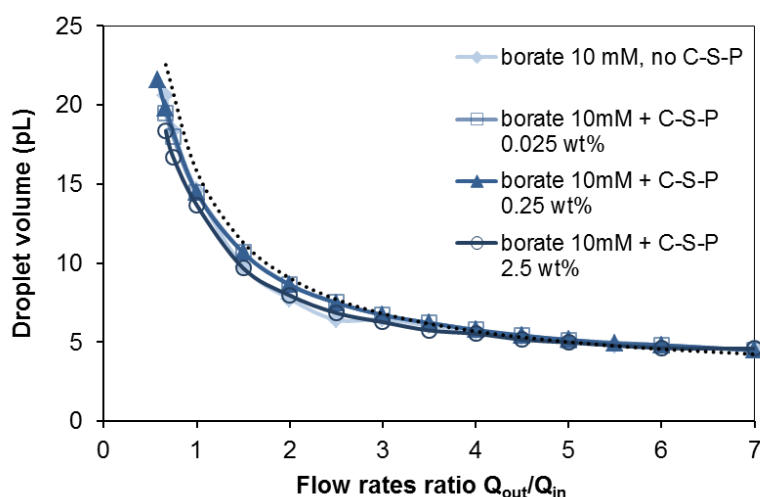


**Figure 3.5** Influence of oil/aqueous flow rates ratio and percentage of core-shell-PEG nanoparticles on the droplet volume at generation. The dashed black curve follows the simple trend  $V \propto Q_{\text{in}} / Q_{\text{out}}$ , in accordance with [20].

As explained in Chapter 1, formation of droplets is characterized by two numbers: first, the dimensionless Capillary number  $Ca$  which is the balance between viscous and capillary stresses [20]:

$$Ca = \frac{U_{out}\eta_{out}}{\gamma} \quad (3.4)$$

where  $U_{out}$  is the mean velocity of the outer (continuous) oil phase arriving in the nozzle,  $\eta_{out}$  its viscosity and  $\gamma$  the interfacial tension. The higher  $Ca$  is, the smaller the droplet. In this experiment, increasing the oil/aqueous flow rate ratio from 0.5 to 7 increases  $Ca$  from 0.003 to 0.03: as expected, droplet volume is dramatically reduced from 22 pL to 5 pL and follows the same trend as described by Abate et al [20]:

$$V \propto Q_{in} / Q_{out} = Q_{aq} / Q_{oil} \quad (3.5)$$

In spite of the wide range of  $Ca$  values, all our droplets are produced in dripping regime.

The other number governing droplet size is the ratio of viscosities of dispersed phase to continuous phase; the higher the value, the bigger the droplet. In our experiments, we observe that for a given flow rates ratio, droplet size remains constant regardless of the SNP weight fraction in the aqueous phase. This is in agreement with a very recent publication by Priest et al [21]. This means that (i) aqueous phase viscosity does not significantly change with SNP content and (ii) in the time needed to form droplets (less than a millisecond, given the aqueous flow rate and droplet volumes), interfacial tension is not modified by increasing SNP fraction. Practically speaking, this invariability of droplet size makes it much easier to get a monodisperse library emulsion: flow rates will not need to be adjusted during library generation, depending on the SNP weight fraction of each library member.

### **3.3 Interaction between nanoparticles and surfactant at the interface: a kinetic study**

Before generating on-chip emulsions including silica nanoparticles, we wanted to learn more about the possible influence of the nanoparticles on the interfacial dynamics. Regarding surfactant adsorption, Baret et al [22] established that for a train of confined droplets in motion in a microfluidic channel, surfactant transport is driven by diffusion, not convection, in agreement with the diffusive model of Song et al presented in section 3.1.1. Moreover, on-chip kinetic measurements established that, as previously modelled and verified by pendant bubble tensiometry measurements [2], micelles themselves, not monomers alone, diffuse to stabilize the interface. We hence investigated if the presence of nanoparticles affected this model and the short-and long-term kinetics of surfactant adsorption at the interface.

### 3.3.1 Preliminary experiment: determination of the CMC and micelle size of EA in HFE 7500

As presented in the first paragraph, adsorption kinetics is strongly influenced by the presence of micelles [2], [23]. As a preliminary experiment, we first determined the CMC of EA surfactant in HFE 7500 by two methods: DLS and pendant drop interfacial tensiometry (**Figure 3.6**):

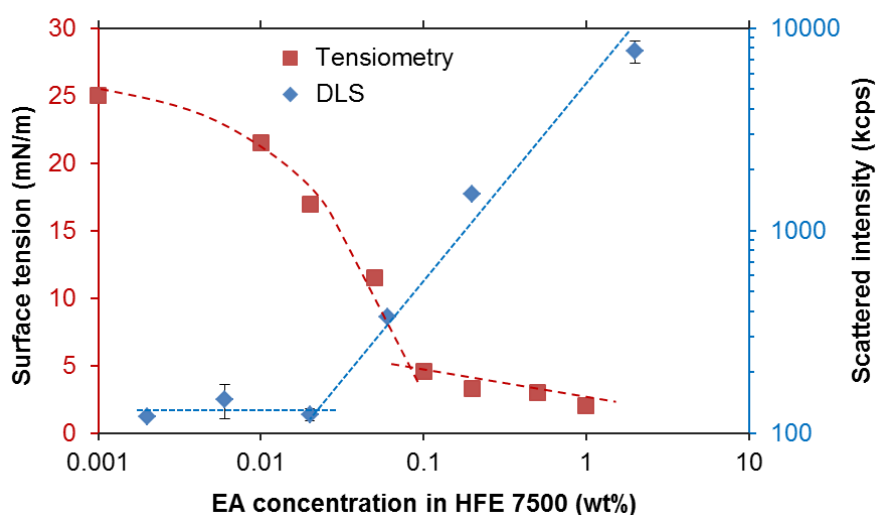


**Figure 3.6** Estimation of the CMC of EA in HFE 7500 by two techniques. Equilibrium surface tension (red squares) and intensity of scattered light (blue diamonds) of various concentrations of EA in HFE 7500. The concentrations at the intersection of the two red curves and the two blue lines respectively correspond to the critical micelle concentration measured by each technique.

The two techniques gave slightly different estimations: between 0.02 and 0.06 wt% with DLS and 0.05 and 0.1 with tensiometry. The absolute value thus lies within 0.02 and 0.1 wt%. In our next experiments we explored kinetic interfacial behavior of droplets for surfactant concentrations below and above this value.

In addition, to calculate the diffusion coefficient of micelles, we also determined micellar size by DLS: we obtained a number average diameter of  $153 \pm 8$  nm.

### 3.3.2 Preliminary calculations: diffusion times of SNP and surfactant

#### Diffusion of nanoparticles

Before starting our kinetic experiments, we first calculated for each tested particle size and weight fraction the number of particles contained in a droplet, in order to compare the surface

potentially covered by the nanoparticles to the droplet interfacial area. For dilute aqueous silica solutions where silica density is  $d_{silica}$  and SNP mass fraction is  $\phi_m^{SNP}$ , the SNP volume fraction is:

$$\phi_v^{SNP} \simeq \frac{\phi_m^{SNP}}{d_{silica}} \quad (3.6)$$

For a suspension of particles of radius  $r_{part}$ , the number of particles per volume unit can be written as :

$$N_v^{SNP} = \frac{\phi_v^{SNP}}{V_{part}} = \frac{\phi_m^{SNP}}{d_{silica} \left( \frac{4}{3} \pi r_{SNP}^3 \right)} \quad (3.7)$$

Considering a diffusion-limited process, as proposed by Hirose et al [12], the  $n$  particles required to cover a fraction  $f$  of the droplet interface are dispersed in a volume inside the droplet over a distance  $\varepsilon$  of the droplet interface,  $\varepsilon$  being much smaller than the drop radius. This leads to

$$n = A_{drop} \varepsilon N_v^{SNP} = f \frac{A_{drop}}{\pi r_{SNP}^2} \quad (3.8)$$

They reach the interface in a time  $\tau_d^{SNP} = \frac{\varepsilon^2}{D_{SNP}}$ .  $D_{SNP}$  is calculated from the particle radius by the Stokes-Einstein equation:

$$D_{SNP} = \frac{k_B T}{6\pi\eta r_{SNP}} \quad (3.9)$$

where  $\eta$  is the aqueous phase viscosity,  $k_B$  the Boltzmann constant and  $T$  the temperature.

Combining the three previous equations, the time needed for particles to diffuse and cover a fraction  $f$  of the interface is:

$$\tau_d^{SNP} = \frac{32 f^2 d_{silica}^2 r_{SNP}^3 \pi \eta}{3 (\phi_m^{SNP})^2 k_B T} \quad (3.10)$$

Using the typical values  $f = 1$ ,  $d_{silica} = 2.4$ ,  $r_{SNP} = 1.75$  nm,  $\eta = 10^{-3}$  Pa.s,  $T = 298$  K and  $\phi_m^{SNP} = 0.025$ , we find:

$$\tau_d^{SNP} = 4.03 \times 10^{-4} \text{ s.}$$

That is the same time range as the time between generation of two droplets (0.12 to 0.5 ms), which means that as the droplet pinches off from the nozzle, SNP do not have time to entirely cover the interface yet. Consequently, if the particles lowered  $\gamma$  upon adsorption, we would have seen the droplet size decrease when nanoparticle fraction increased. Since we did not, we can hypothesize that the particles do not lower the interfacial tension, in accordance with the observations of Vignati [9].

### Diffusion of surfactant

Let us now compare this value with diffusion time for micelles. According to Baret et al [22], when a solution of fluorinated surfactant above the CMC comes in contact with an aqueous droplet, micelle diffusion is the main mechanism driving the surfactant to the interface. With the equation provided in the article:

$$\tau_d^{mic} \sim \frac{f_{surf}^2}{N_A^2 C_{surf}^2 \delta_{surf}^4 D_{mic}} \quad (3.11)$$

we could estimate the necessary time for a sufficiently large number of fluorinated surfactant micelles to diffuse to the interface. Experimental values of  $C_{surf} = 2.73$  mol.m<sup>-3</sup> (2 wt% EA surfactant in HFE 7500),  $D_{mic} = 2.28 \times 10^{-12}$  m<sup>2</sup>.s<sup>-1</sup> (from Stokes-Einstein equation (4.9) using  $R_{micelles} \approx 77$  nm as measured by DLS) and estimated values of the surfactant lateral dimension  $\delta_{surf} = 1$  nm and of the fraction of the surface covered  $f_{surf} = 1$ , led to:

$$\tau_d^{mic} = 0.162 \text{ s} \quad ,$$

which is much longer than the time needed for the interface to be covered with nanoparticles.

### 3.3.3 Short timescale (0.05 – 1 s): on-chip droplet deformation kinetics

Our next objective was to understand how our silica-loaded droplets are stabilized right after formation. To remain close to our on-chip conditions, we sought tensiometry methods that enable subsecond dynamic measurements of micron-scale drops. We used a prototype currently

being developed by the group of Baret et al in MPIDS Göttingen: it consists in measuring kinetics of surfactant adsorption by monitoring droplet deformability over time. As more surfactant adsorbs, the interfacial tension is lowered and the droplet deforms more easily. To induce deformation, the droplets flow through a succession of constrictions and expansions (Figure 3.7). The flow profile induced by the geometry exerts a pulling force transverse (respectively longitudinal) to the direction of the flow in the expansions (constrictions). The result is a deformation of the droplet with respect to the direction of this force (Figure 3.8). By monitoring the maximal deformation of droplets in successive expansions, kinetics of surfactant adsorption can be followed. It is possible to do comparative analysis of analyzing oil/aqueous systems with various contents, if all droplets have the same size and velocity. We thus undertook series of measurements on this device.

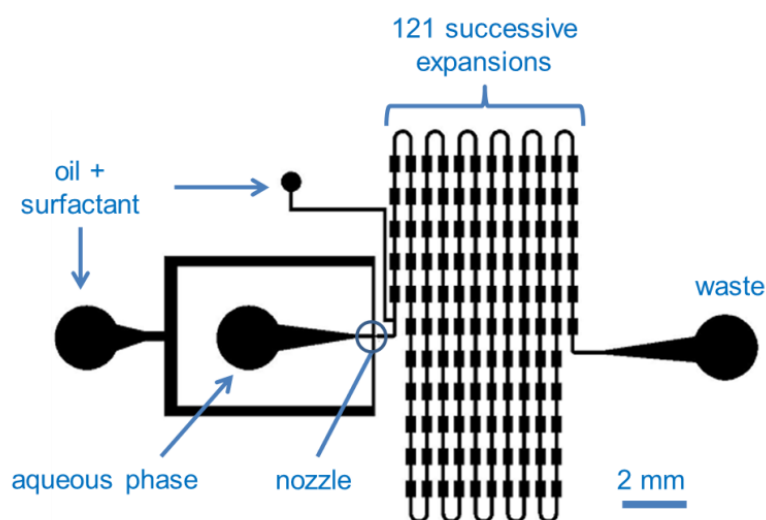


**Figure 3.7** Microfluidic circuit for determination of droplet deformation kinetics. Droplets are formed at the nozzle, spaced with additional oil and surfactant, then go through 121 successive expansions and contractions, causing distortion. From Baret and Brosseau, unpublished.



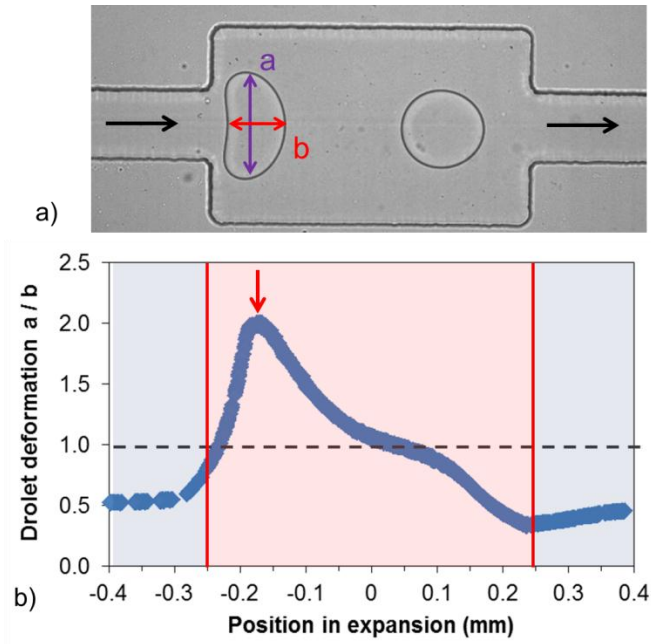


**Figure 3.8** Deformation of the droplet in the expansion. a) Snapshot of consecutive droplets at the beginning and the end of the expansion (arrows indicate direction of flow). As the drop enters the expansion, its sudden deceleration stretches it transversally. Around the middle of the chamber, speed is quite constant: the droplet becomes round again. When it comes closer to the restriction, acceleration stretches the droplet along the flow axis. b) From captured frames, average droplet deformation is calculated for each position in the expansion (shaded in red). Maximal deformation (red arrow) is extracted. From Baret and Brosseau, unpublished.

In this experiment, the droplet observed radius  $R$  at medium height is greater than the channel height  $h$ : it is squeezed and looks like a pancake as schemed below (**Figure 3.9**):

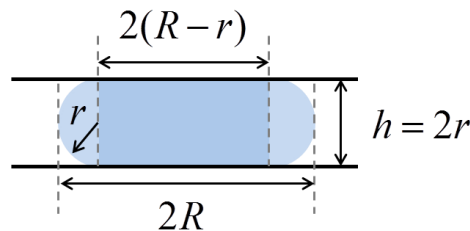


**Figure 3.9** Profile scheme of a circular drop of radius  $R$  squeezed in a channel of height  $h$ .

The drop shape can be approximated by a cylinder of radius  $R - r$  surrounded by a half-tore of small radius  $r$  and large radius  $R - r$ . Using Guldin's theorem for tore surface and volume calculation, the drop area and volume are expressed as:

$$A_{drop} = 2\pi(R - r)^2 + 2\pi^2 r(R - r) \quad (3.12)$$

$$V_{drop} = \pi(R-r)^2 \cdot 2r + \pi^2 r^2 (R-r) \quad (3.13)$$

Using the center drop of **Figure 3.8** as an example ( $R \approx 60 \mu\text{m}$  and  $r = 21 \mu\text{m}$ ), it leads to  $A_{drop} = 2.57 \times 10^4 \mu\text{m}^2$  and  $V_{drop} = 3.70 \times 10^5 \mu\text{m}^3 = 370 \text{ pL}$ .

Knowing the drop volume, equation (4.7) gives us the number of particles for each particle size and weight fraction combination. We deduce how much area would be covered if all particles spread as a hexagonally packed monolayer (equation (4.14)) and compare it to the drop area.

$$S_{coverage}^{SNP} = N_v^{SNP} \frac{\sqrt{12}}{\pi} \pi r_{part}^2 = \sqrt{12} N_v^{SNP} r_{part}^2 \quad (3.14)$$

As a first test, we chose to take a relatively simple system: 1) for the fluorinated phase, EA surfactant in HFE 7500 at an intermediate concentration of 0.2 wt% (slightly above the CMC, to avoid reaching equilibrium too fast, while still observing significant change in deformation). 2) For the aqueous phase, we used core-shell silica without PEG dispersed in borate buffer at 0.5 or 5.0 wt%. To get additional information on the possible influence of silica size, we also performed similar experiments on bigger silica nanoparticles (25 nm in diameter). We obtained the graphs plotted on **Figure 3.10**.

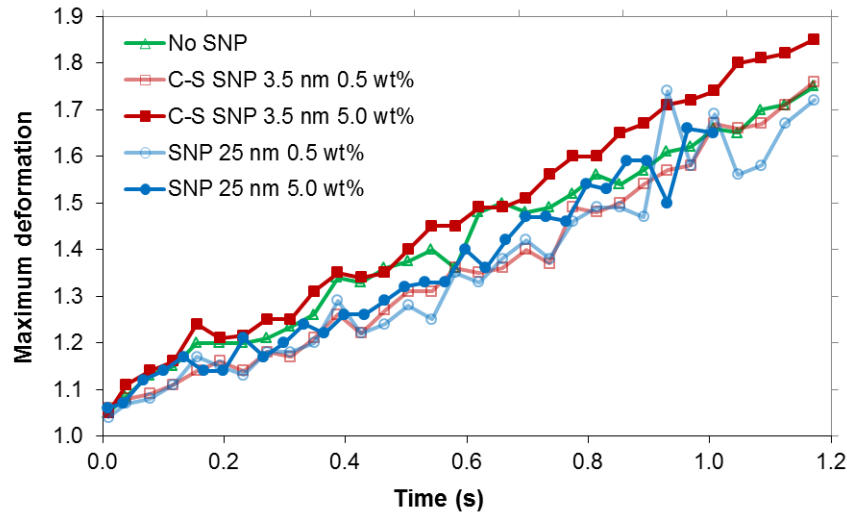


**Figure 3.10** Influence of SNP concentration and size on kinetics of maximum droplet deformation.

As expected, in all cases, maximum deformation increases progressively as the drop travels along the channel: surfactant adsorption decreases interfacial tension, making the droplet less stiff. At this concentration, droplet stabilization time by surfactant is in the second range.

Before analyzing results with regards to particle size and weight fraction, we used equations (4.7) and (4.14) to estimate possible surface coverage by particles in each case (**Table 3.1**). In all cases, there are more particles in each droplet than what is needed to completely cover the droplet surface: total coverage by SNP is hence possible. Since the surface coverage ratio between small and big particles is equal to the inverse of the radius ratios, 1.75 nm particles can cover 7.1 times more surface than 12.5 nm particles and need to diffuse from a smaller distance  $\varepsilon$  to saturate the interface. Moreover, the diffusion rate of big particles is 7.1 times lower than small ones: overall, the small particles will thus take  $(7.1)^2 \sim 50$ -fold less time to saturate the interface than the large ones.

However, as presented in section 3.1.2, adsorption energy is proportional to the square of the particle radius; we expect the 25 nm particles to have much stronger attachment to the interface than the smaller ones. So, depending whether diffusion speed or attachment drive the interaction with surfactant, we can expect to observe either small or big particles to influence deformation kinetics.

As **Figure 3.10** shows, all graphs nearly overlap: presence, concentration and size of silica particles seemingly do not seem have a big impact on surfactant adsorption kinetics at short times. Only the curve for 5.0 wt% of 3.5 nm SNP is always above the others and has a 8 % higher final value, apparently indicating an acceleration in surfactant adsorption kinetics.

		$\phi_m^{SNP}$	
$r_{part}$	Measurement	5.0 wt%	0.5 wt%
1.75 nm	$N_{part} / \text{droplet}$	$3.43 \times 10^{11}$	$3.43 \times 10^{10}$
	$S_{coverage}^{SNP} (\times A_{drop})$	141	14.1
12.5 nm	$N_{part} / \text{droplet}$	$9.42 \times 10^8$	$9.42 \times 10^7$
	$S_{coverage}^{SNP} (\times A_{drop})$	19.8	1.98

**Table 3.1** Calculation of 1) number of silica nanoparticles in a 370 pL droplet, depending on the particle radius and weight fraction in the suspension; 2) corresponding surface covered if all particles pack hexagonally on the same plane.

The interface, at high silica concentration, is first saturated with silica particles which diffuse more than 40 times faster than the micelles (diameter = 154 nm). From this, we can draw two hypotheses: (i) if the surfactant PEG hydrophilic block has a higher affinity for the silica surface than for water, it would take less time for it to adsorb. The fact that this phenomenon would not occur with bigger particles could be that the interface gets less deformable from adsorption of big

particles than small ones because they adsorb more strongly. (ii) If the interface is already saturated with small SNPs, when the surfactant arrives, surfactant hydrophilic headgroup adsorbs only in the small spaces between particles. Upon deformation, particles moving squeeze the surfactant in, which subsequently cannot desorb. Still, given the small difference between the deformation in this case and the others, repeating the experiment would confirm if this variation is just experimental noise or occurs in all cases. Regardless, if there is an influence of particles on surfactant adsorption kinetics, it is very minor in the sub-second time scale.

Since this comparative experiment did not bring a clear conclusion, we decided to try the prototype to observe the influence of another parameter on droplet deformability: the presence or absence of PEG on the particles. To do so, we monitored deformation of droplets containing either C-S particles or C-S-PEG21 particles, all in borate buffer 10 mM. As a control, we also tested droplets containing only PEG21 silane in buffer. The results are plotted on **Figure 3.11**.

Once again, the 4 series follow a similar trend and indicate similar maximal drop deformation at the end of the chip. However, only two of them exactly overlap at all time points: the two runs containing PEG. That indicates that PEG, either free or grafted onto silica has a similar influence. At early times, there is also a small difference in droplet deformation rates, that follow the trend:

$$\text{PEG21} = \text{C-S-PEG21} < \text{C-S} < \text{borate}$$

However, as previously, differences between the various experimental conditions are not very significant.

In both sets of experiments, some experimental bias could partly account this lack of major variations observed: first, droplets size is in the same order of magnitude as channel dimensions: the droplet constantly touches the top and bottom walls, plus the other two in the constrictions. This confinement could have some big impact on adsorption phenomena. Also, the relatively large size of these droplets leads them to deform so much that they do not retain a spheroidal shape (see left droplet on **Figure 3.8**), which might bias the analysis [24]. To circumvent this shape issue, either smaller droplets should be generated, or deformation analysis should include the whole droplet contour, rather than only its eccentricity. Moreover, convection phenomena in either the oil or aqueous phase could also drastically impact adsorption kinetics [4]. To circumvent this bias, complementary sub-second IFT measurements could be done with alternative techniques such as oscillating jet.

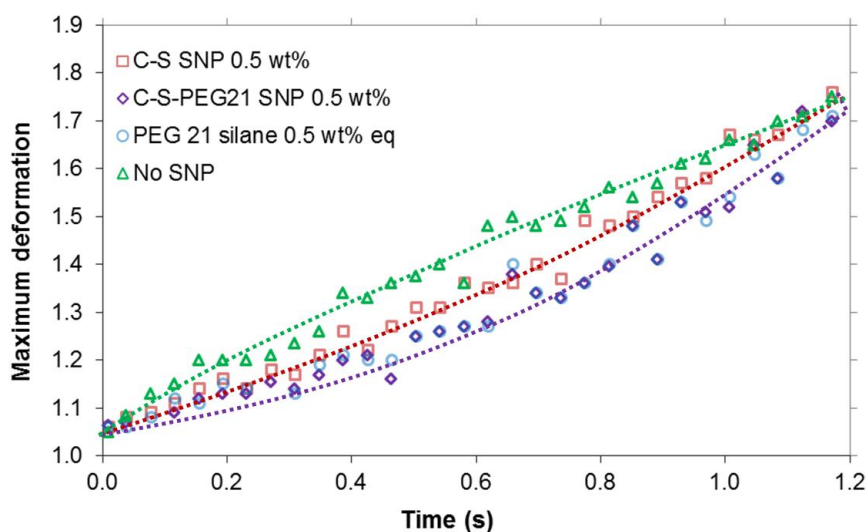


**Figure 3.11** Comparative influence of PEG silane alone, C-S SNP alone, or a combination of both (C-S-P21 SNP) on kinetics of maximum droplet deformation. Dotted lines are an eye guide to indicate the three kinetic trends.

In all cases, drop stabilization at short time scales does not seem much altered by our SNPs. Practically, it means that we do not need to keep the droplets apart on-chip longer than usually before collecting them. To complete our understanding of adsorption phenomena and get kinetic data at longer time scales, we decided to perform complementary dynamic measurements on a standard drop tensiometer.

### 3.3.4 Medium time range (1 – 300 s): dynamic interfacial tension measurements with pendant drop tensiometer

Since the final system is quite complex due to its many (potentially) surface active components (triblock polymeric surfactant, buffer, PEG-coated silica nanoparticles), we ran several series of measurements, first with each component alone, then with different combinations of them, to understand their individual effect on the whole.

#### Influence of surfactant

As a complement to the CMC measurements of EA in HFE 7500 (**Figure 3.6**), we wanted to understand the impact of increasing quantities of surfactant on the dynamic interfacial behavior. We obtained the following  $IFT = f(t)$  trends for 10 mM borate buffer drops in increasing quantities of EA surfactant in HFE 7500 (**Figure 3.12**):

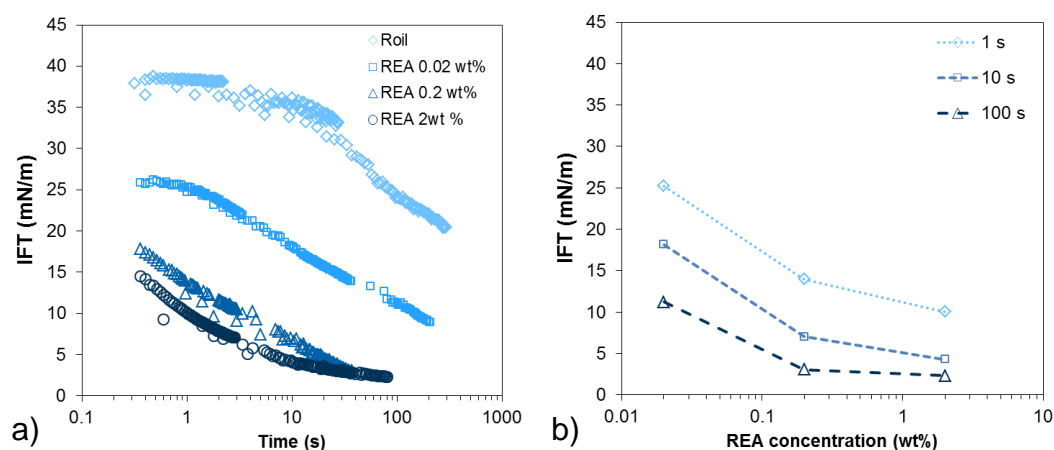


**Figure 3.12** Influence of EA concentration in HFE 7500 on dynamic interfacial tension behavior. Here the aqueous phase is 10 mM borate buffer. a)  $IFT=f(t)$  plot; b)  $IFT=f([REA])$  at three different time points.

As expected, increasing the surfactant concentration dramatically decreases the interfacial tension. This is even noticeable on the first time points around 0.5 s, meaning that surfactant has started adsorbing before this time, as previously indicated by the on-chip experiments. The other striking observation is that even without EA in the fluorinated oil, IFT decreases in time; first slightly, then faster, following a slow but steady decline. This seems to indicate the presence of a surface-active species, an impurity in the oil, which unfortunately happens frequently and can have dramatic effects [25]. Indeed, since these experiments were performed, evidence of contamination of HFE by the rubber stopper in plastic were found (Baret et al, personal communication). However, this steady decline is observed for all plots: the more concentrated the surfactant is, the sooner the slope begins, which rules out the hypothesis of an impurity totally independent from the surfactant. This secondary slope could then indicate either secondary rearrangement of the surfactant at the interface, or adsorption of borate ions.

To get an alternative view, we plotted  $IFT=f([REA])$  at several time points (**Figure 3.12 b**), to monitor the evolution of the Gibbs adsorption isotherm. The hypothesis about a role of borate is confirmed by comparison with the CMC plot (**Figure 3.6**): at long times (100 s), IFT of the interface borate/0.02 wt% EA in HFE 7500 is lower than the equilibrium value measured with pure water for CMC estimation. To circumvent the influence of this undetermined secondary kinetics, Mysels et al recommend to observe only the plots at intermediate times (1 and 10 s in our case) [25], after the adsorption of the surfactant itself is nearly complete and before that of the secondary mechanism takes place. From the slope between points at 0.02 and 0.2 wt% at time points 1 and 10 s, we estimate surfactant coverage at the interface:

$$1.95 \times 10^{-6} < \Gamma_{EA} < 1.98 \times 10^{-6} \text{ mol/m}^2$$

This value is only an approximation, because the  $\text{IFT} = f([\text{REA}])$  plots do not show precise trends, for lack of datapoints around the CMC. Complementary measurement would be helpful to get a more precise figure. Considering that the interface is totally covered with surfactant, we can nevertheless deduce which is the lateral dimension of a hydrophilic head: it is

$$\delta = \sqrt{\frac{1}{\Gamma_{EA} \cdot N_A}} = 0.92 \text{ nm} \quad (3.15)$$

which matches the value that was measured on a Langmuir-Blodgett trough on a PFPE-PEG-PFPE surfactant very similar to ours (Taly et El Abed, personal communication). This value is comparable to the hydrodynamic radius of PEG 600 calculated with Devanand's empirical law [26]:

$$R_H = 0.0145 M_w^{0.571 \pm 0.009} = 0.56 \text{ nm} \quad (3.16)$$

This higher value is not surprising: here PEG is attached to two fluorinated chains and anchored at the surface of the droplet, so it is more extended than in free coiled form in water. Thus indicates that packing of surfactant molecules at the interface is likely quite compact.

### Influence of silica alone

After examining surfactant alone, we then studied core-shell silica particles alone at the interface: we performed similar IFT measurements to estimate the impact of an increasing amount of silica (without PEG coating) on the interfacial properties. The average diameter of the particles used was  $3.5 \text{ nm} \pm 0.4 \text{ nm}$ , as measured by DLS. The IFT measurements are displayed on **Figure 3.13**.

In absence of surfactant, an increase in SNP concentration dramatically decreases the initial IFT value from 38 to 24 mN/m, as **Figure 3.13** a) indicates. This is in accordance with observations and calculations by Levine et al. on silica spheres [8] but in disagreement with Vignati et al [9]. In our case, the increasing concentration of nanoparticles definitely has an influence on interfacial properties. Complementary measurements at shorter times (either on-chip or with other methods like oscillating jet or inclined plate) would be necessary to definitely conclude whether the presence of SNP changes either 1) the bulk properties of the buffer/HFE7500 interface hence the  $\text{IFT}(t \rightarrow 0)$  value, or 2) if this decrease is due to the very

fast diffusion of a sufficient number of nanoparticles to cover the interface ( $\tau_d^{SNP} = 4.03 \times 10^{-4}$  s as calculated in section 3.3.2).

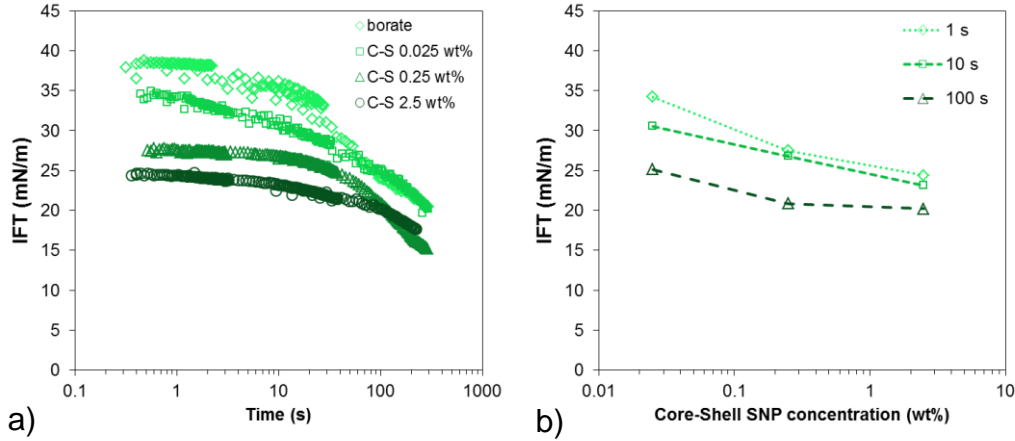


**Figure 3.13** Influence of core-shell SNP concentration in 10 mM borate buffer pH 9 on dynamic interfacial tension behavior. Here the oil phase is HFE 7500 without EA. a)  $IFT=f(t)$  plot; b)  $IFT=f([C-S\ SNP])$  at three different timepoints.

From the  $IFT=f([SNP])$  plot, we observe that the slope does not break when SNP concentration increases, which is normal because slope rupture indicates transition above CMC, a notion that makes no sense when it comes to particles. In time, the slope of this plot remains quite steady, meaning that the surface coverage by SNP remains constant in time. Using the Gibbs adsorption equation (4.2), we get:

$$6.6 \times 10^{-7} < \Gamma_{SNP} < 1.2 \times 10^{-6} \text{ mol/m}^2 \quad (3.17)$$

From this, we approximate the thickness of silica layer at the interface:

$$\epsilon_{SNP} = \frac{\Gamma_{SNP} \cdot M(SiO_2)}{d_{silica}} \in [16.5; 30] \text{ nm} \quad (3.18)$$

This is far more than the particle size, meaning that several layers of particles pile up at the interface. However, as previously, complementary measurements would be necessary to get a more precise measurement from the Gibbs isotherms.

### Influence of silica on surfactant kinetics

In a following series of experiments, we combined increasing concentrations of silica nanoparticles in the aqueous phase with increasing quantities of surfactant in the fluorinated



phase, to see whether the SNP had some influence on the surfactant kinetics and also how both would share the interfacial space. The results are shown on **Figure 3.14**.

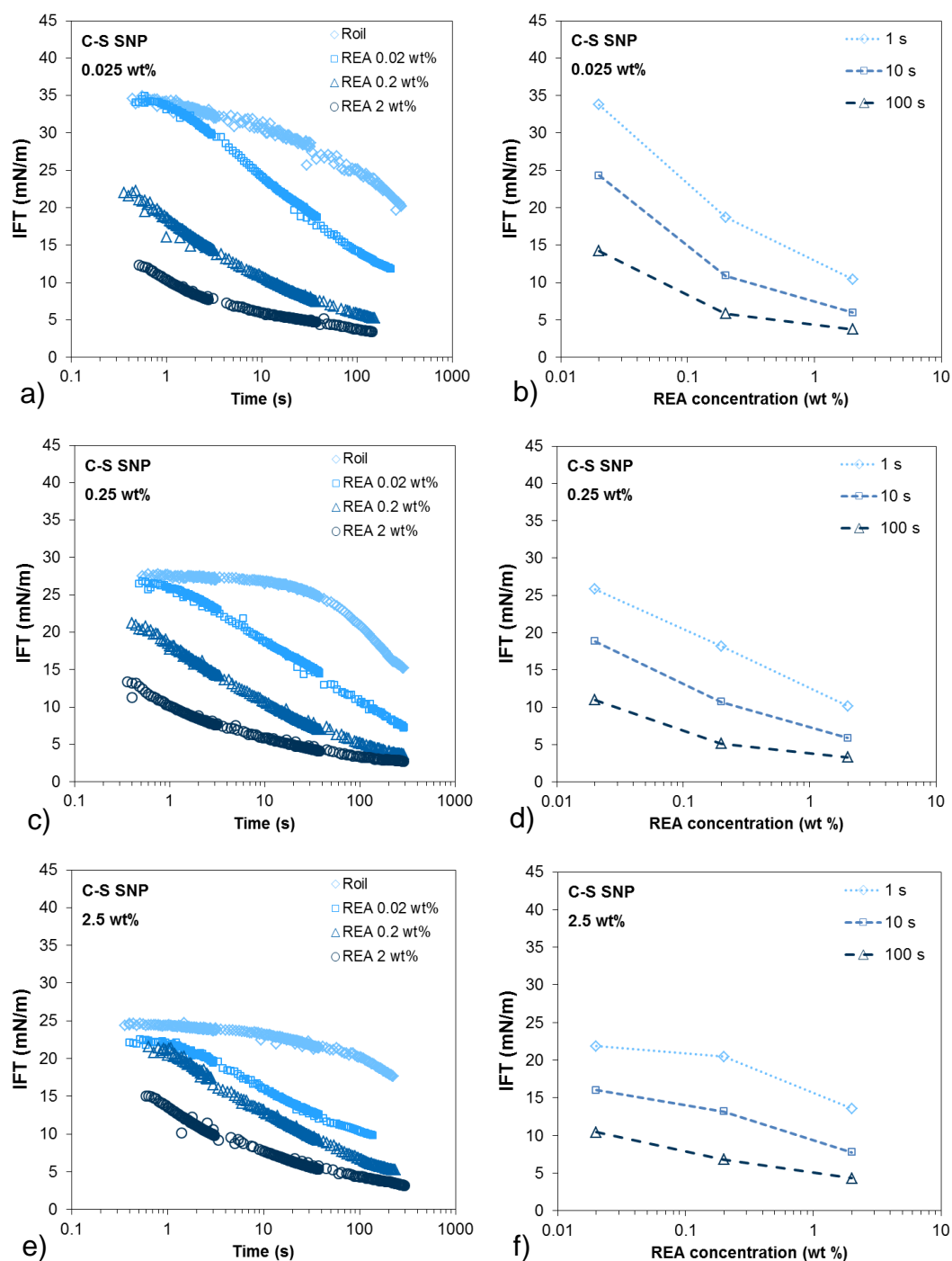


**Figure 3.14** Influence of concentration of CS SNP in 10 mM borate buffer on dynamic interfacial tension behavior of EA in HFE 7500 on. a), c), e):  $IFT=f(t)$  plots; b), d), f):  $IFT=f([EA])$  at three different time points.

If we compare these series of plots with each other and with **Figure 3.12**, many differences appear. First, at early times, the presence of SNP delays the decrease in surface tension caused by diluted surfactant: for example, after 1s, surface tensions of R oil alone and with EA 0.02 wt% in contact with buffer alone are very far apart (38 and 26 mN/m, respectively, as shown on **Figure 3.12 a)**), whereas they overlap when these oil solutions are in contact with CS SNP 0.025 or 0.25 wt%. When even only 0.025 wt% CS SNP are present in the buffer, it takes 0.02 wt% EA solution 7 s to reach the 26 mN/m surface tension it immediately had in absence of SNP (**Figure 3.14 a)**). This highlights some kind of competition taking place between the surfactant and the SNP to reach the interface.

Moreover, for low surfactant concentrations (0.02 wt%), an increasing quantity of SNP decreases the surface tension at early measurement times, in line with the effect displayed on **Figure 3.13**.

To get a more quantitative measurement on how much SNPs slow down EA adsorption at the interface, we plotted the surfactant Gibbs isotherms for each SNP concentration series (**Figure 3.14 b) d) and f)**). If we compare them to **Figure 3.12 b)**, the decrease in the absolute value of the slope between points 0.02 wt% and 0.2 wt% is striking: not only CS particles slow down EA adsorption but they also limit the amount of surfactant adsorbed. From the slopes at 1 and 10 s and using the Gibbs adsorption equation (1.2), we calculated the adsorbed quantities of surfactant for each SNP concentration and reported them in **Table 3.2**.

[CS SNP]	0.025 wt%	0.25 wt%	2.5 wt%
$\Gamma_{EA} (\times 10^{-7} mol / m^2)$	$24.9 \pm 1.4$	$13.8 \pm 0.4$	$3.67 \pm 1.25$

**Table 3.2** Calculated adsorbed EA quantities at the interface, as a function of the core-shell silica concentration.

As SNP concentration in the buffer is multiplied 100-fold, the adsorbed quantity of surfactant is decreased nearly 7-fold: SNPs do provide steric hindrance and limit surfactant adsorption.

To get the reciprocal adsorption data for silica, we plotted the same data differently (**Figure 3.15 a) c) e)**) and deduced the Gibbs adsorption isotherms of silica at various EA concentrations (**Figure 3.15 b) d) f)**)

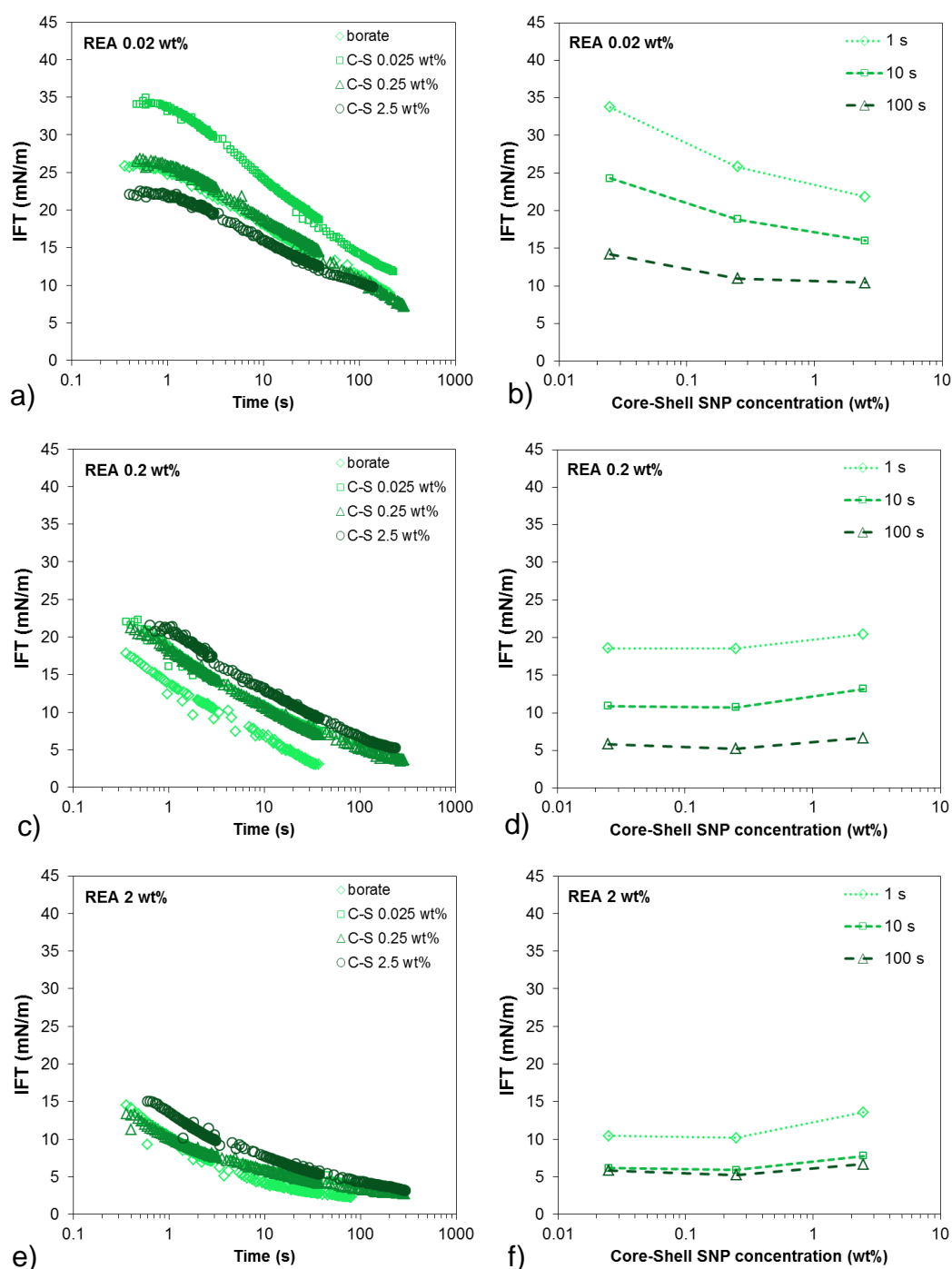


**Figure 3.15** Influence of EA concentration in HFE 7500 on dynamic interfacial tension behavior of CS SNP in 10 mM borate buffer. a), c), e):  $IFT=f(t)$  plots; b), d), f):  $IFT=f([C-S\ SNP])$  at three different time points.

Plotted this way, the behavior of SNP at increasing surfactant concentrations shows some abnormalities: at low EA concentration, it adsorbs similarly as with pure R oil (**Figure 3.13**). However, for higher EA concentrations, the  $IFT=f([C-S\ SNP])$  plots do not have the normal

appearance: IFT does not decrease anymore with increasing  $([C-S\ SNP])$  and even increases. This is only possible if at high silica concentration, the interface is saturated with several layers of silica, blocking access to the interface by the surfactant, which cannot play its tension-lowering role anymore. Another explanation for this apparent interfacial tension increase would be that accumulation of silica modifies the rheology of the interface: if the droplet does not deform so easily, the apparent surface tension is increased. To confirm this hypothesis, complementary interfacial rheology characterization, such as oscillating droplet experiments, would be necessary.

### Influence of PEG alone and grafted on silica

Since the particles we will use in the droplet library are coated with PEG, we explored if the addition of PEG on the silica surface had an impact on the dynamic IFT of such interfaces. Given the already complex quantitative analysis on 2-component systems, we just did comparative analysis of dynamic IFT curves of silica with or without PEG grafting on R oil alone (Figure 3.16 a)).

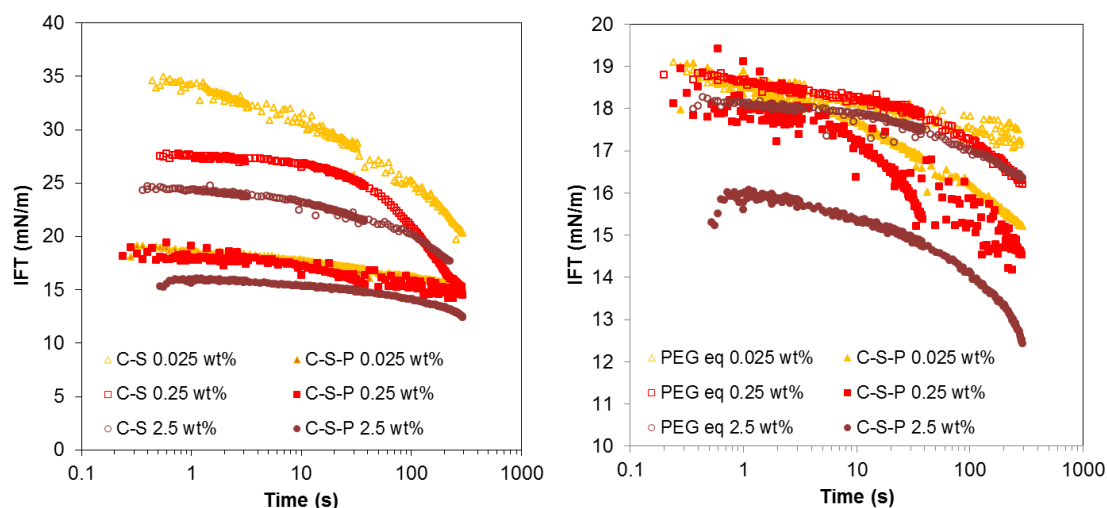


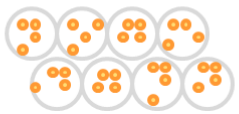
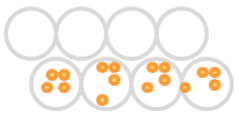

**Figure 3.16** Influence of core-shell-PEG SNP concentration in 10 mM borate buffer pH 9 on dynamic interfacial tension behavior. Here the oil phase is HFE 7500 without EA. a) Comparison between C-S and C-S-P; b) Comparison between PEG and C-S-P.

Observation of the left plot shows a striking influence of PEG grafted on silica: without PEG, IFT of C-S SNP is very dependent on particle concentration: the higher the concentration, the lower the IFT. When PEG is present, the dependence of IFT on particle concentration is far less important: no matter what the amount of grafted particles is, surface tension lies between 20 and 15 mN/m and decreases only slightly in time. This apparently indicates that grafted PEG, even at minute amounts, has a dramatic surface activity and saturates the interface. However, that did not explain if having PEG grafted on particles emphasized that phenomenon or not. As a

control, we compared dynamic IFT of these 3 C-S-P concentrations with equivalent concentrations of PEG alone, without nanoparticles (**Figure 3.16 b**). On the plot, all three IFT plots for PEG alone overlap, confirming the previous hypothesis of PEG displaying a considerable surface activity. Moreover, at concentrations 0.025 and 0.25 wt%, PEG and C-S-P curves overlap, indicating that having free or grafted PEG hardly makes any difference. Only at 2.5 wt% is the IFT of C-S-P somewhat lower than equivalent free PEG. This might be due to a punctual contamination and needs to be confirmed by repeating the experiment.

### 3.4 Long-term stability of emulsions containing SNP

The last piece of our study on influence of SNP consisted in monitoring over time the size distribution of microfluidic droplets containing several amounts of SNP. To examine both the influence of SNP presence on size distribution, as well as the impact of droplets having different contents within the same emulsion, we generated three types of emulsions (**Table 3.3**) and incubated them at 25°C or 37°C. Later we monitored their stability at 25°C and 37°C at different times by direct observation under a microscope in a wide and shallow chamber of height = 25 μm.

Number	1	2	3
Type			

**Table 3.3** Composition of the three emulsions used in long-term size distribution study. Emulsion 1 had 100% droplets containing 2.5 wt% C-S-P21 in borate 10mM pH 9.0, emulsion 2 had 50% droplets containing borate only and 50 % droplets with 2.5 wt% C-S-P21 in borate, and emulsion 3 had 100% droplets containing borate only.

In these conditions, droplets are squeezed and take a pancake-like shape, leading to a satisfactory approximation of volume from the observed area  $V \approx A \cdot h$ . We obtained the snapshots and extracted area distributions on **Figure 3.17** and **Figure 3.18**.

For the two emulsions with homogeneous droplet composition (**Figure 3.17**), no variability in average droplet area is observed over time either at 25°C or at 37°C. Over time, some coalescence takes place, but this is very limited (less than 3 % droplets) and might be caused by shear upon capillary aspiration of the sample in the chip before measurement. Minor splitting of droplets is also noticeable but it is also in the range of a few %. After 7 days of incubation, the

emulsion containing SNP has an area distribution comparable to the droplets with buffer alone. The wider size distribution seen at 25°C but not 37°C might be caused by shear during capillary aspiration of the droplets in the droplet chip. In all cases, droplet stability does not seem to radically improved as could be expected and was recently reported by Priest et al [21]. This is probably because surfactant alone at 2 wt% already provides excellent long-term stabilization, and the improvement brought by SNPs is negligible in comparison. To precisely assess the relative contribution of both, it would be interesting to run complementary experiments with less or no surfactant, and measure the time needed for droplets to coalesce [21], [22].

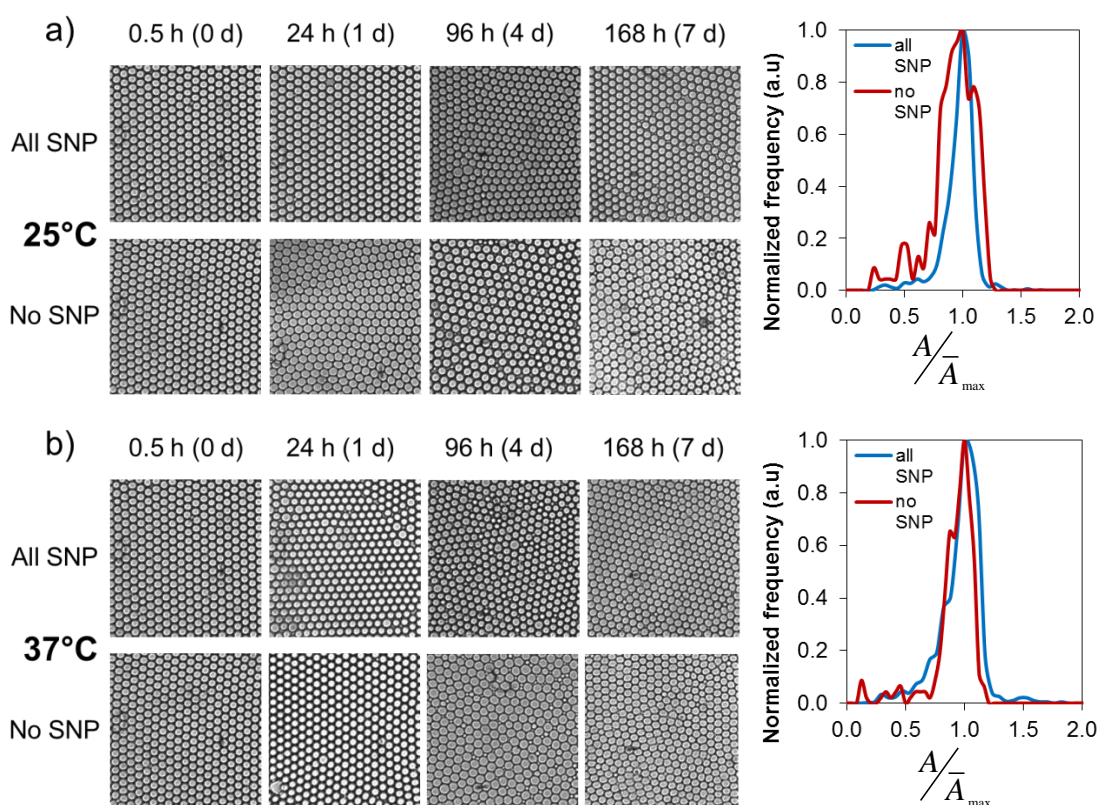


**Figure 3.17** Droplet size distribution of single-component emulsions 1 (100 % droplets containing 2.5 wt% core-shell-PEG SNP) and 3 (100% droplets without SNP) at different incubation times: snapshots of both emulsions (left) and corresponding area distributions after 7 days (right): a) incubation at 25°C, b) incubation at 37°C.

On the other hand, in the case of the dual emulsion (**Figure 3.18**), drastic transformations are noticeable even after 24h and get even more important afterwards: from a very monodisperse emulsion, transition to a clearly bidisperse emulsion takes place. In each case, the two populations have equivalent standard deviations: the monodispersity of each is conserved. This phenomenon clearly highlights osmotic transport of water between droplets, as presented in the Introduction



chapter. Transport of the water is promoted by two mechanisms: solubilization in EA micelles, and in a minor way, slight solubility in HFE 7500.

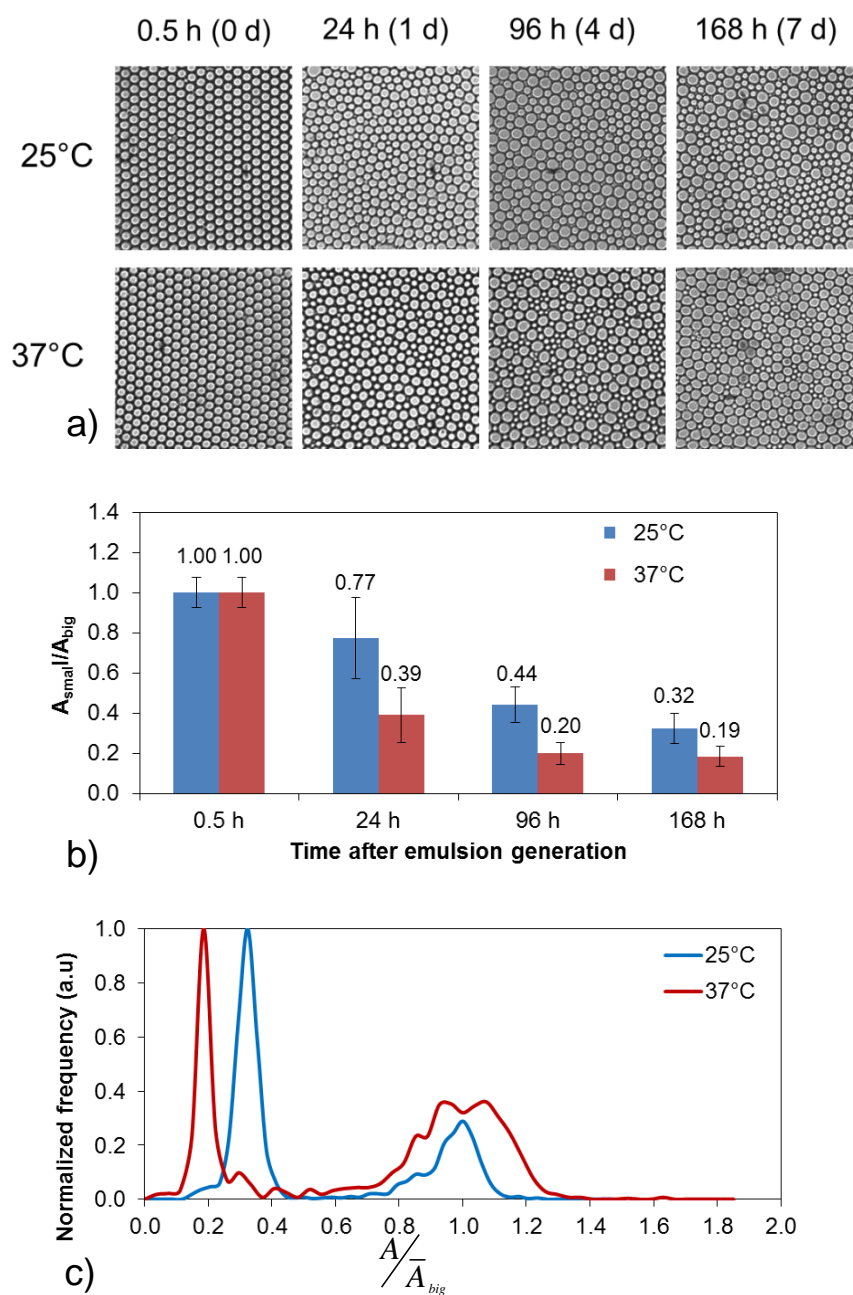


**Figure 3.18** Droplet size distribution of two-component emulsion 2 (50 % droplets containing 2.5 wt% core-shell-PEG SNP and 50% droplets without SNP) at different incubation times: a) snapshots after incubation at 25°C or 37°C; b) corresponding area distributions; c) Droplet area distributions after 7 days incubation at 25°C or 37°C. The droplet size is plotted relative to the average area of the larger droplet.

Indeed, droplets containing buffer alone have a lower chemical potential than droplets containing nanoparticles in addition to the same buffer concentration. To reach equilibrium of chemical potentials, water travels from the “buffer” droplets to the “buffer + nanoparticles” droplets (see **Figure 3.19**). In our system, water can be transported by several mechanisms. First, the collected droplets cream to the top of the emulsion and pack in a hexagonal manner, so they touch each other during incubation: water just has to cross the two surfactant monolayers [27]. Moreover, the surrounding fluorinated oil contains 2 wt% EA surfactant, a concentration far above the CMC: micelles can spontaneously swell and act as water nanocarriers from one droplet to the other [28].

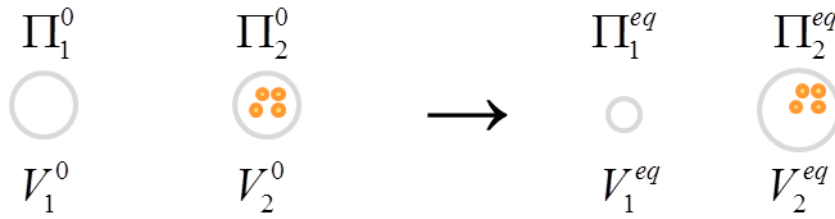


**Figure 3.19** Equilibration of the chemical potentials by osmotic transport. Initially, droplets have the same volume  $V_1^0 = V_2^0$  and different chemical potentials. Water is transported from dilute droplets to concentrated ones. The system reaches equilibrium and transport stops when chemical potentials of both types of droplets get equal:  $\Pi_1^{eq} = \Pi_2^{eq}$ .

From the Morse equation, osmotic pressure in a diluted solution is approximated as:

$$\Pi = i.MRT \quad (3.19)$$

where  $i$  is the van't Hoff factor (equal to 1 in our case of a weak acid),  $M$  is the molarity,  $R$  is the gas constant and  $T$  the temperature. For the initial droplets that contain only 10 mM borate,  $\Pi_1^0 = 24.4$  kPa. Given their initial volume (6 pL), osmotic pressure is far superior to the Laplace pressure which equals  $P_L^0 = \frac{2\gamma}{R} \approx 500$  Pa: we can rule out Ostwald ripening as an alternative transport mechanism. Once osmotic pressures are equilibrated, the two droplet volumes remain constant.

Indeed, that is what is observed for our experiment at 37°C: the droplet area ratio remains constant around 0.2 after 4 days incubation. At 25°C, kinetics are slower and equilibrium is not reached in 7 days. Nevertheless, we can still use equation (3.19) and deduce the molarity at osmotic equilibrium: when  $\Pi_1^{eq} = \Pi_2^{eq}$ , then  $M_1^{eq} = M_2^{eq}$ , which leads to



$$\frac{n_1}{V_1^{eq}} = \frac{n_2}{V_2^{eq}} \quad (3.20)$$

where  $n_1$  and  $n_2$  are the respective amounts of either buffer, or buffer and nanoparticles in droplet types 1 and 2.

Since our droplets are squeezed in a shallow channel, droplet volume and area are proportional so we can deduce  $n_1$  and  $n_2$  from the area ratios:

$$n_2 = \frac{n_1}{V_1^{eq}} V_2^{eq} = 5.n_1 = n_1 + n_{SNP} \quad (3.21)$$

From this and the buffer molarity equal to 10 mM, we deduce that the initial molarity brought by the silica nanoparticles is equal to 40 mM. This does not match theoretical concentration of 2.5 wt% silica solution which is around 400 mM. Maybe this is due to the fact that the small droplets reach a limit minimal size and cannot shrink further. Repeating this experiment with larger initial droplets would allow to conclude with certainty.

Keeping our endgoal in mind, this drastic variation of droplet volume in time due to osmotic imbalance among droplets was not compatible with a library shelf life of several weeks or months. Consequently, we needed to find a way to generate encoded droplets that all have the same exact osmotic pressure. Two strategies could be envisioned: first, to adjust buffer concentration depending on the silica content. It would be quite complicated in practice and would potentially jeopardize colloidal silica stability, if the buffer ionic strength gets too high. We found a simple alternative solution to equilibrate chemical potentials: to keep not only buffer concentration the same in all droplets but also silica quantity, by complementing fluorescent silica by nonfluorescent silica beads. For library preparation, this would consist in doing serial dilutions of the fluorescent silica stock suspensions by nonfluorescent silica suspensions at the same concentration. It is this solution we have implemented in the next chapter.

### 3.5 Conclusion and perspectives

This study of interaction between nanoparticles and droplet interfaces allowed us to answer three practical questions for our later use of these materials in droplet libraries: (i) droplet size at generation is independent of silica percentage inside; (ii) uniformly distributed SNPs do not affect droplet stability: no particle-induced coalescence is observed upon incubation; stability of the

emulsion over a week remains very good; (iii) in the case of a dual emulsion containing droplets with two very different SNP concentrations, osmotic effects affect the overall monodispersity: the initially monodisperse emulsion becomes bidisperse. To overcome this issue, the same total concentration of SNPs must be used in all droplets. However, for every code, the concentration of fluorescent SNP will depend on the desired fluorescence intensity of each color. All codes will have to be SNP-concentration-matched by adding similar but non fluorescent SNPs.

In a more fundamental point of view, to our knowledge, this is the first study of adsorption dynamics of a hybrid system hydrophilic particle-hydrophobic surfactant. Our results led us to two main conclusions: first, our experiments enabled to underline the competition between SNP and surfactant towards population of the interface, as well as considerable influence of PEG in lowering the IFT. Second, as already demonstrated by Laurent Boitard in his PhD thesis [27], osmotic effects in an initially monodisperse dual emulsion can be used as measurement tools, either to characterize properties of materials, or biological processes.

This work opens up many perspectives for fundamental characterization of adsorption phenomena. First, further improvements of the microfluidic dynamic interfacial tensiometer, currently under investigation by Baret and Brosseau in Göttingen, should make this platform a valuable and robust tool to study adsorption dynamics and rheology in droplets. Moreover, after eliminating all sources of contamination, the pendant drop study should be pursued at longer time scales to get equilibrium data. In addition, the osmotic study could be redone fully on-chip, for example using an approach like Boitard et al, in order to get better control of contact surfaces between droplets and avoid parasite coalescence phenomena from pipetting. Finally, based on recent articles on arrested coalescence in Pickering emulsions [21], [29], [30], it would be interesting to study how solid nanoparticles could partially replace surfactants as stabilizing agents in microfluidic emulsions.

## 3.6 Materials and methods

### 3.6.1 Chemicals

All aqueous samples were dispersed or diluted in 10 mM borate buffer pH 9.0 prepared in-house from sodium tetraborate decahydrate (Aldrich) and hydrochloric acid 1.00 M solution. The silica nanoparticles stock dispersions used were the following, from previously synthesized batches: 5 wt% core-shell SNP and 5 wt% core-shell-PEG 21 SNP (containing 1.49 mM PEG 21). 1.49 mM solution of m-PEG21 triethoxysilane (Specific Polymers) as well as 5 wt% suspension of 12.5 nm radius Ludox TMA silica particles (140 m<sup>2</sup>/g) were also used.

Fluorinated phases consisted in various amounts of PFPE-PEG-PFPE triblock EA surfactant (RainDance Technologies) dissolved in HFE 7500 fluorinated oil (3M), from  $1.0 \times 10^{-3}$  to 2.0 wt%. Structures of both molecules are sketched in Appendix A.

#### 3.6.2 CMC measurement by DLS

CMC of EA surfactant in HFE 7500 was measured by preparing serial dilutions of the surfactant from 2.0 wt% down to 0.002 wt%, filtering them with a 0.45  $\mu\text{m}$  PTFE filter (Acrodisc, Pall) to remove dust then transferring them to PMMA semi-micro cuvettes (Brand). DLS measurements were performed on a Zetasizer Nano S (Malvern): scattering distance was set to 0.45 mm and each sample was read 3 times. Depending on surfactant concentration, attenuator was tuned to obtain a scattered intensity between 200 and 1000 kcps. Given that between attenuator values  $n$  and  $n+1$ , there is a 3-fold increase in intensity, for each sample we calculated the number of kcps we would obtain if attenuator was set to 11, its maximal value (minimal attenuation effect). We plotted these values as a function of concentration to get the CMC.

For size measurements, we entered the following parameters: for the carrier fluid, HFE 7500 refractive index, viscosity and absorption coefficient; for the scattering material, Krytox FSH (DuPont) refractive index and absorption coefficient. We ran measurements at several concentrations above the CMC and deduced the average diameter from the number distribution.

#### 3.6.3 CMC measurement by pendant drop tensiometry

Alternative determination of EA CMC was performed using pending droplet method [31] on an OCA instrument and software (Dataphysics). Experiments were run by creating a pendant drop of oil phase immersed downwards in aqueous phase due to buoyancy reasons. The aqueous phase was contained in a plastic syringe (BBraun 1mL) and fluorinated phase in a 4 mL polystyrene cuvette (Fisherbrand). The drop was suspended at the tip of a needle of internal diameter  $0.215\text{mm} \pm 0.005\text{ mL}$  (Nordson). Drop shape was recorded at a frame rate of 2 pictures per second. Young fitting of the droplet curvature was processed live for each image, and surface tension was directly calculated.

#### 3.6.4 Generation of microfluidic droplets for size at generation and long-term stability measurements

Droplets were generated on a LRS 6.6 chip (see design on Appendix B) with a  $15 \times 15 \times 20\ \mu\text{m}$  ( $l \times w \times h$ ) nozzle. Flow rates were controlled by custom OEM pumps (IDEX Corp) controlled by in-house Labview software (National Instruments). For the study of droplet size at

generation, aqueous phase was injected at 150  $\mu\text{L}/\text{h}$  and EA surfactant in HFE 7500 was infused at various flow rates between 150 and 1500  $\mu\text{L}/\text{h}$  and the emulsion was collected in a waste reservoir.

For long-term stability measurements, all aqueous phases were injected at 150  $\mu\text{L}/\text{h}$  and EA surfactant in HFE 7500 was injected at 450  $\mu\text{L}/\text{h}$ . Each emulsion was collected in two 200  $\mu\text{L}$  PCR tubes (Axygen). One was kept at 25°C, while the other one was kept at 37°C.

#### 3.6.5 Measurements of droplet size at generation

During each droplet generation, 5 snapshots of the channel right out of the nozzle were taken using a Guppy CCD camera (Allied Vision Technologies) and 20x magnification. Each stack of images was analyzed using ImageJ software: pixel-length scale was calculated from a reference distance on the chip then average distance between drops was measured. Then, the volume of each drop was calculated by applying the following equation:

$$V_{drop} = Q_{aq} * l_{d-d} * \frac{h.w}{Q_{aq} + Q_{oil}} \quad (3.22)$$

where  $Q_{aq}$  is the aqueous flow rate,  $Q_{oil}$  is the oil flow rate,  $l_{d-d}$  is the distance between 2 consecutive droplets,  $h$  and  $w$  are the downstream channel height and width, respectively.

#### 3.6.6 Fabrication of droplet deformation chip

PDMS devices for deformation kinetics measurements were fabricated using soft lithography [32]. A 5 inch silicon wafer (Si-mat) was spin-coated (Ramgraber GmbH) with SU8-3050 negative photoresist (Microchem Inc.) to get a final thickness of 42  $\mu\text{m}$ . The wafer was then pre-baked on a hotplate at 95°C for 20 min in order to evaporate solvents. A high resolution polyester mask (JD-Photo-Tools) designed with AutoCAD (AutoDesk Inc.) was taped on a soda-lime glass plate, positioned on top of the SU8 coated wafer and exposed with UV light for 20 s using a mask aligner (Electronic Vision, EV620) in continuous power mode. Finally, the mold was post-baked in three heating steps: 65°C for 10 min, 95°C for 10 min, 65°C for 10 min. After cooling down to room temperature, non-cross-linked SU8 was washed away with SU8 developer solution (mr-dev600, Microresist Technologies). The mold was finally rinsed with isopropanol and blow-dried with nitrogen. Channel height was characterized by interferometry (Veeco).

PDMS devices were prepared using Sylgard 184 (Dow Corning) base silicone elastomer and the corresponding curing agent mixed in a 9:1 weight ratio. The mixture (25-30 g) was poured

over the mold in a petri dish and degassed under vacuum. After curing in a 85 °C oven for at least 2 h, the devices were cut and removed from the mold. A 0.75 mm-diameter biopsy punch (Shoney Scientific) was used to punch holes at the inlets and outlets. To close the channels, the channel size of the PDMS slab and a microscope slide (Roth) were exposed to oxygen plasma using a plasma cleaner (Pico, Diener Electronics) and air at pressure 0.4 mbar, then irreversibly bound together. The walls of the chips were then covalently functionalized with commercial fluorinated silane solution (Aquapel, PPG) to create fluorinated monolayer on the surface. First, nitrogen was blown in the channels to remove dust and air moisture that would precipitate the fluorosilane. Then Aquapel was flown through each channel for a few seconds and finally blown away with nitrogen.

#### 3.6.7 On-chip measurement of surfactant adsorption kinetics

The experimental setup was mounted as follows: each phase was contained in a 5 mL plastic syringe (BBraun). Syringes and chip were connected via Teflon tubing (0.56 mm inner diameter, 1.07 outer diameter, Fisher). Syringe pumps (Cetoni, Nemesys) were used to control flow rates. The microfluidic chip included three inlets (see scheme on **Figure 3.7**): two for the oil/surfactant phase and one for the aqueous phase. Aqueous inlet and first oil inlet were positioned to form a flow focusing junction of dimensions  $50 \times 50 \mu\text{m}$ : droplets were generated with oil/surfactant and aqueous flow rates of 30 and  $2 \mu\text{L}/\text{min}$  respectively. After droplet generation, additional oil and surfactant were injected at  $20 \mu\text{L}/\text{min}$ , spacing out droplets so that they never touch each other in the downstream channel: this would impact adsorption kinetics and jeopardize automated image analysis. The downstream microfluidic channel consisted of 121 successive expansions  $300 \mu\text{m}$  wide and  $500 \mu\text{m}$  long, each of them connected by a channel  $100 \mu\text{m}$  wide and  $500 \mu\text{m}$  long. Given the  $42 \mu\text{m}$  chip depth and the total flow rate, droplet time on-chip was 1.17 s. At the outlet, both phases were collected in a waste reservoir.

Video sequences of the droplets passing through these expansions were recorded with a high speed camera (Phantom, V210) coupled to an inverted optical microscope (IX-71, Olympus). Typically, one out of four expansions was observed at 20X magnification. For each, 1000 frames were recorded at 6200 fps and  $2 \mu\text{s}$  exposure. Each video file was then analyzed with a custom written Matlab (Mathworks) routine: First, droplet contour was extracted by thresholding the image. Next, the scale was set between pixel count and length and the following droplet features were extracted: area and perimeter,  $(x; y)$  coordinates of center of mass, as well as major and minor axes  $a$  and  $b$ . The deformation  $\frac{a}{b}$  in function of position  $x$  was calculated from these two

last quantities. Finally, the maximal value for each sequence was extracted and gathered with all the others on a plot.

#### **3.6.8 Interfacial tension measurements by pendant drop technique**

The interfacial tension  $\gamma$  between aqueous and fluorinated phases was measured at room temperature using the pendant drop method [31] on a Krüss DSA100 instrument, controlled by the Drop Analysis software. Experiments were run inside a 4 mL polypropylene cuvette (Brand) by creating a pendant drop of aqueous phase immersed in fluorinated phase. Drop was suspended at the tip of a 1" PTFE-lined dispensing tip (Nordson EFD), to avoid possible wetting by the silica sol. Due to the higher density of the fluorinated phase compared to the aqueous phase, the needle had to be bended in a hook-shape, since the drop detached itself upwards. This needle was plugged to a 1 mL plastic syringe (Braun Omnifix) connected to a 0.2  $\mu\text{m}$  filter with a hydrophilic Supor membrane (Pall Acrodisc). Between runs, each cuvette was covered to limit evaporation and deposit of dust. Also, to dissolve possible SNP aggregates deposited on the needle walls, the needles were washed with a pH 12 sodium hydroxide solution, then rinsed with miliQ water.

The droplet volume was controlled via an automated dosing system included in the Drop Analysis software. During experiments, a video of each drop was captured to record changes in the drop shape over time. The dispensing speed was adjusted so that the drop formation time was negligible compared to the video acquisition time. On each video sequence, individual frames were analyzed: for each, drop contour was detected and fit by the Young-Laplace equation, providing  $\gamma$ , drop area and drop volume for each frame. To span the whole 0.5-300s time range accurately while limiting dataset size and analysis time, three videos of each aqueous/fluorinated system were recorded: one 4 s video at 25 fps, one 40 s video at 2.5 fps, and one 300 s video at 0.25 fps. For each dataset, a different drop was used, with a smaller volume for longer observation times, so as to avoid drop detaching during the measurement. The three corresponding datasets were merged to form a unique plot for each aqueous/fluorinated series. In spite of the non-identical drop volumes for the three datasets, the IFT values connected well without need of correction.

#### **3.6.9 Fabrication of droplet generation (LRS 6.6) and ‘droplet’ chips**

Microfluidic chips were manufactured by conventional soft lithography [32]. Molding masters were fabricated by spin coating SU-8 negative photoresist (MicroChem Corp.) onto 6 inch silicon wafers and transferring the fluidic features designed with AutoCAD (Autodesk Inc.) from photomasks (CAD/Art Services) by contact lithography with a mask aligner (OAI Hybralign

Series 200). Droplet generation chips contained channels with two depths: deep channels ( $100 \pm 10 \mu\text{m}$ ) for transporting fluid from external ports to the functional regions of the chip, and shallow channels ( $20 \pm 1 \mu\text{m}$ ) for droplet generation and detection. ‘Dropslot’ chips contained shallow pools of  $15 \mu\text{m}$  depth. SU-8 photoresists 2100 and 2025 were used for deep and shallow channels respectively. Polydimethylsiloxane (Sylgard 184, Dow Corning) chips were molded from the negative masters within mold housings of custom design. Glass cover slides were permanently bonded to the fluidic side of the chips by surface activation in an oxygen plasma system (AutoGlow, Glow Research) followed by immediate contact bonding. To create hydrophobic surfaces, the microfluidic channels were treated for 2 min with 1H,1H,2H,2H-perfluorodecyltrichlorosilane (Alfa Aesar) dissolved in FC-3283 (3M Specialty Materials) prepared as a mixture of 18 g silane in 100 mL solvent.

#### 3.6.10 Microfluidic emulsion characterization by image analysis

From each collected emulsion,  $3 \mu\text{L}$  of creamed droplets were transferred by capillarity to a droplet observation area ( $28 \text{ mm} \times 1 \text{ mm} \times 25 \mu\text{m}$ ,  $1 l \times w \times h$ ) on the ‘dropslot’ chip. Once immobilized, the emulsion was observed with an upright microscope (Microstar IV, Reichert-Jung). Four snapshots of each emulsion were taken in different spots of the channel with a CCD camera (Guppy 080, AVT Smartview). Each stack of images was analysed using ImageJ software: images were thresholded then each droplet area was calculated from the droplet contours and reported to a table. All area measurements were gathered and an area histogram was plotted for each emulsion.

## References

- [1] K. Shinoda, Colloidal surfactants: some physicochemical properties. New York,: Academic Press, 1963.
- [2] Q. Song, A. Couzis, P. Somasundaran, and C. Maldarelli, “A transport model for the adsorption of surfactant from micelle solutions onto a clean air/water interface in the limit of rapid aggregate disassembly relative to diffusion and supporting dynamic tension experiments,” Colloids and Surfaces A: Physicochemical and Engineering Aspects, vol. 282-283, pp. 162-182, Jul. 2006.
- [3] B. A. Noskov, “Kinetics of adsorption from micellar solutions,” Advances in Colloid and Interface Science, vol. 95, no. 2-3, pp. 237-293, Feb. 2002.
- [4] C.-H. Chang and E. Franses, “Adsorption dynamics of surfactants at the air/water interface: a critical review of mathematical models, data, and mechanisms,” Colloids and Surfaces A: Physicochemical and Engineering Aspects, vol. 100, pp. 1-45, Jul. 1995.

- [5] S. U. Pickering, "Emulsions," *Journal of the Chemical Society, Transactions*, vol. 91, p. 2001, 1907.
- [6] B. P. Binks, "Particles as surfactants--similarities and differences," *Current Opinion in Colloid & Interface Science*, vol. 7, no. 1-2, pp. 21-41, Mar. 2002.
- [7] Y. Lin et al., "Nanoparticle Assembly at Fluid Interfaces: Structure and Dynamics," *Langmuir*, vol. 21, no. 1, pp. 191-194, Jan. 2005.
- [8] S. Levine, B. D. Bowen, and S. J. Partridge, "Stabilization of emulsions by fine particles II. capillary and van der Waals forces between particles," *Colloids and Surfaces*, vol. 38, no. 2, pp. 345-364, 1989.
- [9] E. Vignati, R. Piazza, and T. P. Lockhart, "Pickering Emulsions: Interfacial Tension, Colloidal Layer Morphology, and Trapped-Particle Motion," *Langmuir*, vol. 19, no. 17, pp. 6650-6656, 2003.
- [10] D. E. Tambe and M. M. Sharma, "Factors Controlling the Stability of Colloid-Stabilized Emulsions: I. An Experimental Investigation," *Journal of Colloid and Interface Science*, vol. 157, no. 1, pp. 244-253, Apr. 1993.
- [11] L. Zhang, L. Luo, S. Zhao, and J. Yu, "Studies of Synergism/Antagonism for Lowering Dynamic Interfacial Tensions in Surfactant/Alkali/Acidic Oil Systems, Part 2: Synergism/Antagonism in Binary Surfactant Mixtures," *Journal of Colloid and Interface Science*, vol. 251, no. 1, pp. 166-171, Jul. 2002.
- [12] Y. Hirose, S. Komura, and T. Kato, "Adsorption Dynamics in Pickering Emulsions," 2008.
- [13] B. R. Midmore, "Synergy between silica and polyoxyethylene surfactants in the formation of O/W emulsions," *Colloids and Surfaces A: Physicochemical and Engineering Aspects*, vol. 145, no. 1-3, pp. 133-143, Dec. 1998.
- [14] K.-L. Gosa and V. Uricanu, "Emulsions stabilized with PEO-PPO-PEO block copolymers and silica," *Colloids and Surfaces A: Physicochemical and Engineering Aspects*, vol. 197, no. 1-3, pp. 257-269, Feb. 2002.
- [15] B. P. Binks, A. Desforges, and D. G. Duff, "Synergistic Stabilization of Emulsions by a Mixture of Surface-Active Nanoparticles and Surfactant," *Langmuir*, vol. 23, no. 3, pp. 1098-1106, Jan. 2007.
- [16] R. J. K. U. Ranatunga, C. T. Nguyen, B. A. Wilson, W. Shinoda, and S. O. Nielsen, "Molecular dynamics study of nanoparticles and non-ionic surfactant at an oil-water interface," *Soft Matter*, 2011.
- [17] S. Levine, B. D. Bowen, and S. J. Partridge, "Stabilization of emulsions by fine particles I. Partitioning of particles between continuous phase and oil/water interface," *Colloids and Surfaces*, vol. 38, no. 2, pp. 325-343, 1989.



- [18] C. Vashisth, C. P. Whitby, D. Fornasiero, and J. Ralston, "Interfacial displacement of nanoparticles by surfactant molecules in emulsions," *Journal of Colloid and Interface Science*, vol. 349, no. 2, pp. 537-543, Sep. 2010.
- [19] C. N. Baroud, F. Gallaire, and R. Dangla, "Dynamics of microfluidic droplets," *Lab on a Chip*, vol. 10, no. 16, p. 2032, 2010.
- [20] A. R. Abate, A. Poitzsch, Y. Hwang, J. Lee, J. Czerwinska, and D. A. Weitz, "Impact of inlet channel geometry on microfluidic drop formation," *Physical Review E*, vol. 80, no. 2, p. 026310, 2009.
- [21] C. Priest, M. D. Reid, and C. P. Whitby, "Formation and stability of nanoparticle-stabilised oil-in-water emulsions in a microfluidic chip," *Journal of Colloid and Interface Science*, vol. 363, no. 1, pp. 301-306, Nov. 2011.
- [22] J.-C. Baret, F. Kleinschmidt, A. El Harrak, and A. D. Griffiths, "Kinetic Aspects of Emulsion Stabilization by Surfactants: A Microfluidic Analysis," *Langmuir*, vol. 25, no. 11, pp. 6088-6093, Jun. 2009.
- [23] D. Colegate and C. Bain, "Adsorption Kinetics in Micellar Solutions of Nonionic Surfactants," *Physical Review Letters*, vol. 95, Nov. 2005.
- [24] J. T. Cabral and S. D. Hudson, "Microfluidic approach for rapid multicomponent interfacial tensiometry," *Lab on a Chip*, vol. 6, no. 3, p. 427, 2006.
- [25] K. J. Mysels, "Surface tension of solutions of pure sodium dodecyl sulfate," *Langmuir*, vol. 2, no. 4, pp. 423-428, Jul. 1986.
- [26] K. Devanand and J. C. Selser, "Asymptotic behavior and long-range interactions in aqueous solutions of poly(ethylene oxide)," *Macromolecules*, vol. 24, no. 22, pp. 5943-5947, Oct. 1991.
- [27] L. Boitard, "Mesure du métabolisme de la levure par flux osmotiques entre gouttes d'émulsion," Université Paris VII- Denis Diderot, 2010.
- [28] L. Wen and K. D. Papadopoulos, "Visualization of water transport in W1/O/W2 emulsions," *Colloids and Surfaces A: Physicochemical and Engineering Aspects*, vol. 174, no. 1-2, pp. 159-167, Nov. 2000.
- [29] A. R. Studart, H. C. Shum, and D. A. Weitz, "Arrested Coalescence of Particle-coated Droplets into Nonspherical Supracolloidal Structures†," *The Journal of Physical Chemistry B*, vol. 113, no. 12, pp. 3914-3919, Mar. 2009.
- [30] A. B. Pawar, M. Caggioni, R. Ergun, R. W. Hartel, and P. T. Spicer, "Arrested coalescence in Pickering emulsions," *Soft Matter*, 2011.
- [31] C. E. Stauffer, "The Measurement of Surface Tension by the Pendant Drop Technique," *The Journal of Physical Chemistry*, vol. 69, no. 6, pp. 1933-1938, Jun. 1965.

- [32] J. C. McDonald et al., “Fabrication of microfluidic systems in poly(dimethylsiloxane),” *Electrophoresis*, vol. 21, no. 1, pp. 27-40, Jan. 2000.

## Acknowledgment of collaboration

I designed and conducted this research with specific contributions from others as follows:

I performed all experiments in this chapter (except those from subsection **3.3.2**) at RainDance Technologies in Lexington, MA, USA. Dr. J. Brian Hutchison suggested performing pendant drop tensiometry measurements. Benjamin Miller trained me on the Krüss tensiometer as well as on the microfluidic station for droplet size measurements. Dr. Xinyu Li showed me the ‘droplet’ method for emulsion characterization. LRS 6.6 and ‘droplet’ chips were fabricated by the chip manufacturing team of the company.

I co-performed on-chip droplet deformation tests as well as CMC measurements with Quentin Brosseau in Dr. Jean Christophe Baret’s lab in Max Planck Institute for Dynamics and Self-organization in Göttingen. Quentin Brosseau performed CMC measurements by pendant drop tensiometry, designed and fabricated the chip for deformation kinetics, ran complementary on-chip droplet deformation measurements and performed the Matlab data analysis. Dr. Jean-Christophe Baret provided helpful advice on general strategy to characterize adsorption dynamics.

# Chapter 4. Fluorescently encoded droplet libraries

In Chapter 2, we described the optical properties of our fluorescent silica nanoparticles; the following chapter investigated the effect of these nanoparticles in the aqueous phase on emulsion stabilization. With this in mind, the next step was to combine both aspects and achieve our initial goal: create multi-color fluorescently encoded droplet libraries, as a new critical step towards on-chip high-throughput screening of large libraries of bio active species, or implementation of high-plexed assays in droplet microfluidics.

## 4.1 Introduction

Optical encoding is a topic that has been explored for several decades, and classical black and white barcodes are widely used in the biotech industry for sample identification during assays. More recently, alternative coding systems have been introduced to accelerate novel multiplex assays. However, the increasing interest for microfluidic platforms has launched new efforts to develop coding strategies that fully exploit their advantages. This section will first introduce the latest efforts in multiplexed encoding technologies then will present droplet microfluidics assays that first used fluorescent labels for assay or compound identification. Finally, detecting multiple color labels altogether brings the issue of spectral crosstalk: we will review the latest advances to circumvent it.

### 4.1.1 Current multiplexing platforms

As mentioned in the Introduction, the development of multiplexed assays has stirred the conception of fluorescent labels to identify each assay. Luminex [1] has launched the first fluorescent bead-based multiplexed platform. By combining 5.6 micron polystyrene spheres loaded with various relative proportions of two fluorophores (one orange and one red), they managed to get 64 distinct codes (**Figure 4.1**) [2], [3]. To read out these codes, they used a modified flow cytometer with a 633 nm laser to excite the two fluorophores inside the beads. An additional 488 nm laser excited the assay tags at the the surface of the beads.

Due to the significant spectral spillover of the orange dye in the red channel, the scatterplot was not orthogonal. Consequently, lots of coding space was lost at the top left and bottom right

corners. Setup calibration was performed with two sets of beads with distant emission values in both channels: PMT gain was tuned until both fluorescence values were within the established specs for the two sets.

Two years later, the number of codes was pushed to 100 by improvements of the detection platform, particularly spectral response of the detectors and spectral window of the filters. In 2008, the multiplexing capacity was improved further to 500 codes by adding a third fluorophore in the beads, excited by the same 633 nm laser.

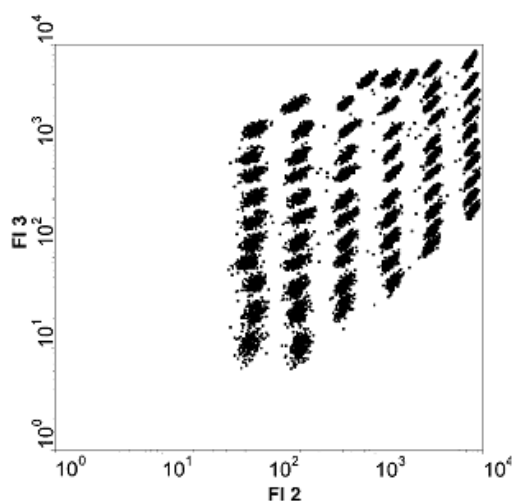


**Figure 4.1** 2D scatterplot of the FI 2 (orange) and FI 3 (red) fluorescence intensity values of a mixture of 64 different microsphere sets. 300 members of each set are displayed on average. Only single microspheres were analyzed. Only about 0.44% of the values do not fall within limits of one of the microsphere sets. Reprinted from [3].

The similarity of their optical system with our laser-induced fluorescence setups already gave us some indication of the important parameters to take into account [3]: (i) noise level; (ii) dynamic range (choice of detectors and filters); (iii) discrimination between levels (minimization of the standard deviation due to distribution of dye concentration in beads, low photon count or optical/electronic noise); (iv) resulting identification errors and (v) spectral crosstalk between coding dyes and from assay dye, implying the choice of appropriate filters).

Other bead-based systems have been introduced on microarrays by Parallel Synthesis [4]: this time, each bead contains a combination of 6 distinct rare earth fluorophores with very narrow emission bands. By varying the ratios of each dye, it is theoretically possible to generate ten billion ( $10^{10}$ ) distinct codes. However, it means that the same number of distinct beads must be fabricated, which is far from feasible.

Finally, a very interesting multiplexing approach was developed on the laboratory of Patrick Doyle at MIT and is now marketed by Firefly Bioworks [5]. It is based on 200  $\mu\text{m}$  gel particles generated by photopolymerization in microfluidic channels [6–8], as explained on **Figure 4.2**. The grid of 20 black or transparent squares generates  $2^{20}$  -more than a million- distinct values. Additional fluorophore and biological probes can also be integrated, so that these particles carry all necessary information for a biological assay.

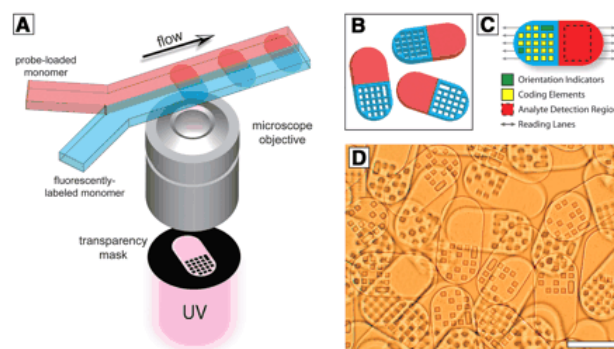


**Figure 4.2** Dot-coded gel microparticles. A) Schematic diagram of the polymerization across two adjacent laminar streams to make single-probe, half-fluorescent particles [shown in (B)]. (C) Diagrammatic representation of particle features for encoding and analyte detection. Encoding scheme shown allows the generation of  $2^{20}$  (1,048,576) unique codes. (D) Differential interference contrast (DIC) image of particles generated by using the scheme shown in (A). Scale bar indicates 100  $\mu\text{m}$ . Reproduced from [7].

Although promising, all these bead-based strategies present a major shortcoming for our application: the size of the materials restricts the miniaturization of channels and the attainable range of droplet sizes. Moreover, in the latter example, 2D readout severely limits throughput, which is about 50- to 1000-fold less than our droplets. That is why a specific approach thus has to be found to implement barcodes in droplet-based microfluidics.

#### 4.1.2 Droplet microfluidic assays using fluorescent barcodes

As described in Chapter 1, the compartmentalization of reagents, combined to many available modules, make droplet microfluidics an ideal tool to carry out an extensive number of biological assays. The high throughput of this technique allows either to significantly increase the number of populations tested at once (screening), or to run several assays in parallel (multiplexing), or a combination of both. This brings a new difficulty: the need to discriminate the different assays or components from each other during the assay readout.

In the last five years, several research teams have tackled this challenge by introducing fluorescent labels in their microfluidic assays. Cell-based assays were the first to benefit from this

additional level of parallelization, either by concurrently testing several cell populations [9] or several concentrations of a bioactive molecule [10], [11]. These studies relied on simultaneous tracking of fluorescence signal in two or three separate channels, so as to monitor three parameters at once: 1) encoded parameter, 2) result of the fluorescent assay and (optional) 3) presence or absence of a cell. One example is depicted on **Figure 4.3** [9]: several low-abundance surface receptors were concurrently analyzed on a line of human monocytic cells. A blue dye codes for receptor-specific antibodies, red quantum dots label cells (indicating their presence or not in each droplet), and a fluorescein-based substrate is used to monitor enzymatic activity.

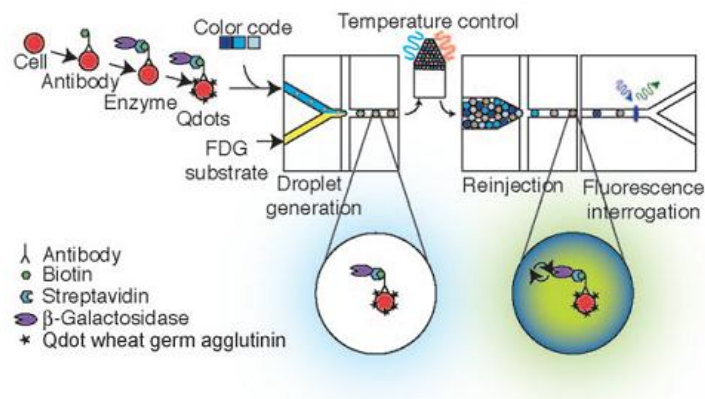


**Figure 4.3** Schematic depiction of the complete cell-marker detection assay. Cells were labelled for a specific cell-surface protein with an antibody-coupled enzyme, and a quantum dot wheat germ agglutinin stain for visualization. Cells were then encapsulated in droplets on the microfluidic chip with a sample-specific color code and a fluorogenic enzyme substrate. After incubation to let the signal develop, fluorescence of each droplet was analyzed. FDG=fluorescein-di- $\beta$ -D-galactopyranoside. Reprinted from [9].

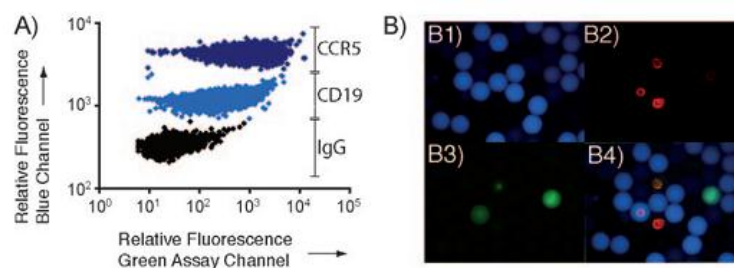


**Figure 4.4** Detection of cell surface markers. A) Scatter plot showing concurrently analyzed CCR5, CD19, and negative control samples; B) Corresponding colored microscope images acquired with three filter sets: B1) blue filter set showing the three Alexa405 color-coding concentrations, where the high concentration appears dark blue, medium concentration appears light blue, and very low concentration appears black; B2) red filter set showing the WGA-655Qdot cell label; B3) green filter set showing the fluorescein assay signal ; B4) images of (B1–3) overlaid to demonstrate that only the specifically labeled cells yield a fluorescein signal. Reprinted from [9].

After selection of droplets with a positive red signal, assay result on all 3 populations could be directly monitored by displaying the 2D scatterplot of green vs blue fluorescence signal (see **Figure 4.4**). The on-chip assay enabled much better discrimination of the 3 population than on a conventional flow cytometer.

Another type of assay, widely used in the pharmaceutical industry, consists in generating dose-response curves, as already introduced in Chapter 1. This common assay was recently transferred in droplet microfluidics format, using increasing concentrations of a certain dye to code for increasing concentrations of the tested molecule. These assays were carried out either on enzymes alone [12], [13] or on cells [10], [11]. Two examples of 2D fluorescence scatterplots directly showing the dose-response curve are given on **Figure 4.5**: in both cases, the barcode concentration levels are very distinct and encompass the same number of droplets. The system on the right is simpler than the other two cell-based assays cited above, because it does not use an additional dye to detect the presence or absence of cells. However, this missing piece of information has an impact on data quality (see the upper plot on **Figure 4.5 b**)), which can be detrimental for further data analysis, such as on-the-fly calculation of  $EC_{50}$ . In addition, the aforementioned assays label the different populations with only one color: depending on the tolerated overlap between code readout and reachable detection dynamic range, this can severely limit the possible number of populations studied, which makes screening of large populations impossible.

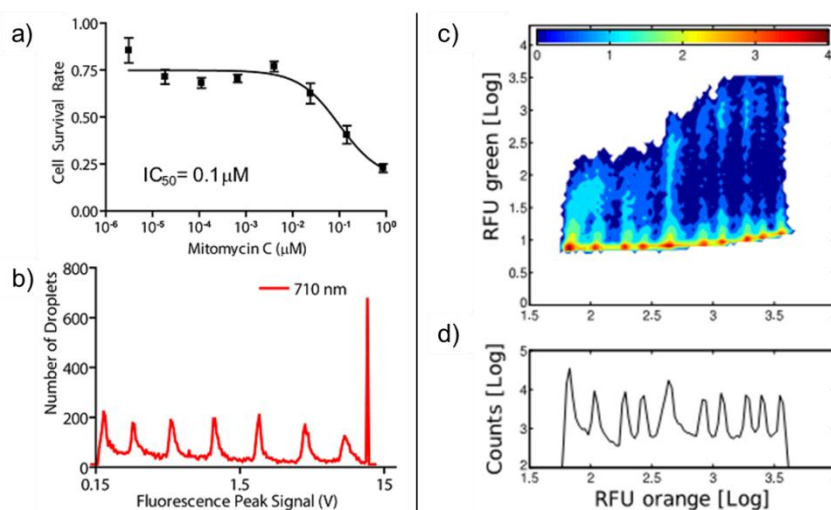


**Figure 4.5** Dose-response assays in encoded microfluidic droplets. a) Cytotoxicity curve of mitomycin C on human monocytic cells. To each drug concentration corresponds a fluorophore concentration in droplets. b) Histogram of the 8 droplet populations. Reprinted from [10]. c) 2D heat map of orange fluorescence (encoding agonist concentration) vs green fluorescence (proportional to the response of the cells). The upper population represents the concentration-dependent response of the cells. d) Histogram

of droplet count vs agonist concentration. The 10 droplet populations are clearly visible. Reprinted from [11].

This year, two-color multiplexing in droplets was first demonstrated for two genetic screening applications [14], [15]. In the first case, detection of an oncogenic mutation of the KRAS gene was demonstrated with great sensitivity: down to 1 mutation in 200,000 wild-type genes were detected. In this system, the fluorescent code was the assay dye itself: a green probe was used to identify the mutant sequence and a red one for the wild type sequence. The occurrence of each was simply determined by counting the number of green and red droplets, as pictured on **Figure 4.6 a)**.

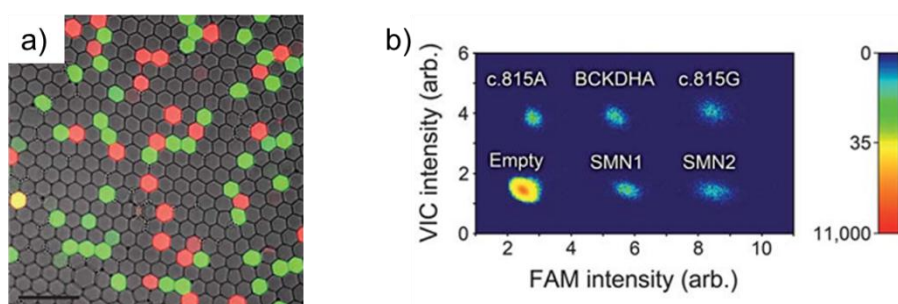


**Figure 4.6** Droplet assays encoded with two fluorophores. a) Detection of a rare DNA mutation. Red droplets contain wild-type DNA, green droplets contain mutant DNA, yellow droplets contain both, and non fluorescent droplets do not contain target DNA. The scale bar is 100  $\mu\text{m}$ . Reprinted from [14]. b) 5-Plex dPCR assay for spinal muscular atrophy encoded with two fluorophores. (a) 2D histogram of droplet fluorescence intensities. The six well resolved droplet populations corresponded to the five individual assays plus the empty droplets. Reprinted from [15].

This “1 target = 1 fluorophore” strategy, although allowing easy discrimination of populations, cannot be much extended while keeping a reasonable number of emission channels. To reach a greater number of possible codes, the next stage is to combine two fluorophores in various amounts for each population tested. Zhong et al. [15] designed a multiplexed assay for spinal muscular atrophy that successfully measured gene copy number across four different target genes and one reference gene (see **Figure 4.6 b)**). This first published result about multiplexed encoded digital PCR is a very motivating first step towards multi-color encoding of large libraries in droplets, and gives further justification to development of multidimensional optical labels. However, the combination of several colors with overlapping spectra raises the question of spectral crosstalk.



### 4.1.3 Spectral crosstalk and compensation

One of the major issues for simultaneously detecting multi-fluorescent signals in several channels comes from the overlap between the individual absorption and emission spectra of each fluorophore: this phenomenon is called ‘spectral crosstalk’ [16]. It is illustrated on **Figure 4.7** in the case of two fluorophores (fluorescein and rhodamine B), two lasers (488 nm and 561 nm) and two detection bands.

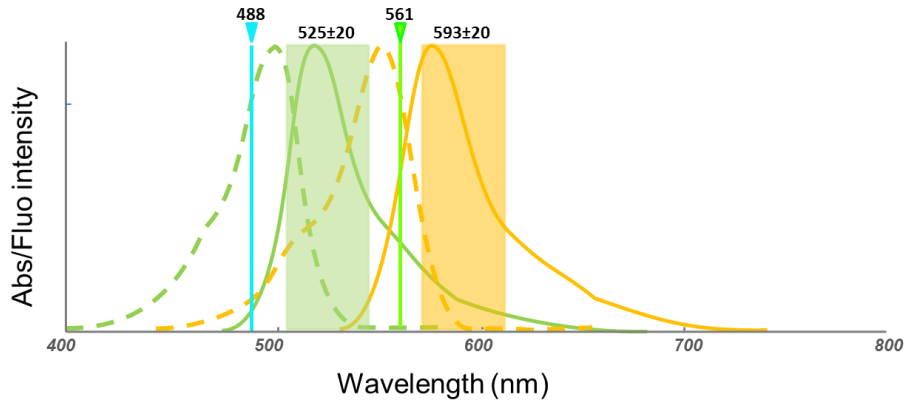


**Figure 4.7** Spectral crosstalk between fluorescein and rhodamine B. Green curves are FITC spectra, Yellow curves are RhBITC spectra. Dotted curves are absorption spectra and full ones are emission spectra. Spectral characteristics of detection setup with two lasers, and two detection channels are indicated. The emission spectrum of FITC is detected on both green and yellow channels.

If only the blue laser is turned on, it excites not only fluorescein, but also crosses the absorption spectrum of rhodamine B, causing it to consequently emit some ‘parasite’ fluorescence. The signal detected by the green channel thus consists of fluorescein emission, but also in a minor way of rhodamine B spillover signal. The yellow channel, which should not detect anything in this situation, gets spillover signal from the tail of fluorescein emission spectrum, as well as signal from slightly excited RhBITC. If now the green laser is switched on as well, the signal in the green channel will mainly consist of FITC fluorescence, but also of the aforementioned parasite signal from the left part of Rhodamine B emission spectrum. Therefore, the signal detected in each channel is not proportional to the corresponding dye intensity, but instead to a linear combination of the fluorescence intensity of each fluorophore alone, plus the channel noise. This can be described by a  $2 \times 2$  matrix [17]:

$$\begin{pmatrix} I_1 \\ I_2 \end{pmatrix} = \begin{pmatrix} 1 & \alpha_2 \\ \beta_1 & 1 \end{pmatrix} \begin{pmatrix} I_1^0 \\ I_2^0 \end{pmatrix} + \begin{pmatrix} n_1^0 \\ n_2^0 \end{pmatrix} \quad (4.1)$$

Or, in other terms:  $Y = CX + N$ , where  $N$  is the noise vector,  $X$  is the vector of true fluorophore intensities,  $C$  is the crosstalk matrix and  $Y$  is the vector of detected fluorescence intensities.

In the case of three fluorophores with overlapping spectra (as will be discussed later), a similar principle applies, leading to a 3x3 matrix:

$$\begin{pmatrix} I_1 \\ I_2 \\ I_3 \end{pmatrix} = \begin{pmatrix} 1 & \alpha_2 & \alpha_3 \\ \beta_1 & 1 & \beta_3 \\ \gamma_1 & \gamma_2 & 1 \end{pmatrix} \begin{pmatrix} I_1^0 \\ I_2^0 \\ I_3^0 \end{pmatrix} + \begin{pmatrix} n_1^0 \\ n_2^0 \\ n_3^0 \end{pmatrix} \quad (4.2)$$

This phenomenon is very problematic in flow cytometry because concentration of various dyes in cells is unknown a priori: to measure it, the signal in each channel must be proportional to the concentration of each dye. In our case, crosstalk is a problem because it can lead to overlaps between labels that would otherwise be well separated: in this case, code identification is jeopardized. To avoid that, codes must be spaced out more, which restricts the multiplexing capacity. Moreover, to detect the code, the most straightforward solution is to map the 2- or 3D scatterplot with a orthogonal grid such as there is only one code in each square or box. If there is crosstalk, the identification algorithm must be more complex. That is why we investigated possible strategies to offset crosstalk.

In the last 30 years, researchers in flow cytometry have studied this phenomenon in great depth, formulating proposals to overcome or compensate it [17–19]. In 1977, a pioneering work by Loken et al [17] presented fundamentals of this phenomenon and ways to correct it electronically by manual adjustment of an electronic cross coupling device. Practically, this compensation consisted in manually orthogonalizing the two lines defining each single color trace in the 2D scatterplot (as depicted on **Figure 4.8**), which mathematically translates into finding the invert matrix  $D$  and multiplying it to vector  $Y$  to get vector  $Y' = X$ :

$$Y' = DY = D(CX + N) = X \quad (4.3)$$

In the case where  $N_i \ll C_{ij}X_j$ , this can be simplified as:

$$Y' = DY = DCX = X \quad (4.4)$$

$$D = C^{-1} \quad (4.5)$$

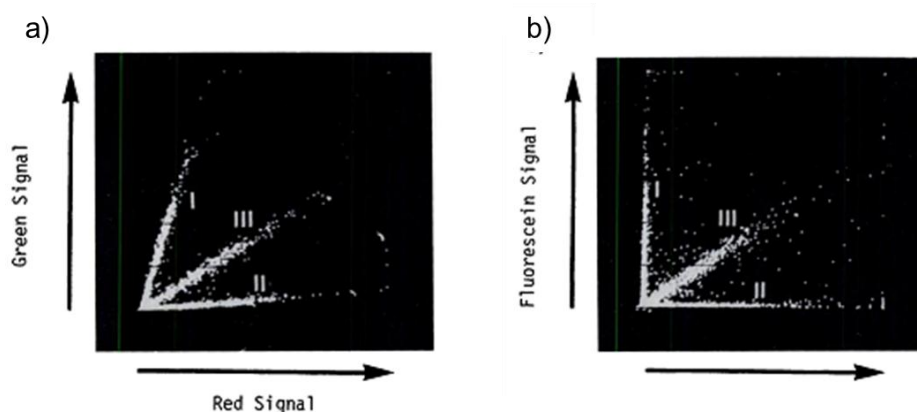


**Figure 4.8** Correction of fluorescent crosstalk on a FACS machine. 2D fluorescence scatterplots of red and green signal of cells labeled 3 different ways. Group I cells were stained with fluorescein; Group II cells were stained with rhodamine; Group III cells were labeled with both fluorescein and rhodamine. Reprinted from [17].

As flow cytometers gained in complexity, the number of lasers and detection channels increased. For  $N$  barcoding dimensions, there are  $N^2 - N$  parameters to adjust to compensate crosstalk: for more than three colors, it becomes nearly impossible to do hardware compensation manually; besides, the addition of more hardware increases overall noise [16]. A more systematic approach had to be implemented. The improvement in computing power opened the field of software compensation, relying in the calculation and inversion of the  $N \times N$  crosstalk matrix after recording the signal in each channel of each color ran separately [18]. However, this calibration-based requires frequent updates if PMT gain needs to be changed.

To speed up the process and spare the calibration steps with each separate color, Choi et al [20] proposed a method to calculate compensation matrix, without prior calibration with single stained samples, but directly from a combinatorially stained specimen.

All these findings led us to explore two crosstalk compensation strategies: (i) Visual estimation of the crosstalk matrix coefficients; (ii) Automated orthogonalization of the 2- or 3D scatterplot.

#### 4.1.4 Goal of this chapter

The first goal of our study was to identify the important parameters to consider when implementing a fluorescent code in droplets. Then, after exploring some of them, we created codes fabricated in two or three colors with our fluorescent silica nanoparticles and evaluated their quality. Subsequently, we introduced several ways to offset fluorescence crosstalk as well as

two methods for barcode identification. Finally, we investigated perspectives to implement these labels in several very different applications.

## 4.2 Preliminary considerations

Since our system is quite complex and involves multiple steps for the preparation of the barcode library, its readout and subsequent data analysis, we needed to define guidelines for each step of the process, especially which parameters can be optimized to improve the final quality of the code.

### 4.2.1 Choice of optical setup

For our barcode fluorescence detection, we chose to excite our fluorophores with lasers, for the reasons mentioned in section 1.3.2 of Chapter 1. We used one separate laser to excite each fluorophore, choosing respective wavelengths close the absorption maxima of each dye in order to excite all of them optimally. To focus the laser and enable magnified observation of the channels, we mounted a microscope objective on the path between the laser and the chip. To clean up excitation signal as well as to detect a narrow emission window for each fluorophore, we used appropriate filters and dichroic beamsplitters, intercalated by mirrors for easier alignment and setup compactness. The signal was detected by photomultiplier tubes, which offer remarkable sensitivity even at low photon counts, broad dynamic range of  $10^5$  and adjustable gain [21]. For our study, we used two different optical setups: one with two lasers, called “PLS3” station, and one with 3 lasers, called “dScreen” station. Full descriptions of their characteristics are in section 4.8.5 and the setup schemes are sketched in Appendix C.

### 4.2.2 Determination of optimal SNP concentration range

A prerequisite before preparing library samples is to determine which range of concentrations each color will cover. With this objective in mind, several constraints of the system have to be considered, as sketched on **Figure 4.9**.

First, the osmotic effects presented in the previous chapter have to be limited or neutralized. To keep the code stable in time, no water must exchange between droplets: as highlighted in the previous chapter, it would compromise emulsion monodispersity and above all, modify individual fluorophore concentration, leading to code degradation in the long run. If the SNPs are diluted by buffer alone, this effect has more or less importance depending on the ionic strength of the buffer compared to the chemical potential of the SNPs. Osmotic effect can be completely offset

by diluting the fluorescent SNPs by a solution of non-fluorescent SNPs at the same concentration in the same buffer: thereby, osmotic pressure will be equal in all droplets.

Second, the concentration range chosen for the particles should preferably be within their linearity range. In terms of upper concentration, it much be chosen below the concentration at which scattering or quenching start to occur. Moreover, at set gain values, the chosen maximal concentration of SNP should not give a signal higher than the saturation level of the PMTs. If the PMTs are nonlinear above a certain voltage, it is preferable to operate below this value, within their linearity range.

Third, as far as the lower concentration goes, the limit is set by the minimal acceptable signal to noise ratio at the chosen PMT gain value. As studied in Chapter 2, fluorophores are brighter in silica than in free state, so in a given optical setup, fluorescent SNP are theoretically detectable at a higher dilution level than when the dye is free in buffer.

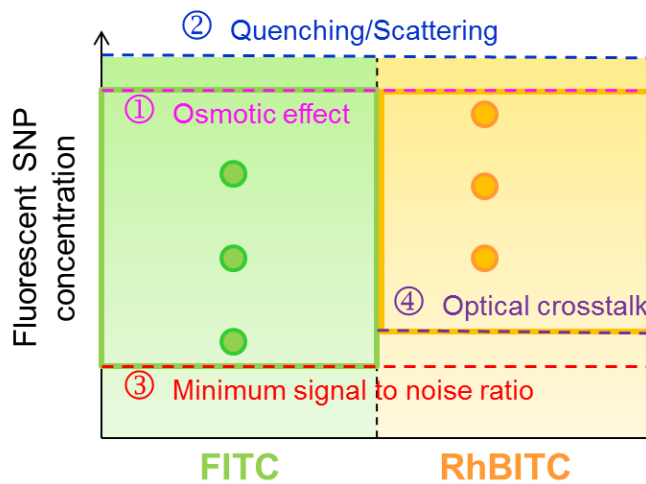


**Figure 4.9** Criteria to consider to choose each fluorophore concentration range. Here the example of FITC and RhBITC is taken. Criteria are the same for both dyes except the “optical crosstalk” criterion which requires higher minimal concentrations of RhBITC, to compensate crosstalk thus get better separation between codes.

Fourth and last, since the multiple dyes present have overlapping emission spectra, crosstalk should preferably be minimized. One situation enables this by dilution: when the spectra of dyes 1 and 2 have their spectra sufficiently spaced so that only fluorescence of dye 1 perceptibly spills into channel 2, but very little the other way round (in other words, when  $\alpha_2 \ll \beta_1$  in equation (4.1) or more generally, when matrix coefficients  $\alpha_{ij} \ll \alpha_{ji}$  for  $i < j$ ). This is for example the case in the example presented on **Figure 4.7** (where dye 1 is FITC and dye 2 is RhBITC). In this case,

fluorescent SNP concentration can be adjusted, so that the SNPs including RhBITC are used at a higher minimal concentration than SNPs including FITC. As a result, even when the upper concentration of FITC SNP is combined to the lower concentration of RhBITC SNP, the fluorescence of the former in the yellow channel will not screen the emission of the latter. An example is given by **Figure 4.10** with arbitrary values  $\alpha_1 = 0$ ,  $\beta_2 = 0.4$  and three concentration values of each color, each spaced from the other by a factor  $\sqrt{10}$ . On the right plot, the concentration range of RhBITC is 10 times higher than on the left plot: as a result, the spacing between codes is much more even than in the left plot because crosstalk is greatly reduced. However, restricting the concentration ranges in certain colors has a big impact on the reachable number of fluorescence levels in this dimension.

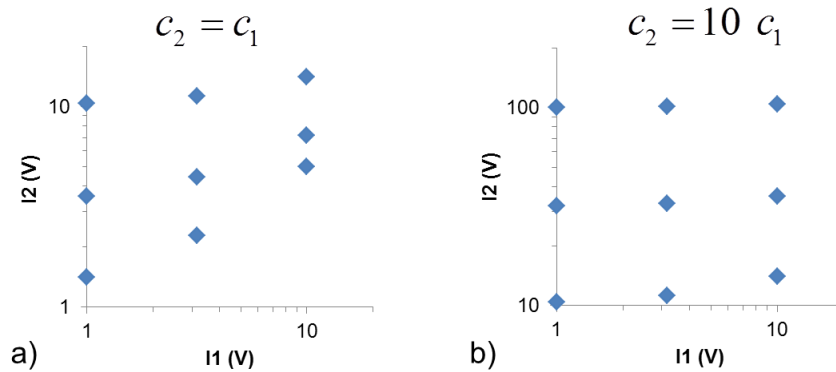


**Figure 4.10** Influence of relative concentration of two dyes with overlapping spectra on observed crosstalk. a) When the same concentration range is used for both dyes, strong crosstalk takes places and barcodes get close to each other (scatterplot scale in log-log). b) When the dye with higher emission wavelength is used at a higher concentration range than the other one, crosstalk effect is reduced.

With these four conditions in mind, the next step is to determine the optimal spacing between levels, depending on the tolerated overlap between populations.

### 4.2.3 Code spacing and standard deviation vs tolerance for overlap

As illustrated by droplet distributions plotted on **Figure 4.5**, each barcode level is not defined by a single point on the scatterplot, but rather by a distribution of intensities in each color, that can be roughly approximated by a lognormal distribution (or a normal -also called Gaussian-distribution in log scale). This spread from a infinitely narrow plug has several sources with regards to droplet library generation, as developed in 4.2.4. The more overlap there is, the more probable it is to wrongly attribute a detected signal to a given code. Depending on the assay, there is more or less tolerance for errors in code readout. It is thus necessary to estimate the

standard deviation in signal for each barcode level, then calculate the necessary spacing between them depending on the tolerated percentage of error.

For a normal distribution of mean  $\mu$  and standard deviation  $\sigma$ , the probability density function for a log (intensity) value  $x$  is a bell-shaped function (see **Figure 4.11**) defined as [22]:

$$f(x) = \frac{1}{\sigma\sqrt{2\pi}} e^{-\frac{(x-\mu)^2}{2\sigma^2}} \quad (4.6)$$

Two populations of same standard deviation  $\sigma$  and respective average log intensities  $\mu_1$  and  $\mu_2$  intersect at  $x = \frac{\mu_1 + \mu_2}{2}$ . The percentage of overlap between them is equal to [22]:

$$\%Overlap = 1 - \operatorname{erf}\left(\frac{\mu_2 - \mu_1}{\sigma\sqrt{2}}\right) = 1 - \operatorname{erf}\left(\frac{\Delta\mu}{2\sigma\sqrt{2}}\right) \quad (4.7)$$

We reported a few values of  $\frac{\Delta\mu}{\sigma}$  and  $\%Overlap$  in **Table 4.1**:

$\frac{\Delta\mu}{\sigma}$	1	2	3	4	5	6
$\%Overlap$	61.7	31.7	14.3	4.5	1.3	0.3

**Table 4.1** Sample values of the codes spacing/standard deviation ratio, and the corresponding percentage of overlap between two code levels.

As the table indicates, modulating the distance between code levels in each dimension has great impact on the overlap between distributions. So, to reduce it, either spacing must be increased, or standard deviation must be reduced. An example of this concept is given on **Figure 4.11**.

#### 4.2.4 Minimization of standard deviation of distributions

As introduced in the previous paragraph, optimizing the protocol for droplet library generation is crucial to reduce dispersion of each barcode level. In the process, three events can generate spreading of the distributions: (i) cross-contamination between successive plugs in the

suction needle or on chip, (ii) Taylor-Aris dispersion in aqueous inlet channel [23], [24] or (iii) small variations in droplet sizes at generation. We examined ways to reduce their occurrence.

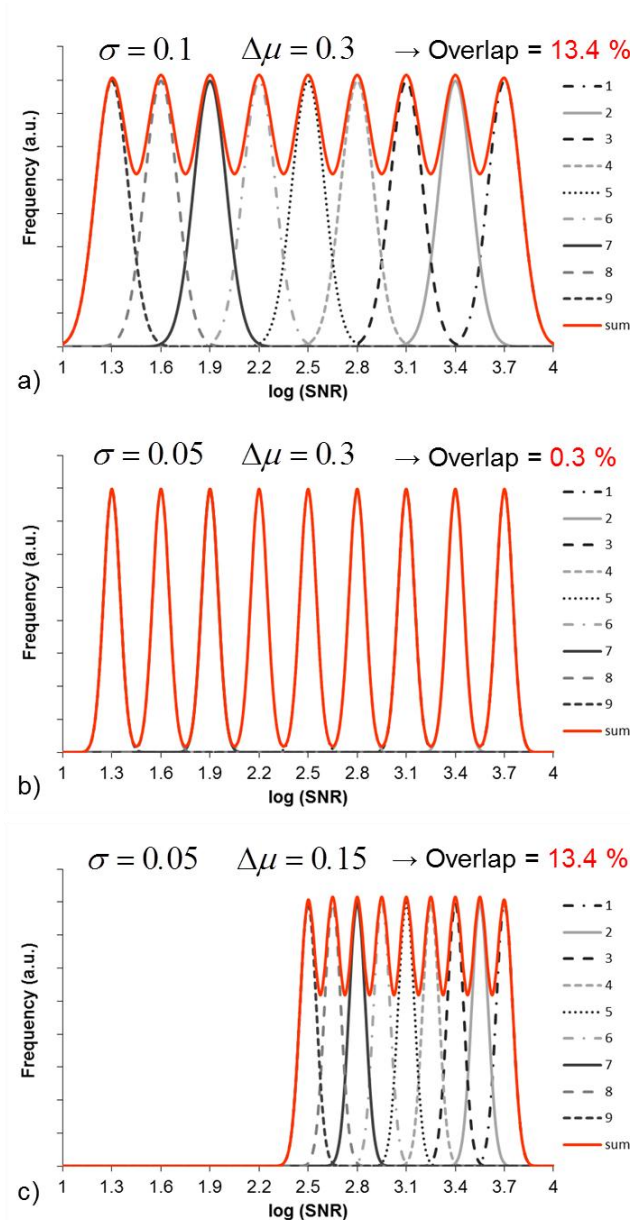


**Figure 4.11** Influence of standard deviation and spacing of codes on resolution. In all cases there are  $N=9$  codes on a 3-log dynamic range. On the log scale, droplet populations of each type are modeled as Gaussian distributions. a) and c) If spacing between levels  $\Delta\mu$  is only 3-fold the standard deviation  $\sigma$ , codes will have about 13.4 % overlap and will be badly resolved. By decreasing both values, more codes will be fit inside the 3-log dynamic range. b) If  $\Delta\mu$  is increased to  $6\sigma$ , then the overlap between populations drastically drops to 0.3 % and codes are extremely well resolved.



Regarding the first aspect, great care has to be taken to use a non-sticking material for the needle: widely used in connectors for chromatography, PEEK tubing shows good performances for this regard. Moreover, the suction needle of the autosampler must be rinsed after loading of each library member into the chip: to do so, two washing steps followed by injection of oil to push rinsing water out were introduced into the automatic routine, as detailed in section 4.8.4. As far as the chip is concerned, channel functionalization with fluorosilane, as introduced in Chapter 1 and described in section 4.8.2, was the solution of choice to reduce undesired sticking. To remove aqueous residues in the aqueous inlet channel after the loading of each code, fluorinated oil with 2 wt% EA surfactant was slowly circulated backwards during needle washing steps. Finally, in case some residues still remained in the needle in spite of precautions taken, we chose to load the fluorescent codes from the most diluted to the most concentrated as specified in the same section.

Concerning Taylor dispersion, since the needle and chip are filled with fluorinated oil before reloading of a new sample, there should not be any dispersion effect since each plug is the only aqueous species in presence at once. Anyway, we can only apply Taylor–Aris theory on the channel at long time scales  $\tau \gg \frac{w^2}{D}$ , or after a downstream distance  $L \gg Pe.w$  [25]. Here  $w$  is the channel width,  $Pe$  the Péclet number defined in Chapter 1,  $D_{SNP}$  the diffusion constant of silica particles and  $L$  the characteristic channel length.

In the case of PEGylated nanoparticles in diluted aqueous buffer,  $r_{SNP} = 3.2$  nm and  $\eta = 10^{-3}$  Pa.s, which leads to  $D_{SNP} = 6.71 \times 10^{-11}$  m<sup>2</sup>/s using Stokes-Einstein equation mentioned in the previous chapter.

The channel dimensions of the aqueous inlet of the LRS 6.6 chip (see design on Appendix B) used for droplet library generation are  $L = 2.00$  cm,  $w = 120$   $\mu$ m,  $w = 20$   $\mu$ m and the flow rate is  $Q_{aq} = 150$   $\mu$ L/h, which leads to a fluid average velocity  $U = 1.73 \times 10^{-2}$  m/s and a Péclet number  $Pe = 5.18 \times 10^6$ . Consequently we have  $Pe.w = 622$ , which is much larger than  $L$ : there is no Taylor dispersion in our case.

#### 4.2.5 Calibration of PMT's gain vs SNP concentration

Our first experiment aimed to determine the optimal PMT gain for each channel, and the corresponding optimal concentration range of SNP, to cover the widest possible dynamic range in all colors. We did a thorough investigation in the 2-color case (FITC and RhBITC) on station “PLS 3”: we measured PMT voltage for 3 orders of magnitude of SNP concentration (each

measured separately) and for the whole possible range of PMT gain values (from SNR=5 to PMT saturation). The results are gathered on **Figure 4.12**.

These two plots show that PMT output voltage of both PMTs follows a power law, as expected from the manufacturer's specifications. In the case of green PMT, the coefficient is close to the manufacturer's specifications ( $\approx 7.1$ ) [21], but for the other PMT, the coefficient is smaller, maybe because of a different sensitivity in the yellow wavelength window. In both cases, the coefficient remains quite constant for all fluorophore concentrations.

From this calibration, we determined the three optimal gain values by plotting the intensity ratios  $\frac{I_{2.5\text{wt}\%}}{I_{0.25\text{wt}\%}}$  and  $\frac{I_{0.25\text{wt}\%}}{I_{0.025\text{wt}\%}}$  for each fluorophore and PMT gain value (when these ratios existed), as shown on **Figure 4.13**. The concentrations ratios being 10 in both cases, the best gain value is the one at which the two ratios mentioned above are both as close to 10 as possible.

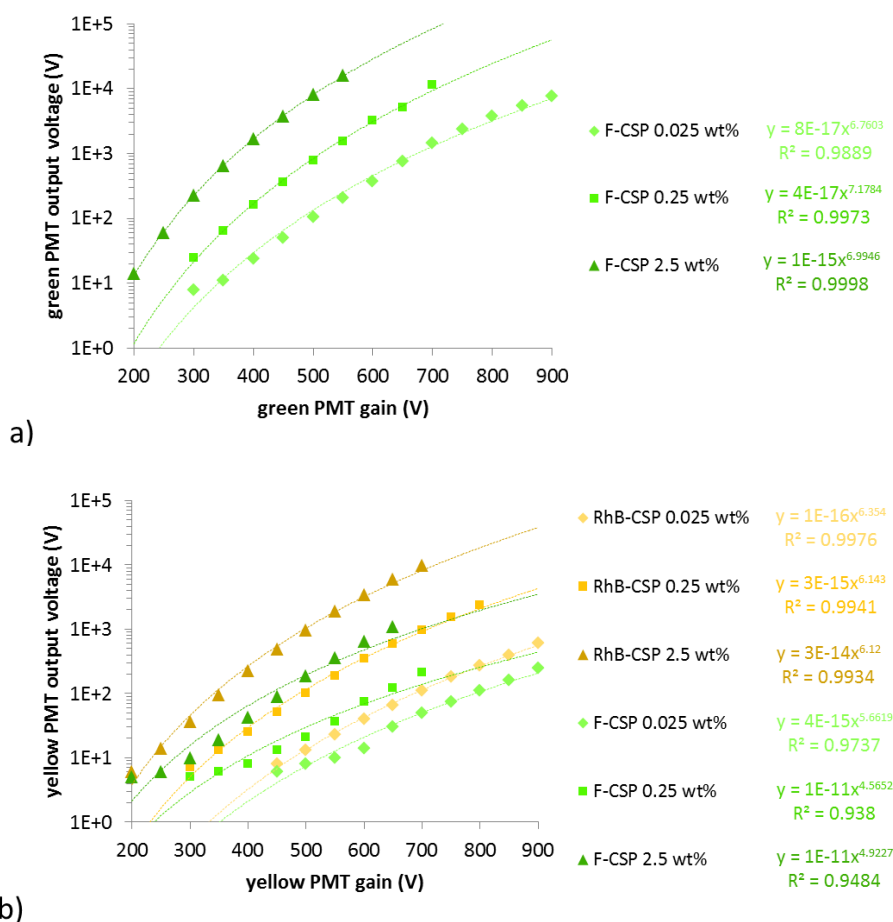


**Figure 4.12** Calibration of the two PMTs of PLS3 station with FITC and RhBITC-loaded core-shell-PEG21 SNPs. a) green emission channel, b) yellow emission channel. The weight percentage indicated is the one of fluorescent SNPs.

As outlined on the figure, for the green PMT, the three optimal gain values are 450 V, 500 V and 550 V (500 V being the best), and for the yellow PMT, they are 600 V, 650 V and 700 V (650 V being the best). We selected these optimal values for detection of our barcodes and selected 0.025 wt% and 2.5 wt% as our respective highest and lowest concentrations.

Another element we noticed is that for all gain values, the ratio for the two highest concentrations was always closer to 10 than for the two lowest. This is because in the case of CSP 0.025 wt%, the signal to noise ratio is quite low, so noise artificially increases the readout value, thus decreasing the ratio  $\frac{I_{0.25\text{wt}\%}}{I_{0.025\text{wt}\%}}$ . Since our concentration working range is already only 100, we decided to not restrict it further to offset this phenomenon, but just to take it into consideration for further data analysis and barcode detection.

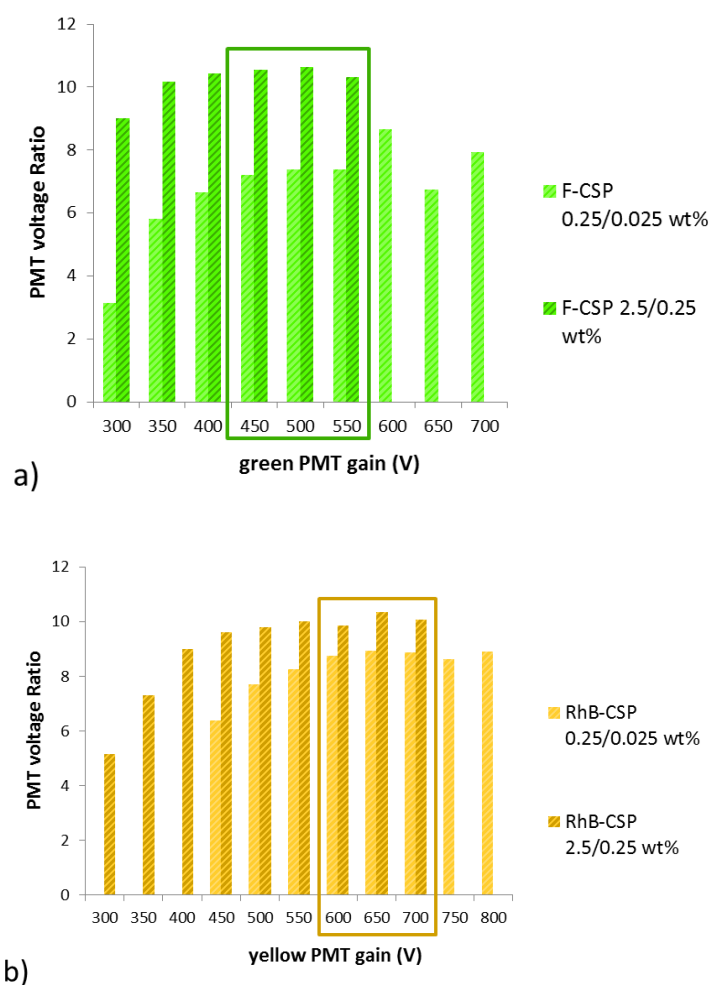


**Figure 4.13** Determination of the optimal PMT gains for SNP detection in both channels. a) Green channel PMT. b) Yellow channel PMT. Boxes indicate the three gain values giving both ratios as close as possible to 10.

After optimizing some essential parameters of the code in terms of library preparation and adjustment of optical setup, we generated two fluorescently encoded libraries with our SNPs: one with two colors FITC and RhBITC (overlapping spectra) and one with three (FITC, RhBITC and Dylight 680-NHS), following the protocols described in sections 4.8.3 to 4.8.6.

## 4.3 Two- and three-dimensional fluorescent codes

### 4.3.1 Two colors (F-SNP and RhB-SNP)

For our first two-color barcode, we decided to pair two fluorophores with emission spectra significantly overlapping, to examine the effects of major crosstalk on barcode resolution. We chose to aim for a 25-member library, which, given our dynamic range, led us to choose a dilution factor of 2 between each level of the same color. We recorded green and yellow fluorescence signal of droplets in PLS3 station. The resulting 2D heat map is on **Figure 4.14**.

The first observation we make is that the number of clusters matches the number of distinct barcodes injected on the library generation chip. However, it is striking that crosstalk between fluorophores significantly alters the “square-grid” shape the scatterplot would have in its absence: instead of all having the same yellow fluorescence intensity, the codes with identical low RhBITC concentration are not aligned but on a curve going upwards with increasing [FITC]. It is even so pronounced that it leads to fusion of three clusters into one. This means that during code identification, three distinct codes would be mistakenly read as the same, which is of course not acceptable. We will discuss in section 4.5 some strategies to solve this problem.

Except this crosstalk, the codes are quite well resolved from each other with no overlap, in spite of some small apparent dilution imprecisions. The expected dynamic range of 16 is well observed in both colors, with a ratio of a  $10^{1.15} = 14.1$  between the highest and lowest green levels and a ratio of a  $10^{1.2} = 15.9$  between the highest and lowest yellow levels. However, if projection of the 2D plot in each channel is drawn, the two resulting histograms do not show 5 identical populations. This lack of overlap between levels is mainly due to crosstalk, and in a minor way to dilution errors. Consequently, in this case, barcode identification by binning each fluorescence detection channel is not possible. Nevertheless, we calculated the standard deviation of the population with the lowest green intensity (for which the five corresponding codes are well aligned): we found the value  $\sigma = 0.024$ . In the same manner we calculated the standard deviation of the population with the second highest yellow intensity and found the value  $\sigma = 0.026$ . We can later use these standard deviation values to calculate the maximal possible spacing between

fluorescence levels of each color for a certain tolerated overlapping level, as explained in section 4.2.3.

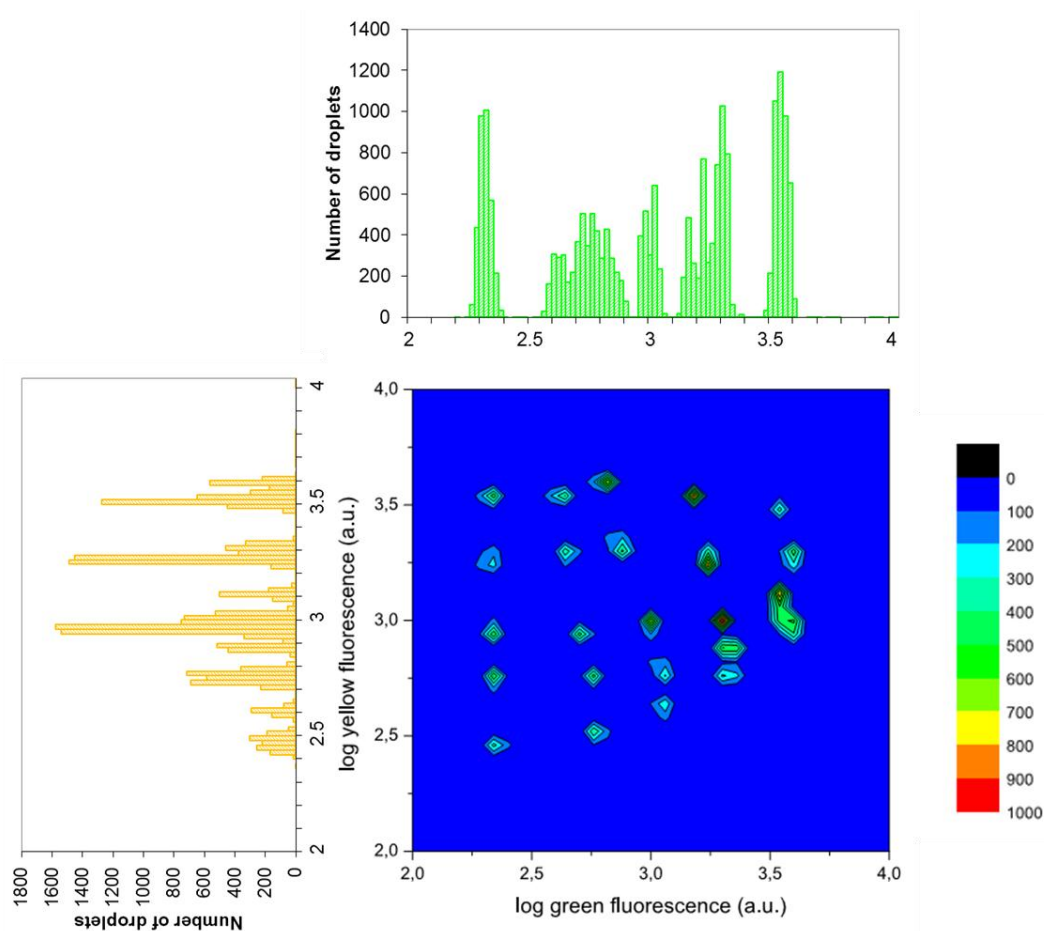


**Figure 4.14** Two-color, 25-member fluorescently encoded library. 20,000 droplets are displayed here. 2D heat map of log (green fluorescence) vs. log (yellow fluorescence) and corresponding fluorescence distributions in each channel.

### 4.3.2 Three colors (F-SNP, RhB-SNP and Dylight 680-SNP)

The second fluorescent multiplexed code we fabricated combined all three colors of SNPs characterized in Chapter 2, in order to generate a 3-dimensional barcode. With the prior results on 2-color codes, this seemed very achievable. To minimize the risk of crosstalk, get comfortable space between barcode levels and to generate an emulsion in a reasonable time (about 4 hours), we opted for a 3x3x3 member library, with a factor of about 3 between two fluorescence levels in each color. We used the dScreen station, whose setup is described on Appendix C, to detect these codes on three fluorescence channels. **Figure 4.15** shows an example of fluorescence timeline in the 3 channels during library reinjection and the code value in each droplet, and **Figure 4.16** the

resulting 3D scatterplot, its projection on three contour plots and the fluorescence intensity histogram for each channel.

The ratios between maximum and minimal code intensities in each channel are  $10^{0.9}=7.9$  for the green and IR channels and  $10^{0.82}=6.6$  for the yellow channel. In all three channels, ratio values are lower than the expected value of 10, because the lowest level signal is close to the noise in all channels as seen on the timeline. Ratio in the yellow channel is lower than the others for two reasons: first, because to detect droplets at a high enough level, we had to bring the PMT gain up, getting closer to saturation level and out of the linearity range. Second, because crosstalk signal from FITC-SNP in the yellow channel brings the background signal up compared to signal without crosstalk.

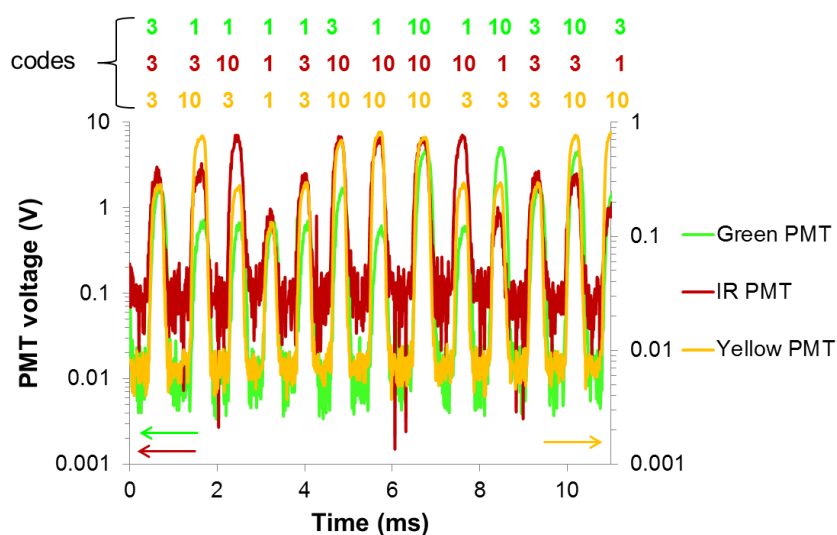


**Figure 4.15** Fluorescence timeline of reinjected library in green, yellow and red channels. The left Y axis is for green and infrared PMTs whereas the right one is for the yellow PMT. As droplets pass by in the microfluidic channel, fluorescence detected by each PMT increases then decreases. In this case, maximal signal-to-noise ratios are 3 orders of magnitude in the green emission channel, 2.7 for the yellow one and 2 for the IR one.

This crosstalk effect is also observed on the yellow-red 2D contour plot: on the first cluster column, a slight cluster splitting is noticeable: there are 2 distinct levels of low yellow fluorescence. Crosstalk of RhBITC on IR channel is also noticeable on **Figure 4.16 b**). To merge these clusters again and give the 3D scatterplot a more cubic shape, post-processing can be done as explained in the next section.

Statistical analysis of the three fluorescence histograms gives us minimal standard deviations of 0.024, 0.020 and 0.026 for green, yellow and red channels respectively. These values are close to the ones obtained for two colors: addition of a third dimension does not apparently affect

#### 4. Fluorescently encoded droplet libraries

dispersion. For an interval of 0.5 (in log scale) between two consecutive levels, it means that the theoretical percentage of overlap between levels is:

$$\%Overlap = 1 - \operatorname{erf}\left(\frac{\frac{0.5}{2}}{0.025\sqrt{2}}\right) \rightarrow 0 \quad (4.8)$$

Of course in reality, as the 3D scatterplot shows, there are some droplets with a fluorescence signal in between the groups of points. Such unwanted intermediates can be filtered further by selecting droplets only within a narrow size window, to rule out accidentally coalesced or split droplets.

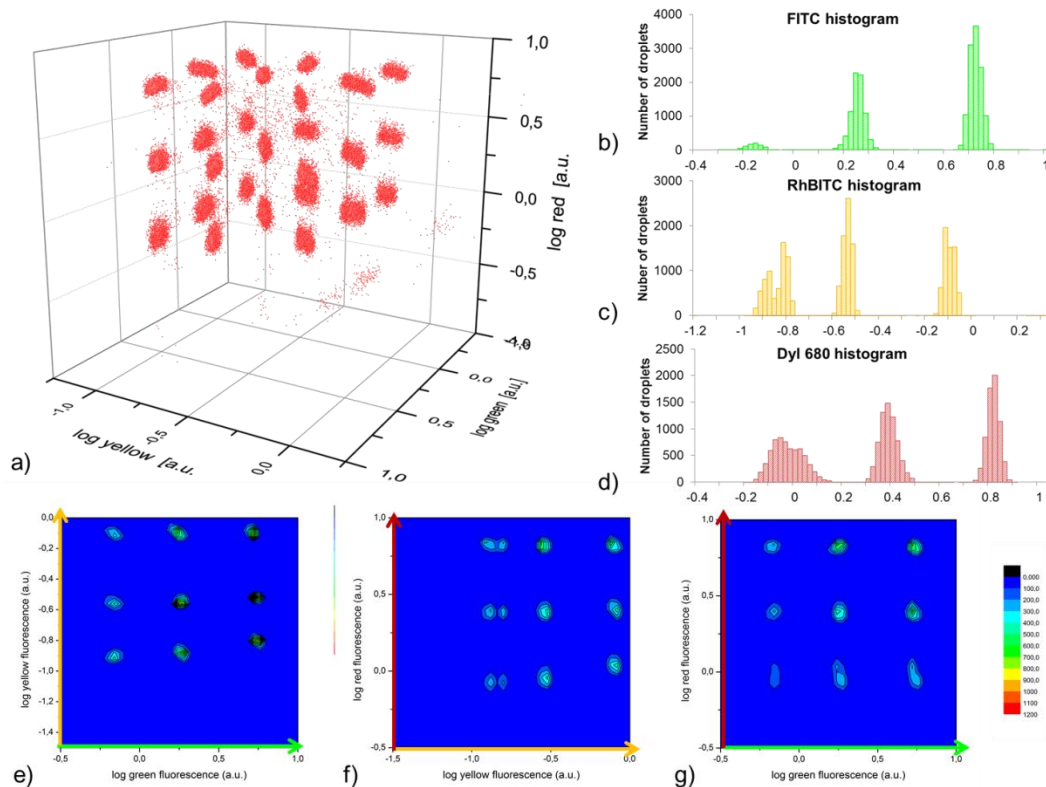


**Figure 4.16** Three-color, 27-member fluorescently encoded library. 20,000 droplets are displayed here. a) 3D scatterplot of log (green fluorescence)/log (yellow fluorescence)/log (infrared fluorescence). b) to d) Fluorescence distributions in each channel. e) to g) Projections of the 3D scatterplot on three 2D heat maps.

## 4.4 Spectral crosstalk reduction and compensation

Once our barcodes libraries were generated in droplets, we looked into several ways to reduce the crosstalk. We ruled out station calibration with reference fluorophores as described in 4.1.3 because it is very time consuming, and needs to be redone before each experiment depending on the PMT gains used. Instead, we first explored how to reduce crosstalk by optimizing the optical setup. Then, we applied the principles exposed in section 4.1.3 to explore several ways to offset the crosstalk still remaining.

### 4.4.1 Influence of optical setup

To assess the influence of optical setup on the crosstalk, we repeated the experiment of section 4.3.1 on the dScreen station, with only the 488 and 561 lasers turned on as well as green and yellow PMTs. The main difference between these two setups lies within the bandpass filters placed in front of the PMTs, as sketched on Figure 4.17 a) and b): on dScreen station, the filters have narrower bandwidths and the filter for the yellow channel is red-shifted compared to the other one. We compared both 2D contour plots obtained upon reinjection of the same emulsion (**Figure 4.17** c) and d)).

Two noticeable differences appear between these two plots: first, codes detected on dScreen station contour plot are much more homogeneously spaced and more aligned than when detected on PLS3: as we could expect from reduced overlapping area between filters bandwidth and FITC emission spectra, the optical crosstalk appears very reduced in the former case. This difference can be explained from the emission filters set up in each station. The yellow emission filter of “PLS3” station has a slightly lower wavelength and a larger bandwidth than the filter of “dScreen” station (fig X b)), allowing more signal from F-SNP fluorescence tail to be detected along with RhB-SNP signal: as far as crosstalk matrix coefficients goes, this means that  $\beta_1^{dScreen} < \beta_1^{PLS3}$ .

As far as green filters go, the one in PLS 3 station intercepts about as much of RhB-SNP fluorescence, which is very little and barely noticeable on both scatterplots: with the exception of small dilution errors, clusters corresponding to a constant F-SNP concentration are vertically aligned without tilt: the matrix coefficient  $\alpha_2$  tends towards 0.

Moreover, on the contour plots drawn from dScreen station, the number of droplets in each cluster reduces as fluorescence intensity in one or both channels gets lower, which is not observed on PLS3 station. This is because on the dScreen station, the trigger for droplet signal recording is set on only one of the two channels, instead of both channels on PLS3; the chance



of missing a droplet with both fluorescent signals lower than their respective channel threshold is much lower than missing a droplet with only the green signal under the green threshold value.

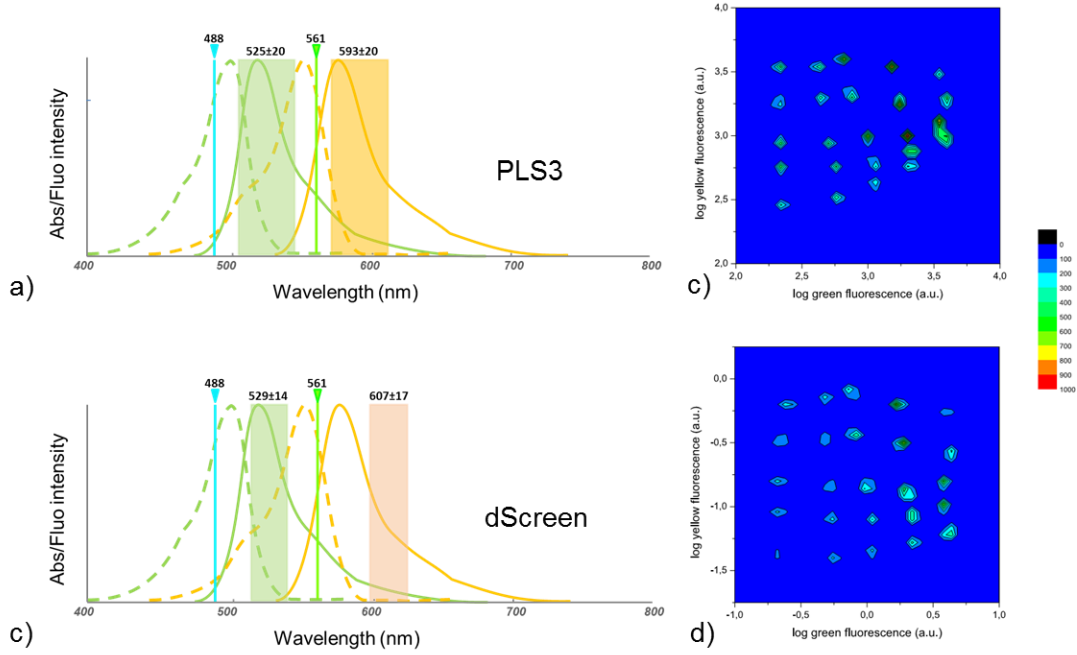


**Figure 4.17** Influence of optical setup spectral features on crosstalk. a) and c) Spectral diagrams positioning wavelengths of blue and green lasers as well as spectral width of bandpass filters positioned in front of PMTs. The absorption (dotted lines) and emission (full lines) spectra of FITC and RhBIC are superimposed. b) and d) 2D heat maps of log (green fluorescence) vs. log (yellow fluorescence) obtained for a 2-color, 25 member library in PLS3 and dScreen stations, respectively.

#### 4.4.2 “Quick and dirty” post-processing: visual adjustment

After examining the role of optical hardware, we investigated compensation methods during data post-processing. A first method we tried was to manually adjust the compensation matrix coefficients until the 2D contour plots looked “square” (a similar approach to the electronic compensation presented by Loken et al [17]). To do so, we used the method in section 4.1.3 and deduced the 2D scatterplot corresponding to the X vector of single fluorophore emission in each channel.

For the 2-color, 25 member libraries, the optimal values  $\alpha_2$  and  $\beta_1$  found for station dScreen are  $\alpha_2 = 0.05$  and  $\alpha_2 = 0.006$ . The corresponding corrected 2D scatterplots are on **Figure 4.18**. The corrected scatterplot is orthogonal, and the irregularities remaining are dilution errors during library preparation in plates.

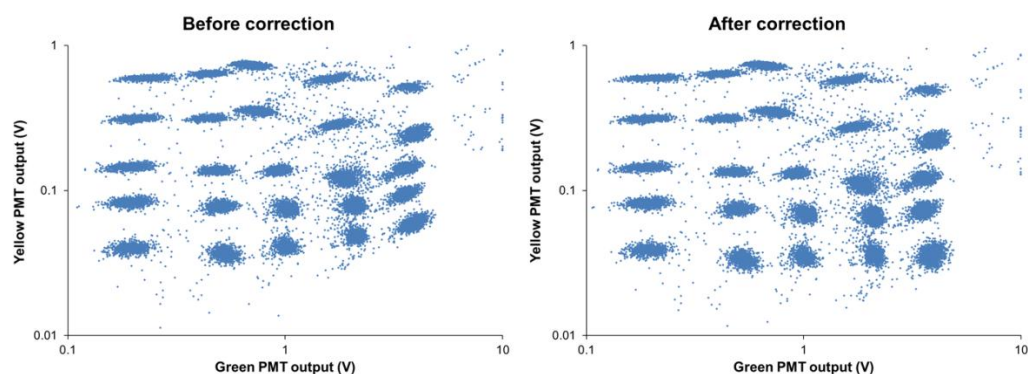


**Figure 4.18** Manual crosstalk matrix compensation on a 2-color fluorescent library. 2D scatterplots of green vs yellow PMT output on PLS3 station a) before correction and b) after correction.

In the 3-color barcode case, starting from a  $3 \times 3$  matrix with six coefficients to adjust seemed intimidating, but the problem could be actually much simplified. Considering the dyes spectra and station filters (see **Figure 4.19**), the backwards crosstalk from RhB-SNP to green and from D680-SNP to yellow and green channels can be neglected:  $\alpha_2$ ,  $\alpha_3$  and  $\beta_3 = 0$ . Moreover, the crosstalk from F-SNP to red is negligible as well:  $\gamma_1 = 0$ . It leaves only  $\beta_1$  and  $\gamma_2$  to figure out. Applying this method to the 3-color data presented above, in a matter of minutes we find:  $\beta_1 = 0.008$  and  $\gamma_2 = 0.4$ . The initial and corrected contour plots are on **Figure 4.20**. The scatterplots after correction are now all orthogonal, and the peak splitting in the yellow-red scatterplot has been eliminated.

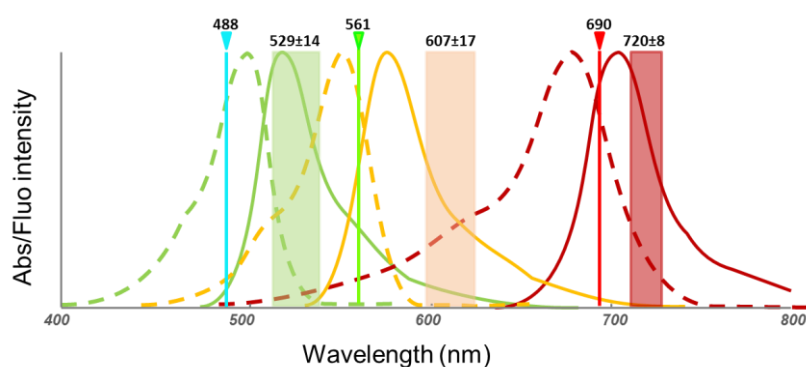


**Figure 4.19** Spectral diagrams positioning wavelengths of blue, green and infrared lasers as well as spectral width of bandpass filters positioned in front of the three PMTs. The absorption (dotted lines) and emission (full lines) spectra of SNP embedding FITC, RhBITC and Dylight 680-NHS are superimposed.

This method, although satisfactory, is neither elegant, nor useable for batch post processing of large numbers of files. That is why we tried an alternative method, where the crosstalk matrix is mathematically calculated from the coordinates of the corners of the scatterplot.

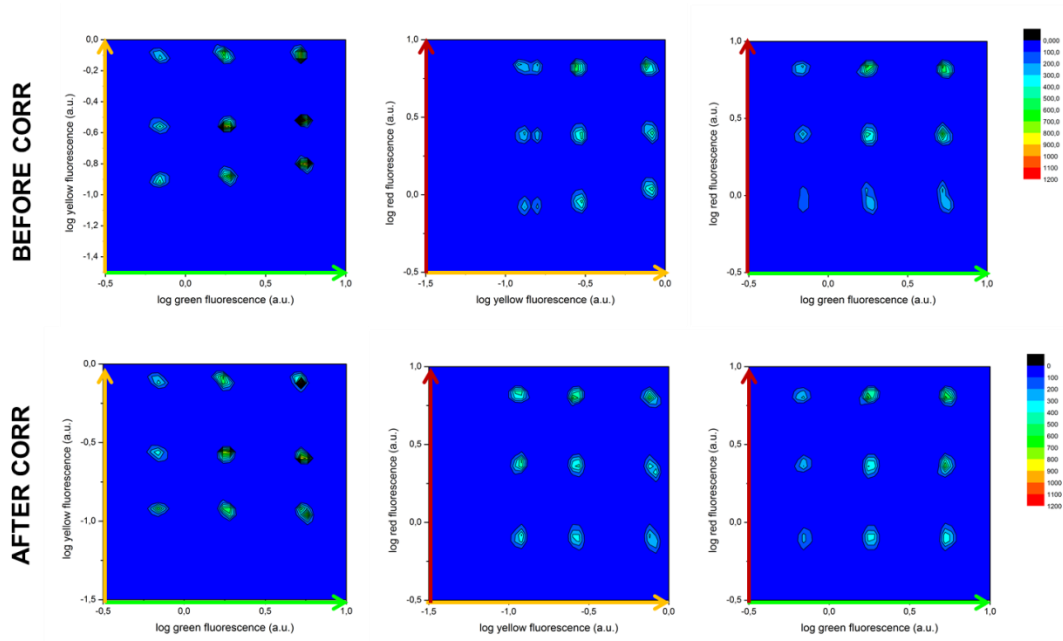


**Figure 4.20** Manual crosstalk matrix compensation on a 3-color fluorescent library. 3D scatterplot of log (green fluorescence)/log (yellow fluorescence)/log (infrared fluorescence before (top) and after (bottom) manual crosstalk matrix compensation.

### 4.4.3 Mathematical post-processing

In this final matrix calculation step, we investigated if we could automatically compute the crosstalk matrix coefficient from the coordinates of the populations in the scatterplot. We chose to test our method on two model situations close to our experimental systems:

- First, a  $5 \times 5$  2-color library with successive dilution ratios of 2 and a minimal intensity of 1. We arbitrarily chose the matrix C coefficients as:

$$C_{2D} = \begin{pmatrix} 1 & \alpha_2 \\ \beta_1 & 1 \end{pmatrix} = \begin{pmatrix} 1 & 0.1 \\ 0.4 & 1 \end{pmatrix} \quad (4.9)$$

- Second, a  $3 \times 3 \times 3$  library with dilution ratios of  $\sqrt{10}$  and a lowest intensity of 1 for all channels. We arbitrarily chose the matrix C coefficients as:

$$C_{3D} = \begin{pmatrix} 1 & \alpha_2 & \alpha_3 \\ \beta_1 & 1 & \beta_3 \\ \gamma_1 & \gamma_2 & 1 \end{pmatrix} = \begin{pmatrix} 1 & 0.1 & 0.02 \\ 0.4 & 1 & 0.1 \\ 0.02 & 0.1 & 1 \end{pmatrix} \quad (4.10)$$

The resulting scatterplots of signal after crosstalk are gathered in **Figure 4.21** and **Figure 4.22**: they are plotted on a linear scale, where they appear as diamond shape, stretched from their initial cubic shape when no crosstalk is applied. All the points corresponding to a single concentration level of one fluorophore are still aligned.

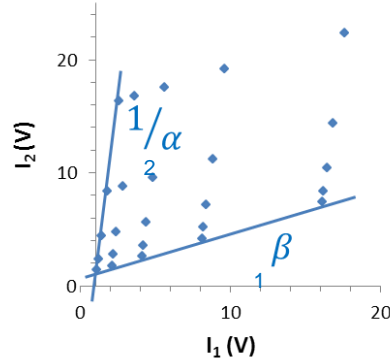


**Figure 4.21** Simulation of a  $5 \times 5$  2-color fluorescent code in the case of strong crosstalk between the two dyes. The slopes relate to crosstalk matrix coefficients  $\alpha_2$  and  $\beta_1$  (see equation 4.1).

In the 2-color case, the 2 slopes of these lines can be expressed as:

$$\text{slope}(AB) = \frac{I_2^B - I_2^A}{I_1^B - I_1^A} \quad (4.11)$$

where A and B are 2 points belonging to the same line. This, expressed with matrix coefficients, reads as:

$$\text{slope}(AB) = \frac{\beta_1 I_1^{0B} + I_2^{0B} - (\beta_1 I_1^{0A} + I_2^{0A})}{I_1^{0B} + \alpha_2 I_2^{0B} - (I_1^{0A} + \alpha_2 I_2^{0A})} \quad (4.12)$$

For the lines at constant (dye 1) concentration,  $I_1^{0B} = I_1^{0A}$  and  $\text{slope}(AB) = \frac{1}{\alpha_2}$ . For the lines at constant (dye 2) concentration  $I_2^{0B} = I_2^{0A}$  and  $\text{slope}(AB) = \beta_1$ , as indicated on the  $5 \times 5$  scatterplot of **Figure 4.21**.

In the same manner, we calculate the lines slopes on the 3-color datapoints, using points belonging to the same line on each of the three scatterplots on **Figure 4.22**. From this calculation, the 6 non-diagonal coefficients of the crosstalk matrix can be found by calculating the 2 slopes of each of the 3 2D scatterplots, leading to the slope values indicated. From those values, the matrix can be inverted and an orthogonal 3D plot generated.

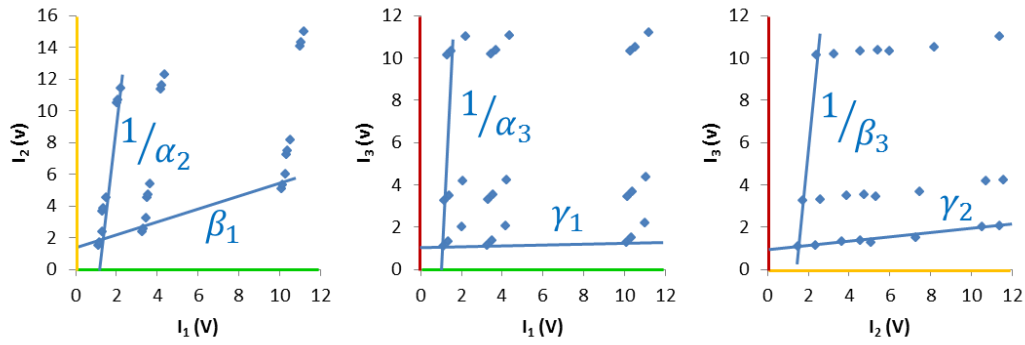


**Figure 4.22** Simulation of a  $3 \times 3 \times 3$  3-color fluorescent code in the case of strong crosstalk between the three dyes. The slopes relate to crosstalk matrix coefficients  $\alpha_2$ ,  $\alpha_3$ ,  $\beta_1$ ,  $\beta_3$ ,  $\gamma_1$  and  $\gamma_2$ .

This final solution appeared as the most elegant and efficient for routine determination of crosstalk matrix coefficients. However, one crucial step still needed to be automated: on-the fly identification of the barcode to automatically calculate the slopes. To implement it, one element is still necessary: identification of the clusters of points. Below we discuss two possible solutions.

## 4.5 Barcode identification: towards automation

### 4.5.1 First “easy” strategy: binning of 2- or 3-D space

For a code library that does not display too much crosstalk, it is possible to discriminate the distinct intensity levels by plotting histograms of the PMT voltage of droplets for each channel. The abscissas of the minima that separate adjacent peaks can be defined as bin limits, in order to map the 2D dynamic range as  $N \times N$  distinct zones. Then, the most primitive form of code identification would be to attribute a code name to each of these zones, and every time a droplet is read, its signals in the different channels would fall in their respective bins, and being labeled. This quite straightforward approach becomes quite unreliable when the intensity levels are very close, or if each distribution is very spread out and largely overlap its neighbors. In this case, the percentage of overlap should be known, determining the percentage of barcode identification error. This value is critical depending on the application the barcode is used for (as discussed later in section 4.6). Moreover, to get this method to work, crosstalk correction is necessary beforehand to obtain a square grid.

### 4.5.2 Second “refined” strategy: cluster analysis

If the code has significant crosstalk, so that its  $N$  dye concentration levels of each dye do not translate as only  $N$  distinct peaks in the channel intensity histogram (but more, up to  $N \times N (\times N)$  peaks, as on **Figure 4.22**), the aforementioned strategy is inapplicable. However, if the  $N \times N (\times N)$  populations have intensity distributions which do not superimpose with their neighbors, it is possible to implement a way to regroup all the datapoints as  $N \times N (\times N)$  clusters using Matlab. Cluster analysis consists of assigning a set of objects into groups (called clusters) so that the objects in the same cluster are more similar (in some sense) to each other than to those in other clusters. Among the several existing clustering methods, agglomerative hierarchical clustering was chosen: it consists in creating a hierarchy of clusters which may be represented in a tree structure called a dendrogram. The hierarchy from the individual elements is built by progressively merging clusters.

A Matlab script was written and tested on fluorescent signals from the previously described 3-color, 27-member barcode library. An agglomerative hierarchical cluster tree [26], [27] was generated with  $N=27$  as the number of clusters. After being determined, the 27 clusters were plotted with a different color each (**Figure 4.23 a**)), then each cluster was represented by its median (**Figure 4.23 b**)) rather than its means, to reduce the impact of points that are far away from the cluster center. Subsequently, the 3 vectors defining the 3D shape were identified in order to orthogonalize it, following the strategy presented in section 4.4.3. The final three 2D projections of the 27 orthogonalized cluster medians are displayed on **Figure 4.23 b**) to e).

On the 3D scatterplot where all datapoints are allocated to clusters, we can see that some points, even quite far away from the cluster center, are still considered as belonging to it. This abnormality could be solved in the future by discarding points further away from the cluster center than a certain distance. However, calculating the median instead of the mean reduces the impact of this spread. The orthogonalized plots show a very good overlap between groups of three points having the same combination of two dye concentrations; the remaining variations are due to minute dilution errors. With these final orthogonal scatterplots, barcode identification is now easy by simply binning each fluorescence channel as explained in section 4.5.1. However, this is not even necessary, because cluster recognition is itself a way to identify the code: it saves the step of orthogonalization. This solution, if implemented on-the-fly, would be by far the most systematic code identification method of all solutions discussed in this chapter.

After this experimental generation of barcodes and theoretical analysis of the data, let us take a step back and go back to the initial goal of our barcoding system – to encode multiplex assays – and discuss how our code could be used for various types of assays.

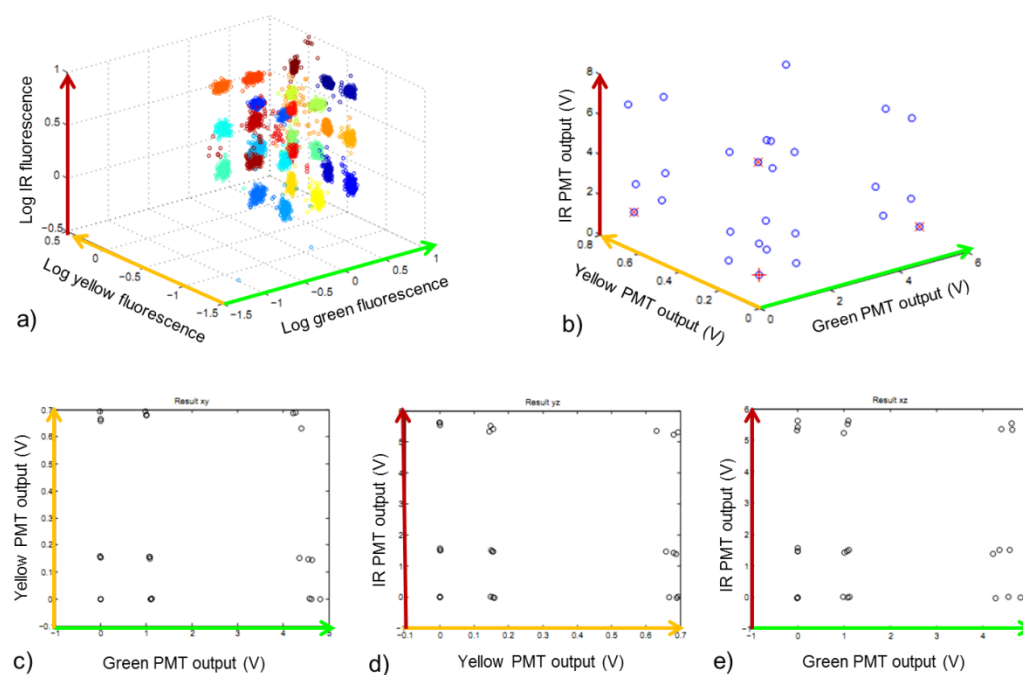


**Figure 4.23** Cluster analysis and orthogonalization of a 3-color, 27-member encoded library. a) 3D scatterplot (in log scale) of 5000 droplets arranged in 27 identified clusters. b) 3D scatterplot (in linear scale) of the 27 cluster medians. The four red crosses identify the 4 points defining the three characteristic shape vectors. c), d), e) The three projections of the orthogonalized set of cluster medians on 2D scatterplots (linear scale).

## 4.6 Barcode strategy vs. application

### 4.6.1 General considerations

As the final use for our fluorescent labels will be to encode biological assays on-chip, the assay's tolerance to barcode identification errors has to be taken into account. Depending on the type of assay, tolerable readout error rate can range from less than 0.1% than up to 50%. This translates into how much overlap there can be between each barcode intensity distribution, how many colors must be used, as well as which strategy is applied for barcode identification. In this section we will review a handful of potential applications and discuss an optimal barcoding strategy.

### 4.6.2 First case: detection of a rare mutation

As presented in the introduction, droplet microfluidics is a very powerful tool to detect rare mutations among a gene population [14], [15]. To do so, a multiplexed assay can be implemented,

where each optical label codes for one mutation or target that is being screened. If the occurrence of each mutation is about  $\frac{1}{N}$  genes, then the error rate on target readout should not be higher than  $\frac{1}{N}.e$ , where  $e$  is the tolerated fraction of false positives. If  $N$  is high ( $10^3$  or more), then there is barely any tolerance for error, which leads to two strong conditions on measurement quality: (i) the number of droplets read has to be very large, to have enough repeats of the positive readout and stay within the 95% confidence interval [14], (ii) the probability of false positives, or code readout errors, has to be less than  $\frac{1}{N}.e$ . If there are  $M$  codes on the scatterplot surrounding the one coding for the positive assay, the percentage of overlap between each and the code of interest has to be less than  $\frac{1}{M}.\frac{1}{N}.e$ . If we take a simple example in one color,  $N=1000$ ,  $M=2$  and  $e=0.1\%$ , then there should be less than 0.0005% misreads. Using the equations in paragraph 4.2.3, it leads to  $\frac{\Delta\mu}{\sigma} = 8.08$ . Since in our 2D code, we had  $\Delta\mu = \log(2) = 0.30$  and  $\sigma = 0.025$  (in log scale), the spacing we used would be sufficient, even for such a low tolerance to error.

#### 4.6.3 Second case: digital PCR with 25-plex assay

Also presented in the chapter introduction, quantitative PCR can also be implemented on-chip, in order to quantify the occurrence in DNA samples of several genes at once in a single assay [15]. In this case, there is a compromise to find between the number of multiplexed assays encoded, and the tolerated overlap between codes. In this case, given the calculations just above, our 2D code would be very suitable for this application, provided it does not overlap the assay fluorophore significantly. If we do not need so much distance between consecutive levels, and provided we manage to have 2.5 orders of magnitude dynamic range, then we can use only one color for the 25 levels. The spacing will be 0.1 on log scale, thus  $\frac{\Delta\mu}{\sigma} = 4$  and an overlap equal to

$$\%Overlap = 1 - erf\left(\frac{\sqrt{2}}{2}\right) = 4.7\%.$$

#### 4.6.4 Third case: HTS of inhibitor libraries

For drug screening applications, as for example determination of the  $IC_{50}$  values of pharmaceutical compounds, the number of compounds screened at once is usually very large (thousands). Such a high number of codes within a dynamic range inferior to 1,000 in each dimension means that overlap between barcodes will be quite important. However, due to high



number of repeats allowed by droplet technology, as well as sophisticated software already being used routinely to sort out data that is out of range, levels of 15% false positives could be sustainable. So if we design a 3-color code on 2.5 orders of magnitude dynamic range with 15% tolerated overlap, then  $\frac{\Delta\mu}{2\sigma\sqrt{2}}=1.02$ , thus  $\Delta\mu=0.072$ . It is hence possible to fit  $\frac{2.5}{0.0719} \approx 35$  levels per color, hence  $\sim 42,000$  codes for three colors, which is about the size of a compound library as found in the pharmaceutical industry. Our coding system is thus also a good solution for encoding very large libraries.

## 4.7 Conclusion and outlook

This final part of the work enabled us to present a proof of principle of the first multi-color barcoding in droplets, using fluorescent silica nanoparticles as the barcoding material.

We first presented the main parameters to consider in order to optimize sample preparation, involving droplet stability, signal to noise ratio and spectral crosstalk altogether. We also had to take the possible on-chip cross-contamination and Taylor dispersion into account. This covered, we next generated 25 distinct barcodes in two colors, and up to 27 barcodes with three colors. This is obviously far less than the possible number of codes achievable with this system, in the range of 10,000-100,000.

This, however, does not take into account the influence of optical crosstalk. We proposed several ways to offset it by calibration of the station, by post-processing or on-the-fly. The latter, provided computing power is sufficient, is obviously the most appealing solution.

We also took a first step towards automatic detection of barcodes, by proposing two methods: (i) divide the whole possible detection space into squares (for two colors) or 3D boxes (for three colors), then assigning each point in the scatterplot to one of these boxes. This is by far the least compute-intensive method, but does not enable adjustment of the CV tolerance, since all data is taken into account. (ii) For each optically encoded library, automatically distribute the points in the scatterplot in the appropriate number of clusters, then define the tolerated CV around the center of each cluster, depending on how much error the assay tolerates. If the droplet signal falls into one of those areas, it is detected as corresponding to the matching code, if not, droplet info is discarded.

Further technical improvements will also involve optimizing the optical setup for fluorescence excitation and readout. To reduce crosstalk while keeping all emulsion components

and optics hardware the same, an appealing strategy would be to add a trigger to the setup, in order to excite and readout each color one by one. For a 1 kHz droplet throughput, a relatively compact emulsion (oil/aqueous = 1) and a two-color barcode, a 30 kHz trigger (already available on the market, and compatible with 200 kHz acquisition on the FPGA card) would be sufficient to detect about 15 points per droplet and per color. An example of signal obtained in one color and 17 kHz modulation is given on **Figure 4.24**.

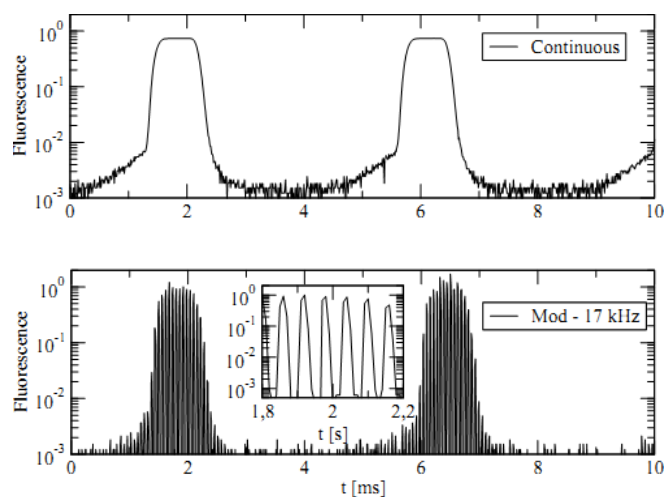


**Figure 4.24** Fluorescence timeline of two droplets detected continuously (top) or with 10 kHz sampling of emission signal (bottom).

Having demonstrated the feasibility of optical barcodes in droplets, the first route to implementing more barcodes with the same number of colors would be to explore the FP dimension by mixing high- and low-FP silica nanoparticles, and of course, upgrade the optical station accordingly.

A more drastic improvement, requiring far more development effort, would be to substitute conventional organic fluorophores for another kind of fluorophore in the silica matrix, so that only single-wavelength excitation would be necessary: this would considerably simplify the optical system. Two kinds of fluorophores could fill in these requirements: first, coordination complexes like Rubpy or Osbpy, that have emission spectra with similar FWHM as organic fluorophores, yet lower quantum yields (1-5%). Another replacement fluorophore could be quantum dots. Although more expensive than conventional fluorophores and having several drawbacks mentioned in chapter 3, their appealing properties (narrow emission peaks, high QY up to 90%) could be exploited, given the cytotoxicity, water solubility and blinking problems can be solved.

In parallel to optimizing the multiplexing capacity, the next challenge will be to implement this barcode in a real screening assay in droplets. A good first starting point would be to use it as

a barcode to screen a library of compounds for their enzyme inhibition properties. An on-chip screening of 704 compounds has already been performed our group (article submitted) to determine their  $IC_{50}$  values against a phosphatase enzyme. However, the sipping of each compound from its microplate well, loading on the chip, mixing with assay reagents, incubation and readout were done sequentially, to keep track of which compound was being screened depending on which well of the microplate it came from. As a consequence, loading of the compounds one by one had to be done at the beginning of each assay, dramatically slowing down the process.

Provided that the compounds can remain in the droplets long enough to be kept for months, preparing the compounds library in droplets all at once could save a significant amount of time for the assay: the loading of compounds and fluorescent barcodes together would have to be done only once. The droplet library could then be homogenized, aliquotted, and every aliquot used for a different screening assay. The major challenge associated with this would be to precisely control the fusion of compounds library with the assay droplets, without losing resolution on the barcode because of the dilution.

In conclusion, we integrated all aspects of our research investigation to implement the first on-chip fluorescent multiplexed system. Many challenges remain to be solved before full implementation of this barcode system, giving way to lots of interesting developments and integration of optics, microfluidic modules and materials science.

## 4.8 Materials and methods

### 4.8.1 Chemicals

#### Continuous phase (oil)

HFE 7500 (3M) with 2 wt-% EB surfactant (RainDance Technologies) was used as the continuous phase for droplet formation.

#### Dispersed phase (SNPs)

Borate buffer 10 mM, pH 9.0 (close to  $pK_a(B(OH)_3/BH_2O_3^-)=9.2$ ) was prepared by dissolving appropriate amounts of sodium tetraborate decahydrate (Sigma) in MilliQ water (Millipore) then bringing the pH down to 9.0 by adding minute amounts of HCl 1M. This solution was used to dilute all SNP solutions when necessary.

The silica nanoparticles used were the fluorescent core-shell-PEG21 SNP described in chapter 3, containing either FITC, RhBITC or Dylight-680-NHS, as well as nonfluorescent core-shell-PEG21 particles made with the exact same sequence of steps, only without the initial APTES-dye grafting step.

### 4.8.2 Chip fabrication

Microfluidic chips were manufactured by conventional soft lithography. Molding masters were fabricated by spin coating SU-8 negative photoresist (MicroChem Corp) onto 6 inch silicon wafers and transferring the fluidic features from photomasks (CAD/Art Services) by contact lithography with an OAI Hybralign Series 200 aligner (OAI). Chips contained channels with two depths: deep channels with low hydrodynamic resistance (100  $\mu$ m) for transporting fluid from external ports to the functional regions of the chip, and shallow channels (20  $\mu$ m) for droplet manipulation and detection. SU-8 photoresists 2100 and 2025 were used for deep and shallow channels respectively. Polydimethylsiloxane (PDMS) (Sylgard 184, Dow Corning) chips were molded from the negative masters within mold housings of custom design. Glass cover slides were permanently bonded to the fluidic side of the chips by surface activation in an AutoGlow oxygen plasma system (Glow Research) followed by immediate contact bonding.

To create hydrophobic surfaces, the microfluidic channels as well as the fluid-exposed surfaces of the emulsion vials were treated for 2 min with 1H,1H,2H,2H-perfluorodecyltrichlorosilane (Alfa Aesar) dissolved in FC-3283 (3M Specialty Materials) prepared as a mixture of 18 g silane in 100 mL solvent.

Two different microfluidic devices were used (see Appendix B), one for droplet generation (LRS 6.6) and the other for reinjection after incubation (ERIA 2.2).

### 4.8.3 Preparation of barcode libraries

#### General library prep

In all cases mentioned below, the position on the plate of each combination of dyes was designed to minimize impact of possible cross-contamination on-chip. Knowing the sequential order of pipetting in each well by the automated sampler, they were injected from low to high concentration, starting by the dye with the highest emission wavelength. Once all library members were pipetted in the wells, the plate was sealed with aluminium foil and centrifuged at 1000 rpm during 1 min to get rid of possible droplets stuck on the well walls. To gently homogenize the plate contents, it was then shaken during 5 seconds, using the Automix mode of a Spectramax M5 (Molecular Devices).

### 5x5, two color library prep

Among the SNPs synthesized in Chapter 2, the PEGylated F-SNP and RhB- were used as synthesized to create a 5×5 fluorescent barcode library. First, each of these two color SNPs solutions were diluted with non-fluorescent SNP in borate buffer 10 mM pH 9.2, by mixing both according to **Table 4.2**. The subsequent F-SNP solutions were called A1 to A16 (green color), RhB-SNP solutions were called B1 to B16 (yellow color). Then, in a 384 well plate (Corning), solutions were mixed as indicated on **Table 4.3** (20uL of each):

### 3x3x3, three color library prep

Among the SNPs synthesized in Chapter 2, the PEGylated F-SNP, RhB-SNP and Dylight 680-SNP samples were used to create a 3x3x3 fluorescent barcode library including the three dyes. Following the same principle as previously, each of these three color SNPs solutions were diluted in series A to C with non-fluorescent SNP in borate buffer 10 mM pH 9.2, by mixing both according to the following table. F-SNP solutions were called A1 to A10 (green color), RhB-SNP solutions were called B1 to B10 (yellow color) and Dylight 680-SNP were called C1 to C10 (dark red color).

Sample name	A1/B1	A2/B2	A4/B4	A8/B8	A16/B16
Dilution factor	1	2	4	8	16
F-SNP solution volume (μL)	128	64	32	16	8
Bare SNP volume (μL)	0	64	96	112	120

**Table 4.2** Preparation of the 5 solutions in each color for the 5×5 library.

#### 4. Fluorescently encoded droplet libraries

Well	A		B		C		D		E	
5	A1	B1	A1	B2	A1	B4	A1	B8	A1	B16
4	A2	B1	A2	B2	A2	B4	A2	B8	A2	B16
3	A4	B1	A4	B2	A4	B4	A4	B8	A4	B16
2	A8	B1	A8	B2	A8	B4	A8	B8	A8	B16
1	A16	B1	A16	B2	A16	B4	A16	B8	A16	B16

**Table 4.3** Preparation of the 5×5 library on a microplate.

Sample name	A1/B1/C1	A3/B3/C3	A10/B10/C10
Dilution factor	1	3	10
F-SNP solution volume (μL)	100	30	10
Bare SNP volume (μL)	0	70	90

**Table 4.4** Preparation of the 3 solutions in each color for the 3×3×3 library.

Then, in a 384 well plate (Corning), solutions were mixed as indicated on **Table 4.5** (10 μL of each):

Well	A			B			C		
9	A1	B1	C1	A1	B1	C3	A1	B1	C10
8	A1	B3	C1	A1	B3	C3	A1	B3	C10
7	A1	B10	C1	A1	B10	C3	A1	B10	C10
6	A3	B1	C1	A3	B1	C3	A3	B1	C10
5	A3	B3	C1	A3	B3	C3	A3	B3	C10
4	A3	B10	C1	A3	B10	C3	A3	B10	C10
3	A10	B1	C1	A10	B1	C3	A10	B1	C10
2	A10	B3	C1	A10	B3	C3	A10	B3	C10
1	A10	B10	C1	A10	B10	C3	A10	B10	C10

**Table 4.5** Preparation of the 5×5 library on a microplate.

#### 4.8.4 Library encapsulation in droplets

This library of barcodes was then aliquotted from microplate to droplets. Some content of each well was automatically pipetted with PEEK tubing filled with 2 wt% EA surfactant in HFE 7500 (see structures on Appendix A). The setup consisted in an automated X-Y moving arm (Parker) and custom OEM pumps (IDEX Corp) controlled by in-house Labview software (National Instruments).

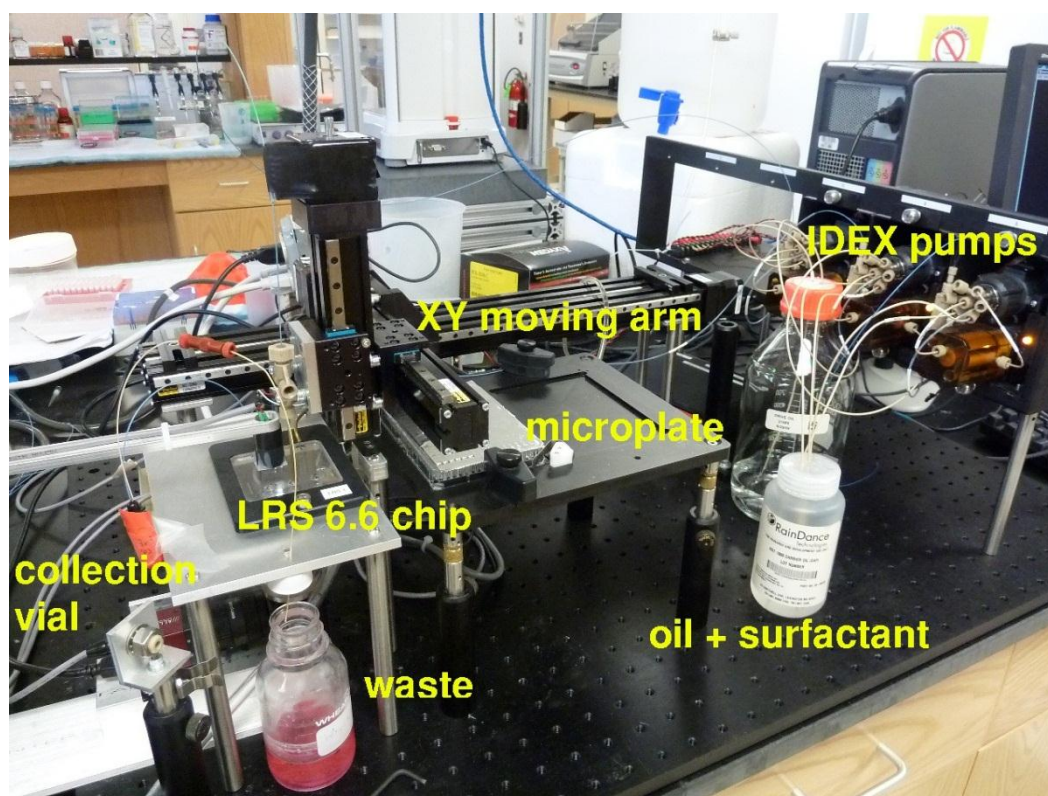


**Figure 4.25** Experimental setup for droplet library generation. The two pumps flow carrier oil/surfactant into the PEEK tubing and oil inlet of the chip. They also withdraw liquid from the microplate in the PEEK tubing. Once the tubing is filled the aqueous sample, the needle is moved from the plate (right) to the the chip (left) to inject the sample in the aqueous inlet. Droplets produced are collected in a custom collection vial (taped in red here). During the rinsing steps, the rinse solution is injected in a small well (between chip and microplate) where the PEEK tubing tip plunges, and discarded in waste afterwards. Meanwhile, oil pumps infuse oil that goes backwards in the aqueous inlet to rinse out remainders of the previous sample.

For each microplate well, the program followed the following steps: (i) 10  $\mu\text{L}$  of solution were aspirated from the well into the tubing. (ii) The solution was then injected during 2 min in a LRS 6.6 chip aqueous inlet (see design on Appendix B) at 150  $\mu\text{L}/\text{h}$  while EA 2 wt% in HFE 7500 was continuously infused at 450  $\mu\text{L}/\text{h}$  via the chip oil inlet. Droplets were generated (**Figure**

**4.26** a)) and the emulsion was collected in a RDT 1000 Input/Output Vial (RainDance Technologies) filled with oil and surfactant and protected from light (see **Figure 4.25**). (iii) After infusion in the chip, 50  $\mu\text{L}$  of needle content (remaining aqueous phase and excess oil + surfactant) were discarded, and the tip was rinsed twice with 20  $\mu\text{L}$  of miliQ water before the next well content was loaded. 4) During this needle washing steps, oil and surfactant being slowly infused through the chip oil inlet, to avoid channels drying out. The pipetting was done row by row, going from right to left, from lower rows to upper rows. For example, the pipetting sequence for the 3x3x3 plate was: well C1, then B1, then A1, followed by well C2, then B2, then A2, etc.).

After droplet generation and collection from all desired wells was completed, the vial was unplugged from the chip, rocked upside down every five minutes during two hours to homogenize the droplet content, then the droplets were reinjected on-chip (**Figure 4.26** b)).

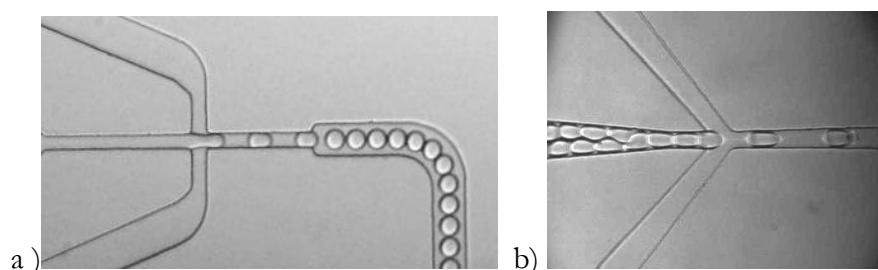


**Figure 4.26** Generation (a) and reinjection (b) of encoded droplet library.

### 4.8.5 On-chip droplet fluorescence measurements

For all libraries, droplets were reinjected on a “test 32.2” chip (design on Appendix B), as presented on **Figure 4.26** b). Custom OEM pumps (IDEX Corp) infused the emulsion at 50  $\mu\text{L}/\text{h}$  and the spacing oil+surfactant at 100  $\mu\text{L}/\text{h}$ . Reinjection was performed 3h and 18h after droplet library generation.

#### “PLS 3” station: green and orange detection channels

The detailed scheme of this optical setup is in Appendix C.

Droplet fluorescence was measured using a custom laser-induced fluorescence setup. The droplets were illuminated by a 20 mW 488 nm Cyan solid-state laser (Picarro) and a 20mW 561 nm Cube laser diode (Coherent). The laser beams were then focused with a 20X, 0.45 NA objective (ELWD, CFI S Plan Fluor, Nikon Corp.), which was also used to collect the emitted light.



The emitted light was filtered by a custom dichroic (Edmund Optics). The green and orange lights were splitted by a FF562-Di02 longpass dichroic (Semrock). The green light was directed to a H9656 photomultiplier (Hamamatsu Photonics KK) after passing through a green FF01-525/40A bandpass filter (Semrock). The orange light was directed to a H9656 photomultiplier (Hamamatsu Photonics KK) after passing through an orange FF01-593/40-25 bandpass filter (Semrock). The two detected signals were transferred by a NI-USB6229 DAQ module (National Instruments) to a in-house Labview software (National Instruments) for direct visualization.

The microfluidic device was visualized using the 20X objective lens; the light source was a 580 nm light-emitting diode (Epoxy-Encased LED780E, Thorlabs, Inc.) protected by a bandpass FF01-593/40-25 (Semrock), the camera was a and a Guppy charge-coupled device camera (Allied Vision Technologies GmbH).

#### **“dScreen” station: green, orange and infrared detection channels**

This optical setup being quite complex to describe, its detailed scheme is included in Appendix C.

#### **4.8.6 Data acquisition and plotting**

On “PLS3” station, the recorded files included all timeline PMT signals recorded during acquisition time, recorded in in-house .rdr format. Consequently, they needed to be further processed using in-house Labview software (National Instruments) to extract fluorescence maxima in each detection channel for each droplet detected, and generate corresponding .txt files.

On “dScreen” station, the real time data acquisition software displayed live scatterplots, allowing easier signal optimization. To limit output datafile size, only droplet width and maximal fluorescence intensities on each channel were recorded and gathered in an ASCII file.

Output ASCII files were directly analyzed and plotted using Origin (OriginLab). As far as data representation and analysis goes, we chose to use log values of our intensities, rather than a linear scale for two reasons: 1) the concentration levels of each fluorophore follow a geometric series; 2) after binning, distributions with the same CV occupy the same number of on bins on a log scale: automated segmentation of the dynamic range for barcode identification becomes much more facile.

To enable easier visualization of datasets containing 20,000 droplets each, contour plots were drawn, rather than scatterplots. Consequently, two preliminary steps were required beforehand: first, calculate the log of each fluorescence value then draw 2D matrixes from the obtained datasets. The bin chosen for all matrixes was 0.04 to get a satisfactory compromise between cluster width and detection of clusters with few droplets.

#### 4.8.7 Compensation matrix calculation

To calculate compensation matrix coefficients as presented in 4.4.2, we plotted the 2D contour plots of our raw 2- or 3- channel signals, corresponding to vector  $Y$  as presented in 4.1.3.

To these series of values, we applied a linear combination defined by the matrix  $D = \begin{pmatrix} 1 & a_2 \\ b_1 & 1 \end{pmatrix}$ ,

then plotted the resulting contour plot  $Y' = DY$ . We iteratively modified coefficients  $a_2$  and  $b_1$ , until scatterplot  $Y'$  looked orthogonal. In this case,

$$Y' = DY = DCX = X \quad (4.13)$$

which leads to determination of  $C$ , which in the 2-color,  $2 \times 2$  matrix, is:

$$C = \begin{pmatrix} 1 & \alpha_2 \\ \beta_1 & 1 \end{pmatrix} = D^{-1} = \frac{1}{1 - a_2 b_1} \begin{pmatrix} 1 & -a_2 \\ -b_1 & 1 \end{pmatrix} \quad (4.14)$$

In the 3-color,  $3 \times 3$  matrix case, if  $D$  is defined by

$$D = \begin{pmatrix} 1 & a_2 & a_3 \\ b_1 & 1 & b_3 \\ c_1 & c_2 & 1 \end{pmatrix} \quad (4.15)$$

$$\text{then } C = \begin{pmatrix} 1 & \alpha_2 & \alpha_3 \\ \beta_1 & 1 & \beta_3 \\ \gamma_1 & \gamma_2 & 1 \end{pmatrix} = D^{-1} = \frac{1}{\det D} \begin{pmatrix} 1 - b_3 c_2 & -(a_2 - b_2 a_3) & a_2 b_3 - a_3 b_2 \\ -(b_1 - b_3 c_1) & 1 - a_3 c_1 & -(b_3 - a_3 b_1) \\ b_1 c_2 - b_2 c_1 & -(c_2 - a_2 c_1) & 1 - b_1 a_2 \end{pmatrix} \quad (4.16)$$

where

$$\det D = [(1 - b_3 c_2) - b_1 (a_2 - a_3 c_2) + c_1 (a_2 b_3 - a_3)] \quad (4.17)$$

### 4.8.8 Cluster recognition

3-color encoded library data was analyzed and replotted using Matlab software (Mathworks). We generated an agglomerative hierarchical cluster tree with  $N=27$  as the number of clusters. The 27 discriminated clusters were identified and plotted with a different color each, then each cluster was represented by its median. Subsequently the 8 corners of the 3D shape were identified in order to orthogonalize it. The final three 2D projections of the 27 clusters were plotted.

## References

- [1] “Luminex Technology Overview.” [Online]. Available: [http://www.panomics.com/index.php?id=product\\_96](http://www.panomics.com/index.php?id=product_96).
- [2] F. S. Ligler and J. S. Kim, *The Microflow Cytometer*. Pan Stanford Publishing, 2010.
- [3] J. R. Kettman, T. Davies, D. Chandler, K. G. Oliver, and R. J. Fulton, “Classification and properties of 64 multiplexed microsphere sets,” *Cytometry*, vol. 33, no. 2, pp. 234-243, Oct. 1998.
- [4] “Parallel Synthesis Technologies, Inc.” [Online]. Available: <http://www.parallel-synthesis.com/>.
- [5] “Firefly BioWorks, Inc.” [Online]. Available: <http://www.fireflybio.com/technology.html>.
- [6] D. Dendukuri, D. C. Pregibon, J. Collins, T. A. Hatton, and P. S. Doyle, “Continuous-flow lithography for high-throughput microparticle synthesis,” *Nat Mater*, vol. 5, no. 5, pp. 365-369, mai 2006.
- [7] D. C. Pregibon, M. Toner, and P. S. Doyle, “Multifunctional Encoded Particles for High-Throughput Biomolecule Analysis,” *Science*, vol. 315, no. 5817, pp. 1393 -1396, Mar. 2007.
- [8] W. S. Tan, C. L. Lewis, N. E. Horelik, D. C. Pregibon, P. S. Doyle, and H. Yi, “Hierarchical Assembly of Viral Nanotemplates with Encoded Microparticles via Nucleic Acid Hybridization,” *Langmuir*, vol. 24, no. 21, pp. 12483-12488, Nov. 2008.
- [9] H. N. Joensson et al., “Detection and Analysis of Low-Abundance Cell-Surface Biomarkers Using Enzymatic Amplification in Microfluidic Droplets,” *Angewandte Chemie International Edition*, vol. 48, no. 14, pp. 2518-2521, Mar. 2009.
- [10] E. Brouzes et al., “Droplet microfluidic technology for single-cell high-throughput screening,” *Proceedings of the National Academy of Sciences*, vol. 106, no. 34, pp. 14195-14200, 2009.

- [11] J.-C. Baret, Y. Beck, I. Billas-Massobrio, D. Moras, and A. D. Griffiths, "Quantitative Cell-Based Reporter Gene Assays Using Droplet-Based Microfluidics," *Chemistry & Biology*, vol. 17, no. 5, pp. 528-536, May 2010.
- [12] L. Frenz, "Development, integration and application of modules for droplet-based microfluidics," PhD thesis, 2010.
- [13] J. Clausell-Tormos, A. D. Griffiths, and C. A. Merten, "An automated two-phase microfluidic system for kinetic analyses and the screening of compound libraries," *Lab on a Chip*, vol. 10, no. 10, pp. 1302-1307, 2010.
- [14] D. Pekin et al., "Quantitative and sensitive detection of rare mutations using droplet-based microfluidics," *Lab on a Chip*, vol. 11, no. 13, p. 2156, 2011.
- [15] Q. Zhong et al., "Multiplex digital PCR: breaking the one target per color barrier of quantitative PCR," *Lab on a Chip*, vol. 11, no. 13, p. 2167, 2011.
- [16] H. M. Shapiro, *Practical flow cytometry*. John Wiley and Sons, 2003.
- [17] M. R. Loken, D. R. Parks, and L. A. Herzenberg, "Two-color immunofluorescence using a fluorescence-activated cell sorter.," *Journal of Histochemistry & Cytochemistry*, vol. 25, no. 7, pp. 899 -907, juillet 1977.
- [18] C. B. Bagwell and E. G. Adams, "Fluorescence Spectral Overlap Compensation for Any Number of Flow Cytometry Parameters," *Annals of the New York Academy of Sciences*, vol. 677, no. 1, pp. 167-184, Mar. 1993.
- [19] J. W. Tung, D. R. Parks, W. A. Moore, L. A. Herzenberg, and L. A. Herzenberg, "New approaches to fluorescence compensation and visualization of FACS data," *Clinical Immunology*, vol. 110, no. 3, pp. 277-283, Mar. 2004.
- [20] H. Choi, K. R. Castleman, and A. C. Bovik, "Color compensation of multicolor fish images," *IEEE Transactions on Medical Imaging*, vol. 28, no. 1, pp. 129-136, Jan. 2009.
- [21] Hamamatsu, "Photomultiplier tubes - Basics and applications." 2006.
- [22] F. W. J. Olver and N. I. of S. and T. (U.S.), *NIST handbook of mathematical functions*. Cambridge University Press, 2010.
- [23] G. Taylor, "Dispersion of Soluble Matter in Solvent Flowing Slowly through a Tube," *Proceedings of the Royal Society of London. Series A, Mathematical and Physical Sciences*, vol. 219, no. 1137, pp. 186-203, 1953.
- [24] R. Aris, "On the Dispersion of a Solute in a Fluid Flowing through a Tube," *Proceedings of the Royal Society of London. Series A, Mathematical and Physical Sciences*, vol. 235, no. 1200, pp. 67-77, Apr. 1956.
- [25] T. Squires and S. Quake, "Microfluidics: Fluid physics at the nanoliter scale," *Reviews of Modern Physics*, vol. 77, no. 3, pp. 977-1026, Oct. 2005.

- [26] “Construct agglomerative clusters from linkages - MATLAB.” [Online]. Available: <http://www.mathworks.fr/help/toolbox/stats/cluster.html>.
- [27] “Agglomerative hierarchical cluster tree - MATLAB.” [Online]. Available: <http://www.mathworks.fr/help/toolbox/stats/linkage.html>.

## Acknowledgment of collaboration

I designed and conducted this research with specific contributions from others as follows:

All experiments in this chapter were performed at RainDance Technologies in Lexington, MA, USA. Drs Thomas Mangeat and Qun Zhong designed and assembled the dScreen station. Dr Qun Zhong gave me microfluidic designs for emulsion reinjection and advice for crosstalk compensation analysis. Dr. Hu Gang gave me microfluidic designs for library generation, trained me on the library generation automated setup and suggested ideas for crosstalk compensation analysis. Dr Xinyu Li showed me how to operate the PLS3 station. Dr Benoît Semin (MPIDS Göttingen) wrote the Matlab algorithm for cluster analysis and orthogonalization.



# Chapter 5. Summary and perspectives

## 5.1 Context

In the last two decades, drug development costs have been exploding in spite of constant improvements in automation and miniaturization of high-throughput screening platforms. Nowadays, microplates, the most used screening platforms, have reached their downsizing limits and microarrays, although a significant improvement in terms of miniaturization, lack universality and flexibility. That is why microfluidics and lab-on-a-chip technologies have recently emerged as appealing alternatives. In particular, droplet-based microfluidics enables compartmentalization of fluids into femto- to nanoliter droplets at several kHz. Since each of them embodies an individual reactor, encapsulating molecular libraries in droplets would provide increased throughput, dramatically reduced reagent consumption and reliable statistics, allowing complete dose-response analysis even at early screening stages. However, to make it truly efficient, it would be useful to generate a compound library in droplets once and split it in small aliquots that could each be used on a separate assay. Since positional information is lost in this case, it is hence necessary to devise a strategy to encode the compounds in droplets for direct identification during assay readout. Since fluorescence is a universal characterization tool in biology, we chose to use it as well for our encoding system. The aim of this PhD project was to develop a multi-dimensional fluorescent labeling system to encode large libraries of droplets for high-throughput assays in microfluidic chips.

## 5.2 Synthesis and characterization of novel fluorescent silica nanoparticles

The first part of our work consisted in finding a proper material to carry the code. After examining the many options available (organic and inorganic molecular fluorophores, fluorescent polymer microbeads, quantum dots, fluorescent silica...), we opted for the latter. Indeed, silica is inexpensive, non-toxic, optically transparent, chemically inert and is reported to enhance the properties of the fluorophore it encapsulates. In addition, nanometer-sized particles do not set an lower limit on droplet size and do not sediment in or clog the channels. However, among the

variety of available synthesis routes for fluorescent silica, no one allowed formation of dense particles smaller than 10 nm (to make it more universal) and in an aqueous solvent (to reduce washing and aqueous stabilization steps). We hence chose to adapt a route published by Persello in 1991, which consists in neutralizing an alkaline sodium silicate solution down to pH 9.0 to initiate silica nucleation, leading to particles down to 2 nm.

To avoid colloidal destabilization from screening of the surface negative charges by addition of a strong acid, the acidification was performed by a strongly acidic ion exchange resin. After finding out the proper equivalence between silicate ions and acidic resin to get the desired pH, we tested different strategies based on growth of successive shells on a silica core, in order to tune particle size from 2 to 10 nm. Secondary nucleation and probable redissolution of silica cores appeared to occur, requiring fine-tuning of the silicate quantity added at every step: maximal size reached was 6.2 nm. Addition of a single equivalent silica at every step proved to be the most reliable strategy: from silica cores of 2.5 nm, we reached maximal sizes of 4.5 nm; lower than our initial goal. However, this method being very time consuming to reach sizes > 5 nm, we opted for a simple core/single shell synthesis. To ensure long-term colloidal stabilization in buffers and DMSO, we chose to graft PEG chains at the particle surface.

Fluorophore addition in the silica matrix was also studied. With one of the fluorophores (Dylight 800 NHS), we highlighted a drastic blue shift characteristic of the phenomenon called ‘exciton splitting of dimers’, which suggested that silanized fluorophores undergo partial polymerization in polar solvents. We hence ruled out this fluorophore and carried out silanization in DMSO. Dye encapsulation was much more effective for Rhodamine B ITC and Dylight 680 NHS than for Fluorescein ITC, possibly because of both the repulsion between negative charges of dye and silica and limited efficiency of the isothiocyanate-amine grafting in our experimental conditions.

We also evaluated efficiency of PEG-silane grafting on the surface of the nanoparticles. Surprisingly, even if the grafting reaction takes place in water, self-condensation of the PEG-triethoxysilane does not appear to take place after hydrolysis if particles are present: We conclude that silane-silica bonding is more favorable than self-condensation.

The second part of our study on these novel materials was the characterization of their fluorescence properties. Their absorption and emission spectra matched very well those of the starting free fluorophores but quantitatively, the brightness (integrated emission spectrum over maximal absorbance) of the dye trapped in silica was increased up to 2.5-fold compared to when free in buffer. This increase, giving apparent quantum yield superior to 1.0, even led us to question the traditional method to measure quantum yields, which does not account from



specific local environment of the fluorophore trapped in silica. As expected, we also observed an increase in FP from encapsulation, which was moderated at high dye loading. This is due to partial depolarization effects taking place in the silica matrix as dye molecules are very close to each other and undergo FRET. Finally, photobleaching experiments highlighted the protection that the silica matrix offers from photo-oxidation, slowing down emission degradation in time, especially in the case of RhBITC. From these observations, we conclude that our materials, the smallest fluorescent silica particles ever synthesized, significantly improve optical properties of organic fluorophores, in line with previous reports on other types of silica.

### 5.3 Silica nanoparticles at fluorinated oil/water interfaces

Before using our fluorescent nanomaterials to fluorescently encode droplets, we undertook to examine whether they influence the dynamics of droplet formation, stabilization by surfactant and long-term resistance to coalescence. Indeed, both surfactants and nanoparticles are used to stabilize emulsions, but the interaction of water-dispersed particles on dynamics of droplet stabilization by a fluorophilic surfactant dissolved in fluorinated oil has never been reported. We first monitored the effect of an increased concentration of particles on the size of droplet generated in various conditions: no change was detected, indicating that at the sub-millisecond time scale of droplet formation, particles do not modify interfacial tension. Practically, it means that during generation of our encoded library, flow conditions will not have to be adjusted if SNP concentration varies.

Then, we used a prototype of microfluidic dynamic tensiometer currently developed by Baret and Brosseau in Göttingen's Max Planck Institute, in order to monitor sub-second kinetics of droplet stabilization by surfactant with or without particles. For all parameters tested (particle concentration, size and presence/absence of PEG), only minor variations in droplet deformation kinetics were noted, which could be within experimental error: at this time scale, particles do not seem to impact surfactant adsorption kinetics at the interface. However, more repeats should be performed and a wider range of conditions tested, to conclude with certainty. Moreover, internal recirculation and droplet shear in channels might bias the adsorption pattern.

Consequently, to get a complementary picture of adsorption dynamics and observe it at longer time scales, we ran experiments on a classic pendant drop apparatus. With this setup, clear impact of nanoparticles was seen: in the absence of surfactant, increasing proportions of particles up to 2.5 wt% in buffer led to drastic decrease in interfacial tension from 38 to 24 mN/m after 1 s. Nevertheless, this decrease is less important than the one caused by surfactant alone at 2 wt% in fluorinated oil, down to 15 mN/m after 1 second. In both cases, we calculated the adsorbed

quantity of both species separately and found it was between 6 and  $20 \times 10^{-7}$  mol/m<sup>2</sup>. When combined, we found evidence that increased silica adsorption reduced the adsorbed quantity of surfactant: there is some competition between both surface-active agents. PEG displayed a very strong surface activity as well, dominating the one of silica alone.

Finally, we evaluated the impact of nanoparticles on the droplet's resistance to coalescence over several days. For emulsions with 2 wt% surfactant containing either 100 % buffer or 100 % nanoparticles in buffer, only a minor improvement of droplet stability by particles was detected, contrary to reports in the literature. This is probably because the surfactant at this concentration is such a good stabilizer already that it screens the influence of nanoparticles. On the other hand, when the emulsion contains 50 % droplets with particles and 50 % without, dramatic osmotic transport between droplets takes place. We conclude that for our barcode, we need to balance the unequal concentration of fluorescent particles across droplets by diluting them not with buffer alone, but with particles at the same starting concentration, to balance total SNP concentration over all droplets and avoid this phenomenon.

### 5.4 Fluorescently encoded droplet libraries

Having cleared the potential negative impact of our nanoparticles on emulsion stability, the final part of this project could be undertaken. We first reviewed all important parameters to take into consideration: (i) the choice of optical setup (lasers, filters, detectors) with regards to the dyes chosen; (ii) the concentration range of fluorescent SNP with regards to osmotic effects, linearity, PMT dynamic range and minimization of spectral crosstalk; (iii) the spacing between code levels vs. the standard deviation of emitted signal at each level; (iv) the precautions taken in droplet library generation steps to minimize cross-contamination and Taylor dispersion; (v) the optimal PMT gain for the concentration range chosen of each color.

Consequently, we generated two multiplexed fluorescently labeled droplet libraries: one with two colors (green and yellow) and  $5 \times 5 = 25$  codes and one with three colors (green, yellow and infrared) and  $3 \times 3 \times 3 = 27$  codes. Both of them showed very good separation between levels, in spite of some observable spectra crosstalk. We partly solved that problem by using a station equipped with emission filters of narrower bandwidth. For the remaining crosstalk, we proposed several ways to orthogonalize the scatterplot: either (i) visually by finding the coefficients of the crosstalk matrix that give the most 'square' scatterplot, or (ii) computationally by finding the two (for 2 colors) or three (for three colors) characteristic vectors that define the 2D or 3D scatterplot.

In addition, we proposed several methods to identify barcodes during readout: either by simple binning of the detection range in each channel, or by attributing each signal to a cluster of points among the  $N \times N (\times N)$  possibilities. This last solution, compared to the other one, has the advantage of still being effective without compensation in case crosstalk takes place, which saves considerable data processing time and allows on-the-fly identification.

Thanks to its moderate dispersion and its wide range of colors, our barcoding system can be used to label a variety of different assays, from the most stringent in terms of low tolerance to error (such as detection of rare genetic mutations), to the most demanding in terms of encoding and multiplexing capacity (compound libraries of thousands of molecules). Together with the work of others in the field, the work in this thesis presents significant advances towards further implementation of droplet-based microfluidics for high-throughput screening, that have the potential to reshape the way it is both conceived and implemented.

### 5.5 Perspectives

The synthesis of our novel 2.5 nm fluorescent silica nanoparticles, even though already well explored, would benefit from further investigation, in order to answer some questions left: (i) see if FRET depolarization effects can be observed and controlled by high loading of fluorophores into the silica matrix (more than 1 fluorophore per particle on average); (ii) achieve particle growth up to 10 nm by exploring different synthesis conditions and (iii) complete the characterization of optical properties: fluorescence lifetime, polarization dynamics, fluorescence correlation spectroscopy. In addition, since our applications are biology assays, thorough biocompatibility and colloidal stability tests need to be performed in various buffer conditions with several types of cells. Finally, alternative surface functionalization of the particles by proteins or antibodies could make them useful tools for single-molecule imaging of biological processes.

The investigation of interfacial properties of particles have left some questions unanswered: (i) do SNP ever influence surfactant adsorption at sub-second scales? (ii) How universal is the microfluidic tensiometer and which bias does droplet flow and shear bring to the measurement? The last part about osmotic transport showed that by controlling this phenomenon, it is possible to use it as a tool to precisely characterize droplet contents. This has some great potential in life sciences, for example to monitor metabolisms of small organisms.

Finally, as far as codes are concerned, more developments need to be undertaken, especially in terms of maximizing coding capacity: complete investigation of sources of dispersion, as well as optimization of the optical setup in terms of dynamic range and dye selectivity, will be required

to assess more precisely the actual reachable number of codes. After that, the next big step will be to implement them to encode a real assay. In particular, two main efforts will have to be pushed: (i) designing a proper microfluidic chip to perform all steps sequentially and (ii) minimize crosstalk between assay and code, to make readout of both truly reliable.

# Chapter 6. Résumé de thèse

## 6.1 Contexte du projet

Dans le domaine des biotechnologies, le criblage de nouveaux médicaments manipule des volumes de données considérables : les candidats sont sélectionnés parmi des banques de centaines de milliers de molécules. Afin d'accélérer et d'automatiser les analyses, divers outils ont vu le jour ces vingt dernières années. Tout d'abord, les microplaques, initialement à 96 puits, ont évolué vers 1536 et même 3456 ou 9600 puits. Elles atteignent aujourd'hui leurs limites de miniaturisation, en raison des phénomènes d'évaporation et de capillarité et du manque de précision sur la distribution de volumes sub-microlitre. Développées plus récemment, les puces à ADN et autres types de *microarrays* ont permis de considérablement paralléliser et miniaturiser les tests, tout en divisant les volumes de réactifs par un facteur mille. Néanmoins, certains problèmes demeurent : sensibilité insuffisante, temps d'incubation longs, fixation fragile des biomolécules.

Pour contourner ces limitations tout en réduisant encore les quantités de réactifs, la microfluidique en gouttes représente une alternative séduisante. Son principe : dans des puces en élastomère sont moulés des microcanaux dans lesquels circulent des gouttelettes aqueuses, séparées les unes des autres par une phase continue fluorocarbonée. Chacune de ces gouttes, de l'ordre du picolitre, constitue un microréacteur indépendant qui peut contenir toutes sortes de composants : molécules, ADN, protéines ou cellules. Ces gouttelettes peuvent être générées, manipulées et analysées à une fréquence qui peut atteindre 10 kHz, soit 36 millions de tests par heure : de tels débits permettraient d'effectuer des courbes de dose-réponse dès les premières étapes de criblage, améliorant considérablement la fiabilité et la qualité des données.

Pour encore accélérer le temps d'analyse, on peut imaginer encapsuler chaque banque de milliers de composés une seule fois, puis diviser l'émulsion ainsi obtenue en plusieurs petits échantillons qui pourront chacun servir pour un test différent. Néanmoins, cette méthode impose alors de marquer chaque composé pour pouvoir l'identifier ultérieurement lors du criblage sur puce, même après des mois, sans altérer la réponse du test biologique. Il faut en outre s'assurer que le matériau utilisé pour ce codage demeure à l'intérieur de celle-ci : l'échange moléculaire entre gouttes serait très nuisible à la fiabilité du code.

Parmi les types de stratégie de codage (en position, en composition chimique, électronique, magnétique, spectrométrique), la fluorescence est une technique de choix : en effet, elle est un

outil de caractérisation massivement utilisé en biologie en raison de sa grande sensibilité, qui permet de détecter jusqu'à une seule molécule fluorescente. Utiliser le même système de détection pour le test biologique et le code est donc la solution la plus simple.

Ce travail de thèse s'est déroulé en plusieurs étapes : un premier objectif a été de mettre au point un matériau fluorescent qui réponde au cahier des charges, puis de caractériser ses propriétés de fluorescence. Ensuite, nous avons vérifié sa compatibilité avec les gouttes, notamment en terme de résistance à la coalescence et autres types de dégradation. Enfin, nous avons conçu le système de codage proprement dit : en premier lieu, les principaux paramètres gouvernant la qualité du code ont été identifiés, puis deux codes modèles ont été réalisés. Ils ont ensuite servi à étudier différentes voies de correction de recouvrement spectral et à explorer plusieurs stratégies pour l'identification du code lors du test.

## **6.2 Synthèse et caractérisation de nanoparticules de silice fluorescentes**

Une fois choisie la méthode d'encodage en fluorescence, une pléthore de matériaux s'offrait à nous : fluorophores moléculaires organiques ou inorganiques, quantum dots, billes de polystyrène fluorescentes, silice fluorescente... Cependant, nous devons respecter un cahier des charges drastique : le matériau choisi devait être fluorescent, biocompatible, inerte chimiquement, injectable dans une puce microfluidique, ne pas fuir des gouttes et ne pas interférer avec le test biologique. Nous avons donc arrêté notre choix sur des nanoparticules de silice incorporant des fluorophores organiques. Tout d'abord, nous avons exploré la voie de synthèse Stöber, la plus citée dans la littérature. La nécessité de réduire encore la taille des particules nous a amenés à adapter une voie de synthèse alternative publiée par Persello en 1991 basée sur la neutralisation de silicates pour une croissance de silice à pH 9.0. Pour limiter la déstabilisation colloïdale par écrantage des charges de surface, l'acidification est réalisée par une résine acide échangeuse d'ions. Cette synthèse présente plusieurs avantages : elle est moins toxique, ne nécessite pas de dialyse et produit des nanoparticules plus denses, donc moins enclines à laisser fuir le fluorophore.

En préambule, nous avons donc déterminé les quantités de réactifs nécessaires à la croissance de cœurs de silice à pH 9,0 puis différentes stratégies ont été essayées pour moduler la taille des particules jusqu'à 10 nm. Des phénomènes de nucléation secondaire et redissolution partielle des cœurs nous ont obligés à opter pour une croissance très progressive par additions successives de petites quantités de silicate condensées sur des cœurs de silice synthétisés au préalable. Ainsi nous avons atteint un diamètre maximal de 6.2 nm.

Basé sur ces résultats et sur la littérature foisonnante sur les nanoparticules de silice fluorescente, nous avons opté pour le schéma de synthèse suivant pour assurer l'encapsulation de notre fluorophore et la stabilisation colloïdale à long terme de nos particules (**Figure 6.1**):

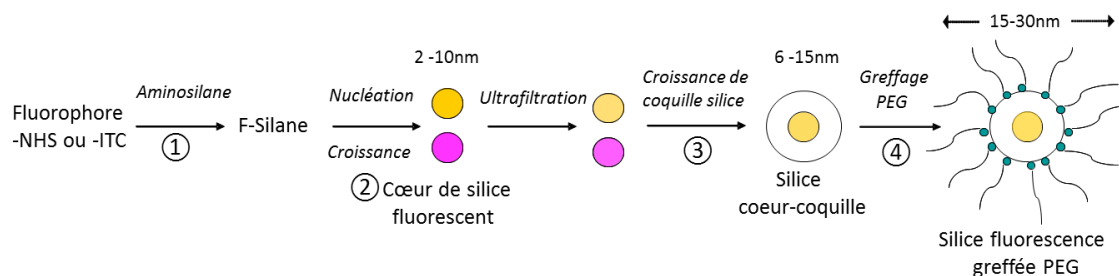


**Figure 6.1** Aperçu des étapes successives de synthèse des nanoparticules de silice fluorescentes greffées PolyEthylèneGlycol.

Parmi les quatre fluorophores choisis pour être greffés de manière covalente dans la silice (fluorescéine isothiocyanate, rhodamine B isothiocyanate, Dylight 680 N-hydroxy succinimide et Dylight 800 N-hydroxy succinimide), le dernier a été écarté : après greffage, un décalage spectral de 100 nm vers le bleu se produit en solvant polaire, nuisant à la séparation spectrale entre les codes. Ce phénomène a été identifié comme dû à une polymérisation partielle des fluorophores silanisés. Pour limiter ce phénomène, nous avons donc choisi d'effectuer la silanisation des autres fluorophores dans le DMSO anhydre. Comparés aux deux autres fluorophores restants, le taux d'encapsulation de la fluorescéine s'est montré bien inférieur, probablement dû à une conjonction de sa charge négative entraînant une répulsion électrostatique avec la silice et le groupement ITC, moins réactif que le groupe NHS.

Nous avons aussi mesuré le rendement de greffage du PEG-silane à la surface de nos nanoparticules. Malgré le milieu de réaction aqueux, l'hydrolyse totale du PEG-triéthoxysilane ne conduit pas à sa condensation sur lui-même en présence de particules ; nous en déduisons que la réaction du PEG-silanol sur la silice est plus favorable que l'auto-polymérisation.

Après avoir optimisé notre réaction, nous nous sommes penchés sur la caractérisation des propriétés de fluorescence de nos matériaux. Leurs spectres d'absorption et d'émission, très comparables aux spectres des fluorophores libres, mettent néanmoins en évidence une brillance (intégrale du spectre de fluorescence divisée par l'absorbance à la longueur d'onde d'excitation) des fluorophores encapsulés 2,5 fois supérieure aux fluorophores libres. Le rendement quantique calculé avec des méthodes classiques nous a conduits à des valeurs supérieures à 1, ce qui n'a pas de sens physiquement : ceci met en évidence le besoin de tenir compte dans le calcul de l'environnement local du fluorophore, eau dans le cas du fluorophore libre et silice dans le cas des particules.

Comme nous pouvions nous y attendre, nous avons aussi mesuré une augmentation de la valeur de polarisation de fluorescence (FP) des trois fluorophores au fil des étapes de synthèse et de la croissance des nano-objets. En chargeant fortement les particules en fluorophore, nous avons réussi à moduler cette valeur de FP, grâce à une dépolariation partielle par homo-FRET quand la distance entre fluorophores passe sous un certain seuil, ouvrant des perspectives pour un codage dans la dimension FP en plus de la dimension ‘intensité de fluorescence’.

Finalement, nous avons mesuré une augmentation de la résistance au photoblanchiment des fluorophores une fois encapsulés dans la silice, surtout dans le cas de la rhodamine B. Cela est en accord avec les publications dans le domaine : la matrice de silice offre une barrière efficace contre la photo-oxydation des fluorophores. Tous ces résultats mettent bien en évidence que nos matériaux, les plus petites nanoparticules de silice fluorescente jamais synthétisées, améliorent bien les propriétés des fluorophores qu’elles encapsulent.

### 6.3 Nanoparticules de silice aux interfaces eau/huile fluorée

Avant d’incorporer les nanoparticules de silice dans les gouttes, nous avons au préalable étudié l’impact éventuel des premières sur la stabilité des secondes. En effet, des particules solides sont fréquemment utilisées pour stabiliser des émulsions par *pickering* : les nanoparticules dispersées dans une des phases tendent à spontanément migrer vers l’interface. Nous avons voulu voir si en présence de tensioactif, une compétition ou une synergie entre les deux entités stabilisatrices a lieu. Nous avons donc tout d’abord mesuré la taille de gouttes générées sur puce microfluidique à différents débits relatifs huile/eau et concentration en particules dans la phase aqueuse : aucune influence de ce dernier paramètre sur le volume des gouttes n’a été détectée : nous en déduisons qu’à des échelles de temps sub-milliseconde, la tension interfaciale n’est pas modifiée par les particules.

Nous avons ensuite étendu l’étude de la dynamique d’adsorption jusqu’à une seconde, à l’aide d’un prototype de tensiomètre dynamique sur puce actuellement mis au point par Baret et Brosseau à l’institut Max Planck de Göttingen. Quel que soient les paramètres testés (concentration ou diamètre des particules, présence ou non de PEG en surface), seules des différences mineures ont été observées, ne permettant pas de conclure sur un impact des particules sur la dynamique sub-seconde d’adsorption du tensioactif à l’interface.

Nous avons donc ensuite étendu l’étude à la dynamique jusqu’à 300 s, via un dispositif classique de goutte pendante. Cette fois, une influence notable des particules a été observée : en



l'absence de tensioactif, elles réduisent la tension interfaciale à temps courts d'autant plus que leur concentration est importante. Combinées au tensioactif, il apparaît qu'elles ralentissent l'adsorption de celui-ci : il semble donc y avoir compétition entre les deux espèces. Enfin, nous observons une influence drastique du PEG dans la diminution de tension interfaciale, qu'il soit greffé aux particules ou libre en solution.

Nous avons conclu notre étude des particules dans les gouttes stabilisées par du tensioactif par un suivi de leur stabilité sur plusieurs jours en présence ou absence de particules : aucune amélioration notable de la résistance à la coalescence n'a été observée, contrairement à plusieurs antécédents dans la littérature. Ceci est sans doute dû à la prépondérance du tensioactif dans le processus de stabilisation : des expériences complémentaires avec peu ou pas de tensioactif nous permettraient d'en savoir plus. Par contre, le suivi d'une émulsion contenant 50 % de gouttes avec particules et 50 % sans a mis en évidence un important transport d'eau entre gouttes dû à un déséquilibre osmotique. Pour le codage par la suite, il faut donc équilibrer les potentiels chimiques dans toutes les gouttes, en utilisant une dispersion de nanoparticules non fluorescentes pour diluer les particules fluorescentes, afin d'avoir la même concentration totale en particules dans toutes les gouttes.

### 6.4 Banques de gouttes codées en fluorescence

Après cette étude de l'impact des particules sur la stabilité des gouttes, nous pouvions désormais nous atteler à notre objectif initial : fabriquer des banques de gouttes encodées par plusieurs couleurs de nanoparticules fluorescentes. Avant de commencer, nous avons passé en revue tous les paramètres à considérer et optimiser dans la mise au point de la plate-forme de codage : (i) le choix du montage optique (lasers, filtres, détecteurs) en fonction des fluorophores choisis ; (ii) la gamme de concentration de nanoparticules fluorescentes optimale en termes de linéarité, de gamme dynamique des photomultiplicateurs (PMTs), de minimisation du recouvrement spectral et des effets osmotiques ; (iii) l'espacement entre les niveaux de code au sein d'une même couleur, par rapport à l'écart-type pour chaque niveau et le pourcentage toléré d'erreur de recouvrement entre les populations ; (iv) les précautions à prendre lors de l'encapsulation en gouttes pour minimiser la contamination croisée et la dispersion de concentration lors de l'écoulement ; (v) le gain optimal de chaque PMT par rapport à la gamme de concentration choisie pour chaque fluorophore.

Nous avons ensuite généré des codes avec deux puis trois couleurs (**Figure 6.2**). En combinant les couleurs est apparu le problème de *crosstalk*. Celui-ci est dû au recouvrement partiel des spectres d'émission des différents fluorophores, qui émettent sur plusieurs canaux de

détection au lieu d'un seul. En changeant les filtres d'émission, nous avons pu le réduire. Ensuite, deux stratégies ont été appliquées pour le compenser totalement, basées sur l'inversion de la matrice de recouvrement spectral : compensation visuelle ou orthogonalisation numérique des données.

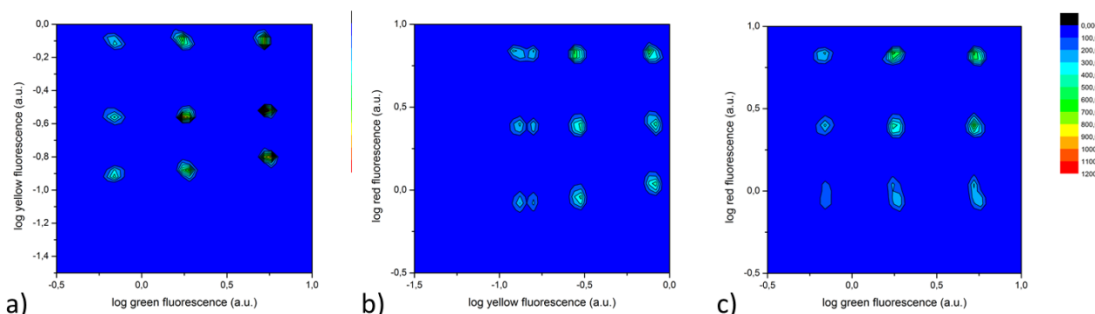


**Figure 6.2** Code à 3 couleurs (fluorescéine, rhodamine B et Dylight 680) et 27 combinaisons : a) projection sur le plan vert-jaune, b) projection sur le plan jaune-rouge, c) projection sur le plan vert-rouge. Sur a) et b), les points ne sont pas équidistants à cause du recouvrement spectral entre fluorophores.

Enfin, connaissant la dispersion de fluorescence pour chaque code, nous avons pu déterminer le nombre maximal de codes par couleur en fonction du taux de recouvrement acceptable suivant le test biologique envisagé. Notre système, de par sa dispersion assez réduite, permet aussi bien d'encoder des tests à très faible tolérance de recouvrement comme du diagnostic de mutations rares, que de larges banques de composés. En combinant toutes les dimensions de codage, notre système, poussé à ses limites, peut permettre de générer près de 50.000 codes distincts avec environ 15 % de recouvrement entre niveaux. Pour atteindre des capacités de codage encore plus grandes, reste à améliorer encore davantage le montage optique pour réduire le *crossstalk*, à augmenter la gamme dynamique dans chaque canal et à utiliser des particules qui permettent de moduler la FP.

## 6.5 Conclusion et perspectives

Ce travail de thèse a permis de faire un pas supplémentaire vers la généralisation de tests de criblage à haut débit en microfluidique en gouttes. Dans ce but, nous avons mis au point une nouvelle gamme de fluorophores, des nanoparticules de silice fluorescentes, les plus petites jamais synthétisées (à partir de 2.5 nm). Leur taille réduite, combinée à leurs excellentes propriétés optiques (photoblanchiment réduit, fluorescence exaltée) et à leur facilité de greffage, en font un matériau à fort potentiel pour des applications de diagnostic et d'imagerie cellulaire à haute

résolution. Nous avons aussi mis en évidence leur interaction avec le tensioactif dans la stabilisation des gouttes. Enfin, en combinant jusqu'à trois couleurs de nanoparticules, nous avons réalisé un code en fluorescence en gouttes microfluidiques, ouvrant la voie au criblage de banques de plusieurs milliers de composés en quelques minutes, mais aussi à de multiples autres applications : diagnostic de cancers, PCR digitale, évolution dirigée et bien d'autres.



# Appendix A. Fluorinated compounds

## A.1 Fluorinated oil HFE 7500

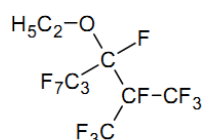


Figure A.1 Molecular structure of HFE 7500 fluorinated oil. MW = 414 g/mol

## A.2 Fluorinated surfactant EA

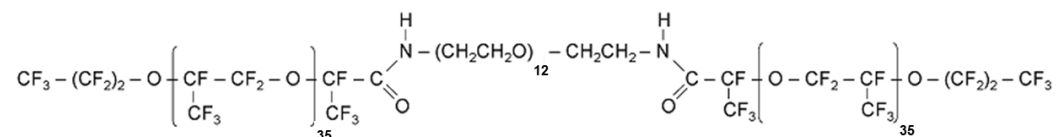
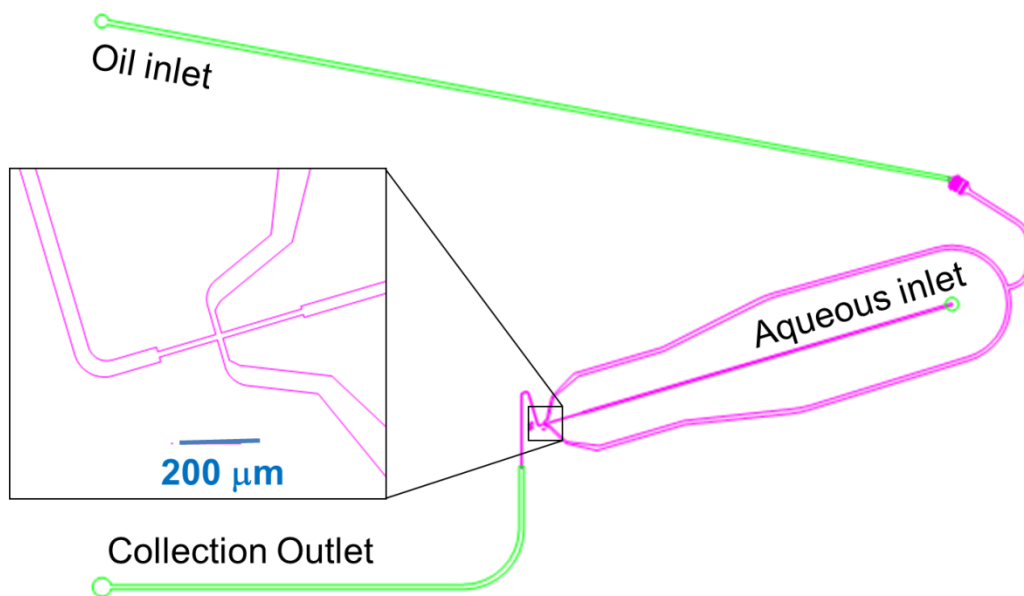


Figure A.2 Molecular structure of EA surfactant. MW = 12750 g/mol



# Appendix B. Microfluidic designs

## B.1 Library generation chip ‘LRS 6.6’



**Figure B.1** AutoCAD drawing of the LRS 6.6 library generation chip. Pink channels are: 20  $\mu\text{m}$  deeps, green channels are 100  $\mu\text{m}$  deep.

## B.2 ‘Dropslot’ emulsion analysis chip



**Figure B.2** AutoCAD drawing of the ‘Dropslot’ emulsion analysis chip. Pink channels are: 25  $\mu\text{m}$  deep, blue channels are 260  $\mu\text{m}$  deep.

### B.3 Library reinjection chip ‘test 32.2’

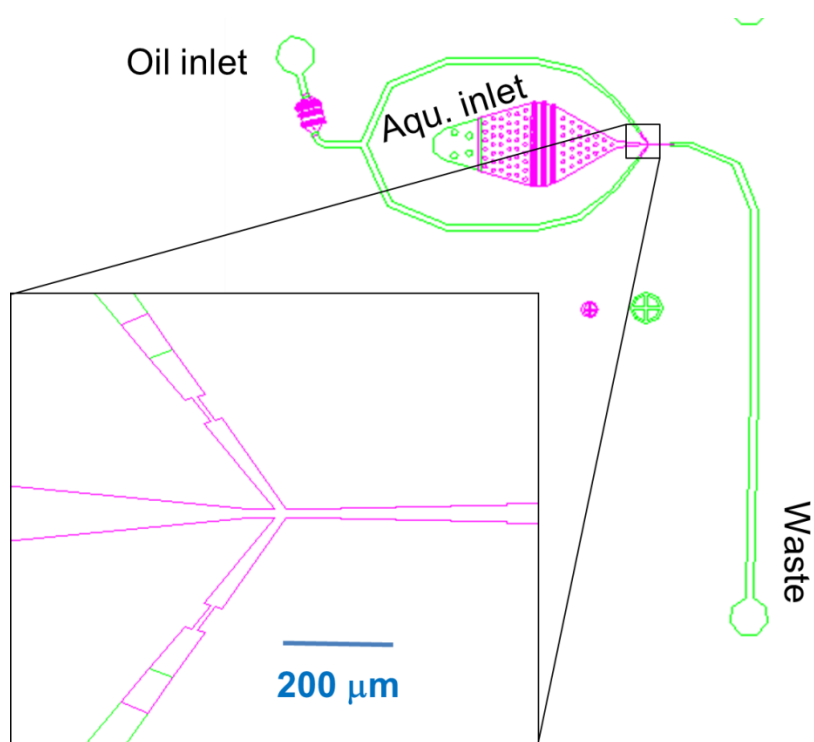


**Figure B.3** AutoCAD drawing of the ‘test 32.2’ library reinjection chip. Pink channels are: 20 μm deep, green channels are 100 μm deep.



# Appendix C. Optical stations

## C.1 'PLS 3' station

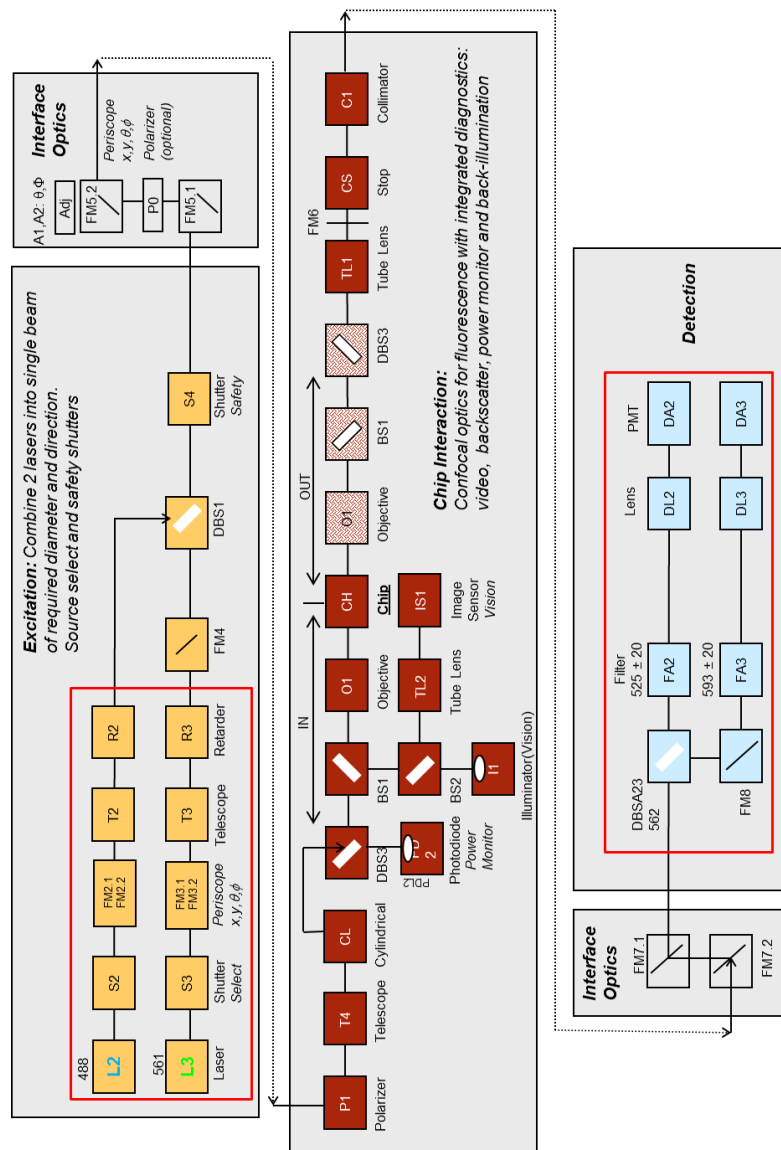


**Figure C.1** Detailed schematic of PLS3 setup. The system is utilizing two different lasers to excite the fluorophores, and is capable to detect two distinct wavelengths.



**FLUORESCENT SILICA NANOPARTICLES FOR  
MULTIDIMENSIONAL BARCODING IN DROPLETS:  
TOWARDS HIGH-THROUGHPUT SCREENING IN TWO-  
PHASE MICROFLUIDICS**

## Résumé

Le criblage à haut débit a connu des avancées significatives en 20 ans. Néanmoins, les technologies microplaque ou *microarray* ne sont pas toujours optimales. C'est pourquoi de nouvelles plates-formes, basées sur la microfluidique en gouttes, pourraient significativement augmenter le débit et réduire les coûts.

Cependant, une fois en dehors de la puce, les gouttes perdent leur information spatiale : il est donc nécessaire de marquer les molécules encapsulées pour les identifier. Nous avons choisi un marquage fluorescent, car cette technique est très utilisée en biologie. Le but de ce travail était de fabriquer un matériau fluorescent compatible avec la microfluidique en gouttes, puis de produire plusieurs banques de gouttes encodées avec ce matériau.

Nous avons opté pour des nanoparticules de silice comprenant un fluorophore organique attaché de manière covalente. Notre nouvelle synthèse a produit des particules de 2,5 nm, les plus petites jamais synthétisées. Elles sont plus brillantes que les fluorophores organiques, résistent mieux au photoblanchiment et ont une polarisation modulable.

Nous avons ensuite étudié les propriétés de surface des particules, en particulier leur interaction avec le tensioactif. A temps longs, une compétition se produit. De plus, des effets osmotiques ont été mis en évidence, si la concentration en particules varie entre d'une goutte à l'autre.

Enfin, nous avons examiné les paramètres majeurs dans l'élaboration du code, les optimisations possibles et des stratégies pour réduire le recouvrement spectral. Nous avons produit des banques de gouttes encodées avec deux et trois couleurs, qui peuvent être utilisées dans de nombreuses applications.

Mots-clés : criblage à haut débit, microfluidique en gouttes, nanoparticules, fluorescence, silice, codage

## Résumé en anglais

High-throughput screening has seen significant advances in the last 20 years. However, microtiter plate or microarray technologies are not optimal for all types of assays. Hence, implementation of droplet-based microfluidic platforms could bring a breakthrough in terms of throughput and reduction of costs.

However, once out of the chip, droplets lose positional information to identify drop contents. It is thus necessary to label the encapsulated compounds. Since fluorescence is a common assay readout method, we opted for this strategy. The goal of this PhD was to produce a fluorescent material compatible with the specificities of droplet microfluidics, then to generate several optically encoded droplet libraries with it.

We opted for silica nanoparticles (SNPs) covalently encapsulating organic fluorophores. We developed a novel synthesis route that enabled us to reach sizes down to 2.5 nm, the smallest ever synthesized. The SNPs are brighter than starting fluorophores, better resist photobleaching and have tunable fluorescence polarization.

Then, we studied the surface properties of these particles, especially their interaction with the surfactant. At long time scales, competition between particles and surfactant was shown. In addition, dramatic osmotic effects were highlighted in case of unequal particle concentration across droplets.

Last, we investigated crucial parameters in fluorescent code design, then generated two- and three-color encoded droplet libraries. We also discussed optimizations and on-the-fly identification. We finally identify many applications would benefit from this encoding system.

Keywords: high-throughput screening, droplet-based microfluidics, nanoparticles, fluorescence, silica, coding